



January 2015

Development Of Molecular Biosensors And Multifunctional Graphene-Based Nanomaterials

Xu Wu

[How does access to this work benefit you? Let us know!](#)

Follow this and additional works at: <https://commons.und.edu/theses>

Recommended Citation

Wu, Xu, "Development Of Molecular Biosensors And Multifunctional Graphene-Based Nanomaterials" (2015). *Theses and Dissertations*. 1851.
<https://commons.und.edu/theses/1851>

This Dissertation is brought to you for free and open access by the Theses, Dissertations, and Senior Projects at UND Scholarly Commons. It has been accepted for inclusion in Theses and Dissertations by an authorized administrator of UND Scholarly Commons. For more information, please contact und.common@library.und.edu.

DEVELOPMENT OF MOLECULAR BIOSENSORS AND MULTIFUNCTIONAL
GRAPHENE-BASED NANOMATERIALS

by

Xu Wu
Master of Science, Hunan University, 2010

A Dissertation

Submitted to the Graduate Faculty

of the

University of North Dakota

In partial fulfillment of the requirements

for the degree of

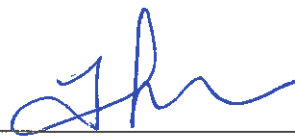
Doctor of Philosophy

Grand Forks, North Dakota

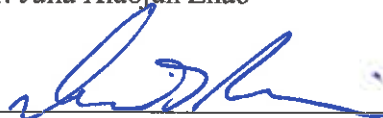
May
2015

Copyright 2015 Xu Wu

This dissertation, submitted by Xu Wu in partial fulfillment of the requirements for the Degree of Doctor of Philosophy from the University of North Dakota, has been read by the Faculty Advisory Committee under whom the work has been done, and is hereby approved.



Dr. Julia Xiaojun Zhao



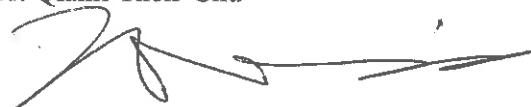
Dr. David T. Pierce



Dr. Alena Kubátová



Dr. Qianli 'Rick' Chu



Dr. Min Wu

This dissertation is being submitted by the appointed advisory committee as having met all of the requirements of the Graduate School at the University of North Dakota and is hereby approved.



Wayne Swisher
Dean of the School of Graduate Studies

February 25, 2015

Date

PERMISSION

Title Development of Molecular Biosensors and Multifunctional
Graphene-Based Nanomaterials

Department Chemistry

Degree Doctor of Philosophy

In presenting this dissertation in partial fulfillment of the requirements for a graduate degree from the University of North Dakota, I agree that the library of this University shall make it freely available for inspection. I further agree that permission for extensive copying for scholarly purposes may be granted by the professor who supervised my dissertation work or, in her absence, by the Chairperson of the department or the dean of the School of Graduate Studies. It is understood that any copying or publication or other use of this dissertation or part thereof for financial gain shall not be allowed without my written permission. It is also understood that due recognition shall be given to me and to the University of North Dakota in any scholarly use which may be made of any material in my dissertation.

Xu Wu
May 2015

TABLE OF CONTENTS

LIST OF FIGURES	IX
LIST OF TABLES	XVIII
LIST OF SCHEMES.....	XIX
ACKNOWLEDGEMENTS.....	XX
ABSTRACT.....	XVII
CHAPTER	
I. A REVERSIBLE FLUORESCENT LOGIC GATE FOR SENSING MERCURY AND IODIDE IONS BASED ON A MOLECULAR BEACON	1
1. INTRODUCTION	1
2. EXPERIMENTAL SECTION	3
2.1. <i>Chemicals and Instruments.</i>	3
2.2. <i>Investigation of Feasibility of the Logic Gates.</i>	3
2.3. <i>Investigation of Reversibility of the Logic Gate.</i>	4
2.4. <i>Detection of Hg²⁺.</i>	4
2.5. <i>Detection of I⁻.</i>	5
3. RESULTS AND DISCUSSION.....	5
3.1. <i>Design of the Logic Gate.</i>	5
3.2. <i>Optimization of the Logic Gate Conditions.</i>	10
3.3. <i>Hg²⁺ Detection.</i>	12
3.4. <i>Iodide Ion Detection.</i>	14
3.5. <i>Real Sample Detection.</i>	16
4. CONCLUSIONS.....	16
II. ULTRASENSITIVE DETECTION OF 3'→5' EXONUCLEASE ENZYMATICAL ACTIVITY USING MOLECULAR BEACONS	18
1. INTRODUCTION	18
2. EXPERIMENTAL SECTION	20
2.1. <i>Chemicals and Materials.</i>	20
2.2. <i>Apparatus</i>	20
2.3. <i>Exo III Detection Based on FAM-MB.</i>	21
2.4. <i>Distinguishing Exonucleases Based on Dual-MB System.</i>	22
3. RESULTS AND DISCUSSION.....	22

3.1. <i>Detection of Exo III with MB</i>	22
3.2. <i>The Stability and Effect of Ions</i>	26
3.3. <i>Design of Dual-MB System</i>	27
3.4. <i>Complex Samples Investigation</i>	29
4. CONCLUSIONS.....	34
III. LABEL-FREE FLUORESCENCE ASSAY COUPLED EXONUCLEASE REACTION AND SYBR GREEN I FOR THE DETECTION OF T4 POLYNUCLEOTIDE KINASE ACTIVITY	
1. INTRODUCTION	35
2. EXPERIMENTAL	36
2.1. <i>Materials and Apparatus</i>	36
2.2. <i>T4 PNK Detection and Optimization</i>	37
2.3. <i>T4 PNK Inhibitor Evaluation</i>	37
3. RESULTS AND DISCUSSION.....	37
3.1. <i>Scheme of the T4 PNK Activity Detection</i>	37
3.2. <i>Optimization of SG Concentration</i>	39
3.3. <i>Optimization of the Detection Parameters</i>	40
3.4. <i>Monitoring of the Phosphorylation Process of T4 PNK</i>	43
3.5. <i>Inhibition Investigation</i>	44
4. CONCLUSIONS.....	44
IV. FABRICATION OF HIGHLY FLUORESCENT GRAPHENE QUANTUM DOTS USING L-GLUTAMIC ACID FOR <i>IN VITRO/IN VIVO</i> IMAGING AND SENSING	
1. INTRODUCTION	46
2. EXPERIMENTAL SECTION.....	48
2.1. <i>Materials</i>	48
2.2. <i>Synthesis of GQDs</i>	48
2.3. <i>Characteristics of GQDs</i>	49
2.4. <i>Detection of Quantum Yields</i>	49
2.5. <i>Detection of Fluorescence Lifetime</i>	50
2.6. <i>In Vitro Fluorescence Imaging of Cells</i>	50
2.7. <i>In Vivo Fluorescence Imaging of Mice</i>	50
2.8. <i>Detection of H₂O₂ Based on the GQD's Catalytic Activities</i>	51
3. RESULTS AND DISCUSSION.....	51
3.1. <i>Design of the Highly Fluorescent GQDs</i>	51
3.2. <i>Characterization of the Morphology and Composites of the GQDs</i>	53
3.3. <i>Fluorescence Properties of the GQDs</i>	56
3.4. <i>In Vitro Fluorescence Imaging Using GQDs</i>	62

3.5. <i>In Vivo Fluorescence Imaging Using GQDs.</i>	63
3.6. <i>Colorimetric Detection of H₂O₂ Using GQDs.</i>	64
4. CONCLUSIONS	68
V. ONE-POT SYNTHESIS OF REDUCED GRAPHENE OXIDE/METAL (OXIDE) NANOCOMPOSITES AND ITS APPLICATION FOR ELECTROCHEMICAL ANALYSIS	69
1. INTRODUCTION	69
2. EXPERIMENTAL SECTION.....	72
2.1. <i>Materials.</i>	72
2.2. <i>Preparation of RGO/Metal (Oxide) Nanocomposites.</i>	72
2.3. <i>Characterization.</i>	73
2.4. <i>Electrochemical Measurement.</i>	73
3. RESULTS AND DISCUSSION.....	74
3.1. <i>Design and Synthesis of the RGO/Metal (Oxide) Nanocomposites.</i> .	74
3.2. <i>Characterization of Designed Nanocomposites.</i>	76
3.3. <i>Optimization of Nanocomposite Synthesis.</i>	83
3.4. <i>Electrochemical Detection of L-AA, DA and UA using a RGO/Au- Modified GCE as a Catalyst.</i>	87
4. CONCLUSION	95
VI. ENHANCED SYNERGETIC ANTIBACTERIAL PROPERTIES OF REDUCE GRAPHENE OXIDE/AG NANOCOMPOSITE.....	96
1. INTRODUCTION.	96
2. MATERIALS AND METHODS.	98
2.1. <i>Materials and Instruments.</i>	98
2.2. <i>Preparation of RGO/Ag Nanocomposite.</i>	99
2.3. <i>Antibacterial Activity Tests.</i>	99
2.4. <i>Cell Wall/Membrane Integrity Investigation.</i>	100
2.5. <i>Cytotoxicity of RGO/Ag Nanocomposite to Mammalian Cells.</i>	100
2.6. <i>Detection of Reactive Oxygen Species (ROS).</i>	101
3. RESULTS AND DISCUSSION.....	101
3.1. <i>Synthesis and Characterization of RGO/Ag Nanocomposite.</i>	101
3.2. <i>Photothermal Effect of RGO/Ag Nanocomposite.</i>	104
3.3. <i>Synergistically Enhanced Antibacterial Activity of RGO/Ag Nanocomposite.</i>	105
3.4. <i>RGO/Ag Nanocomposite Caused Cell Integrity Disruption and ROS Generation with the Irradiation.</i>	108
3.5. <i>Cytotoxicity Investigation.</i>	111
4. CONCLUSIONS.....	112

VII. LONG RANGE FLUORESCENCE QUENCHING OF GRAPHENE OXIDE WITH RIGID SILICA SHELL AS TUNABLE SPACER.....	113
1. INTRODUCTION	114
2. METHODS AND MATERIALS.	115
2.1. <i>Materials and Instruments</i>	115
2.2. <i>Synthesis of SiNPs@TAMRA</i>	116
2.3. <i>Formation of SiNPs@TAMRA@Si-NH₂</i>	116
2.4. <i>Formation of SiNPs@Rubpy@Si-NH₂</i>	117
2.5. <i>Fluorescence Quenching Investigation</i>	117
2.6. <i>Fluorescence Lifetime Measurement</i>	118
3. RESULTS AND DISCUSSION.....	118
3.1. <i>Design of SiNPs@TAMRA@Si-NH₂ Wrapped with GO</i>	118
3.2. <i>Characterization of GO</i>	119
3.3. <i>Fluorescence Quenching of GO to SiNPs@TAMRA@Si-NH₂</i>	120
3.4. <i>Fluorescence Quenching of GO to SiNPs@Rubpy@Si-NH₂</i>	125
4. CONCLUSIONS.....	128
VIII. GRAPHENE OXIDE KILLS KLEBSIELLA PNEUMONIA BACTERIUM IN MACROPHAGES AND IN MICE.....	129
1. INTRODUCTION	129
2. METHODS AND MATERIALS.	131
2.1. <i>Materials and Instruments</i>	131
2.2. <i>Antibacterial Activity Tests</i>	132
2.3. <i>Cell Infection</i>	133
2.4. <i>Mouse Infection</i>	133
2.5. <i>Statistical Analysis</i>	135
3. RESULTS AND DISCUSSION.....	135
3.1. <i>Characterization of GO</i>	135
3.2. <i>Antibacterial Property of GO at the Level of Bacteria</i>	137
3.3. <i>GO Increases Host Cells Resistance to Kp</i>	138
3.4. <i>GO Increases Resistance to Kp in Mice</i>	139
4. CONCLUSIONS.....	145
REFERENCES	146

LIST OF FIGURES

Figure	Page
1. (A) Fluorescence intensities of the MB logic gate at 518 nm in the presence of different inputs. (B) Truth table for the INHIBIT logic gate	7
2. Real-time fluorescence intensities of the MB logic gate with the addition of Hg ²⁺ (200 nM) and I ⁻ (12.80 μM). λ _{ex} = 480 nm, λ _{em} = 518 nm	8
3. Fluorescence emission spectra of the MB logic gate to different inputs: a) I ⁻ (0 μM) + Hg ²⁺ (0 nM); b) I ⁻ (6.40 μM) + Hg ²⁺ (0 nM); c) I ⁻ (0 μM) + Hg ²⁺ (200 nM); d) I ⁻ (6.40 μM) + Hg ²⁺ (200 nM).	9
4. Reversible fluorescence signal changes of the MB logic gate with cyclic treatment of Hg ²⁺ (200 nM) and I ⁻ (0.40 μM)	10
5. (A) Fluorescence intensity of the logic gate at different concentrations of assistant probe. 1: without Hg ²⁺ ; 2: 300 nM Hg ²⁺ . (B) The fluorescence intensity ratio of the logic gate with 300 nM Hg ²⁺ to that without 300 nM Hg ²⁺ changed with the concentration of the assistant probe. MB: 10 nM; temperature: 32°C; λ _{ex} = 480 nm, λ _{em} = 518 nm. (C) Fluorescence intensity of the sensor at different temperatures. F: fluorescence intensity of the sensor in the presence of the 300 nM Hg ²⁺ ; F ₀ : fluorescence intensity of the sensor in the absence of the Hg ²⁺ . MB: 10 nM; assistant probe: 200 nM. λ _{ex} = 480 nm, λ _{em} = 518 nm	11
6. (A) Fluorescence response of the MB logic gate to Hg ²⁺ . The fluorescence emission spectra are shown for different Hg ²⁺ concentrations from 0, 10, 50, 100, 200, 500 to 1000 nM. (B) Changes of the fluorescence intensity at 518 nm of the MB based logic gate with different concentrations of Hg ²⁺ . The inset is the calibration curve of the MB based logic gate to the detection of Hg ²⁺	13
7. Interference test of different metal ions for the logic gate. Concentration of Hg ²⁺ : 200 nM; concentration of other metal ions: 1000 nM	13
8. (A) Fluorescence response of the MB logic gate to I ⁻ ions. The fluorescence emission spectra are shown for different I ⁻ concentrations from 0, 0.05, 0.10, 0.20, 0.40, 0.80, 1.60, 3.20, 6.40 to 12.80 μM. (B) Changes of the fluorescence intensity at 518 nm of the MB based logic gate with different concentrations of I ⁻ . The inset is the calibration curve of the MB based logic gate for the detection of I ⁻	15

9. Interference study of different anions to the MB-based logic gate. The concentration of all the ions: 6.40 μ M	15
10. (A) The working principle of the detection of Exo III enzymatic activity based on FAM-MB. (B) Fluorescence emission spectra of 10 nM FAM-MB in 50 μ L 1X NEBuffer 4. (a) 4.00 U/mL Exo III; (b) 4.00 U/mL heat-inactivated Exo III; (c) no Exo III. λ_{ex} = 480 nm	23
11. The detection of Exo III based on FAM-MB. (A) Time-dependent fluorescence responses in the presence of different concentrations of Exo III. From bottom to top: 0, 0.04, 0.10, 0.20, 0.40, 1.00, 2.00, 4.00, 8.00 U/mL of Exo III in 1 \times NEBuffer 4. (B) The plot of the fluorescence enhancement of different concentrations of Exo III. Reactions were performed in 50 μ L of 1 \times NEBuffer 4 with 10 nM FAM-MB at 37 $^{\circ}$ C for 200 s. Inset: the two calibration curves in different concentration ranges. (C) Selectivity of the assay for Exo III over other exonucleases. Fluorescence enhancement of the FAM-MB system responded to 4.00 U/mL exonucleases.....	24
12. The stability investigation of the MB system for the detection of Exo III. (A) The effect of pH on the reaction rate of the MB system to Exo III. (B) The effect of divalent ions on the Exo III activity of the MB system to Exo III	26
13. The fluorescence intensity responded to 10 nM FAM-MB (a), added with 4.00 U/mL T5 exoclease (b) or 4.00 U/mL Exo III (c).....	27
14. (A) Schematic illustration of the dual-MB system for distinguishing different exonucleases. (B) Fluorescence enhancement patterns of the dual-MB system with 4.00 U/mL Exo III, T5 exonuclease and RecJf. The dual-MBs system 20 contained 10 nM FAM-MB and 10 nM Cy5-MB in 50 GL of 1 \times NEBuffer 4, incubated at 37 $^{\circ}$ C for 200 s to detect the fluorescence intensity. λ_{ex} (FAM)=480 nm, λ_{em} (FAM)= 518 nm. λ_{ex} (Cy5)= 645 nm, λ_{em} (Cy5)= 660 nm	28
15. The fluorescence enhancements of FAM-MB in different solutions. The concentrations of Exo III were 4.00 U/mL	30
16. (A) The fluorescence enhancements of FAM-MB and Cy5-MB in 10 times diluted fetal bovine serum with the addition of 4 U/mL Exo III, T5 Exo and RecJf Exo. (B) Time-dependent fluorescence responses in the presence of different concentrations of Exo III. From bottom to top: 0, 0.04, 0.20, 0.40, 2.00, 4.00, 8.00 U/mL of Exo III in 10 times diluted fetal bovine serum. (C) The plot of the fluorescence enhancement of different concentrations of Exo III. Reactions were performed in 50 μ L of 10 times diluted fetal bovine serum with 10 nM FAM-MB and 10 nm Cy5-MB at 37 $^{\circ}$ C for 200 s. Inset: the two calibration curves in different concentration ranges	32

17. (A) Time-dependent fluorescence responses in the presence of different concentrations of Exo III. From bottom to top: 0, 0.08, 0.20, 0.40, 0.80, 2.00, 4.00, 8.00 U/mL of Exo III in 10 times diluted fresh mice serum. (C) The plot of the fluorescence enhancement of different concentrations of Exo III. Reactions were performed in 50 μ L of 10 times diluted fresh mice serum with 10 nM FAM-MB and 10 nM Cy5-MB at 37 $^{\circ}$ C for 200 s. Inset: the two calibration curves in different concentration ranges	33
18. Schematic diagram of monitoring the T4 PNK activity by a label-free DNA probe coupled with SG and λ exo.	38
19. Fluorescence spectra of the dsDNA system without T4 PNK (a) and with 20 U/mL T4 PNK (b). Reactions were performed in 100 μ L of 1x NEBuffer 4 (pH = 7.9) with 20 nM dsDNA at 37 $^{\circ}$ C for 30 min. The concentrations of ATP and λ exo were 0.1 mM and 0.25 units, respectively. $\lambda_{ex} = 480$ nm.	39
20. (A) Fluorescence spectra of 40 nM SG incubated with 20 nM ssDNA (Curve a) and dsDNA (Curve b). (B) Fluorescence intensity of dsDNA and ssDNA with the change of the concentration of SG. (C) The fluorescence intensity ratio of dsDNA to ssDNA with the change of the concentration of SG. Fluorescence intensity was measured in 100 μ L of 1x NEBuffer 4 (pH = 7.9) with 20 nM ssDNA or dsDNA at 37 $^{\circ}$ C. $\lambda_{ex} = 480$ nm.....	40
21. (A) Optimization of ATP concentration. The concentrations of λ exo, dsDNA, and T4 PNK were 1 unit, 20 nM, and 20 U/mL, respectively. (B) Optimization of the amount of λ exo. Inset: the relationship of signal-to-background ratio with the amount of λ exo. The concentrations of dsDNA, ATP and T4 PNK were 20 nM, 0.1 mM and 20 U/mL, respectively. (C) Optimization of the reaction time. The concentrations of λ exo, dsDNA, ATP and T4 PNK were 0.25 units, 20 nM, 0.1 mM and 20 U/mL, respectively. $\lambda_{ex} = 480$ nm... ..	41
22. Monitoring the T4 PNK activity. (A) Relative fluorescence intensity with different concentrations of T4 PNK (top to bottom, 0, 0.25, 0.50, 1.00, 5.00, 10.00, 20.00 U/mL). (B) Concentration curve for T4 PNK. Inset indicated the linear relationship between fluorescence intensity change and the concentration of T4 PNK from 0 to 1.00 U/mL. Fluorescence intensity was measured in 100 μ L of 1x NEBuffer 4 (pH = 7.9) at 37 $^{\circ}$ C after 30 min incubation. The concentrations of λ exo, dsDNA, and ATP were 0.25 units, 20 nM, and 0.1 mM, respectively. $\lambda_{ex} = 480$ nm.... ..	43
23. The effect of different concentrations of T4 PNK inhibitor. (A) Effect of (NH ₄) ₂ SO ₄ (0-120 mM); (B) Effect of Na ₂ HPO ₄ (0-90 mM). Fluorescence intensity was measured in 100 μ L of 1x NEBuffer 4 (pH = 7.9) at 37 $^{\circ}$ C after 30 min incubation. The concentrations of λ exo, dsDNA, ATP and T4 PNK were 0.25 units, 20 nM, 0.1 mM, and 10 U/mL respectively. $\lambda_{ex} = 480$ nm..... ..	44

24. (A) The HRTEM image of GQDs with a scale bar of 5 nm. Inset: A typical single GQD with the lattice parameter of 0.246 nm. The scale bar was 1 nm; (B) The size distribution of GQDs calculated from more than 100 dots.....	53
25. EDS spectra of L-glutamic acid (A) and GQDs (B), and the relative atomic percentage of L-glutamic acid and GQDs(C)	54
26. (A) Raman spectra of GQDs. (B) XRD patterns of GQDs.....	55
27. (A) FT-IR spectra of L-glutamic acid (a) and GQDs (b). (B) The zeta potential of GQDs in different pH solutions	55
28. (A) The absorption (curve a), excitation (curve b) and emission spectra (curve c) of GQDs. Inset: from left to right are the GQDs solutions under bright light, violet, blue and green irradiation, respectively; (B) Fluorescence emission spectra of GQDs with different excitation wavelengths; (C) - (E) The confocal fluorescence images of the GQDs under different excitation wavelengths. (C) 359 nm excitation; DAPI channel; (D) 488 nm excitation, LP 505 nm; (E) 514 nm excitation, BP 530-600 nm	57
29. Lifetime measurement curves for reference (a) and GQDs at different emission wavelengths with 370 nm LED irradiation. Emission wavelengths: (b) 445 nm; (c) 505 nm; (d) 650 nm, and (e) 815 nm.....	59
30. Comparison of the photostability of the GQDs with a fluorescent dye molecule FITC under the irradiation of a confocal laser. A, the confocal fluorescence images of FITC; B, the confocal fluorescence images of GQDs; C, the photostability of these two fluorescent materials; D, the effect of pH on the fluorescence intensity of the GQDs.....	60
31. (A) Fluorescence emission spectrum of the GQDs in the visible-NIR region. (B) NIR fluorescence spectra of the GQDs under different excitation wavelengths. (C) The NIR fluorescence intensity vs. the concentration of GQDs	61
32. Laser scanning confocal fluorescence microscopy images of MH-S cells. (A) Control MH-S cells without GQDs; (B) the MH-S cells treated with GQDs for 1 hour. All the scale bars was 20 μm	63
33. <i>In vivo</i> fluorescence imaging of mice injected GQDs subcutaneously (spot a) and intramuscularly (spot b). The images were taken under various excitation wavelengths and emission wavelengths indicated on the top of each image. A 100 μL aliquot of 25 mg/mL GQDs was injected into each spot. The following emission bandpass filters were used: GFP: 515-575 nm; DsRed: 575-650 nm; Cy5.5: 695-770 nm.....	64

34. UV-vis absorption spectra of the ABTS solution containing a) 9 mM H₂O₂; b) 2.7 mg/mL GQDs with 9 mM H₂O₂; and c) 2.7 mg/mL GQDs. Inset: The corresponding photographs of these three samples 65
35. Optimization of the reaction conditions for the detection of H₂O₂. (A) pH; (B) temperature; (C) concentration of ABTS; (D) concentration of GQDs 67
36. (A) The relationship of the absorption with the concentrations of H₂O₂ (from the bottom to the top: 0, 0.1, 0.2, 0.3, 0.4, 0.5, 1.0, 5.0 and 10.0 mM); (B) The calibration curve of the label-free colorimetric method for the detection of H₂O₂ 67
37. The STEM (A₁, B₁, C₁, D₁ and E₁) and FE-SEM (A₂, B₂, C₂, D₂ and E₂) images of GO (A₁ and A₂), RGO (B₁ and B₂), RGO/Au (C₁ and C₂), RGO/Ag (D₁ and D₂) and RGO/Cu₂O (E₁ and E₂) nanocomposites. Reaction conditions: 100.0 mL GO solution, 160.0 mg glucose, 80 μL NH₄OH was boiling for 20 min followed by the addition of 1.0 mL different metal precursors for another 15 min 78
38. EDS of RGO/Au (A), RGO/Ag (B) and RGO/ Cu₂O (C) nanocomposites. Reaction conditions: 100.0 mL GO solution, 160.0 mg glucose, 80.0 μL NH₄OH was boiling for 20 min followed by the addition of 1.0 mL different metal precursors for another 15 min 79
39. (A) Absorption spectra, of GO (a), RGO (b), RGO/Au (c), RGO/Cu₂O (d) and RGO/Ag (e) nanocomposites. (B) FT-IR spectra of glucose (a), GO (b), RGO (c), RGO/ Cu₂O (d), RGO/Au (e) and RGO/Ag (f) nanocomposites. (C) Raman spectra of GO (a), RGO (b), RGO/Au (c), RGO/ Cu₂O (d) and RGO/Ag (e) nanocomposites. (D) XRD patterns of GO (a), RGO (b), RGO/Au (c), RGO/ Cu₂O (d) and RGO/Ag (e) nanocomposites. Reaction conditions: 100.0 mL GO solution, 160.0 mg glucose, 80.0 μL NH₄OH was boiling for 20 min followed by the addition of 1.0 mL different metal precursors for another 15 min 81
40. (A) Absorption spectra of GO (curve a) and GO/Au nanocomposite (curve b) without glucose addition. (B) SEM images of the GO/Au nanocomposites without addition of glucose. (C) Photographs of aqueous dispersions of 0.05 mg/mL GO (a), RGO reduced by glucose (b), RGO/Au nanocomposites (c) and RGO reduced by the hydrazine hydrate (d). Solution (a), (b) and (c) were stored for about 3 months. Solution (d) was stored for 1 day 84
41. SEM images of the RGO/Au nanocomposites with different glucose-to-HAuCl₄ ratios. (A) 1.60/1, g/mL; (B) 0.32/1, g/mL; (C) 0.16/1, g/mL; and (D) 0.10/1, g/mL. The concentration of HAuCl₄ was 1.0 %. The amount of GO was fixed at 20.0 mg 86

42. SEM images of the RGO/Au nanocomposites with different glucose-to-GO ratios. (A) 32/1; (B) 16/1; (C) 8/1. The amount of 1.0 % HAuCl₄ was fixed at 1.0 mL.....87
43. (A) CVs of the bare-GCE (a), GO-GCE (b), RGO-GCE (c) and RGO/Au-GCE (d) in 0.01 M PBS (pH 7.0) containing 1 mM L-AA. Scan rate: 50 mV/s; (B) Plot of oxidation peak of RGO/Au-GCE versus square root of the scan rate in 0.01 M PBS (pH 7.0) containing 1 mM L-AA; (C) DPV curves of RGO/Au-GCE in 0.01 M PBS (pH 7.0) containing different concentrations of L-AA (0.1, 0.2, 0.4, 0.6, 0.8 and 1.0 mM); (D) Plot of oxidation currents versus different concentration of L-AA at -0.014 V. I: oxidation peak current in the presence of L-AA; I₀: oxidation peak current in the absence of L-AA. Inset shows: the calibration curve of oxidation peak current response versus concentration of L-AA in the linear range of 0.1 - 1.0 mM 89
44. (A) CVs of the bare-GCE (a), GO-GCE (b), RGO-GCE (c) and RGO/Au-GCE (d) in 0.01 M PBS (pH 7.0) containing 160 μM DA. Scan rate: 50 mV/s; (B) Plot of oxidation peak of RGO/Au-GCE versus square root of the scan rate in 0.01 M PBS (pH 7.0) containing 80 μM DA; (C) DPV curves of RGO/Au-GCE in 0.01 M PBS (pH 7.0) containing different concentrations of L-AA (1.0, 2.5, 5.0, 10.0 and 20.0 μM); (D) Plot of oxidation currents versus different concentration of DA at 0.160 V. I: oxidation peak current in the presence of DA; I₀: oxidation peak current in the absence of DA. Inset shows: the calibration curve of oxidation peak current response versus concentration of DA in the linear range of 1.0-20.0 μM..... 90
45. (A) CVs of the bare-GCE (a), GO-GCE (b), RGO-GCE (c) and RGO/Au-GCE (d) in 0.01 M PBS (pH 7.0) containing 200 μM UA. Scan rate: 50 mV/s; (B) Plot of oxidation peak of RGO/Au-GCE versus square root of the scan rate in 0.01 M PBS (pH 7.0) containing 200 μM UA; (C) DPV curves of RGO/Au-GCE in 0.01 M PBS (pH 7.0) containing different concentrations of L-AA (5, 10, 20, 40, 80 and 120 μM); (D) Plot of oxidation currents versus different concentration of UA at 0.290 V. I: oxidation peak current in the presence of UA; I₀: oxidation peak current in the absence of UA. Inset shows: the calibration curve of oxidation peak current response versus concentration of UA in the linear range of 5-120 μM91
46. (A) DPV curves at bare-GCE (a), GO-GCE (b), RGO-GCE (c) and RGO/Au-GCE (d) in 0.01 M PBS (pH 7.0) containing 2.2 mM L-AA, 160 μM DA, and 200 μM UA; (B)DPVs curves at RGO/Au-GCE in 0.01 M PBS (pH 7.0) containing different concentrations of L-AA, DA and UA. (a) 0.6 mM L-AA, 10 μM DA, 20 μM UA; (b) 1.2 mM L-AA, 20 μM DA, 40 μM UA..... 93

47. (A) DPV curves of the RGO/Au modified GCE in 10-times diluted serum containing individual concentration of AA, DA and UA mixture. [L-AA]: 0.2, 0.4, 0.8, 1.2, and 1.6 mM. [DA]: 1.0, 2.0, 4.0, 6.0 and 8.0 μM . [UA]: 5.0, 10.0, 20.0, 40.0 and 60.0 μM . The calibration curves for L-AA (B), DA (C) and UA (D) in the 10-times diluted serum.....	94
48. STEM (A) and SEM (B), and EDS (C) of RGO/Ag nanocomposite	102
49. Absorption spectra of GO, AgNPs, RGO, RGO/Ag nanocomposite.....	103
50. (A) FTIR of GO, RGO and RGO/Ag nanocomposite; (B) XRD pattern of RGO/Ag nanocomposite	104
51. Temperature evolution profile of H ₂ O, AgNPs, GO, RGO and RGO/Ag nanocomposite upon NIR (808 nm, 0.3 W/cm ²) irradiation	105
52. (A) Bacterial cell viability of <i>E. coli</i> after treatments with 15 $\mu\text{g/mL}$ AgNPs, 15 $\mu\text{g/mL}$ pure GO, 15 $\mu\text{g/mL}$ pure RGO and 15 $\mu\text{g/mL}$ RGO/Ag nanocomposite with and without NIR irradiation (808 nm, 0.3 W/cm ²). (B) Bacterial cell viability of <i>Kp</i> after treatments with 30 $\mu\text{g/mL}$ AgNPs, 30 $\mu\text{g/mL}$ pure GO, 30 $\mu\text{g/mL}$ pure RGO and 30 $\mu\text{g/mL}$ RGO/Ag nanocomposite with and without NIR irradiation (808 nm, 0.3 W/cm ²).....	106
53. (A) Bacterial cell viability of <i>E. coli</i> after treatments with different concentrations of RGO/Ag nanocomposite with and without NIR irradiation (808 nm, 0.3 W/cm ²). (B) Bacterial cell viability of <i>Kp</i> after treatments with different concentrations of RGO/Ag nanocomposite with and without NIR irradiation (808 nm, 0.3 W/cm ²)	107
54. (A) Representing photographs of <i>E. coli</i> colonies treated with RGO/Ag nanocomposite formed on LB-agar plates. (a) control; (b) control with laser irradiation; (c) 15 $\mu\text{g/mL}$ RGO/Ag nanocomposite; (d) 15 $\mu\text{g/mL}$ RGO/Ag nanocomposite with laser irradiation. The laser irradiation was conducted under 808 nm with 0.3 W/cm ² . Representing photographs (B) and luminescence images (C) of <i>Kp</i> colonies treated with RGO/Ag nanocomposite formed on LB-agar plates. (a) control; (b) control with laser irradiation; (c) 30 $\mu\text{g/mL}$ RGO/Ag nanocomposite; (d) 30 $\mu\text{g/mL}$ RGO/Ag nanocomposite with laser irradiation. The laser irradiation was conducted under 808 nm with 0.3 W/cm ²	108
55. Fluorescence images of live and dead <i>E. coli</i> cells after incubation with 15 $\mu\text{g/mL}$ of RGO/Ag nanocomposites for 2h: (A) <i>E. coli</i> with laser treatment; (B) <i>E. coli</i> with RGO/Ag nanocomposites; (C) <i>E. coli</i> treated with RGO/Ag nanocomposite and laser irradiation. Blue fluorescence shows bacterial quasi nuclear stained with DAPI, while red fluorescence shows dead bacteria stained with PI. The scale bar is 20 μm	109
56. ROS generation of <i>E. coli</i> by the treatment of RGO/Ag nanocomposite (15 $\mu\text{g/mL}$) and 10 NIR irradiation.....	110

57. Relative cell viability of SW620 and MH-S after culturing with different concentrations of RGO/Ag nanocomposite varying from 0, 5, 10, 20, 30 to 40 $\mu\text{g/mL}$ for 24 h at 37 $^{\circ}\text{C}$. After the addition of MTT reagent and 4 h incubation at 37 $^{\circ}\text{C}$, stop solution was added and followed by overnight incubation. The absorbance of each sample was recorded at 570 nm to determine the cell proliferation rate.....	111
58. SEM (A), STEM (B) images and absorption spectrum (C) of GO.....	120
59. Absorption (A) fluorescence (B) spectra of SiNPs@TAMRA without (a) and with (b) GO. $\lambda_{\text{ex}} = 540 \text{ nm}$. (C) Lifetime measurements of SiNPs@TAMRA without (b) and with (c) GO. Curve a is the reference. 492 nm LED laser was used in the lifetime measurement. (D) SEM image of SiNPs@TAMRA with GO. Inset is TEM image of SiNPs@TAMRA with GO, bar is 200 nm. The white arrows indicate the wrinkle of GO wrapped on the surface of nanoparticles.....	122
60. Fluorescence quenching of SiNPs@TAMRA with different concentration of GO. (A) Fluorescence spectra of SiNPs@TAMRA with different concentrations of GO. From top to bottom: 0, 1.0, 2.0, 3.0, 4.0, 5.0, 7.5, 10.0 and 20.0 $\mu\text{g/mL}$. (B) Quenching efficiency GO to SiNPs@TAMRA with different concentrations. $\lambda_{\text{ex}} = 540 \text{ nm}$; $\lambda_{\text{em}} = 575 \text{ nm}$	123
61. TEM images of SiNPs@TAMRA@Si-NH ₂ with different thickness of 0, 0.3, 1.2, 6.5, 14.7, and 34.5 nm (A to F).....	124
62. (A) Fluorescence spectra of SiNPs@TAMRA@Si-NH ₂ with GO. The distances between TAMRA and GO were 0, 0.3, 1.2, 6.5, 14.7, 34.5 nm (curve a to f). Curve g was SiNPs@TAMRA without addition of GO. (B) Quenching efficiency of the doped TAMRA as a function of the distance. The quenching efficiency was calculated based on average fluorescence lifetime (squares) and from steady-state fluorescence intensity (circles). The concentrations of nanoparticles were equi <i>ca</i> 0.1 nM of TAMRA. $\lambda_{\text{ex}} = 540 \text{ nm}$; $\lambda_{\text{em}} = 575 \text{ nm}$	125
63. TEM images of SiNPs (A), SiNPs@Rubpy (B), and SiNPs@Rubpy@Si-NH ₂ with different thicknesses of 2.4, 3.0, 3.7, 4.8, 7.8, 10.1, and 15.6 nm (C to I).....	126
64. Fluorescence quenching of SiNPs@Rubpy with different concentrations of GO. (A) Fluorescence spectra of SiNPs@ RuBpy with different concentrations of GO. From top to bottom: 0, 10, 20, 30, 40 and 50 $\mu\text{g/mL}$. (B) Quenching efficiency GO to SiNPs@ RuBpy@Si-NH ₂ with different concentrations. $\lambda_{\text{ex}} = 460 \text{ nm}$; $\lambda_{\text{em}} = 600 \text{ nm}$	126

65. (A) Fluorescence spectra of SiNPs@Rubpy (a) and SiNPs@Rubpy@Si-NH₂ with 50 µg/mL GO. The distances between Rubpy and GO were separated by 2.4, 3.0, 3.7, 4.8, 7.8, 10.1, and 15.6 nm silica space (curve b to h). (B) Quenching efficiency of the doped Rubpy as a function of the distance. The concentrations of nanoparticles were equi *ca* 0.1 nM of Rubpy. $\lambda_{\text{ex}} = 460 \text{ nm}$; $\lambda_{\text{em}} = 600 \text{ nm}$ 128
66. Characterization of GO. (A) STEM image of GO. (B) EDS pattern of GO. (C) The zeta potential of GO. (D) The UV-vis spectrum of GO..... 136
67. Antibacterial property of GO with different concentration. (A) The *Kp* survival rate after treatment of different concentrations of GO. Inset: Bioluminescence images of *Kp* bacteria after incubation with different concentrations of GO. From left to right: 0, 62.5, 125.0, 250.0, and 500.0 µg/mL. (B) Representing photographs (a and b) and bioluminescence images (c and d) of *Kp* bacterial colonies treated with (a and c) and without (b and d) GO formed on LB-agar plates. (C) The *E.coli* survival rate after treatment of different concentration of GO. (D) The *Pa* survival rate after treatment of different concentration of GO 138
68. Relative viability of MH-S cells infected by *Kp* after treatment with different concentrations of GO (0.0, 62.5, 125.0, 250.0 and 500.0 µg/mL) at 37 °C through MTT assay 139
69. GO decreased infection severity in mice. (A) Bioluminescent images were obtained using IVIS Lumina XR system at different time points and the mice intraperitoneally injected with GO-treated *Kp* and untreated *Kp*. (B) Semiquantitively bioluminescence intensity of the two groups in (A) ... 141
70. GO decreased mortality rates and tissue damage. (A) Kaplan-Meier survival curves were obtained by infecting mice with GO-treated and untreated *Kp*, respectively (n=5 mice per group). (B) Morphological evidence of lung injury and inflammatory responses as assessed by H & E staining histological analysis (20×, scale bar = 50 µm) 141
71. (A) Cell viability of AM after bacterial infection by MTT assay. (B) ROS production in AM cells detected using an NBT assay. (C and D) PMN infiltration in the BAL and blood was counted by HEMA staining (Thermofisher). ***p < 0.001; RLU: relative LUC units..... 143
72. The lung (A), liver (B), spleen (C), and kidneys (D) showed significantly decreased bacterial burdens in GO-*Kp* infected mice (Mann Whitney U test). **p < 0.01; ***p < 0.001 144
73. Decreased MPO activity in the lung (A), liver (B), spleen (C), and kidney (D) of GO-*Kp* treated mice at 8 h and 24 h. Data are shown as mean + SEM of n = 3 mice per group and are representative of three independent experiments. **p < 0.01; ***p < 0.001; one-way ANOVA (Tukey's post hoc). RLU: relative LUC units..... 144

LIST OF TABLES

Table	Page
1. Detection of Hg^{2+} and I^- in tap water samples	16
2. The properties of different exonucleases. “+” indicates fluorescence enhancement; “-” indicates constant fluorescence.....	29
3. Fluorescence lifetime of GQDs at different emission wavelengths with 370 nm excitation	59

LIST OF SCHEMES

Scheme	Page
1. A schematic illustration of the MB-based INHIBIT logic gate for the sensing of the Hg^{2+} and I^-	6
2. Schematic diagram of the formation of GQDs through pyrolysis of L-glutamic acid	53
3. Illustration of the synthetic process of RGO/metal (oxide) nanocomposites using glucose as the reducing agent. (A) GO was stirred with glucose without heating; (B) GO was reduced to form RGO by glucose with boiling for 20 min; (C) RGO/Au nanocomposite was formed through the injection of HAuCl_4 in (B) for boiling another 15 min.....	75
4. Schematic of synthesis of $\text{SiNPs@TAMRA@Si-NH}_2$ nanocomposite and investigation of fluorescence quenching ability of GO to TAMRA with distance (d) dependent	119

ABBREVIATIONS

ABTS	2,2'-azino-bis(3-ethylbenzothiazoline-6-sulphonic acid)
AgNPs	silver nanoparticles
AM	alveolar macrophages
APTES	3-ami-nopropyltriethoxysilane
ATP	adenosine triphosphate
BAL	bronchoalveolar lavage
BHQ1	black hole quencher-1
CFU	colony-forming unit
CV	cyclic voltammetry
DA	dopamine hydrochloride
DAPI	4' -6-diamidino-2-phenylindole
DPV	differential pulse voltammetry
E. coli	Escherichia coli
EDS	energy-dispersive X-ray spectroscopy
EPA	environmental protection agency
FAM	6-carboxyfluorescein
FBS	fetal bovine serum
FITC	fluorescein isothiocyanate
FRET	fluorescence resonance energy transfer

FTIR	fourier transform infrared
GCE	glass carbon electrode
Glu	L-glutamic acid
GO	graphene oxide
GQDs	graphene quantum dots
H ₂ DCFDA	2',7'-dichlorodihydrofluorescein diacetate
HRTEM	high-resolution transmission electron microscope
Kp	klebsiella pneumoniae
L-AA	L-ascorbic acid
LB	lysogeny broth
LOD	limit of detection
MB	molecular beacon
MDR	multiple-drug-resistant
MH-S	murine alveolar macrophage cells
MPO	myeloperoxidase
MTT	3-(4,5-dimethyl-2-thiazolyl)-2,5-diphenyltetrazolium bromide
NBT	nitroblue tetrazolium
NIR	near-infrared fluorescence
Pa	pseudomonas aeruginosa
PAGE	polyacrylamide gel electrophoresis
PBS	phosphate buffered saline
PI	propidium iodide

QDs	quantum dots
RGO	reduced graphene oxide
ROS	reactive oxygen species
RSD	relative standard deviation
Rubpy	tris(bipyridine)ruthenium (II) chloride
SEM	scanning electron microscope
SG	SYBR green I
SiNPs	silica nanoparticles
T4 PNK	T4 polynucleotide kinase
TAMRA-SE	carboxytetramethylrhodamine-succinimidyl ester
TCSPC	time-correlated single photon counting
TEOS	tetraethylorthosilicate
TMB	3,3,5,-tetramethylbenzidine
UA	uric acid
λ Exo	λ exonuclease

ACKNOWLEDGEMENTS

First of all, I would like to express my deepest appreciation and gratitude to my advisor, Dr. Julia Xiaojun Zhao, for the patient guidance, encouragement, and mentorship she provided to me throughout my entire graduate career. She not only encouraged me to design and conduct the research independently, but also offered me many opportunities to write scientific papers and proposals. All of these have truly prepared me for my future career. Moreover, she also guided me in my personal life to get into American way of life. I am grateful for everything she did for me.

I would also like to thank all of my committee members: Dr. David T. Pierce, Dr. Alena Kubátová, Dr. Qianli 'Rick' Chu, and Dr. Min Wu. Thank Dr. Pierce for his guidance in my research, his mentoring in my electrochemical research project and his revision for my research paper. Thank Dr. Kubátová for offering several opportunities to join the outreach activities, which is a great experience for becoming a faculty. Thank Dr. Chu for his thought-provoking suggestions for my project during my OPR. I also would like to thank Dr. Wu for providing me several opportunities to write review papers, which improved my scientific writing skill. Also, I am really thankful for the guidance of Dr. Wu in my research projects. I wish to thank all of the chemistry department faculty for their education and office staff for their assistant when needed.

Next, I would like to thank the members of Dr. Zhao's analytical group. They are Dr. Song Liang, Dr. Carrie John, Dr. Jiao Chen, Shaina Strating, Dr. Fei Tian, Yuqian Xing, Xiao Liu, Joseph Birrenkott, Kali Shepherd, Aaron Hanson, Robert Ducioame, Yang Zhao, Nenny Fahrudin, Wei Lin, Kevin Zeng, and Kirby Huber.

Special thanks to Shirui Tan from Dr. Wu's group, with whom I finished several nano-biomedical projects.

Thanks to the financial support from the UND graduate school, ND EPSCoR and chemistry department. I can't finish my projects and present my research at conferences without their support. Meanwhile, my truly thanks also give to the technical support from the Basic Science Imaging Center for training me on the microscopes and allowing me to use these instruments independently.

Finally, and most importantly, I would like to thank my entire family: my parents, my dear wife, and my two joyful boys. They gave me the support, encouragement, tolerance, joy and love to complete this work.

ABSTRACT

In the first project, a simple, rapid, and reversible fluorescent DNA INHIBIT logic gate has been developed for sensing mercury (Hg^{2+}) and iodide (I^-) ions based on a molecular beacon (MB). In this logic gate, a mercury ion was introduced as the first input into the MB logic gate system to assist in the hybridization of the MB with an assistant DNA probe through the thymine– Hg^{2+} –thymine interaction, which eventually restored the fluorescence of MB as the output. With this signal-on process, mercury ions can be detected with a limit of detection as low as 7.9 nM. Furthermore, when iodide ions were added to the Hg^{2+} /MB system as the second input, the fluorescence intensity decreased because Hg^{2+} in the thymine– Hg^{2+} –thymine complex was grabbed by I^- due to a stronger binding force. Iodide ions can be detected with a limit of detection of 42 nM. Meanwhile, we studied the feasibility and basic performance of the DNA INHIBIT logic gate, optimized the logic gate conditions, and investigated its sensitivity and selectivity. The results showed that the MB based logic gate is highly selective and sensitive for the detection of Hg^{2+} and I^- over other interfering cations and anions.

In the second project, an ultrasensitive and rapid turn-on fluorescence assay has been developed for the detection of 3'-5' exonuclease activity of exonuclease III (Exo III) using molecular beacons (MBs). This method has a linear detection range from 0.04 to 8.00 U mL⁻¹ with a limit of detection of 0.01 U mL⁻¹. In order to improve the selectivity of the method, a dual-MB system has been developed to distinguish between different exonucleases. With the introduction of two differently designed MBs which respond to different exonucleases, the T5 exonuclease, Exo III and RecJf exonucleases can be easily distinguished from each other. Furthermore, fetal bovine

serum and fresh mouse serum were used as complex samples to investigate the feasibility of the dual-MB system for the detection of the enzymatic activity of Exo III. As a result, the dual-MB system showed a similar calibration curve for the detection of Exo III as in the ideal buffer solution. The designed MB probe could be a potential sensor for the detection of Exo III in biological samples.

In the third project, A sensitive label-free fluorescence assay for monitoring T4 polynucleotide kinase (T4 PNK) activity and inhibition was developed based on a coupled λ exonuclease cleavage reaction and SYBR Green I. In this assay, a double-stranded DNA (dsDNA) was stained with SYBR Green I and used as a substrate for T4 PNK. After the 5'-hydroxyl termini of the dsDNA was phosphorylated by the T4 PNK, the coupled λ exonuclease began to digest the dsDNA to form mononucleotides and single-stranded DNA (ssDNA). At this moment, the fluorescence intensity of the SYBR Green I decreased because less affinity with ssDNA than dsDNA. The decrease extent was proportional to the concentration of the T4 PNK. After optimization of the detection conditions, including the concentration of ATP, amount of λ exonuclease and reaction time, the activity of T4 PNK was monitored by the fluorescence measurement, with the limit of detection of 0.11 U/mL and good linear correlation between 0.25-1.00 U/mL ($R^2=0.9896$). In this assay, no label was needed for the fluorescence detection. Moreover, the inhibition behaviours of the T4 PNK's inhibitors were evaluated by this assay. The result indicated a potential of using this assay for monitoring of phosphorylation-related process.

In the fourth project, a facile bottom-up method for the synthesis of highly fluorescent graphene quantum dots (GQDs) has been developed using a one-step pyrolysis of a natural amino acid, L-glutamic acid, with the assistance of a simple heating mantle device. The developed GQDs showed strong blue, green and red

luminescence under irradiation with ultra-violet, blue and green light, respectively. Moreover, the GQDs emitted near-infrared (NIR) fluorescence in the range 800–850 nm with an excitation-dependent manner. This NIR fluorescence has a large Stokes shift of 455 nm, providing a significant advantage for the sensitive determination and imaging of biological targets. The fluorescence properties of the GQDs, such as the quantum yields, fluorescence life times, and photostability, were measured and the fluorescence quantum yield was as high as 54.5%. The morphology and composites of the GQDs were characterized using TEM, SEM, EDS, and FT-IR. The feasibility of using the GQDs as a fluorescent biomarker was investigated through in vitro and in vivo fluorescence imaging. The results showed that the GQDs could be a promising candidate for bioimaging. Most importantly, compared to the traditional quantum dots (QDs), the GQDs are chemically inert. Thus, the potential toxicity of the intrinsic heavy metal in the traditional QDs would not be a concern for GQDs. In addition, the GQDs possessed an intrinsic peroxidase-like catalytic activity that was similar to graphene sheets and carbon nanotubes. Coupled with 2,20-azino-bis(3-ethylbenzothiazoline-6-sulphonic acid) (ABTS), the GQDs can be used for the sensitive detection of hydrogen peroxide with a limit of detection of 20 mM.

In the fifth project, a general, environmental-friendly, one-pot method for the fabrication of reduced graphene oxide (RGO)/metal (oxide) (e.g. RGO/Au, RGO/Cu₂O, and RGO/Ag) nanocomposites was developed using glucose as the reducing agent and stabilizer. The RGO/metal (oxide) nanocomposites were characterized using STEM, FE-SEM, EDS, UV-vis absorption spectroscopy, XRD, FT-IR and Raman spectroscopy. The reducing agent, glucose, not only reduced GO effectively to RGO, but it also reduced the metal precursors to form metal (oxide) nanoparticles on the surface of RGO. Moreover, the RGO/metal (oxide) nanocomposites were stabilized by gluconic acid on

the surface of RGO. Finally, the developed nanomaterials were successfully applied to simultaneous electrochemical analysis of L-ascorbic acid (L-AA), dopamine (DA) and uric acid using RGO/Au nanocomposite as an electrode catalyst.

In the sixth project, a reduced graphene oxide/silver nanoparticle (RGO/Ag) nanocomposite using glucose as the environmental-friendly reducing agent was developed. The antibacterial activity of RGO/Ag nanocomposite was carefully investigated using *Escherichia coli* (*E. coli*) and *Klebsiella pneumoniae* (*Kp*) as bacterial models. We found that, compared with AgNPs, graphene oxide (GO) and RGO, RGO/Ag nanocomposite had higher antibacterial efficiency. Furthermore, under the near-infrared (NIR) irradiation, RGO/Ag nanocomposite demonstrated enhanced synergistic antibacterial activity through the photothermal effect. Almost 100 % of *E. coli* and *Kp* were killed by the treatment of 15 $\mu\text{g/mL}$ and 20 $\mu\text{g/mL}$, respectively, with NIR irradiation. Moreover, the membrane integrity assay and ROS species assay demonstrated that RGO/Ag nanocomposite under NIR irradiation caused the cell membranes disruption and generation of ROS species, providing other possible mechanisms for their high antibacterial activity besides photothermal effect.

In the seventh project, a rigid distance spacer, silica shell, was used between GO and dyes in this work to elucidate the quenching ability of GO. First, an organic dye was doped in silica nanoparticles, followed by the modification of another layer of silica shell with a different thickness. Due to the electrostatic interaction between GO and positively charged silica nanoparticles, GO wrapped the silica nanoparticles when they were mixed together. Therefore, the distance between GO and organic dyes was adjusted by the thickness of the silica shell. The quenching efficiency of GO to two different organic dyes, including Tetramethylrhodamine (TAMRA) and Tris(bipyridine)ruthenium(II) chloride (Rubpy), was measured at various distances.

This quenching ability investigation of GO to dyes with distance-dependent manner would provide a guideline for the design of the fluorescent functional composite using GO in the future.

In the eighth project, we characterized the antibacterial activity of GO in both cell culture and animal models. *Klebsiella pneumoniae* (*Kp*) is one of the most common multidrug resistant (MDR) pathogens in causing persistent nosocomial infections and is very difficult to eradicate once established in the host. First, we demonstrated that GO exerted direct killing of *Kp* in agar dishes and afforded the protection of alveolar macrophages (AM) from *Kp* infection in culture. We then evaluated the mortality, tissue damage, polymorphonuclear neutrophil (PMN) penetration, and bacterial dissemination in *Kp*-infected mice. Our results revealed that GO can counteract the invasive ability of *Kp in vivo*, resulting in lessened tissue injury, significant but subdued inflammatory response, and prolonged mouse survival. These findings indicate that GO may be an alternative agent for controlling MDR pathogens in clinics.

CHAPTER I

A REVERSIBLE FLUORESCENT LOGIC GATE FOR SENSING MERCURY AND IODIDE IONS BASED ON A MOLECULAR BEACON

1. Introduction

Molecular Boolean logic gates are advanced microdevices that can perform various logical operations based on molecules.¹ The basic types of Boolean logic gates include AND, OR, NOT, INHIBIT, NOR, NAND, XOR, and XNOR. The advanced logical calculation could be performed through combination of these types of logic gates. Therefore, Boolean logic gate is promising in the fabrication of molecular computation,²⁻⁴ becoming a potential substitute for the traditional silicon-based computation.⁵ Among the molecular Boolean logic gates, DNA-based logic gates have attracted great attention because of the easy manipulation of DNAs. They could be fabricated based on various behaviors of DNAs such as hybridization, cleavage and allosteric regulation.⁶ A number of DNA based logic gates, including the methods coupled with graphene oxide as the quencher,^{7, 8} DNAzyme,^{3, 9, 10} and aptamers¹¹ were reported recently. Compared with other molecular logic gates, such as an enzyme-inhibitor¹² and a small super-molecule system,¹³ a DNA logic gate shows a number of advantages. The most significant benefits include low cost, specific genetic information recognition, simplicity, various input species (e.g., metal ions,¹⁴⁻¹⁸ DNA sequences,¹⁹⁻²¹ small biomolecules,²² and proteins²³) and different types of output signals.^{4, 15, 18, 24} Meanwhile, the excellent selectivity of a DNA probe for its target inputs provides a promising platform for biosensing applications. For instance, the specific binding of the thymine-Hg²⁺-thymine (T-Hg²⁺-T) and cytosine-Ag⁺-cytosine (C-Ag⁺-C) were

widely used for the multi-ions detection with fluorescence²⁵ and colorimetric methods.²⁶ However, most of the fluorescence output-based DNA logic gates were fabricated through coupling with fluorescence nano-quenchers. For example, graphene oxides were widely used to fabricate different types of logic gates.^{16, 22} The nanomaterials bring complicity to DNA logic gates. In contrast, molecular beacon-based self-quenched DNA logic gates are more feasible.

A molecular beacon (MB) is a designed hairpin-structured DNA strand labeled with a fluorophore and a quencher at both ends. MBs have been widely used for the fabrication of different biosensors.²⁷ The high selectivity and sensitivity of the MB-based biosensors are benefitted from its loop-stem structure and low background signal. Recently, a MB has been used for the fabrication of different types of Boolean logic gates.²⁸ For example, Park et al. constructed several types of Boolean logic gates using DNA sequences as inputs.¹⁹ The developed logic gates could be operated reversibly and reset to the original state. Yang et al. developed a half-adder and half-subtractor through combining a MB-based AND gate and a XOR gate, an INHIBIT gate and a XOR gate, respectively.²⁹ However, all of these MB based logic gates used DNA sequences as inputs, which limited their applications.

Herein, a reversible INHIBIT logic gate based on a MB was developed with two ions as inputs and fluorescence as output for the detection of Hg^{2+} and I^- . Hg^{2+} is considered as one of the most hazardous pollutants for human health and environmental protection.^{30, 31} The US Environmental Protection Agency (EPA) has a standard maximum allowable level for Hg^{2+} of 10 nM in drinking water. Iodide ion is an essential nutrient for humans. The lack of I^- would lead to serious health problems.^{32, 33} Recently, several papers reported the sensitive sensing systems for the detection of Hg^{2+} using DNA probes. Liu et. al used a thrombin-binding aptamer labeled with a fluorophore and

a quencher at its 5' and 3' termini to detect Pb^{2+} and Hg^{2+} with the detection limit of 300 pM and 5.0 nM, respectively.³⁴ However, this is a turn-off method for the sensing, which might increase the background signal. Also, several nanomaterials, such as gold nanoparticles,³⁵ quantum dots,¹⁷ carbon nanotubes³⁶ and graphene oxides,⁷ have been used for the fabrication of Hg^{2+} and other ions sensors. These methods have some limitations, including complicated synthesis of the modified nanomaterials, high cost, and low stability for the long-time sensing. Therefore, the development of a novel system for the detection of these two ions is important for human health and environmental protection.

2. Experimental Section

2.1. Chemicals and Instruments.

DNA sequences used in this work were purchased from Fisher Scientific. The sequences for MB was: 5'-FAM-CCA CCA GTT TTT TAG CTG AGG GTG G-BHQ1-3'; and the sequences for an assistant probe was 5'-CCCT CAG CTT AAT AACT-3'. NiCl_2 , CaCl_2 , ZnCl_2 , CuCl_2 , MnCl_2 , CoCl_2 , $\text{Pb}(\text{NO}_3)_2$, FeCl_2 and HgCl_2 were purchased from Sigma-Aldrich (reagent-grade). All experiments were performed in a pH7.4 buffer solution made of 10 mM Tris-HCl, 50 mM NaCl, and 10 mM MgCl_2 . The DI water (18.3 $\text{M}\Omega\cdot\text{cm}$) was produced from the Millipore water purification system.

All fluorescence experiments were carried out using a Fluorolog-3 Spectrofluorometer with a 450 W xenon lamp (Jonin Yvon-Spex, Instruments S.A., Edison, NJ). Both excitation and emission slit widths were set to be 5.0 nm. FAM was excited at 480 nm with a fluorescence emission range of 500 - 600 nm.

2.2. Investigation of Feasibility of the Logic Gates.

A 1.0 μL aliquot of 1.0 μM MB and 0.2 μL of 100.0 μM assistant MB probe were mixed in 100.0 μL buffer solution that was incubated at 32 °C for 5 min. The final

concentrations of MB and the assistant MB probe were 10.0 nM and 200.0 nM, respectively. Afterwards, 0.2 μL of 100.0 μM Hg^{2+} was added to the reaction system. After 5 min of reaction, aliquot of I⁻ was added to the solution to react for 2 min. The final concentration of I⁻ was 12.8 μM . Fluorescence intensity at 518 nm was monitored via the function of time.

2.3. Investigation of Reversibility of the Logic Gate.

A 1.0 μL aliquot of 1.0 μM MB, 0.2 μL of 100.0 μM assistant MB probe and 0.2 μL of 100.0 μM Hg^{2+} were mixed in a 100.0 μL reaction buffer at 32 °C for 5 min, and then the fluorescence intensity was detected. Then, 0.2 μL of 200.0 μM I⁻ was added and the fluorescence intensity was monitored within 2 min. Afterwards, 0.2 μL of 100.0 μM Hg^{2+} was injected again to measure the fluorescence intensity in 5 min. This process was repeated for two times.

2.4. Detection of Hg^{2+} .

A 1.0 μL aliquot of 1.0 μM MB and 0.2 μL of 100.0 μM assistant MB probe were added in a 100.0 μL reaction buffer at 32 °C for 5 min and recorded the fluorescence intensity. Different concentrations of Hg^{2+} were added into the solution. The Hg^{2+} concentrations were 0, 10, 50, 100, 200, 500 and 1000 nM. After 5 min of the reaction, the fluorescence intensity of the solution was detected.

The investigation of the selectivity of the MB logic gate over other interfered metal ions was conducted in a similar way. A 1.0 μL aliquot of 1.0 μM MB and 0.2 μL of 100.0 μM assistant MB probe were mixed in a 100.0 μL reaction buffer at 32 °C for 5 min and the fluorescence intensity was measured. Afterwards, different ions, including Ni^{2+} , Zn^{2+} , Cu^{2+} , Mn^{2+} , Co^{2+} , and Fe^{2+} , were added into the solution and were incubated for 5 min. The final concentration of these ions was 1.0 μM . Finally, the fluorescence intensity of each solution was detected.

2.5. Detection of I⁻.

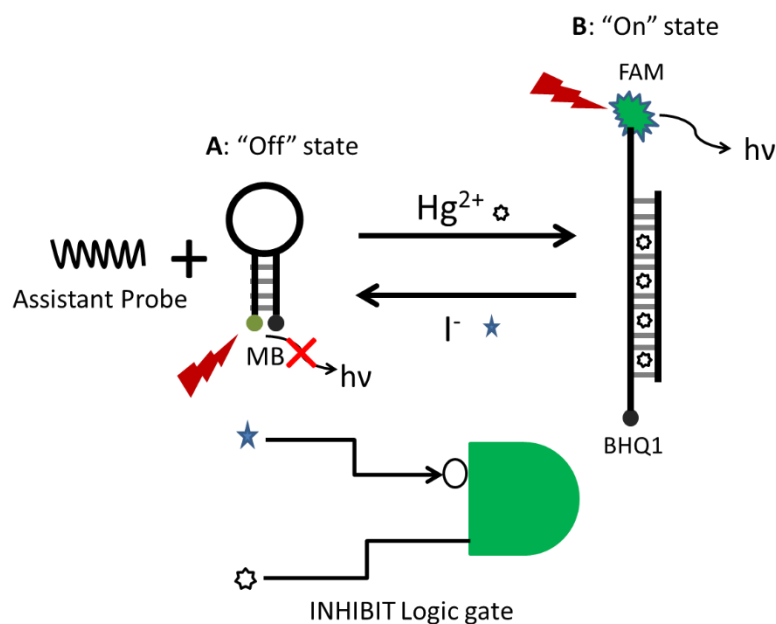
A 1.0 μL aliquot of 1.0 μM MB, 0.2 μL of 100.0 μM assistant MB probe and 0.2 μL of 100.0 μM Hg^{2+} were added in a 100.0 μL reaction buffer at 32 $^{\circ}\text{C}$ for 5 min followed by fluorescence intensity measurement. Afterwards, different concentrations of I⁻ were added to the reaction solution. The concentrations of I⁻ were 0, 0.05, 0.10, 0.20, 0.40, 0.80, 1.60, 3.20, 6.40 and 12.80 μM . After 2 min of the reaction, the fluorescence intensity was measured.

The investigation of the selectivity of the MB logic gate over other interfered anions was conducted in a similar way. A 1.0 μL aliquot of 1.0 μM MB, 0.2 μL of 100.0 μM assistant MB probe and 0.2 μL of 100.0 μM Hg^{2+} were added in a 100.0 μL reaction buffer at 32 $^{\circ}\text{C}$ for 5 min and the fluorescence intensity was recorded. Afterwards, different anions, including Cl⁻, Br⁻, F⁻, SO₄²⁻, ClO₃⁻, HCO₃⁻, HPO₄⁻, NO₃⁻, IO₃⁻ and I⁻, were added. The final concentration of these ions was 6.40 μM . After 2 min of incubation the fluorescence intensity of each solution was detected.

3. Results and Discussion

3.1. Design of the Logic Gate.

In this work, we have fabricated a DNA INHIBIT logic gate based on a molecular beacon (MB) using Hg^{2+} and I⁻ as inputs and the fluorescence signal as an output. This logic gate could be used to detect trace amount of Hg^{2+} and I⁻ as shown in Scheme 1. A MB has a hairpin structure that induces fluorescence resonance energy transfer (FRET) between the modified dye and the quencher at each end, showing fluorescence “off” state. An assistant DNA probe was employed, which had two T-T mismatch bases when it hybridized with MB. Due to the T-T mismatch, the hybridization between the MB and the assistant probe was limited. Therefore, the loop of the MB could not be open, keeping fluorescence “off” status (Scheme 1 A).



Scheme 1. A schematic illustration of the MB-based INHIBIT logic gate for the sensing of the Hg^{2+} and I^- .

It has been demonstrated that Hg^{2+} could conjugate two mismatched thymines (T) in DNA sequences to form T– Hg^{2+} –T complex.¹⁷ The binding constant between T and Hg^{2+} is about 106.37. Based on this principle, in our design Hg^{2+} was chosen as the first input. In the presence of Hg^{2+} , the mismatched assistant DNA probe could easily hybridize with MB, forming T– Hg^{2+} –T in the DNA duplex. At this moment the fluorescence of the MB was restored as an output, resulting in the fluorescence “on” state (Scheme 1 B). The fluorescence intensity would be proportional to the concentration of Hg^{2+} . Therefore, the Hg^{2+} could be detected based on the fluorescence measurement. This is the first cycle of the logic gate.

The second cycle of the logic gate can be used to detect I^- . At this cycle, I^- could be functional as the second input. The principle is based on the strong binding affinity between I^- and Hg^{2+} . Their binding constant is 10^{29} that is much larger than that of the T– Hg^{2+} –T complex.¹⁶ As a result, with the addition of I^- , the T– Hg^{2+} –T complex was disrupted by the formation of HgI_2 . At this moment, due to the loss of Hg^{2+} between the MB and the assistant probe, the MB would reform to the original hairpin structure,

leading to the quenching of the fluorescence, again displaying the fluorescence “off” state (Scheme 1 A). The extent of the fluorescence decrease would be proportional to the concentration of I⁻. Therefore, by measuring the fluorescence intensity changes, the concentration of I⁻ could be detected. In this cycle the fluorescence decrease was an output.

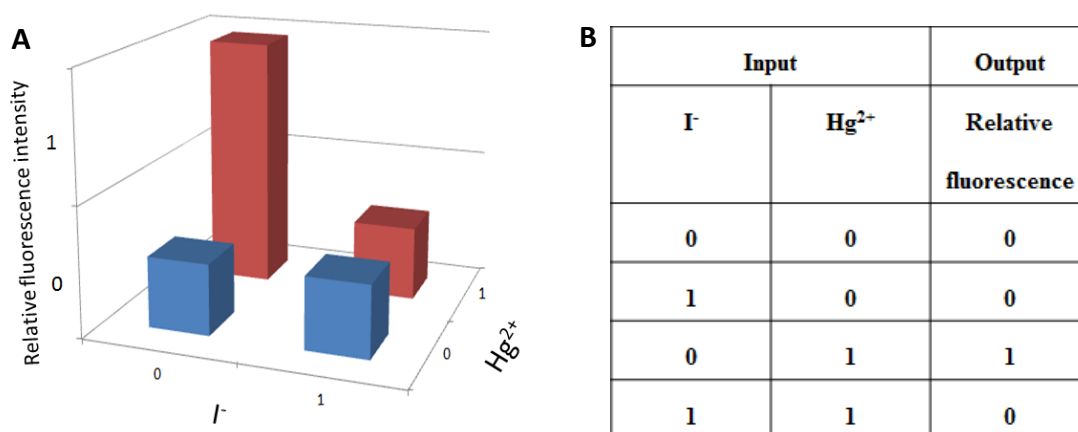


Figure 1. (A) Fluorescence intensities of the MB logic gate at 518 nm in the presence of different inputs. (B) Truth table for the INHIBIT logic gate.

Hg²⁺ and I⁻ were defined as the two inputs for our logic gate, and fluorescence intensity change at 518 nm was defined as an output. For input, the presence of Hg²⁺ and I⁻ was defined as 1, and their absence was defined as 0. For output, the original fluorescence intensity of MB was considered as 0, and the enhanced fluorescence was defined as 1 (Figure 1A). The four possible input combinations were (0, 0), (1, 0), (0, 1) and (1, 1), as shown in the truth table (Figure 1B). With no input, or with I⁻ input alone, the output was 0. With Hg²⁺ input alone the output signal was 1. When the two inputs were introduced together into the system, the strong binding force between Hg²⁺ and I⁻ released the Hg²⁺ from the T–Hg²⁺–T complex and the fluorescence output signal was 0.

3.1.1. Feasibility of the DNA INHIBIT logic gate for the detection of Hg²⁺ and I⁻.

The feasibility of the designed fluorescent MB logic gate for the detection of Hg^{2+} and Γ^- was investigated by monitoring the fluorescence intensity changes as a function of the reaction time. The result is shown in Figure 2. First, the fluorescence of the logic gate increased as the injection of 200 nM Hg^{2+} , and it plateaued at 300 s.

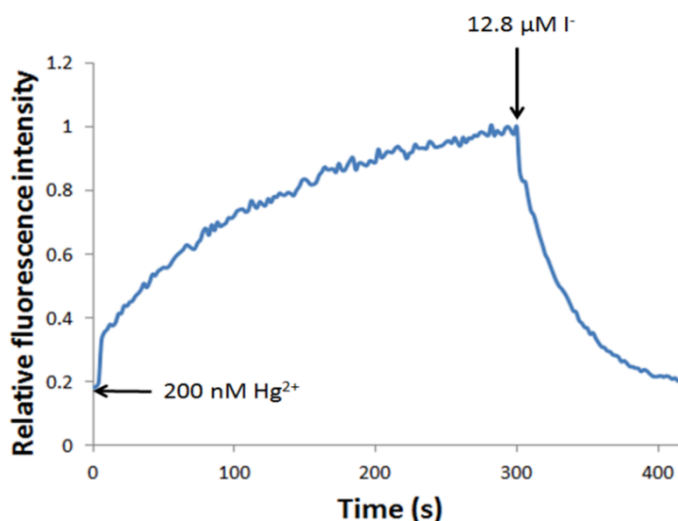


Figure 2. Real-time fluorescence intensities of the MB logic gate with the addition of Hg^{2+} (200 nM) and Γ^- (12.80 μM). $\lambda_{\text{ex}} = 480 \text{ nm}$, $\lambda_{\text{em}} = 518 \text{ nm}$.

This process demonstrated that the MB logic gate could be triggered to “on” state when the input Hg^{2+} was present. At the plateaued moment, 12.80 μM Γ^- was added to the system for turning off the logic gate. The result demonstrated that the fluorescence intensity decreased immediately after the addition of Γ^- . After 120 s the fluorescence signal returned to the original level where the Hg^{2+} input was not added. Clearly, the second input of Γ^- quickly led to the fluorescence logic gate “off”. Ultimately, this fluorescence MB logic gate could be used for sensing both Hg^{2+} and Γ^- by measuring the fluorescence intensity changes.

3.1.2. Performance of the DNA INHIBIT logic gate.

The performance of the logic gate was tested as shown in Figure 3. At no input (Figure 3, curve a) and I⁻ input alone (Figure 3, curve b), the output of fluorescence intensity changes showed 0. When the Hg²⁺ input was added, the Hg²⁺ mediated MB hybridization with the assistant probe and led to the open structure of MB and the fluorescence intensity of MB increased dramatically, giving an output signal of 1 (Figure 3 curve c). Finally, the two inputs with the concentrations of 200 nM and 6.40 μM of Hg²⁺ and I⁻ were introduced together into the system. As designed, the fluorescence output signal was 0 (Figure 3, curve d). The whole digital behavior could be finished within 7 min. The INHIBIT gate process was performed in the aqueous solution, showing convenience of the logic gate.

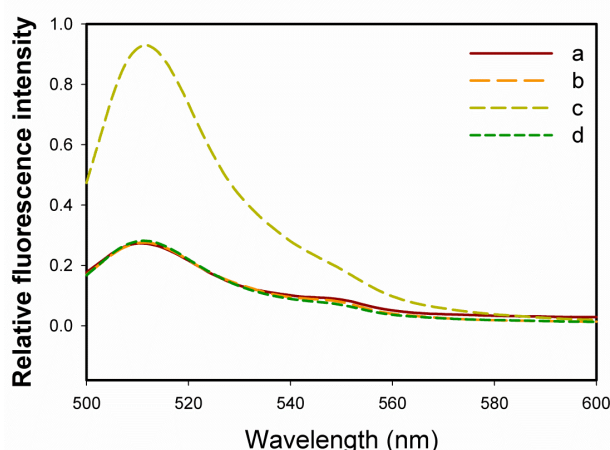


Figure 3. Fluorescence emission spectra of the MB logic gate to different inputs: a) I⁻ (0 μM) + Hg²⁺ (0 nM); b) I⁻ (6.40 μM) + Hg²⁺ (0 nM); c) I⁻ (0 μM) + Hg²⁺ (200 nM); d) I⁻ (6.40 μM) + Hg²⁺ (200 nM).

The operation reversibility of this logic gate was investigated by alternating the addition of Hg²⁺ and I⁻. As shown in Figure 4, the on/off switching behavior of the logic gate was reversible although after a cyclic treatment the fluorescence intensity was slightly decreased at the “on” state and increased at the “off” state. The slight decreases at the “on” state might result from the dilution because the total volume increased by alternating addition of Hg²⁺ and I⁻. And the slight increases at the “off” state might be due to the presence of extra Hg²⁺ in the complex. Overall, the results

indicated that the operation of the logic gate was reversible, providing its application potential.

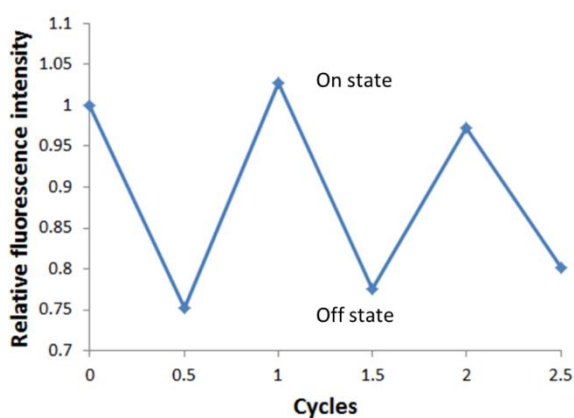


Figure 4. Reversible fluorescence signal changes of the MB logic gate with cyclic treatment of Hg^{2+} (200 nM) and I^- (0.40 μM).

3.2. Optimization of the Logic Gate Conditions.

In order to obtain optimal results, some reaction conditions that would affect the MB hybridization and fluorescence intensity were investigated.

3.2.1. Concentration of the assistant MB probe.

The function of the assistant MB probe was to hybridize MB. The concentration of this probe would significantly affect the function of the logic gate. As a result, the optimal concentration of the assistant probe was investigated. A 1.0 μL aliquot of 1.0 μM MB and 0.3 μL , 100.0 μM Hg^{2+} were mixed in a 100.0 μL reaction buffer. Afterwards, various concentrations of assistant probe from 100 nM to 350 nM were added into the solution. The fluorescence intensity of the solutions with and without Hg^{2+} was detected under different assistant probe concentrations.

As shown in Figure 5A, at a high concentration of the assistant probe, the MB was easily opened without Hg^{2+} , resulting in a high background signal (column 1). However, at a low concentration of the assistant probe, it was difficult to open the MB even in the presence of Hg^{2+} (column 2), resulting in a decreased fluorescence signal for the detection of Hg^{2+} . Both situations would decrease the detection sensitivity. The

effect of the assistant probe concentration on the fluorescence enhancement of the MB logic gate was further calculated as shown in Figure 5 B. The optimal concentration of the DNA assistant probe was 200 nM that gave the highest signal-to-noise ratio. In the following experiments, a concentration of 200 nM assistant probe was chosen as the optimal concentration.

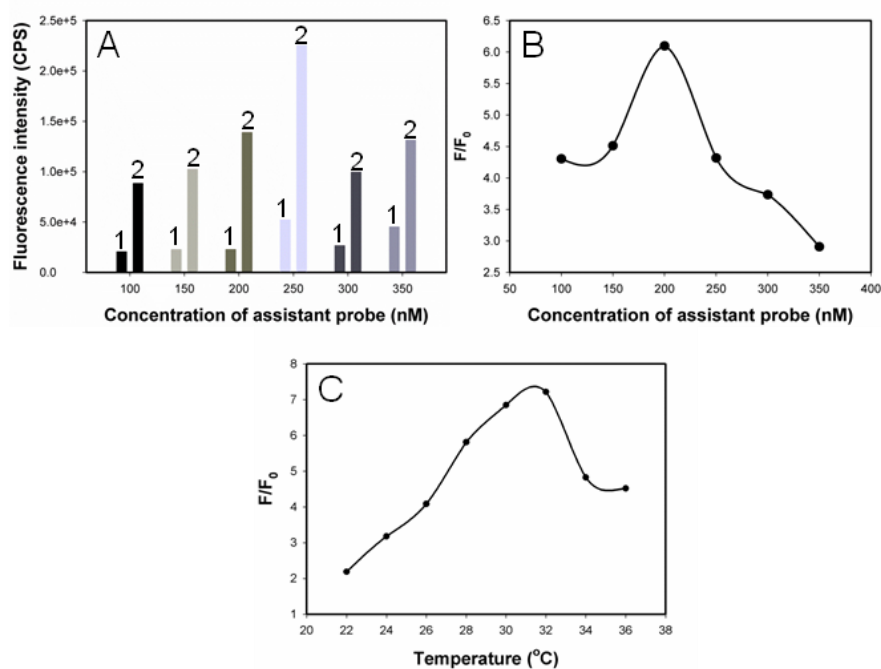


Figure 5. (A) Fluorescence intensity of the logic gate at different concentrations of assistant probe. 1: without Hg²⁺; 2: 300 nM Hg²⁺. (B) The fluorescence intensity ratio of the logic gate with 300 nM Hg²⁺ to that without 300 nM Hg²⁺ changed with the concentration of the assistant probe. MB: 10 nM; temperature: 32°C; $\lambda_{\text{ex}}=480$ nm, $\lambda_{\text{em}}=518$ nm. (C) Fluorescence intensity of the sensor at different temperatures. F: fluorescence intensity of the sensor in the presence of the 300 nM Hg²⁺; F₀: fluorescence intensity of the sensor in the absence of the Hg²⁺. MB: 10 nM; assistant probe: 200 nM. $\lambda_{\text{ex}}=480$ nm, $\lambda_{\text{em}}=518$ nm.

3.2.2. Temperature effect.

Temperature of the reaction solution affected the hybridization of the MB with the assistant probe, and further impacted the fluorescence intensity of the MB logic gate. Over a certain range, the higher the temperature, the easier the double-stranded DNA dehybridization. Therefore, the effect of temperature on the fluorescence enhancement of the logic gate was investigated. Based on the DNA hybridization reaction temperature range, we choose 22 – 36°C for investigation of the temperature effect on

the signal-to-noise ratio. For different temperatures, the fluorescence intensity of the system with and without Hg^{2+} was measured as shown in Figure 5B. The signal-to-noise ratio increased with the increase of temperature in the range of 22 - 32°C, and then decreased after 32°C. Therefore, 32 °C was chosen as the optimal temperature for the assay.

3.3. Hg^{2+} Detection.

3.3.1. Sensitivity study.

To test the sensitivity of the designed MB based logic gate for the Hg^{2+} detection, the MB logic gate system was mixed with various concentrations of Hg^{2+} and the fluorescence intensities of the system were detected under the optimal conditions. As shown in Figure 6A, upon increasing the Hg^{2+} concentration, the peak value of the fluorescence spectra increased, indicating a more efficient hybridization process between the assistant probe and MB and leading to the opening of MB and the restoration of the fluorescence intensity. The fluorescence enhancement of the MB logic gate system was sensitive to Hg^{2+} in a concentration-dependent manner (Figure 6B). The linear relationship between the fluorescence intensity and the Hg^{2+} concentration was in the range of 10 - 200 nM ($R^2 = 0.9834$). The limit of detection (LOD) was 7.9 nM based on 3 times of signal-to-noise ratio. The result was lower than US EPA defined toxicity level of Hg^{2+} in drinking water (10 nM).

3.3.2. Selectivity study.

To validate the selectivity of this assay for Hg^{2+} detection, competing metal ions, including Ni^{2+} , Zn^{2+} , Cu^{2+} , Mn^{2+} , Co^{2+} , and Fe^{2+} , were tested under the same condition with a concentration of 5 times higher than that of Hg^{2+} . As shown in Figure 7, the fluorescence intensity of the MB logic gate system showed little changes in the presence of the majority of the interference metal ions. The Mn^{2+} gave a higher

signal than other ions. However, it was only 14.2 % of the fluorescence intensity of Hg^{2+} ions. The results showed the excellent selectivity for the Hg^{2+} detection over other metal ions.

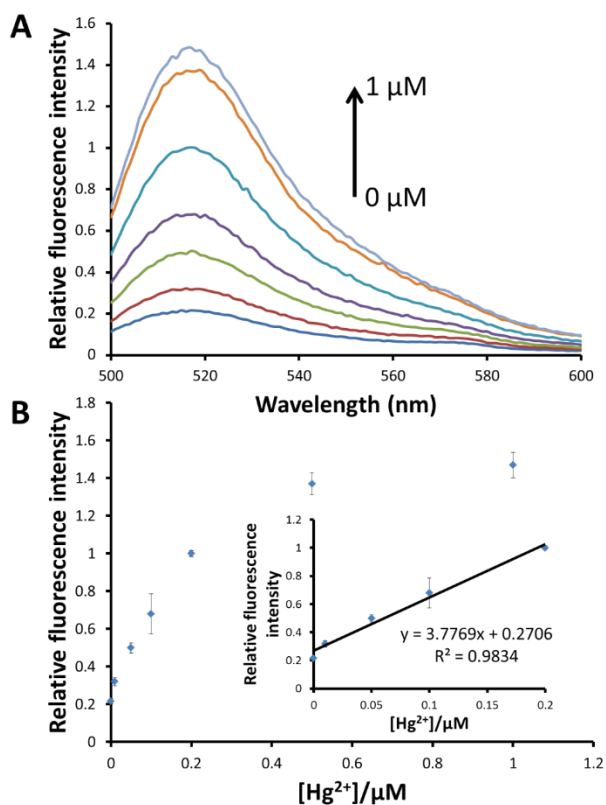


Figure 6. (A) Fluorescence response of the MB logic gate to Hg^{2+} . The fluorescence emission spectra are shown for different Hg^{2+} concentrations from 0, 10, 50, 100, 200, 500 to 1000 nM. (B) Changes of the fluorescence intensity at 518 nm of the MB based logic gate with different concentrations of Hg^{2+} . The inset is the calibration curve of the MB based logic gate to the detection of Hg^{2+} .

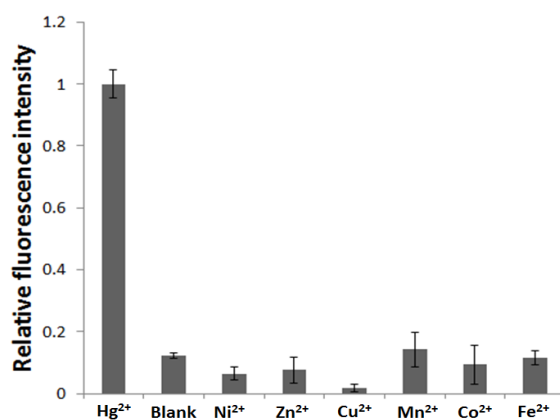


Figure 7. Interference test of different metal ions for the logica gate. Concentration of Hg^{2+} : 200 nM; concentration of other metal ions: 1000 nM.

3.4. Iodide Ion Detection.

3.4.1. Sensitivity study.

As discussed previously, I^- as a second input will turn off the logic gate. The change of the fluorescence intensity will be related to the amount of I^- . To investigate the sensitivity for I^- detection, different concentrations of I^- were added into the 200 nM Hg^{2+} , 10 nM MB system to monitoring the fluorescence intensity. As shown in Figure 8A, with the increase of I^- concentration, a gradual decrease of the fluorescence was observed. This demonstrated the competition between I^- and thymine for Hg^{2+} . Figure 8B showed that the fluorescence decrease was dependent on the concentration of I^- . Linear relationship ($R^2 = 0.9983$) between the fluorescence decrease and the I^- concentration was obtained when the concentration of I^- varied from 0 to 0.40 μM (inset of Figure 8B). The LOD for I^- was calculated to be 42 nM that was lower than the reported colorimetric method of 6 μM ³⁷ and the graphene oxide based fluorescence method of 100 nM.¹⁶ In addition, the process for the detection of I^- using Hg^{2+} /MB system was faster than the reported methods. Compared to the graphene oxide based fluorescence method for the iodide detection, this reaction time was 6 times shorter (Figure 2).¹⁶

3.3.2. Selectivity study.

The selectivity of this assay for the detection of I^- was investigated by testing some common competing anions, including Cl^- , Br^- , F^- , SO_4^{2-} , ClO_3^- , HCO_3^- , HPO_4^- , NO_3^- and IO_3^- , at a concentration of 6.40 μM under the same condition. The results showed that only I^- decreased the fluorescence intensity dramatically (Figure 9), showing a 71.7% decrease of the original value. While, other anions showed insignificantly changes on the fluorescence signals of the Hg^{2+} /MB system. Among them, the largest decrease was from Br^- , showing an 8.6% decrease on the fluorescence

intensity. This was 8.3 times lower than that with I^- . The student t test ($p < 0.01$) showed that there was significant difference between the addition of I^- and Br^- . Overall, the sensitivity and selectivity investigation for the I^- detection demonstrated that this Hg^{2+}/MB system was suitable for the detection of I^- against other competing anions.

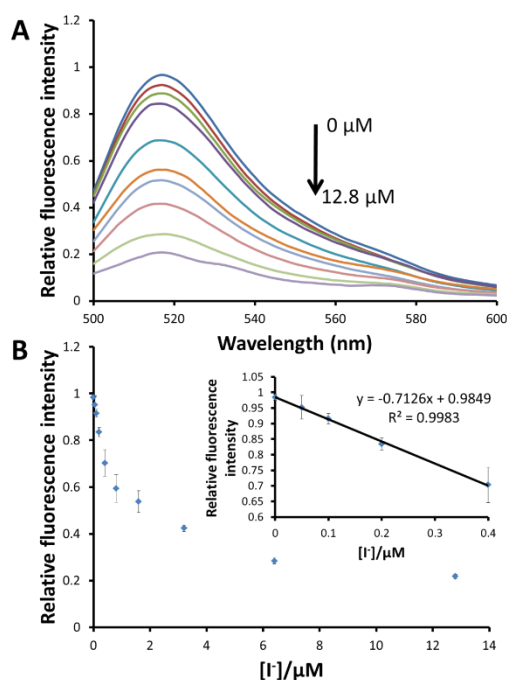


Figure 8. (A) Fluorescence response of the MB logic gate to I^- ions. The fluorescence emission spectra are shown for different I^- concentrations from 0, 0.05, 0.10, 0.20, 0.40, 0.80, 1.60, 3.20, 6.40 to 12.80 μM . (B) Changes of the fluorescence intensity at 518 nm of the MB based logic gate with different concentrations of I^- . The inset is the calibration curve of the MB based logic gate for the detection of I^- .

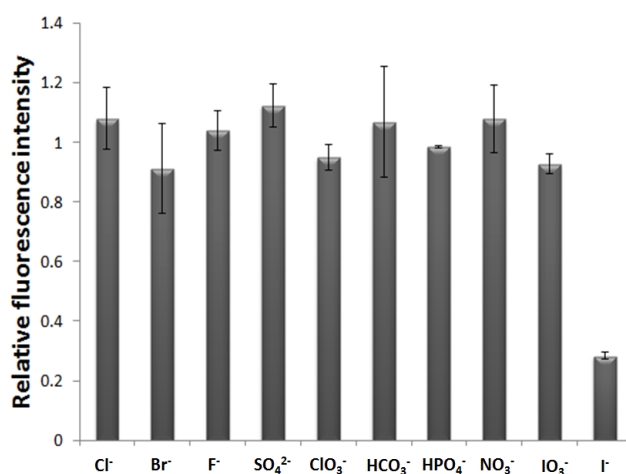


Figure 9. Interference study of different anions to the MB-based logic gate. The concentration of all the ions: 6.40 μM .

3.5. Real Sample Detection.

Table 1. Detection of Hg^{2+} and I^- in tap water samples ($n=3$).

<i>Target</i>	<i>Added</i>	<i>Found</i>	<i>Recovery</i>
Hg^{2+}	100 nM	108 ± 15 nM	108%
	150 nM	145 ± 16 nM	97%
I^-	0.10 μM	0.10 ± 0.03 μM	100%
	0.30 μM	0.31 ± 0.06 μM	103%

To demonstrate the real application of the developed sensing system, we detected tap water using the logic gate. Different amounts of Hg^{2+} and I^- were spiked into the tap water samples. All samples were first filtered with a 0.2 μm membrane. Afterwards, the concentration of Hg^{2+} and I^- in the samples were analyzed. The results are shown in Table 1. The recoveries ranged from 97% to 108%. This result indicated that the present logic gate would be applicable for the detection of Hg^{2+} and I^- .

4. Conclusions

In conclusion, a simple, rapid and sensitive logic gate based on a MB was developed for sensing Hg^{2+} and I^- . The fluorescence of MB logic gate increased with the assistant of Hg^{2+} in a concentration-dependent manner. With this assay, the LOD of Hg^{2+} was achieved as low as 7.9 nM. Furthermore, the fluorescence intensity of the Hg^{2+} /MB system decreased with the addition of I^- because of a stronger binding force between the Hg^{2+} and I^- . The LOD of I^- was calculated to be 42 nM which was lower than other reports. Based on the fluorescence change of the MB logic gate system with the addition of Hg^{2+} or/and I^- , a DNA INHIBIT logic gate was constructed. To the best of our knowledge, this was the first molecular MB based logic gate to detect Hg^{2+} and

I, which expanded the applications of the MB in the fabrication of the chemical Boolean logic gates.

CHAPTER II

ULTRASENSITIVE DETECTION OF 3'-5' EXONUCLEASE ENZYMATIC ACTIVITY USING MOLECULAR BEACONS

1. Introduction

DNA exonucleases are enzymes that digest DNA sequences from 3' termini or 5' termini. Within the exonuclease family, the enzymatic activity of 3'-5' exonuclease plays a key role for several important cellular and physiological processes, such as promoting genetic recombination reactions,³⁸ keeping fidelity of DNA replication³⁹ and repairing DNA double-strand breaks.⁴⁰ Both overexpression and lack of 3'-5' exonuclease enzymatic activity will cause serious diseases and lead to more susceptible to cancers and other diseases under stress conditions.^{41, 42} For example, a major 3'-5' exonuclease named TREX1 could inhibit the innate immune response to HIV.^{43, 44} Therefore, the detection of the 3'-5' exonuclease activity could be used for the diagnoses and therapies for several diseases.

Traditional approaches for the detection of 3'-5' exonuclease activity are based on radioisotope labeled DNA,⁴⁵ which are cost-prohibitive, time-consuming, and could cause safety concerns.⁴⁶ Therefore, it is urgent and useful to develop an efficient, sensitive and easily-operated method for evaluating the 3'-5' exonuclease activity. Recently, fluorescence-based methods have been developed for the detection of different enzymes,

such as polymerases, ligases, and endonucleases.⁴⁷⁻⁵⁰ However, only a few studies were published for the detection of 3'- 5' exonuclease activity with the fluorescence-based assay.^{51, 52} For example, Leung et al. developed a label free fluorescence assay for the detection of 3'- 5' exonuclease activity based on the G-quadruplex-binding probe.⁵³ This assay showed great advantages over the traditional methods. However, its limit of detection was 5 U/mL only. Recently, Su et al. used the single-labelled DNA probe to detect the activity of Exo III with the limit of detection of 0.04 U/mL. However, a phosphorothioated base in the 3' terminal should be modified in order to achieve the selectivity to the Exo III, which increased the cost and complexity of the detection system.⁵⁴ To overcome these limitations of these methods, we developed a fast, sensitive and cost-effective method to detect the activity of 3'- 5' exonuclease based on the traditional molecular beacon (MB).

A MB is a single-stranded DNA sequence that can form a hairpin structure modified with a fluorophore and a quencher on the 5' - and 3'-ends, respectively. MBs have been developed rapidly for biosensor applications in the last few decades.^{55, 56} Because of the low background fluorescence signal and excellent selectivity of MBs, a high signal-to-background ratio can be achieved using MBs for detection of DNA, mRNA, proteins, metal ions, and small molecules.^{10, 27, 57-61} Moreover, MBs have been used for the detection of enzymatic activities, such as the activity of the endonuclease,⁴⁷ polymerase,⁴⁸ ligase⁴⁹ and other enzymes which can change the nucleic acid conformation.⁶² However, so far, the traditional MBs have not been applied for the detection of exonuclease activities. Therefore, an ultrasensitive and ultra-rapid fluorescence assay for the detection of 3'- 5' exonuclease activity based on MBs was developed

in this work. Exo III was used as a model that contains the activities of 3'- 5' exonucleases to illustrate the proof-of-concept of our method. Surely, Exo III does not exist in human body. However, other enzymes containing the 3'- 5' exonucleases activities in human are expected to be detected by this method because they contain the same enzymatic activity. The dual-MB system developed in this work can detect the 3'- 5' exonucleases activities with limit of detection of 0.01 U/mL in buffer and 0.04 U/mL in 10 times serum sample. This implied that the dual-MB system has the potential for evaluating the 3'- 5' exonucleases activities in order to investigate the disease generating process, diagnosis and therapy strategies.

2. Experimental Section

2.1. Chemicals and Materials

DNA sequences used in this work were purchased from Fisher Scientific. The sequences for molecular beacons (MBs) were: 5'-FAMCCACCAGTTTTTTAGCTGAGGGTGG-BHQ1-3' (FAM-MB) and 5'-Cy5-CCTCGAGTTTTTTAGCTGATCGAGGTTGTG-BHQ2-3' (Cy5-MB), respectively. All the exonuclease enzymes (Exo III, Exo I, T7 Exo, T5 Exo, Exo T and RecJf) and 10X NEBuffer 4 (20 mM Tris-acetate, 50 mM potassium acetate, 10 mM Magnesium Acetate and 1 mM Dithiothreitol pH 7.9 @ 25 °C) were purchased from New England Biolabs, Inc. The deionized water (18.3 M Ω •cm) was produced from the Millipore water purification system.

2.2. Apparatus

Fluorescence experiments were all performed using a Fluorolog-3 Spectrofluorometer with a 450 W xenon lamp (Jonin Yvon-Spex, Instruments S.A., Edison, NJ). For the FAM fluorescence detection, the excitation wavelength was 480

nm with an emission range of 500-600 nm. The fluorescence intensity at 518 nm was used to evaluate the performance of the proposed assay. For the detection of Cy5, the excitation was 645 nm with an emission range of 655-750 nm. The fluorescence intensity at 660 nm was used to evaluate the performance of the proposed assay. Both the excitation and emission slit widths were set to 5.0 nm. All the experiments were carried out at 37 °C for 200 s.

2.3. Exo III Detection Based on FAM-MB

A 10 nM FAM-MB sample was incubated in 50 µL 1X NEBuffer 4 at 37 °C. A 0.20 U Exo III aliquot was then added into the solution to incubate for 200s. Finally, the fluorescence of the solution was detected. In contrast, no Exo III was added to the control solution and the fluorescence intensity was monitored for 200 s.

To investigate the sensitivity of the assay for Exo III, FAM-MB (10 nM) was mixed with different concentrations of Exo III varying from 0.04 U/mL to 4.00 U/mL. The fluorescence intensity of FAM at 518 nm was recorded after 200s. The calibration curve was obtained by plotting the relative fluorescence intensity *vs* the concentrations of the Exo III. The selectivity of the assay for the detection of Exo III was investigated by incubating FAM-MB (10 nM) with different exonucleases including T7 Exo, Exo I and RecJf at the concentration of 4.00 U/mL. The fluorescence intensity was also measured at 200 s for each exonuclease.

The effects of pH on the enzymatic activity of Exo III were investigated by incubating 10 nM FAM-MB in 50 µL 1X NEBuffer 4 at 37 °C, with the addition of 0.20 U Exo for 200 s. The pH varied from 5.5 to 9.5. For the investigation of effect of divalent ions, 10 nM FAM-MB was incubated in 50 µL 1X NEBuffer 4 at 37 °C with addition of 0.3 mM Cu²⁺, Ca²⁺ and Mn²⁺, respectively. Then, 0.20 U Exo III was added into each solution to incubate for 200 s.

2.4. Distinguishing Exonucleases Based on Dual-MB System

FAM-MB (10 nM) and Cy5-MB (10 nM) were incubated in 50 μ L 1X NEBuffer 4 at 37 $^{\circ}$ C. 0.20 U Exo III, T5 Exo and RecJf were then added to the solution to incubate for 200 s. Finally, the fluorescence of FAM and Cy5 were detected. Properties and expected responses of the exonucleases in dual-MB system are summarized in Table 1.

3. Results and Discussion

3.1. Detection of Exo III with MB

As shown in Figure. 10A, a 6-carboxyfluorescein (FAM) modified MB (FAM-MB) with blunt 3'-termini was used as the probe. Because of the hairpin structure of the MB, FAM was close to the quencher (Black Hole Quencher-1, BHQ1) modified on the 3'-termini. The fluorescence of the FAM was quenched by BHQ1 through effective Förster resonance energy transfer (FRET). However, in the presence of Exo III, whose substrate is blunt or recessed 3'-termini, the FAM-MB would be digested by Exo III from the 3'-termini. Because the quencher was modified on the last mononucleotide of the 3'-termini, with the removal of the last mononucleotide, the quencher was also removed from the MB by Exo III. As a result, the fluorescence of the FAM was restored. As shown in Figure. 1B, the fluorescence intensity of FAM-MB solution increased by about 18 times after the reaction with 4.00 U/mL Exo III for 200 seconds (Figure. 10B, curve a) compared to the control that has no Exo III (Figure. 10B, curve c), demonstrating that the designed FAM-MB could be an ultrasensitive fluorescence probe to detect 3'- 5' exonuclease activity of Exo III. In order to further confirm that the fluorescence increase is due to the addition of active Exo III, a heat-inactivated Exo III was used as the second control. The Exo III was heated at 80 $^{\circ}$ C for 30 min to be inactivated before incubation with the FAM-MB. The result showed that the

fluorescence intensity of FAM-MB was significantly diminished (Figure. 10B, curve b).

In the investigation of sensitivity of the assay, a 10 nM FAM-MB solution was incubated with various concentrations of Exo III (0-8.00 U/mL) at 37 °C in 50 μ L 1X NEBuffer 4. The FAM's fluorescence intensity increased as the concentration of Exo III increased (Figure. 11A). The signal-to-background ratio reached 27 when the concentration of Exo III was 8.00 U/mL. The total detection time is less than 200 s because the fluorescence intensity reached a plateau at 200 s after the addition of Exo III. In the following experiments, the incubation time of 200 s was chosen.

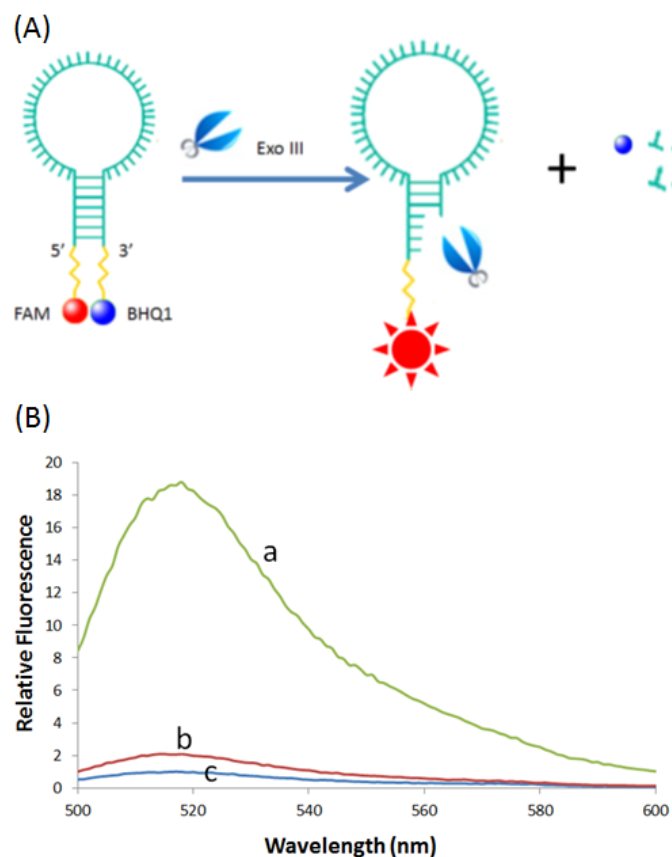


Figure 10. (A) The working principle of the detection of Exo III enzymatic activity based on FAM-MB. (B) Fluorescence emission spectra of 10 nM FAM-MB in 50 μ L 1X NEBuffer 4. (a) 4.00 U/mL Exo III; (b) 4.00 U/mL heat-inactivated Exo III; (c) no Exo III. λ_{ex} = 480 nm.

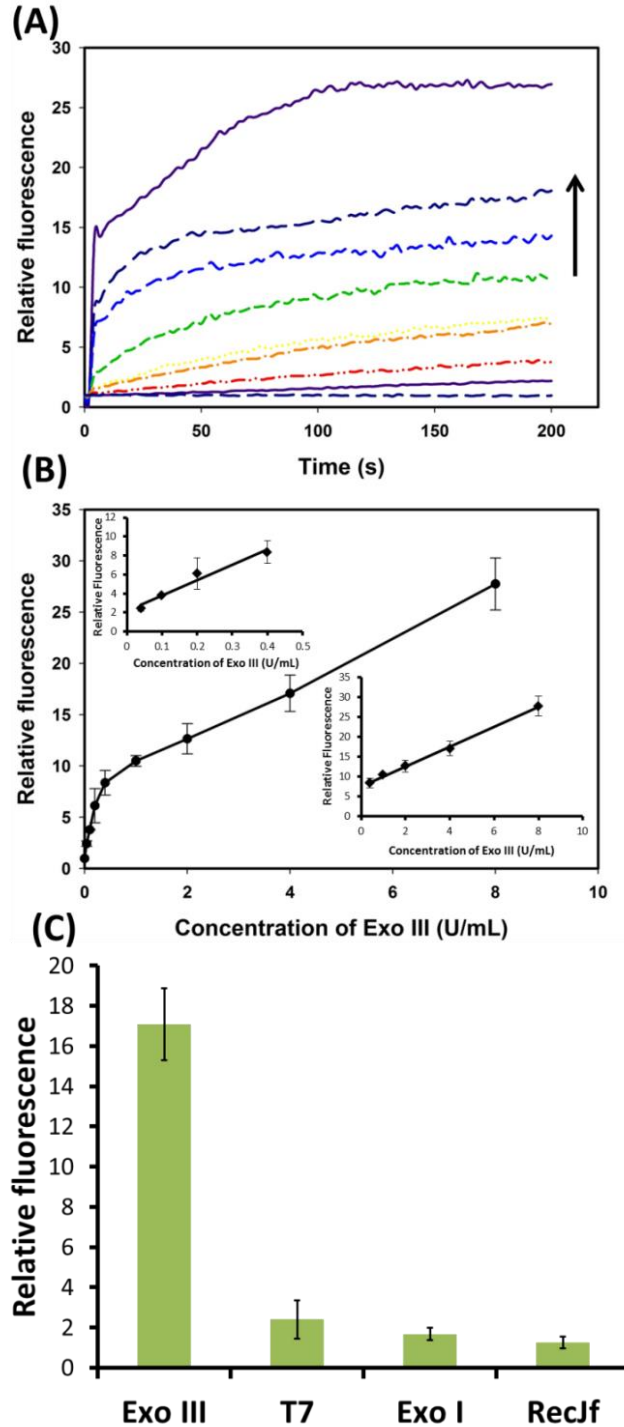


Figure 11. The detection of Exo III based on FAM-MB. (A) Time-dependent fluorescence responses in the presence of different concentrations of Exo III. From bottom to top: 0, 0.04, 0.10, 0.20, 0.40, 1.00, 2.00, 4.00, 8.00 U/mL of Exo III in $1 \times$ NEBuffer 4. (B) The plot of the fluorescence enhancement of different concentrations of Exo III. Reactions were performed in $50 \mu\text{L}$ of $1 \times$ NEBuffer 4 with 10 nM FAM-MB at $37 \text{ }^\circ\text{C}$ for 200 s. Inset: the two calibration curves in different concentration ranges. (C) Selectivity of the assay for Exo III over other exonucleases. Fluorescence enhancement of the FAM-MB system responded to 4.00 U/mL exonucleases.

The fluorescence enhancement of the FAM-MB system was proportional to the concentration of Exo III. The dynamic range was from 0.04 U/mL to 8.00 U/mL. There were two linear ranges for the calibration curve. The first one was in the low concentration range (0.04 U/mL-0.40 U/mL); the calibration curve in the first linear range is showed in the top inset of Figure 11B. The regression equation was $Y = 18.029X + 1.6564$ with a correlation coefficient of 0.9766. The second linear range was from 0.40 U/mL to 8.00 U/mL whose calibration curve was showed in the bottom inset of Figure. 11B. The regression equation was $Y = 2.5011X + 7.5561$ with a correlation coefficient of 0.9989. Y and X represented the relative fluorescence and the concentration of Exo III in the unit of U/mL, respectively. The limit of detection (LOD) was 0.01 U/mL based on three times of the signal-to-noise level. This was 500 times lower than that of the G-quadruplex-binding label-free fluorescence method.¹⁶

Next, we investigated whether this FAM-MB assay could selectively detect Exo III from other types of exonucleases. According to the property of Exo III, any exonucleases containing a duplex DNA substrate may interfere with the detection of Exo III. T7 exonuclease is such an exonuclease, which acts on duplex DNA in the 5'-3' direction. In addition, Exo I and RecJf belong to the similar exonuclease family with Exo III. Exo I can catalyze the removal of nucleotides from single-stranded DNA in the 3'-5' direction, and RecJf can catalyze the removal of deoxynucleotide monophosphates from single-stranded DNA in the 5'-3' direction. Therefore, these three exonucleases were chosen to investigate the assay selectivity. Encouragingly, the T7 exonuclease did not induce dramatic fluorescence enhancement with the same concentration of the Exo III (Figure. 11C). This result may have benefited from the rapid detection of the fluorescence within 200 s of reaction time. Similarly, the fluorescence enhancement from Exo I and RedJf were limited as well (Figure. 11C).

3.2. The Stability and Effect of Ions

The stability of the probe was also investigated. Generally, the pH not only would affect the hybridization of the MB, but could also affect the activity of the exonuclease. Thus, the pH value should play a crucial role in the stability of the MB probe. We chose five buffer solutions with different pH values in the range of 5.5 to 9.5 to test the fluorescence intensity of the MB probe. The results are shown in Figure. 12A. The highest signal-to-background ratio was gained when the pH was 7.5. Both the acid and alkali conditions led to the decrease of the signal-to-background ratio. Apparently, the pH value significantly affects the stability of the MB probe.

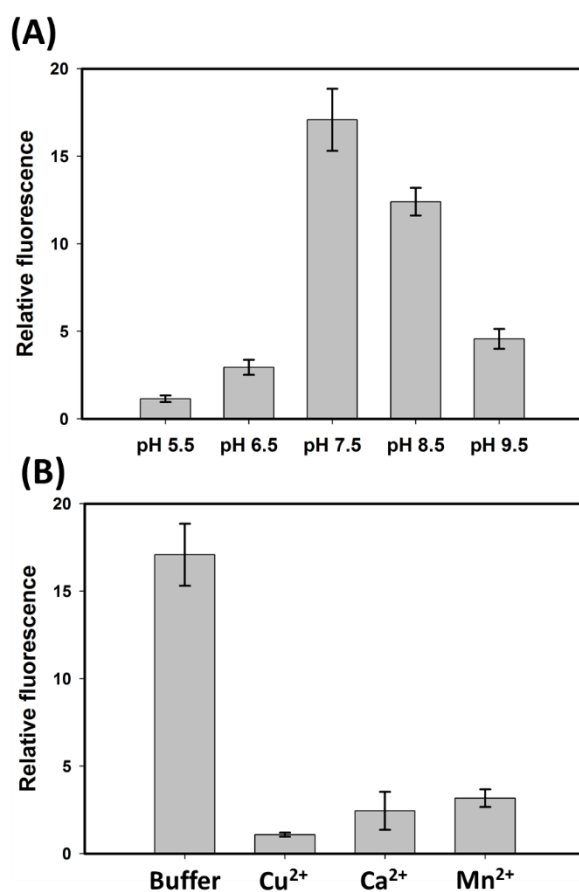


Figure 12. The stability investigation of the MB system for the detection of Exo III. (A) The effect of pH on the reaction rate of the MB system to Exo III. (B) The effect of divalent ions on the Exo III activity of the MB system to Exo III.

Furthermore, we investigated the effects of metal ions on the activity of exonucleases. It was reported that some divalent ions would inhibit the activity of the exonucleases to cleave DNA phosphodiester bonds.⁶³ Thus, the effects of three common divalent ions, including Cu^{2+} , Ca^{2+} and Mn^{2+} , on the activity of the Exo III were investigated. These cations might be present in complex samples including serum or cells. As shown in Figure. 12B, the addition of any of these ions would dramatically affect the activity of Exo III compared to the control. Under the same concentration, the Cu^{2+} reduced the MB probe signal over 95 %. Therefore, the designed MB probe has fairly good selectivity to the Exo III over both other types of exonucleases and metal ions.

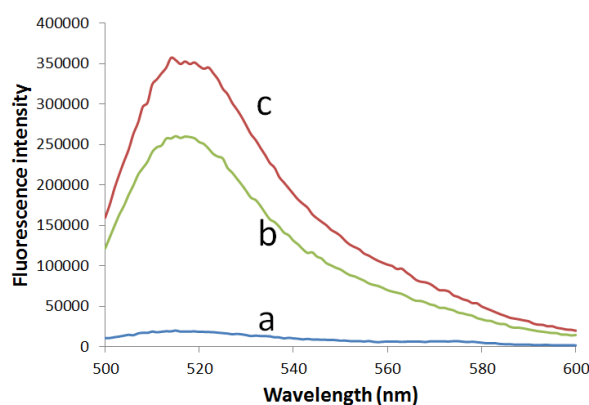


Figure 13. The fluorescence intensity responded to 10 nM FAM-MB (a), added with 4.00 U/mL T5 exonuclease (b) or 4.00 U/mL Exo III (c).

3.3. Design of Dual-MB System

However, even though the T7 exonuclease did not affect the detection of Exo III, other similar exonucleases may give a false signal if they could react fast with the MBs. We found that the T5 exonuclease, an exonuclease that has 5'-3' exonuclease activity, degraded DNA in the 5'-3' direction in both single-stranded and double-stranded DNAs. When the T5 exonuclease was incubated with the FAM-MB system for 200 s, the fluorescence of the FAM increased as the addition of Exo III (Figure 13).

In order to overcome this interference, a dual-MB system was developed, containing not only FAM-MB, but also a Cy5-MB with a 3' extension terminus.

As shown in Figure 14A, in the dual-MB system, the Exo III could only catalyze the digestion of the duplex DNA with blunt or recession 3'-termini to induce the fluorescence enhancement of the FAM, but not the Cy5. In contrast, the T5 exonuclease could catalyze both single-stranded DNA and double-stranded DNA from 5'-termini; as a result, it would induce the fluorescence enhancement of both FAM and Cy5. RecJf exonuclease, which can only catalyze the removal of deoxynucleotide monophosphates from a single-stranded DNA in the 5'-3' direction, would not induce any fluorescence enhancement. The properties of the three exonucleases and anticipating fluorescence responses were summarized in the Table 2.

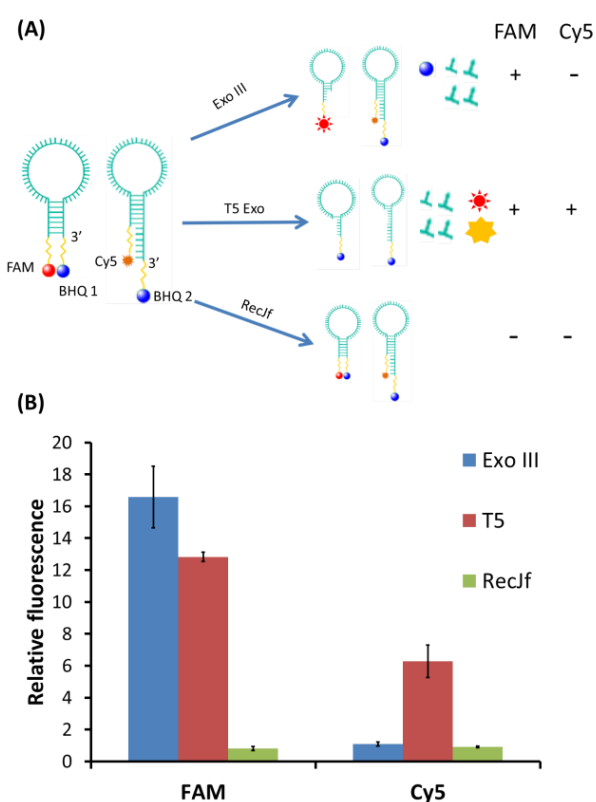


Figure 14. (A) Schematic illustration of the dual-MB system for distinguishing different exonucleases. (B) Fluorescence enhancement patterns of the dual-MB system with 4.00 U/mL Exo III, T5 exonuclease and RecJf. The dual-MBs system 20 contained 10 nM FAM-MB and 10 nM Cy5-MB in 50 μ L of 1 \times NEBuffer 4, incubated at 37 $^{\circ}$ C for 200 s to detect the fluorescence intensity. λ_{ex} (FAM)=480 nm, λ_{em} (FAM)= 518 nm. λ_{ex} (Cy5)= 645 nm, λ_{em} (Cy5)= 660 nm.

Table 2. The properties of different exonucleases. “+” indicates fluorescence enhancement; “-” indicates constant fluorescence.

<i>Exonuclease</i>	<i>Substrate</i>	<i>Direction</i>	<i>FAM-MB</i>	<i>Cy5-MB</i>
Exo III	dsDNA	3'- 5'	+	-
T5 Exo	dsDNA,ssDNA	5'- 3'	+	-
RecJf	ssDNA	5'- 3'	-	-

Using this dual-MB system, three exonucleases at the concentration of 4.00 U/mL were detected (Figure 14B). As the negative control, the RecJf exonuclease showed no fluorescence enhancement of FAM and Cy5, which meant that both FAM-MB and Cy5-MB were not digested by the RecJf exonuclease. When Exo III was added into the solution, the fluorescence of FAM increased by 16.6 times, while the fluorescence of the Cy5 did not change because this 3' extension Cy5-MB was not the substrate of Exo III. However, when T5 exonuclease was added into the solution, the fluorescence intensity of FAM increased by 12.8 times and the fluorescence intensity of Cy5 increased by 6.3 times. If the fluorescence enhancement for each dye was defined as 1, and no fluorescence enhancement defined as 0, the responses of the dual-MB system in the manner of (FAM, Cy5) for Exo III, T5 exonuclease, and RecJf were (1, 0), (1, 1) and (0, 0), respectively. From these different response patterns, Exo III, T5 exonuclease, and RecJf could be distinguished from each other.

3.4. Complex Samples Investigation

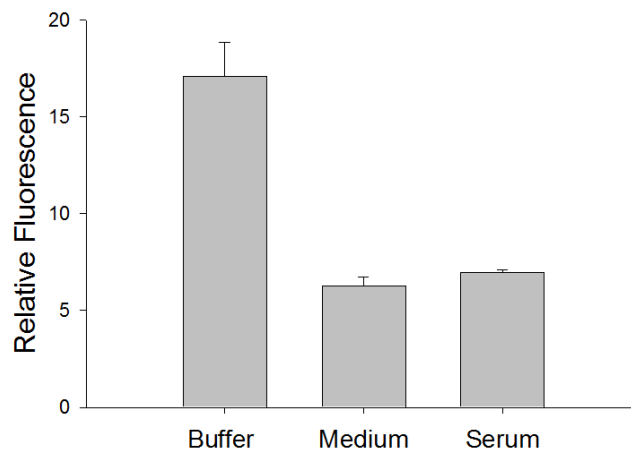


Figure 15. The fluorescence enhancements of FAM-MB in different solutions. The concentrations of Exo III were 4.00 U/mL.

To test the feasibility of the designed MB probe for the detection of Exo III we applied the probe to complex samples, including cell culture medium and fetal bovine serum. As shown in Figure 15, with the same concentration of Exo III, the fluorescence enhancements of FAM in the 10 times diluted RPMI 1640 medium and fetal bovine serum were lower than that of the ideal buffer solution. The lower fluorescence enhancements of FAM in the complex samples compared with the ideal buffer might be due to the high background signal of these two matrixes when they were excited at 488 nm irradiation. In order to show how much the other exonucleases would interfere the detection of Exo III, T5 exonuclease and RecJf were added into the dual-MB system in the complex sample. As shown in Figure 16A, T5 exonuclease induced the fluorescence enhancement of both FAM and Cy5 in the serum sample. In contrast, RecJf exonuclease did not cause any fluorescence enhancement for these two dyes. The fluorescence intensity of FAM increased with the addition of Exo III. In contrast, the fluorescence intensity of Cy5 kept constant (Figure 16A), which was consistent with the results in the buffer solution. Therefore, this dual-MB system could eliminate the interference of other exonuclease for the detection of the 3'-

5' exonuclease enzymatic activity in complex sample by the different fluorescence enhancement combinations.

Because the fluorescence enhancements in these two complex samples were not consistent with that in the ideal buffer, a new calibration curve had to be prepared for the detection of the Exo III in the complex samples. The fetal bovine serum was chosen as the example of the complex sample for the preparation of the calibration curve. As shown in Figure. 16B, the complex time fluorescence enhancements of FAM in the dual-MB system with addition of different concentrations of Exo III were monitored in 10 times diluted fetal bovine serum. Figure. 16C demonstrated the calibration curve of the dual-MB system for the detection of Exo III in the 10 times diluted fetal bovine serum. A similar curve at the concentration from 0 to 8.00 U/mL was exhibited as that in the ideal buffer except the corresponding relative fluorescence intensity was lower than those in the ideal buffer. Two linear ranges from 0 to 0.40 U/mL and 0.40 to 8.00 U/mL were observed in the complex sample, respectively. In order to further investigate the feasibility of this method for the detection of Exonuclease III activity in complex biological sample, fresh mice serum was used as another complex sample. As shown in Figure 17, the detection range was from 0 to 8 U/mL with similar two different linear ranges, including 0 to 0.4 and 0.4 to 8 U/mL. The limit of detection in this sample was 0.03 U/mL according based on three times of the signal-to-noise level. This is 3 times higher than that in ideal buffer, which might be caused by the complexity of the mice serum. However, all the results indicated that this dual-MB system might be used in complicated samples for the real-time detection of the enzymatic activity of Exo III.

As shown in Figure 11B and Figure 16C, the Exo III calibration curves in buffer and 10 times-diluted fetal bovine serum demonstrated an initially high slope up to Exo III concentration of 0.4 U/mL followed by a decrease in slope. This might be due to the fixed substrate's concentration. Theoretically, the calibration curve should

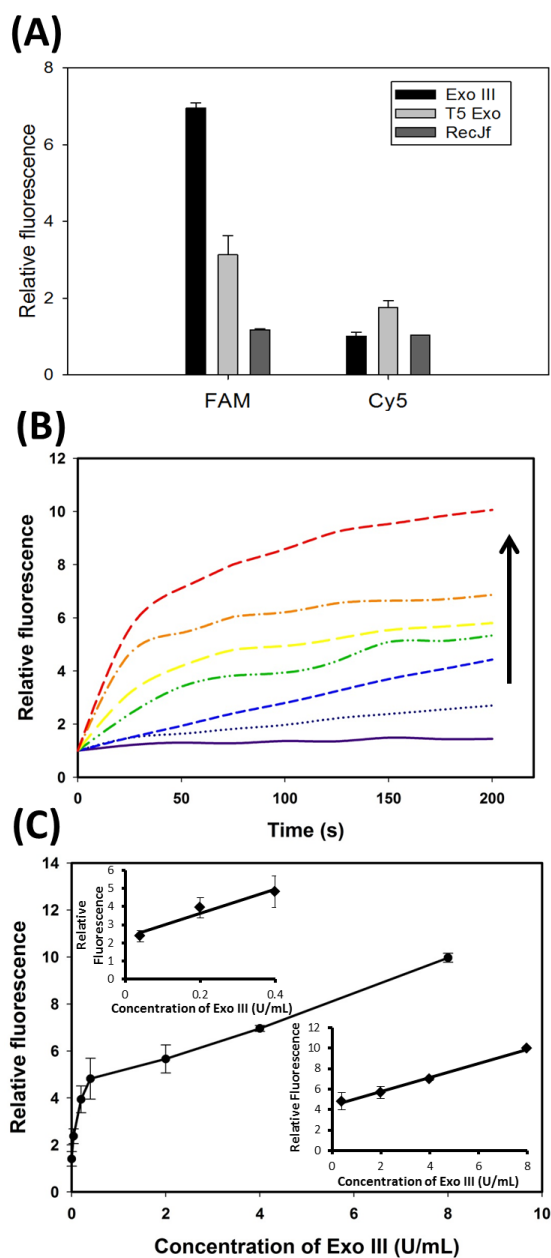


Figure 16. (A) The fluorescence enhancements of FAM-MB and Cy5-MB in 10 times diluted fetal bovine serum with the addition of 4 U/mL Exo III, T5 Exo and RecJf Exo. (B) Time-dependent fluorescence responses in the presence of different concentrations of Exo III. From bottom to top: 0, 0.04, 0.20, 0.40, 2.00, 4.00, 8.00 U/mL of Exo III in 10 times diluted fetal bovine serum. (C) The plot of the fluorescence enhancement of different concentrations of Exo III. Reactions were performed in 50 μ L of 10 times diluted fetal bovine serum with 10 nM FAM-MB and 10 nm Cy5-MB at 37 $^{\circ}$ C for 200 s. Inset: the two calibration curves in different concentration ranges.

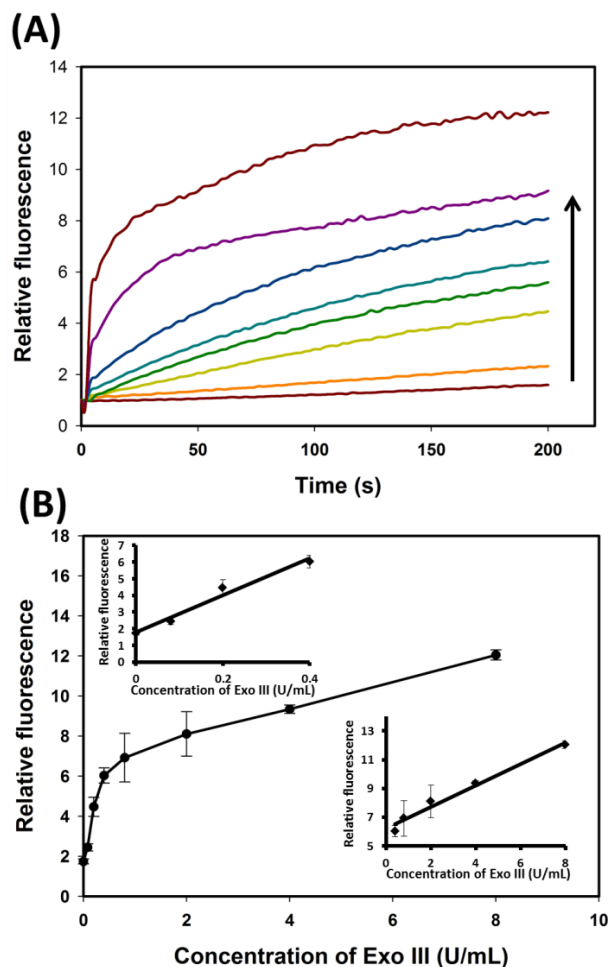


Figure 17. (A) Time-dependent fluorescence responses in the presence of different concentrations of Exo III. From bottom to top: 0, 0.08, 0.20, 0.40, 0.80, 2.00, 4.00, 8.00 U/mL of Exo III in 10 times diluted fresh mice serum. (C) The plot of the fluorescence enhancement of different concentrations of Exo III. Reactions were performed in 50 μ L of 10 times diluted fresh mice serum with 10 nM FAM-MB and 10 nm Cy5-MB at 37 $^{\circ}$ C for 200 s. Inset: the two calibration curves in different concentration ranges.

be off from the linear range when the concentration is higher than the saturated concentration. The reason for the second linear range might be from the excess residue intact the MB, which could be slowly digested by higher concentration of Exo III beyond the theoretical linear concentration limit. In this case, Exo III with a concentration of 0.40 U/mL was enough to digest most of the FAM-MB in the system. This triggered a larger slope of the calibration curve in the low concentration range. However, when the concentration of Exo III was higher than the turning point of 0.40 U/mL, even most of the FAM-MB was digested by the Exo III, the excess Exo III would

no longer have enough substrate to digest. As a result, the slope of the calibration curve in the higher concentration range decreased.

4. Conclusions

In conclusion, an ultrasensitive, rapid and simple fluorescence method has been developed for the detection of Exo III. The dynamic range of the assay was 0.04 U/mL to 8.00 U/mL with the detection limit of 0.01 U/mL. The total incubation time for the assay was 200 s which was about 10 times faster than the label-free fluorescence method. The assay showed good selectivity over T7 exonuclease, Exo I and RecJf exonuclease. Even the T5 exonuclease would interfere the detection of Exo III, the dual-MB system was successful for eliminating the interference of other exonucleases. Finally, the designed dual-MB probe was applied to the monitoring of the enzymatic activity of Exo III in complex samples. The results suggested a great potential of the dual-MB probe for the detection of Exo III levels in complex samples. The proposed fluorescence assay is expected to be used for disease diagnosis and therapy related to the overexpression or loss of 3'→5' exonucleases and to expand the application of MBs in the enzymatic analysis.

CHAPTER III

LABEL-FREE FLUORESCENCE ASSAY COUPLED EXONUCLEASE REACTION AND SYBR GREEN I FOR THE DETECTION OF T4 POLYNUCLEOTIDE KINASE ACTIVITY

1. Introduction

Phosphorylation, a transferring of γ -phosphate residues of adenosine triphosphate (ATP) to 5'-hydroxyl terminus of polynucleotides, plays an important role in DNA replication, DNA repair and recombination^{64, 65}. In these normal cellular processes, several factors, such as chemical substances, ionizing radiation⁶⁶ and nucleases⁶⁷, would cause nucleic acid lesions that contain 5'-hydroxyl termini. This 5'-hydroxyl termini may lead to failure of 5'-phosphate terminal dependent repair processes for nucleic acids, resulting in severe gene damage and diseases^{68, 69}. Therefore, it is highly desirable to monitor the polynucleotide kinase activity and inhibition for further understanding phosphorylation and related biological processes.

Normally, methods used to study the phosphorylation of nucleic acids included radical isotope ³²P-labeling, polyacrylamide gel electrophoresis (PAGE) and autoradiography⁶⁹⁻⁷¹. However, these methods have safety concerns (radio labelling), and are time-consuming and complex. Recently, several electrochemical and fluorescence sensors for monitoring kinase activities were developed⁷²⁻⁷⁶. The replacement of radio labelling using fluorescence labelling in these assays eliminated safety concerns; however, labelling fluorophores to nucleic acids increased the cost of the assay. For example, Tang *et al.* reported a fluorescence

assay for monitoring phosphorylation process using a dual-label molecular beacon⁷⁷, and Song *et al.* developed a real-time method for the kinase activity detection using a singly labelled molecular beacon⁷⁵. By using graphene oxide as a quencher platform, Lin *et al.* developed a novel method for the kinase activity and inhibition monitoring with a FAM modified dsDNA⁷⁶. These methods provided high sensitivity for detections in spite of labelling requirements. The development of labelling-free methods for the detection of phosphorylation kinase activities and inhibition is still a challenge.

Integrated DNA dyes, such as SYBR Green I (SG), are very powerful tools for fabricating DNA sensors based on their different affinities to the ssDNA and dsDNA^{78, 79}. They have been widely used for the detection of DNAs⁸⁰, metal ions⁸¹⁻⁸³, proteins and small molecules⁸⁴ with high sensitivity and low cost. Therefore, SG could provide a low-cost alternative for label-free detection of phosphorylation kinase activities and inhibition. λ exonuclease (λ exo) is an enzyme that catalyzes efficiently cleavage of dsDNA from 5'-phosphate termini to generate ssDNA and mononucleotides. However, the cleavage efficiency of the λ exo is greatly reduced if the 5'-termini of dsDNA is hydroxyl. In this work, we developed a simple, label-free sensitive method for kinase activity and inhibition analysis based on the coupled λ exo cleavage reaction and the SYBR Green I. The label-free method developed in this work can detect phosphorylation kinase activities in the linear range of 0.25 to 1.00 U/mL with a limit of detection of 0.11 U/mL.

2. Experimental

2.1. Materials and Apparatus

DNA sequences were purchased from Eurofins MWG Operon (Alabama, USA). The sequences for hair-pin probe were: 5'-TGC CTA CGA CCA ATT CCA CCT CAG CTA CCA GCA ACA GT-3' and 5'- ACT GTT GCT GGT AGC T-3'. The

exonuclease enzymes (T4 polynucleotide kinase and λ exo) and 10X NEBuffer 4 (50 mM potassium acetate, 20 mM Tris-acetate, 10 mM magnesium acetate and 1 mM DTT, pH 7.9.) were purchased from New England Biolabs, Inc (NEB, U.K.). SYBR Green I was purchased from Fisher Scientific (Pennsylvania, USA). The deionized water (18.3 M Ω •cm) was produced from the Millipore water purification system. Fluorescence experiments were performed using a Fluorolog-3 Spectrofluorometer with a 450 W xenon lamp (Jonin Yvon-Spex, Instruments S.A., Edison, NJ).

2.2. T4 PNK Detection and Optimization

In a typical phosphorylation and cleavage assay, 0.1 μ L 10x SG, 20 nM dsDNA probe, 0.1 mM ATP, 0.25 units of λ exo, and a series of different concentrations of T4 PNK were added to 100 μ L of 1x NEBuffer 4. After 30 min incubation at 37 $^{\circ}$ C, the fluorescence spectra were recorded with the excitation wavelength of 490 nm and emission from 505 nm to 650 nm. The fluorescence intensity at 518 nm was used as the detection signal. The optimal values of phosphorylation time, concentrations of λ exo and ATP were investigated.

2.3. T4 PNK Inhibitor Evaluation

To investigate effects of the T4 PNK inhibitors on the phosphorylation process, the reactions were performed at various concentrations of inhibitors, including (NH₄)₂SO₄ (0-120 mM), and Na₂HPO₄ (0-90 mM). All mixtures contained 0.1 μ L 10x SG, 20 nM dsDNA probe, 0.1 mM ATP, 0.25 units of λ exo, and 10 U/mL T4 PNK.

3. Results and Discussion

3.1. Scheme of the T4 PNK Activity Detection

Based on the high affinity of SG to dsDNA and the unique property of λ exo, a label-free method was designed for the detection of T4 PNK activity. The proposed scheme for the PNK activity detection was illustrated in Figure 18. A double-stranded

DNA with one duplex 5'-hydroxyl termini was used as the label-free DNA probe. An integrating dye molecule, SG, was selected as the fluorescence signal source. The dsDNA coupled with SG would generate strong fluorescence intensity. With the addition of the T4 PNK, the 5'-hydroxyl termini of the dsDNA would be transferred to 5'-phosphate termini in the presence of ATP (Figure 18, step A). In the following step, the dsDNA probe was digested by the λ exo from the duplex 5'-phosphate termini to generate mononucleotides and ssDNA (Figure 18, step B). The binding force between the ssDNA and SG decreased dramatically, which led to a reduction of the fluorescence intensity. The extent of the fluorescence decrease was proportional to the concentration of T4 PNK. As a control, in the absence of T4 PNK, the λ exo digestion of the 5'-hydroxyl termini dsDNA was limited due to the lack of preferred substrate. As a result, the fluorescence intensity of the SG would have little change. With this strategy, no fluorescence label was needed to perform the detection of T4 PNK activity.

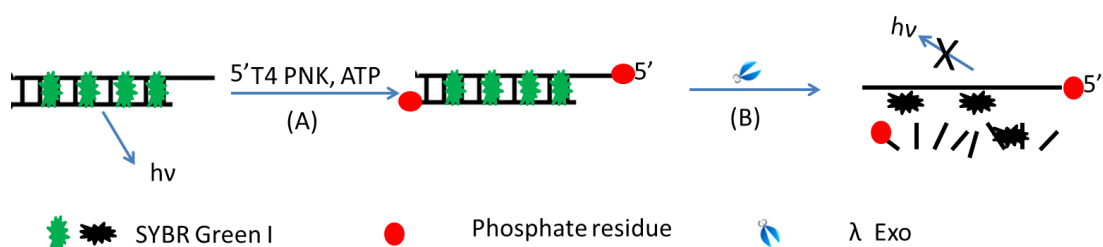


Figure 18. Schematic diagram of monitoring the T4 PNK activity by a label-free DNA probe coupled with SG and λ exo.

The phosphorylation process of T4 PNK could be monitored by measuring fluorescence changes of the system using SG as the integrating dye. As shown in Figure 19, when the dsDNA probe was treated with λ exo only, it exhibited high fluorescence intensity in the presence of SG (Figure 19 curve a). However, when the T4 PNK was added to phosphorylate the 5'-termini of the dsDNA probe followed by the digestion of the λ exo, much lower fluorescence intensity was observed (Figure 19, curve b). Up to 90% fluorescence emission disappeared upon the addition of the 20 U/mL T4 PNK.

The main reason was that the phosphorylated 5'-termini dsDNA was the preferred substrate of λ exo. It was reported that the reaction rate of the λ exo for dsDNA with 5'-phosphorol was over 300 times faster than that with 5'-hydroxyl termini⁸⁵. As a result, the dsDNA probe phosphorylated by the T4 PNK was digested much more rapidly than that without T4 PNK treatment by λ exo. The generated mononucleotides and ssDNA had low affinity to the SG, resulting in low fluorescence emission signal. The dsDNA probe without T4 PNK treatment remained the double-stranded structure which emitted high fluorescence signal with the interaction of the SG. The following experimental results showed that the fluorescence decrease was proportional to the activity and concentration of the T4 PNK, which demonstrated that this label-free system could be used for the detection of the T4 PNK activity.

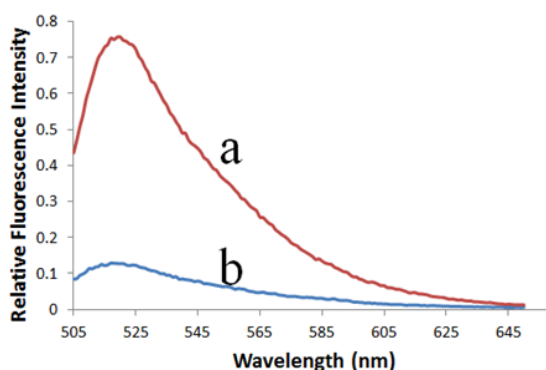


Figure 19. Fluorescence spectra of the dsDNA system without T4 PNK (a) and with 20 U/mL T4 PNK (b). Reactions were performed in 100 μ L of 1x NEBuffer 4 (pH = 7.9) with 20 nM dsDNA at 37 $^{\circ}$ C for 30 min. The concentrations of ATP and λ exo were 0.1 mM and 0.25 units, respectively. $\lambda_{ex} = 480$ nm.

3.2. Optimization of SG Concentration

SG played a crucial role in this designed assay. Therefore, the optimal concentration to distinguish ssDNA and dsDNA had to be investigated to obtain the highest sensitivity of the assay. In the presence of ssDNA, a very limited fluorescence signal was appeared (Figure 20A, curve a). However, the fluorescence intensity of SG enhanced several times when a dsDNA was added to the solution (Figure 20 A, curve b). The dramatic difference between curve a and curve b was the basis for distinguishing

ssDNA and dsDNA. To obtain the optimum detection ability, the concentration of SG must be optimized since it would affect the signal-to-background ratio of the detection. As shown in Figure. 3B, with the increase of the concentration of SG, both the fluorescence intensities of dsDNA and ssDNA solutions increased. To obtain the highest difference between dsDNA and ssDNA, the fluorescence intensity of dsDNA-to-ssDNA ratio was plotted against the SG concentration as shown in Figure 20C. The highest fluorescence dsDNA-to-ssDNA ratio was reached at the concentration of 20 nM. Therefore, 20 nM SG was chosen as the optimal concentration for the following experiments.

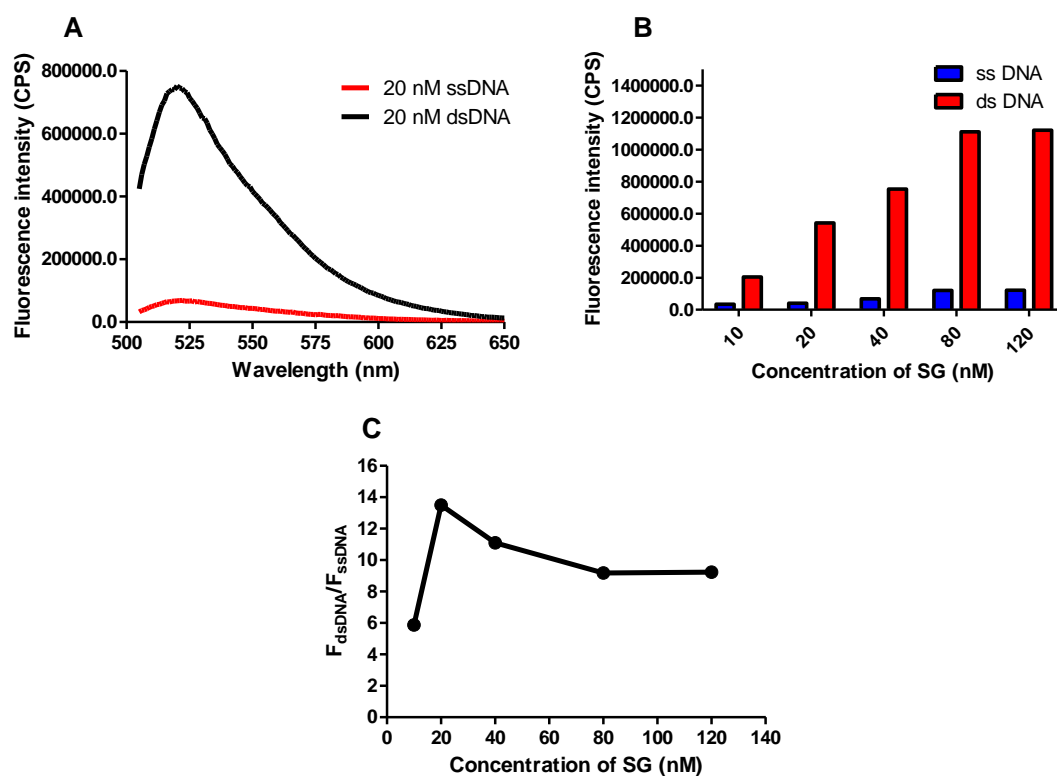


Figure 20. (A) Fluorescence spectra of 40 nM SG incubated with 20 nM ssDNA (Curve a) and dsDNA (Curve b). (B) Fluorescence intensity of dsDNA and ssDNA with the change of the concentration of SG. (C) The fluorescence intensity ratio of dsDNA to ssDNA with the change of the concentration of SG. Fluorescence intensity was measured in 100 μ L of 1x NEBuffer 4 (pH = 7.9) with 20 nM ssDNA or dsDNA at 37 $^{\circ}$ C. λ_{ex} = 480 nm.

3.3. Optimization of the Detection Parameters

In the phosphorylation process of DNA, there are several factors that will affect the catalysis efficiency. ATP is a co-factor for assisting in T4 PNK phosphorylation because it provides the phosphate group to be modified on the DNA strands. The concentration of ATP may affect the activity of the T4 PNK in the system. To gain better analytical performance, the effect of ATP concentration on the fluorescence intensity was studied as shown in Figure 21A. Because the fluorescence intensity of SG will decrease when the T4 PNK was present, we used the fluorescence intensity change as a measurement to evaluate the effect of ATP on the T4 PNK activity.

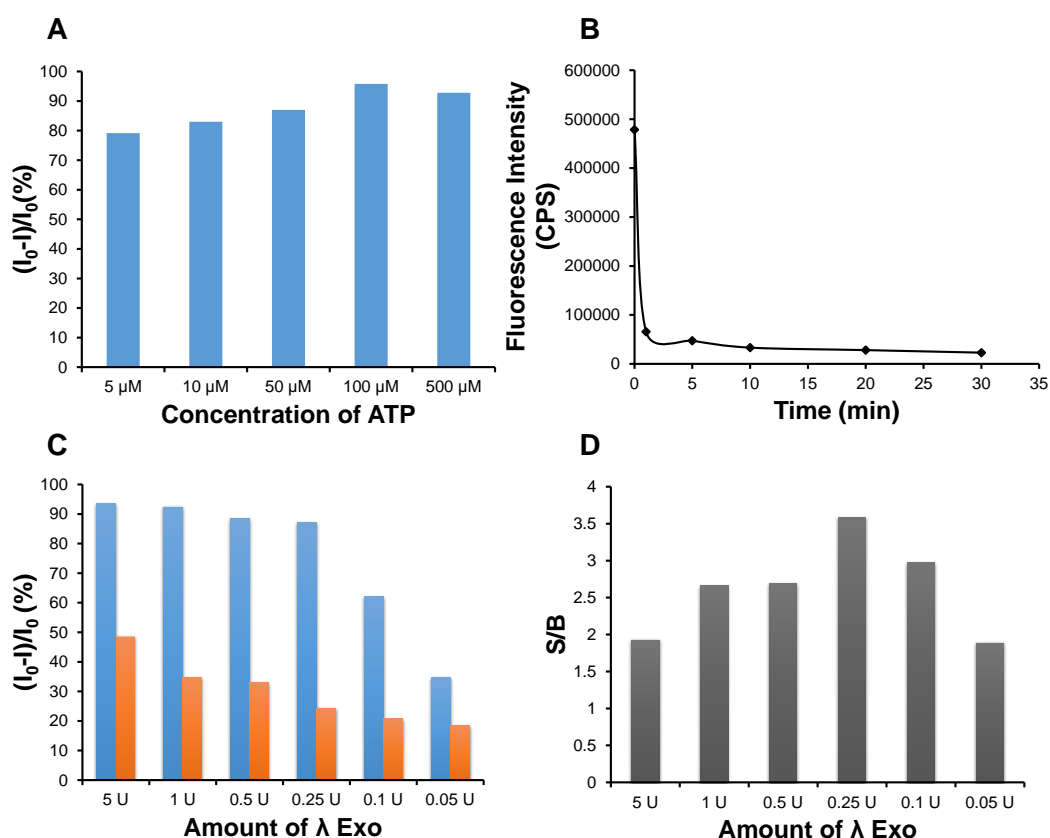


Figure 21. (A) Optimization of ATP concentration. The concentrations of λ exo, dsDNA, and T4 PNK were 1 unit, 20 nM, and 20 U/mL, respectively. (B) Optimization of the reaction time. The concentrations of λ exo, dsDNA, ATP and T4 PNK were 0.25 units, 20 nM, 0.1 mM and 20 U/mL, respectively. $\lambda_{\text{ex}} = 480$ nm. (C) Optimization of the amount of λ exo. (D) The relationship of signal-to-background ratio (S/B) with the amount of λ exo. The concentrations of dsDNA, ATP and T4 PNK were 20 nM, 0.1 mM and 20 U/mL, respectively.

With the increase of the ATP concentration, the fluorescence intensity change reached the highest point as 93% fluorescence intensity disappeared when 100 μM ATP was introduced. As a result, 100 μM was chosen as the optimum concentration of ATP in the phosphorylation and cleavage processes.

In this assay, λ exo was used as an enzyme to digest dsDNA after the phosphorylation by T4 PNK. The concentration of the λ exo should be a primary factor for affecting fluorescence intensity of the system. A higher concentration of λ exo would increase fluorescence background signal by digesting the dsDNA that without the phosphorylation by T4 PNK, which led to the lower signal-to-background ratio (S/B) ratio. In contrast, the lower amount of λ exo was not enough to digest the phospholated-dsDNA. Therefore, it is necessary to investigate the optimal concentration of λ exo. As shown in Figure 21C, with the increase of the λ exo concentration, the fluorescence intensity change of both solutions with T4 PNK or without T4 PNK increased. To get the optimum (S/B), the relationship of the S/B ratio with the amount of the λ exo was studied. It was shown that the highest S/B value was obtained in the presence of 0.25 units of λ exo (Figure 21 D). Therefore, 0.25 units of λ exo were used in the following experiments.

The reaction time of the T4 PNK catalysed phosphorylation and the coupled λ exo digestion was the other crucial factor. As shown in Figure 21B, the fluorescence intensity of SG decreased dramatically through the incubation time. The results showed that the fluorescence intensity decreased with the increase of the incubation time to 30 min. In the first 2 min, 87.5 % fluorescence was decreased, followed by the gradual decrease until 30 min. This is due to the rapid catalytic activity of λ exo when T4 PNK was added to phosphorylate the dsDNA. The stable fluorescence intensity after 30 min

suggested the complete phosphorylation and digestion. As a result, 30 min was chosen for the incubation time in the following experiments.

3.4. Monitoring of the Phosphorylation Process of T4 PNK

Under the optimized conditions, a series of concentrations of T4 PNK from 0 to 20 U/mL was applied to quantify the kinase activity of the T4 PNK. As shown in Figure 22A, the fluorescence signals gradually decreased as the concentration of T4 PNK increased. The relative fluorescence intensity reached the saturation when the T4 PNK concentration reached 10 U/mL. The calibration curve between the fluorescence intensity change and T4 PNK concentration was shown in Figure. 5B. There was a good linear range between 0.25 to 1.00 U/mL (Figure 22B inset). The linear relationship can be demonstrated as $Y = 2.5011X + 7.5561$ with a correlation coefficient of 0.9896. Y and X represented the fluorescence intensity change and concentration of T4 PNK in units of U/mL, respectively. The limit of detection (LOD) was 0.11 U/mL according to the definition of $3s/slope$. This result demonstrated the method as a potentially simple, quantitative and label-free strategy for polynucleotide kinase activity assay.

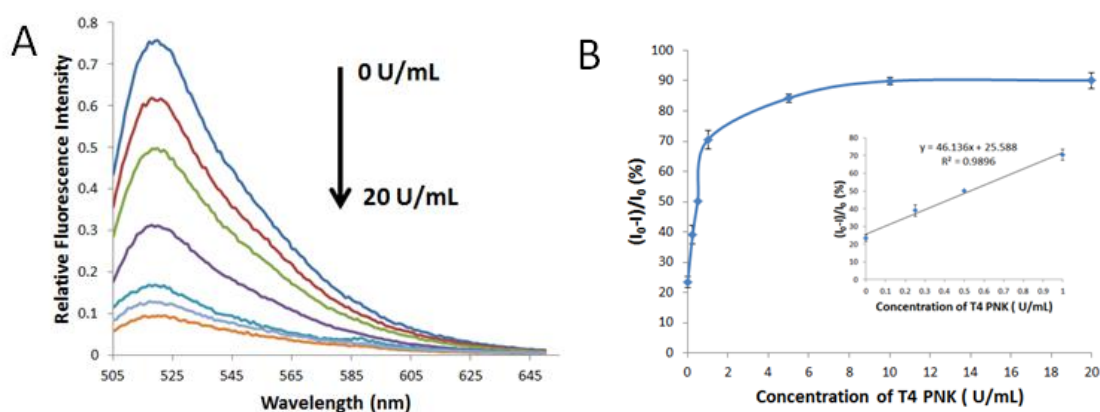


Figure 22. Monitoring the T4 PNK activity. (A) Relative fluorescence intensity with different concentrations of T4 PNK (top to bottom, 0, 0.25, 0.50, 1.00, 5.00, 10.00, 20.00 U/mL). (B) Concentration curve for T4 PNK. Inset indicated the linear relationship between fluorescence intensity change and the concentration of T4 PNK from 0 to 1.00 U/mL. Fluorescence intensity was measured in 100 μ L of 1x NEBuffer 4 (pH = 7.9) at 37 $^{\circ}$ C after 30 min incubation. The concentrations of λ exo, dsDNA, and ATP were 0.25 units, 20 nM, and 0.1 mM, respectively. $\lambda_{ex} = 480$ nm.

3.5. Inhibition Investigation

Since phosphorylation plays important roles in several bio-processes, the inhibition to the T4 PNK activity was also important to evaluate. Therefore, the inhibition effects of the ammonium sulphate and sodium hydrogen phosphate on phosphorylation were also investigated through this label-free fluorescence assay. It was reported that these inhibitors had no effect on the activity of the λ exo⁷⁶; thus, they can be used for the evaluation of the inhibition on the T4 PNK activity. As shown in Figure 23, the phosphorylation activity of T4 PNK was inhibited by both ammonium sulphate and sodium hydrogen phosphate depending on the concentration of the inhibitors. With the increase of the concentration of the inhibitors, the relative fluorescence intensity of the system increased which indicated that the phosphorylation process was inhibited by the high concentration inhibitors. The results showed that this assay could investigate the various effects on phosphorylation quantitatively.

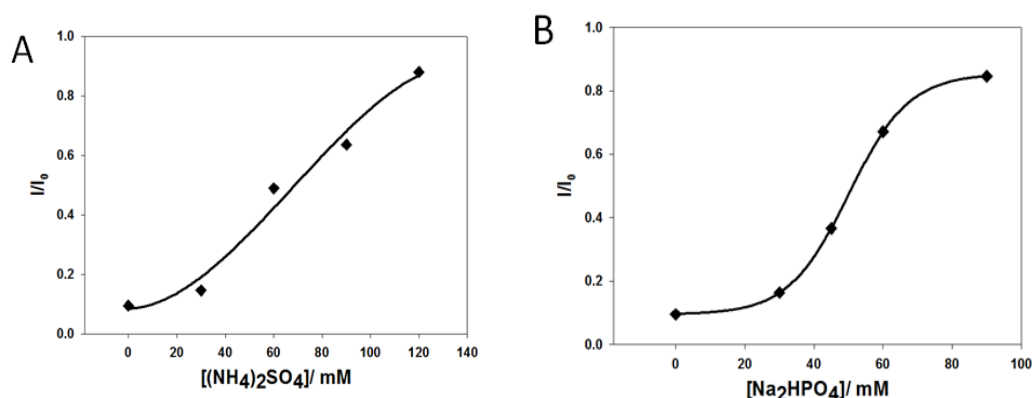


Figure 23. The effect of different concentrations of T4 PNK inhibitor. (A) Effect of $(\text{NH}_4)_2\text{SO}_4$ (0-120 mM); (B) Effect of Na_2HPO_4 (0-90 mM). Fluorescence intensity was measured in 100 μL of 1x NEBuffer 4 (pH = 7.9) at 37 $^\circ\text{C}$ after 30 min incubation. The concentrations of λ exo, dsDNA, ATP and T4 PNK were 0.25 units, 20 nM, 0.1 mM, and 10 U/mL respectively. $\lambda_{\text{ex}} = 480$ nm.

4. Conclusions

In conclusion, we have developed a facial, quantitative, cost-effective and label-free fluorescence assay for the detection of T4 PNK activity and inhibition coupled with λ exo and SG. In this sensing platform, the 5'-hydroxyl group of the dsDNA was

phosphorylated by T4 PNK in the presence of ATP, the resulting 5'-phosphoryl termini dsDNA was digested by the λ exo in the following step. As a result, the SG integrated in the dsDNA was released from the dsDNA which lead to the fluorescence intensity decrease of the system. This assay offered a new opportunity in the development of phosphorylation monitoring and related drug screening and clinical diagnostics.

CHAPTER IV

FABRICATION OF HIGHLY FLUORESCENT GRAPHENE QUANTUM DOTS USING L-GLUTAMIC ACID FOR *IN VITRO/IN VIVO* IMAGING AND SENSING

1. Introduction

Recently, graphene and its derivative graphene oxide have attracted remarkable attention due to their extraordinary optical and electronic properties and biocompatibility.⁸⁶⁻⁸⁹ However, applications of graphene in the fields of bioimaging and optoelectronics are limited because graphene is a zero-bandgap semiconductor.⁹⁰ To generate a bandgap in graphenes, a zero-dimensional derivative, graphene quantum dots (GQDs) have been developed.^{14, 91-95} GQDs have strong quantum confinement and edge effect when their sizes are in the range of 3-10 nm.^{96,97} Compared to zero-bandgap graphene sheets, GQDs exhibit stronger photoluminescence for bioimaging,⁹⁸ light-emitting diodes,⁹⁹ and biosensors.⁹² The photoluminescence is not only attributed to the quantum confinement effect, but also to the edge effect of the small graphene quantum dots. Most importantly, compared to the traditional quantum dots (QDs),^{17, 100-104} GQDs are chemically inert. Thus, the potential toxicity of the intrinsic heavy metal in traditional QDs would not be a concern for GQDs. Even though the mechanism of photoluminescence needs further investigation, a wide variety of applications of GQDs have been developed, such as photovoltaic devices,¹⁰⁵ biosensing,¹⁰⁶ drug delivery,¹⁰⁷ cellular imaging,⁹⁷ and the interaction with biological systems.¹⁰⁸

A number of methods have been developed for the synthesis of GQDs. Generally, the approaches can be divided into two groups: top-down and bottom-up methods. The top-down methods are based on cutting large carbon materials, such as carbon nanotubes, graphene sheets and carbon fibers, to form small GQDs. For example, Pan et al. synthesized blue GQDs by a hydrothermal method using a pre-oxidized graphene sheet.¹⁰ Zhou et al. broke C-C bonds of a graphene oxide using the photo-Fenton reaction to produce GQDs.¹⁰⁸ With controlling of the photo-Fenton reaction conditions, the nanoporous graphene sheets and GQDs were generated. Using microwave as an energy source, Li et al. synthesized greenish-yellow luminescent GQDs by cutting a graphene oxide under acid conditions.¹⁰⁹ Furthermore, several other methods were developed such as acid treatment coupled with the chemical exfoliation of carbon fibers,⁹³ the electrochemical etching of a graphene electrode,¹¹⁰ and the ultrasonication breaking of graphene.^{110, 111} Although luminescent GQDs could be obtained from carbon sources by these top-down methods, the reaction conditions and purification processes were complicated and time-consuming.

In contrast to the top-down approaches, bottom-up methods fabricate GQDs from small carbon precursors including glucose,⁹⁹ hexa-peri-hexabenzocoronene,¹¹² citric acid,⁹² etc.¹¹³ The bottom-up methods produced GQDs with controllable morphology and well-distributed sizes. However, harsh reaction conditions, such as using a strong acid or alkali, a long treatment period of time, and necessary separation processes, are limitations of the bottom-up methods. To overcome these limitations in this work, we have developed a simple and rapid bottom-up synthetic method by carbonizing a common amino acid, L-glutamic acid (Glu), using a heating mantle for pyrolysis. This is the first

report to use the L-glutamic acid for the synthesis of highly fluorescent nitrogen-doped GQDs with a simple heating process. The obtained GQDs emitted various wavelengths of fluorescence including the near-infrared fluorescence (NIR). In the NIR region, biological samples have low background fluorescence signals, providing high signal to noise ratio. Meanwhile, NIR radiation can penetrate into sample matrices deeply due to low light scattering. Thus, the GQDs are promising labeling reagents for sensitive determination and imaging of biological targets. The fluorescence quantum yield of the developed GQDs was about 5 times higher than the GQDs from citric acids.⁹² We have demonstrated the feasibility of using the GQDs in the *in vitro* and *in vivo* fluorescence imaging. Besides the bioimaging applications, the GQDs showed a peroxidase-like catalytic activity that was used for the sensitive detection of H₂O₂.

2. Experimental Section

2.1. Materials.

L-glutamic acid, Ludox SM-30 colloidal silica (30 wt. % suspension in water), hydrogen peroxide, 2,2'-azino-bis(3-ethylbenzothiazoline-6-sulphonic acid) (ABTS), fluorescein isothiocyanate (FITC) isomer I, rhodamine-101 and phosphate buffered saline (PBS) tablet were purchased from Sigma-Aldrich. The deionized water (18.3 M Ω ·cm) was produced from the Millipore water purification system.

2.2. Synthesis of GQDs.

The GQDs was synthesized by pyrolyzing L-glutamic acid. Briefly, 2.0 g L-glutamic acid was added to a glass bottle and heated to 210 °C with a heating mantle. After the solid L-glutamic acid changed to liquid, the boiling colorless liquid turned to brown in 45 s, which indicated the formation of GQDs. Then, 10.0 mL water was added to the solution followed stirring for 30 min. When the solution temperature reached

room temperature, the solution was centrifuged at 10,000 g for 30 min and the supernatant was collected. The resultant GQD solution could be stored at the room temperature for at least 5 months without precipitation.

2.3. Characteristics of GQDs.

A JEOL JEM-2100 high-resolution transmission electron microscope (HRTEM) was used to characterize the GQDs at an operating voltage of 200 kV. The size distribution of the GQDs was measured and graphed using Image J. Fourier transform infrared (FTIR) spectra were obtained on a FT-IR spectrometer (Peking). The Energy-dispersive X-ray spectroscopy (EDS) (Oxford), which was attached on the Hitachi SU8010 field emission scanning electron microscope (SEM) with an operating voltage of 5 kV, was used to analyze the relative contents of carbon, nitrogen and oxygen in L-glutamic acid and GQDs. X-ray diffraction (XRD) profiles were obtained with Bruker AXS D8 advanced powder x-ray diffraction system using Cu K α radiation. Raman spectra were performed on an Aramis labRAM Raman spectrometer (Horiba JobinYvon) using the helium-neon laser at 542 nm. A Shimadzu UV-250 UV/vis spectrometer was used for the measurements of the UV/vis absorption of GQDs. The fluorescence spectra, lifetime, and quantum yields were measured using a Jobin-Yvon-Horiba Fluorometer 3 Model (FL 3-11 spectrofluorometer). The zeta potential was detected using the Zetasizer (Marlwen, model of Nano-ZS) by adjusting the pH of the GQDs from 2.0 to 12.0 using PBS buffer.

2.4. Detection of Quantum Yields.

Fluorescein in 0.1 M NaOH (QY = 92 %) was chosen as a reference.^{114, 115} The quantum yield was calculated according to the following equation:

$$\Phi_X = \Phi_{ST} \left(\frac{A_{ST}}{A_X} \right) \left(\frac{I_X}{I_{ST}} \right) \left(\frac{\eta_X^2}{\eta_{ST}^2} \right)$$

Where the subscripts ST and X denote standard and sample, respectively. Φ is the quantum yield. I represents the measured integrated fluorescence intensity. A is the absorbance at the excitation wavelength, and η is the refractive index of the solvent. The refractive index for the standard and sample are 1.33. The GQDs were excited at 360 nm with an emission range of 380-650 nm.

2.5. Detection of Fluorescence Lifetime.

The fluorescence lifetime of GQDs was measured using time-correlated single photon counting (TCSPC) with the LED (370 nm) equipped on the Jobin-Yvon-Horiba Fluorometer 3. A Ludox SM-30 colloidal silica was used as the reference. The emission wavelength of GQDs changed from 455 to 505 and 650 nm. An emission wavelength of 815 nm was used for the NIR fluorescence lifetime measurement.

2.6. *In Vitro* Fluorescence Imaging of Cells.

The fluorescence imaging of cells treated with GQDs was conducted at various wavelengths (Zeiss LSM-510 Meta Confocal Microscope). Briefly, murine alveolar macrophage cells (MH-S) were cultured overnight at 37 °C on plates in RPMI 1640 medium containing 10 % fetal bovine serum in a 5 % CO₂ environment. Then, the cultured cells were washed twice with PBS buffer (pH 7.4). Afterwards, a 2 mL aliquot of 10 mg/mL GQDs in PBS was added to the cell culture medium followed by 1 hour culture at 37 °C in a 5% CO₂ environment. Finally, the MH-S cells were washed twice using the PBS buffer and imaged using the Zeiss LSM-510 Meta confocal microscope.

2.7. *In Vivo* Fluorescence Imaging of Mice.

The *in vivo* fluorescence imaging of mice treated with GQDs was carried out using the IVIS imaging system (IVIS Lumina XR, Caliper). The athymic BALB/c-nu mice with weight of 20-25 g were obtained from Charles River (Wilmington, MA), and

maintained in the University of North Dakota animal center. All animal operations were in accord with the institutional animal use and care regulations, according to protocol No. 1204-4 and 1204-5. The feasibility of the GQDs for *in vivo* fluorescence imaging was investigated by subcutaneous and intramuscular injection. The mice were anesthetized and injected with 100 μL of 25 mg/mL GQD PBS solution (pH 7.4) subcutaneously on the back, and 100 μL of 25 mg/mL GQD intramuscularly in the right back leg. The fluorescence images of the mice were taken immediately with different excitation and emission filter combinations.

2.8. Detection of H_2O_2 Based on the GQD's Catalytic Activities.

5.4 mg/mL GQDs was dissolved in 110 μL of 10 mM Tris-HCl buffer (pH = 5.0), followed by the addition of 7.2 mM ABTS. The control samples were prepared using the same condition except for no GQDs or H_2O_2 , respectively. The absorption spectra of these three samples were recorded after 2 min of the reaction. Then, the reaction conditions, such as pH, temperature, concentrations of ABTS, and concentrations of GQDs, were optimized. Different concentrations of H_2O_2 were added into the solution for the investigation of sensitivity. The absorbance at 416 nm against the reaction time of 120 s was measured.

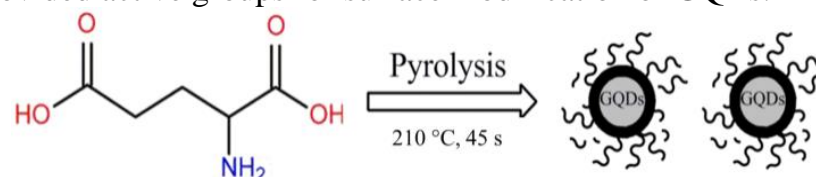
3. Results and discussion

3.1. Design of the Highly Fluorescent GQDs.

The objective of this work was to develop a simple bottom-up method for the synthesis of highly fluorescent GQDs. The key factor of our design was the usage of a green and natural L-glutamic acid as the precursor. Traditionally the "bottom up" methods for the preparation of GQDs used some special organic precursors, such as 3-iodo-4-bromoaniline,¹¹³ resulting in a complicated synthetic process. However, in the synthesis of carbon nanodots, some common

organic molecules, including citric acid,¹¹⁶ histidine¹¹⁷ and glucose,¹¹⁸ were used as the precursors with the assistance of microwave. These studies revealed a possibility of using common organic molecules to generate GQDs. Most recently, using a citric acid as the precursor, Chen et al. successfully developed fluorescent GQDs and graphene oxide.⁹² Inspired by this pioneer work, we considered using a natural amino acid as a precursor to synthesize N-doped GQDs based on the pyrolysis of the precursor. Our criteria for the selection of the precursor were non-toxic, common/natural materials, containing nitrogen groups for easy surface modification of the GQDs during their applications, and no further capping process is needed. Considering of these criteria, we selected L-glutamic acid. Our result demonstrated that the L-glutamic acid was an excellent precursor for making the GQDs. The formation of a GQD from the L-glutamic acid was illustrated in Scheme 2. The solid L-glutamic acid was first directly heated to 210 °C using a heating mantle. This temperature is the boiling point of the L-glutamic acid. At this condition, the L-glutamic acid melted and boiled very soon. The colorless liquid changed to pale yellow and brown within 45 s, indicating the carbonization of L-glutamic acid during the pyrolysis. At this moment, distilled water was added into the brown liquid to dissolve and disperse the GQDs under vigorous stirring to avoid aggregation. Unlike other methods, surface passivation agents or other inorganic additives were not needed for the generation of high quantum yield GQDs. The residue L-glutamic acid could act as a surface passivation agent, resulting in the extremely stable and highly fluorescent GQDs in solution. The GQDs were formed in one step of the

pyrolysis of the precursor. Moreover, the amino group on the L-glutamic acid surface provided active groups for surface modification of GQDs.



Scheme 2. Schematic diagram of the formation of GQDs through pyrolysis of L-glutamic acid.

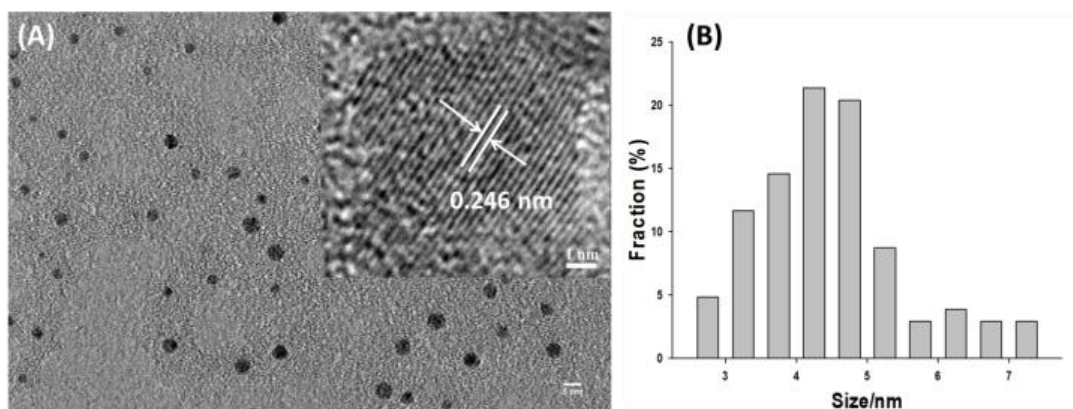


Figure 24. (A) The HRTEM image of GQDs with a scale bar of 5 nm. Inset: A typical single GQD with the lattice parameter of 0.246 nm. The scale bar was 1 nm; (B) The size distribution of GQDs calculated from more than 100 dots.

3.2. Characterization of the Morphology and Composites of the GQDs.

The morphology of the obtained GQDs was first characterized using a high resolution TEM (Figure 24A). The high crystallinity of the GQDs was shown as in the inset of Figure 24A. The GQDs' lattice space was accurately measured to be 0.246 nm at the HRTEM image, which is comparable to that of graphitic.¹¹⁹ The average diameter of the GQDs was 4.66 ± 1.24 nm according to the statistic calculation of more than 100 dots (Figure 24B). The size distribution showed uniform dimension of the developed GQDs.

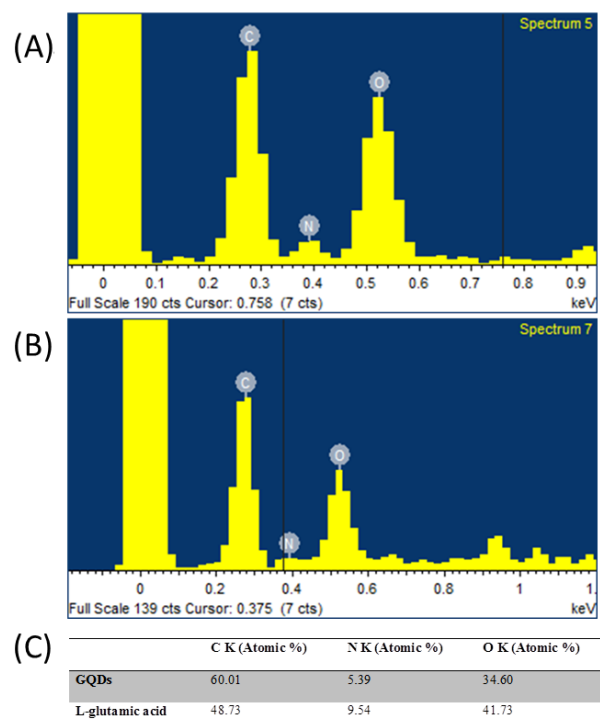


Figure 25. EDS spectra of L-glutamic acid (A) and GQDs (B), and the relative atomic percentage of L-glutamic acid and GQDs(C).

The element content of the GQDs was analyzed using EDS. As a control, the relative atomic percentage of L-glutamic acid were 48.73% (C), 9.54% (N), and 41.73% (O) (Figure 25A and C), which was similar to the theoretically relative atomic percentage of L-glutamic acid (50 % of C, 10 % of N and 40 % of O). After the pyrolysis of the L-glutamic acid, the GQDs were formed. Their carbon content increased from 48.73 % to 60.01 %. Meanwhile, the oxygen content decreased from 41.73 % to 34.60 %, and the nitrogen content decreased from 9.54 % to 5.39 % (Figure 25B and C). This result indicated that the L-glutamic acid was carbonized after pyrolysis.

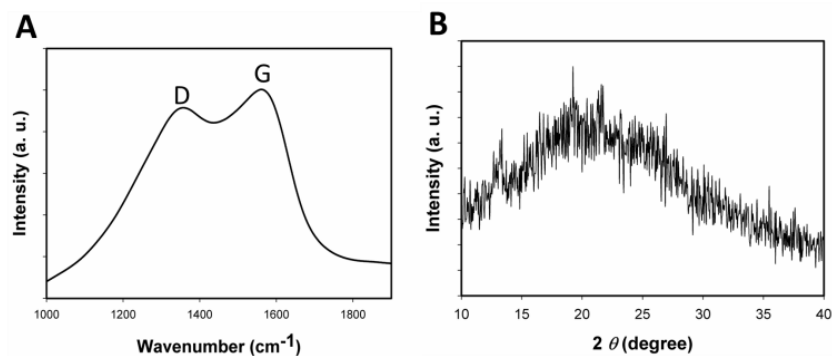


Figure 26. (A) Raman spectra of GQDs. (B) XRD patterns of GQDs.

To confirm the formation of GQDs XRD pattern and Raman spectroscopy were used to characterize the product. As shown in Figure 26A, the Raman spectrum of GQDs has two typical peaks at ca. 1355 cm⁻¹ and 1580 cm⁻¹. The G band (1580 cm⁻¹) was related to the vibration of the *sp*²-bonded C atoms in the graphene materials; and the D band (1355 cm⁻¹) corresponded to the destruction of the *sp*² network by the *sp*³-bonded C atoms. Figure 26B showed a typical XRD profile of GQDs. It had a broad (002) peak centered at ca. 20.0 °, which is similar to the GQDs synthesized by other methods.⁹⁹

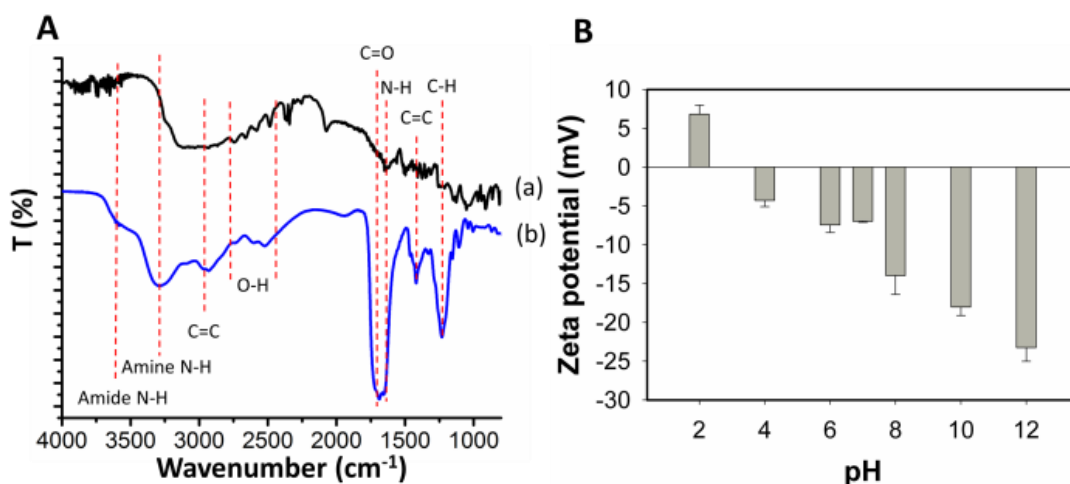


Figure 27. (A) FT-IR spectra of L-glutamic acid (a) and GQDs (b). (B) The zeta potential of GQDs in different pH solutions.

The structural change of the L-glutamic acid during the formation of the GQDs was further characterized using the FT-IR spectra (Figure 27A).

Compared curve a with b in Figure 27A, the C=C stretching of graphite was formed as indicated by the appearance of the 3000 cm^{-1} and 1500 cm^{-1} peaks, which demonstrated the formation of GQDs.¹²⁰ The broad peak area from $2500 - 2800\text{ cm}^{-1}$ was from the carboxylic acid O-H stretch. Meanwhile, the strong peak from 1600 to 1730 cm^{-1} resulted from the combination of carboxylic acid C=O stretch and amide C=O stretch in the GQDs. The carboxylic acid O-H stretching and C=O stretching peaks demonstrated the presence of the carboxyl groups. The amide C=O stretching and new formed amide N-H stretching peak ($3700 - 3500\text{ cm}^{-1}$) indicated the formation of the amides between the amine group and the carboxyl group. The stretching vibrations of amine N-H (*ca.* 3360 cm^{-1}) in both curves indicated the presence of amine groups in the L-glutamic acid and GQDs. The oxygen-containing and nitrogen-containing groups promised the high water solubility and stability in solution.

The zeta potential of the GQDs in different pH values was also investigated. As shown in Figure 27B, the zeta potential changed from positive 6.81 mV to negative 23.2 mV by increasing the pH value from 2 to 12. This large change of the zeta potential with the pH was related to the presence of the amino and carboxyl groups in the GQDs. Because of the reaction activity of the amino and carboxyl groups, the biomolecules, such as antibodies and aptamers, could be easily conjugated onto GQDs for further applications.

3.3. Fluorescence Properties of the GQDs.

The significant feature of the developed GQDs relies on their fluorescence properties. We have investigated the fluorescence properties using

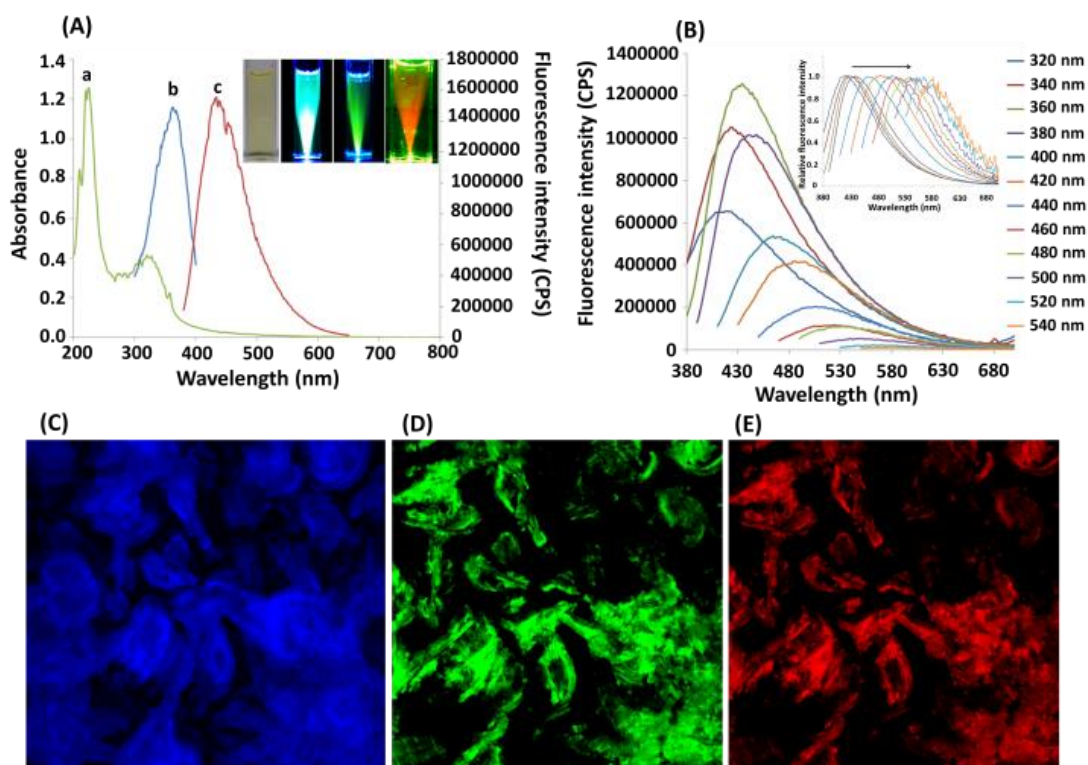


Figure 28. (A) The absorption (curve a), excitation (curve b) and emission spectra (curve c) of GQDs. Inset: from left to right are the GQDs solutions under bright light, violet, blue and green irradiation, respectively; (B) Fluorescence emission spectra of GQDs with different excitation wavelengths; (C) - (E) The confocal fluorescence images of the GQDs under different excitation wavelengths. (C) 359 nm excitation; DAPI channel; (D) 488 nm excitation, LP 505 nm; (E) 514 nm excitation, BP 530-600 nm.

both the spectroscopy and the microscopy. The obtained UV-vis absorption spectra and photoluminescence spectra were shown in Figure 28A. The GQDs showed two obvious absorption peaks at 238 nm and 335 nm, respectively (Figure 28A, curve a). The peak around 238 nm was attributed to π - π^* transitions of C=C bonds. The apparent peak at 335 nm indicated the major uniform size of the sp^2 clusters in the GQDs even though these sp^2 clusters were doped in the sp^3 matrix. The color of GQDs in the aqueous solution was yellow (Inset of Figure 28A). When the GQDs were excited at 360 nm (Figure 28A curve b), the GQDs showed a strong fluorescence peak at 440 nm (Figure 28A curve c). More importantly, the fluorescence is strong enough to be observed by naked eyes

(Inset of Figure 28A), which has promising applications for fluorescence imaging. In addition, the fluorescence emission spectra showed an excitation-dependent manner. The emission peak of GQDs shifted from 415 nm (violet) to 580 nm (red) when the excitation wavelength was changed from 320 nm to 540 nm (Figure 28B).

We then investigated the fluorescence property of GQDs using a fluorescence microscope. With the irradiation of the violet (330-385 nm), blue (460-500 nm) and green (535-585 nm) light, the GQDs emitted strong blue, green and red fluorescence, respectively (Figure 28C, D, E). It should be noted that the precursor of the GQDs showed no absorption in the violet region and no fluorescence in the range of violet to visible. Thus, all these fluorescence properties should come from the formation of GQDs.

To further explore the fluorescence features of the developed GQDs, we measured their fluorescence quantum yield and lifetime. Using fluorescein as a reference dye the quantum yield of GQDs was measured to be 54.5 % under the excitation of 360 nm. This relative high quantum yield might be benefited from the protection of the residue L-glutamic acid as the surface passivation agent. The fluorescence lifetime of the GQDs was analyzed using the TCSPC method at different emission wavelengths with 370 nm excitation. All three fluorescence emissions exhibited well fitted triple-exponential function as shown in Figure 29. The observed lifetimes of GQDs at 445 nm, 505 nm, 650 nm and 815 nm were summarized in Table 3. Their average lifetime was in the range of 1.48 to 2.40 ns. The nanosecond lifetime of GQDs demonstrated their potential for optoelectronic and biological applications.

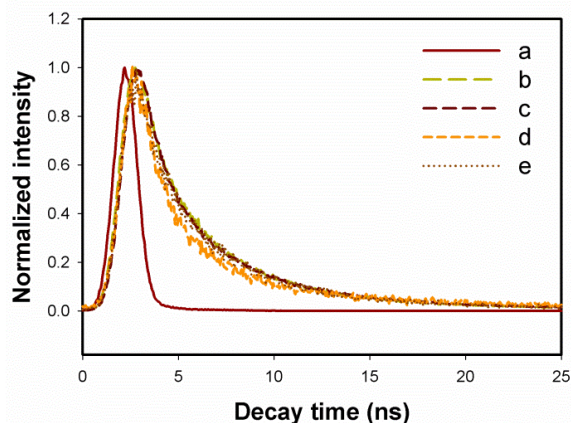


Figure 29. Lifetime measurement curves for reference (a) and GQDs at different emission wavelengths with 370 nm LED irradiation. Emission wavelengths: (b) 445 nm; (c) 505 nm; (d) 650 nm, and (e) 815 nm.

Table 3. Caption Fluorescence lifetime of GQDs at different emission wavelengths with 370 nm excitation.

Ex (nm)	Em (nm)	τ_1 (ns)	τ_2 (ns)	τ_3 (ns)	$Av. \tau$ (ns)	Chi
370	445	0.81	3.64	11.55	2.40	1.14
370	505	3.78	0.80	12.04	2.22	1.27
370	650	2.35	6.77	0.47	1.48	1.13
370	815	3.23	0.47	8.70	1.91	0.97

Compared to the traditional organic dyes, such as FITC, the GQDs not only could emit fluorescence at different wavelengths, but also showed much higher photostability. As shown in Figure 30, the fluorescence of FITC was bleached by 70 % under a confocal laser within 2 min (Figure 30A, C). However, the fluorescence of GQDs still showed strong intensity (47 % was bleached) even after 18 min of the same irradiation (Figure 30B, C). This

increased photostability provided the GQDs with a great potential for *in vitro* and *in vivo* fluorescence imaging.

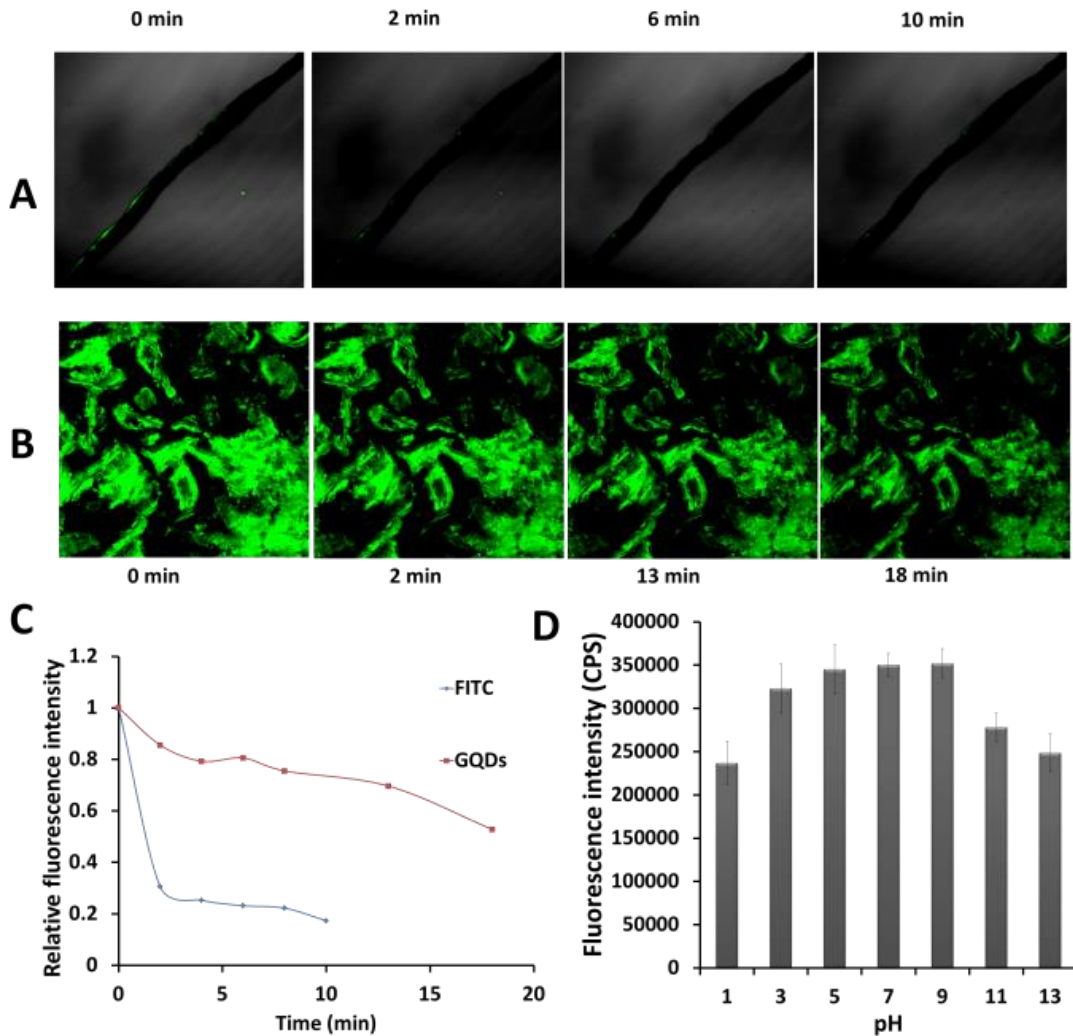


Figure 30. Comparison of the photostability of the GQDs with a fluorescent dye molecule FITC under the irradiation of a confocal laser. A, the confocal fluorescence images of FITC; B, the confocal fluorescence images of GQDs; C, the photostability of these two fluorescent materials; D, the effect of pH on the fluorescence intensity of the GQDs.

We also investigated the stability of the GQDs at different pH values (Figure 30D). The results showed that at pH 7.0 the GQDs had the highest fluorescence intensity. In the range of pH 5.0-9.0, the changes of the fluorescence intensity were less than 1.4 %. This range covered the majority of pH values of living systems. When the pH value was below 5.0 or higher than 9.0, the fluorescence intensity of the GQDs was reduced by 32.3 %. The significant

stability of the GQDs over the broad pH range might come from the surface amino groups and carboxyl groups, which could resist the pH effect on the fluorescence intensity of GQDs.

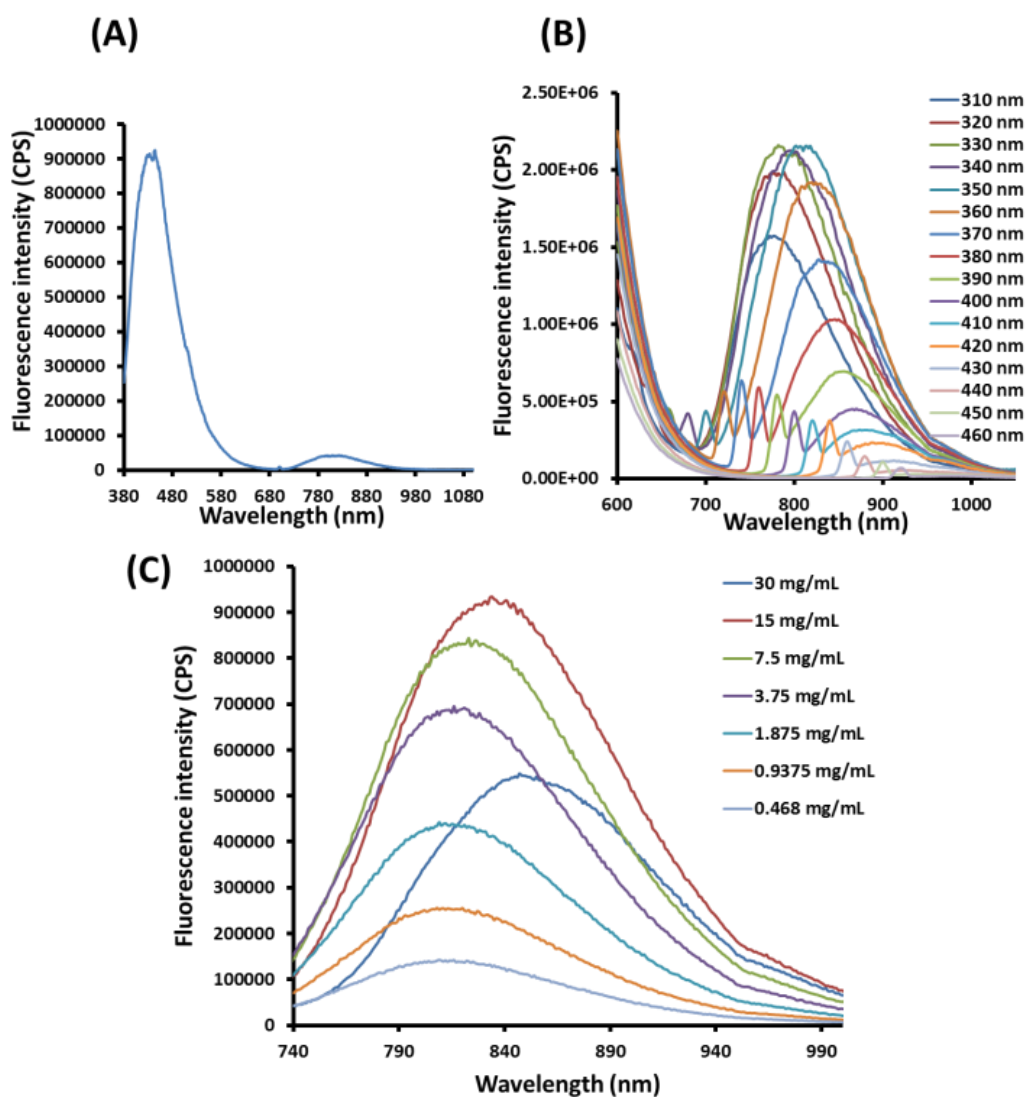


Figure 31. (A) Fluorescence emission spectrum of the GQDs in the visible-NIR region. (B) NIR fluorescence spectra of the GQDs under different excitation wavelengths. (C) The NIR fluorescence intensity vs. the concentration of GQDs.

Besides the fluorescence emission in blue, green and red regions, the GQDs emitted relatively lower NIR fluorescence around 815 nm with the irradiation of 360 nm. The intensity ratio of 815 nm to 440 nm was 0.2 according to the fluorescence spectra (Figure 31A). The NIR peak was significantly higher than the 2λ diffraction peak as shown in Figure 31B. Similar to the fluorescence

property in the visible region, the peak in the NIR region showed red shift if the excitation wavelength became longer (Figure 31B). Meanwhile, the fluorescence intensity of the GQDs in the NIR region was proportional to the concentration of the GQDs in the range of 0.468-15.000 mg/mL (Figure 31C). This relationship indicated that the NIR fluorescence must be attributed to the GQDs even though the mechanism was not clear yet. Notably, the Stokes shift of this NIR fluorescence was as large as 455 nm. The large Stokes shift provided the GQDs with significant advantages for fluorescence bioimaging and biosensing. The lifetime of the fluorescence at 815 nm with excitation of 370 nm was examined (Figure 29e). The result showed a similar value to that of the visible fluorescence. The short lifetime value eliminated the possibility of phosphorescence of the 815 nm peak.

3.4. *In Vitro* Fluorescence Imaging Using GQDs.

Based on these excellent fluorescence properties, the bioimaging applications of the fluorescent GQDs were further investigated *in vitro* and *in vivo*. The *in vitro* fluorescence imaging using the developed GQDs was explored under different excitation wavelengths. After the GQDs were incubated with MH-S cells for 1 h, the fluorescence images of the cells were taken using a confocal microscope. As shown in Figure 32B, the MH-S cells incubated with GQDs in PBS buffer showed strong green (LP475) and red (LP 530) colors upon excitation at 458 nm and 514 nm, respectively. However, no apparent fluorescence was observed from the control group that was not incubated with the GQDs under the same conditions (Figure 32A). Our results demonstrated that the GQDs can emit strong fluorescence in the range of green to red for *in vitro* fluorescence imaging. The strong fluorescence on the MH-S cells incubated with

GQDs suggested that GQDs had penetrated into the cells and were able to label both the cell membrane and the cytoplasm of MH-S cells. The uptake of GQDs by MH-S cells would be similar to the pathway of nanoparticles, which is endocytosis.¹²¹

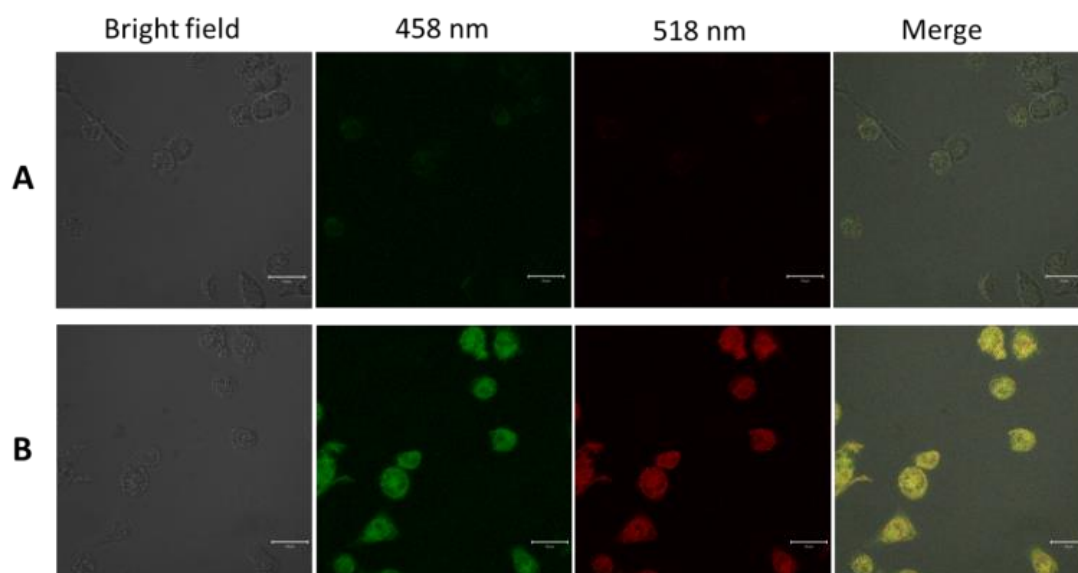


Figure 32. Laser scanning confocal fluorescence microscopy images of MH-S cells. (A) Control MH-S cells without GQDs; (B) the MH-S cells treated with GQDs for 1 hour. All the scale bars was 20 μm .

3.5. *In Vivo* Fluorescence Imaging Using GQDs.

The feasibility of the GQDs for *in vivo* bioimaging was investigated in mice. A 100 μL aliquot of 25 mg/mL GQDs were injected subcutaneously into the back of nude mice and intramuscularly into the right back leg. The fluorescence images of the mice under different excitation and emission filters were captured. As shown in Figure 33, various excitations from blue to red centered at 430, 465, 500, 535 and 605 nm were applied for the *in vivo* fluorescence imaging. The emission bandpass filters for each excitation wavelength were illustrated on the top of each image in Figure 33. With the excitation wavelength increased, all the fluorescence intensity decreased. Moreover, the detectable fluorescence region had extended with the longer

excitation and emission wavelengths from the intramuscularly injection spot of the right back leg. This result demonstrated that the longer wavelengths had better penetration ability than the short wavelengths for the *in vivo* fluorescence imaging. Considering the decreased fluorescence intensity in the longer wavelengths, the optimal excitation and emission bandpass to obtain the highest signal-to-background ratio should be investigated in the future for further imaging applications. Overall, the *in vivo* fluorescence imaging in mice under subcutaneous and intramuscular injection indicated that the GQDs could be used as a fluorescent labeling agent for bioimaging in both visible and NIR regions.

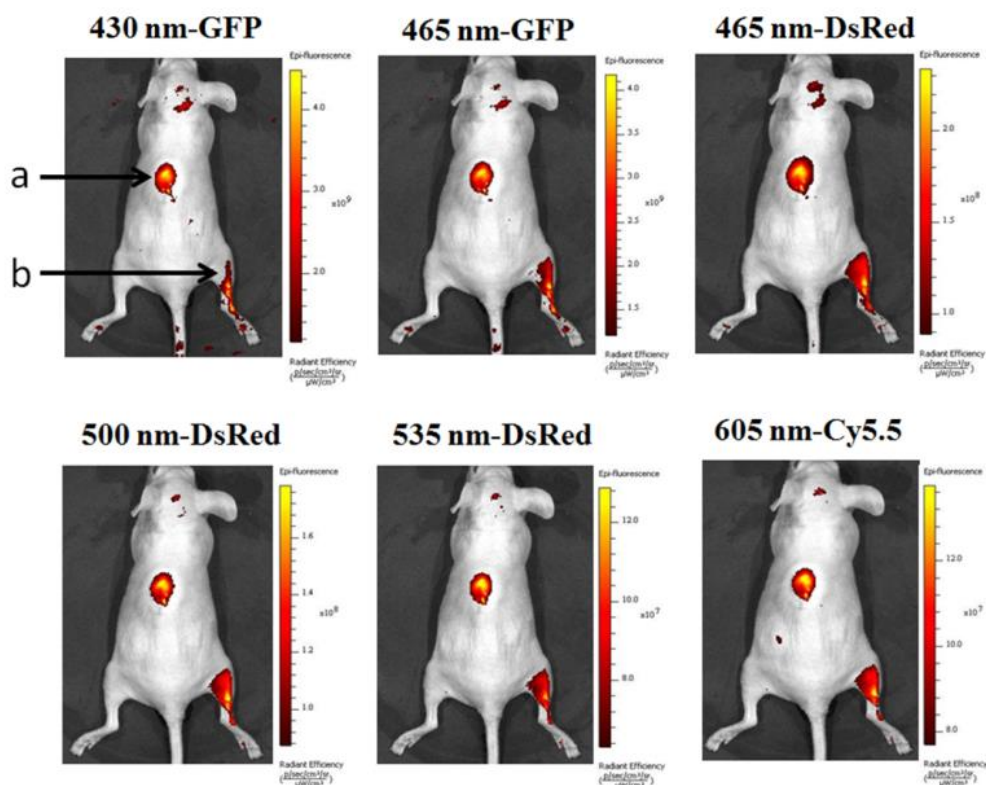


Figure 33. *In vivo* fluorescence imaging of mice injected GQDs subcutaneously (spot a) and intramuscularly (spot b). The images were taken under various excitation wavelengths and emission wavelengths indicated on the top of each image. A 100 μL aliquot of 25 mg/mL GQDs was injected into each spot. The following emission bandpass filters were used: GFP: 515-575 nm; DsRed: 575-650 nm; Cy5.5: 695-770 nm.

3.6. Colorimetric Detection of H_2O_2 Using GQDs.

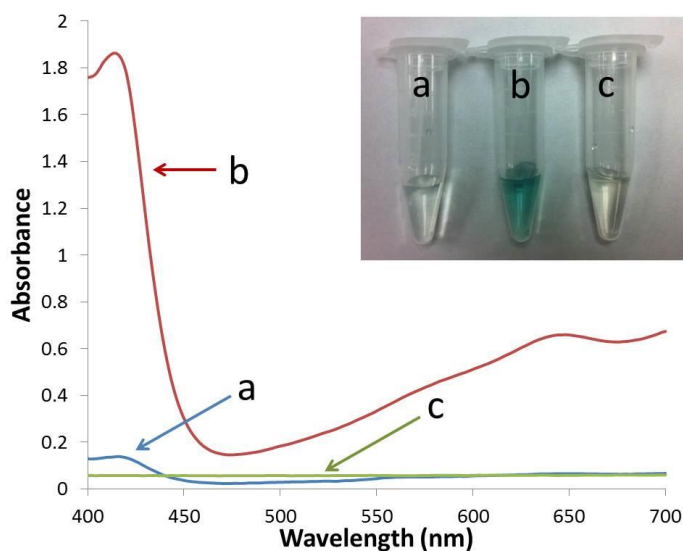


Figure 34. UV-vis absorption spectra of the ABTS solution containing a) 9 mM H_2O_2 ; b) 2.7 mg/mL GQDs with 9 mM H_2O_2 ; and c) 2.7 mg/mL GQDs. Inset: The corresponding photographs of these three samples.

To extend the application fields of the GQDs, in addition to the optical properties, we have investigated the catalytic ability of the GQDs. It was reported that the materials containing aromatic sp^2 carbon clusters had the intrinsic peroxidase-like catalytic activity to produce a blue color reaction in the presence of H_2O_2 and peroxidase substrate, 3,3,5,5-tetramethylbenzidine (TMB). For example, both carbon nanotubes and graphene sheets were used for the label-free detection of glucose and single-nucleotide polymorphism through their intrinsic peroxidase-like catalytic activity.^{122, 123} Inspired by this work, we explored whether our GQDs could be used for label-free colorimetric sensing as a catalyst. With the addition of H_2O_2 , the GQDs catalyzed the reduction of hydrogen peroxide indicated by the color change of the solution to green in the presence of the peroxidase substrate ABTS (Figure 34 inset). The absorbance change of ABTS at 416 nm could be used for monitoring the reaction rate and the peroxidase-like catalytic activity (Figure 34). Compared to the control groups including the solution without GQDs or H_2O_2 , the signal-to-background ratio was

higher than 9. Thus, the peroxidase-like catalytic activity of the GQDs would be used for the detection of H_2O_2 , an important reactive oxygen species in the biomedical context.

We then optimized the detection conditions for catalyzing H_2O_2 reaction using the GQDs. The conditions included pH, reaction temperature, and concentrations of ABTS and GQDs. The pH value was a critical factor for the detection of H_2O_2 . It was reported that the optimal pH for a carbon nanoparticle catalyzed H_2O_2 reaction was 4.0.¹²⁴ Our results showed that, in a low pH range (3.0-5.0), the reaction rate was very stable (Figure 35A). However, the reaction rate decreased above pH 5.0. Therefore, the pH 5.0 was chosen as the optimal pH. Meanwhile, the reaction temperature would affect the catalytic reaction rate. As shown in Figure 35B, high temperature would increase the reaction rate. Considering normal mammalian body temperature, 37 °C was selected as the standard condition for analyzing H_2O_2 . Apparently, the ABTS as a substrate could affect the sensitivity of the colorimetric detection of H_2O_2 . As shown in Figure 35C, the reaction rate increased as the concentration of ABTS increased until a concentration of 7.2 mM was reached. Therefore, 7.2 mM of ABTS was chosen as the optimal concentration. Moreover, the concentration of GQDs was proportional to the reaction rate (Figure 35D). However, a high concentration of GQDs would affect the absorption of the ABTS. Therefore, a concentration of 5.40 mg/mL GQDs was chosen as the optimal concentration for the detection.

Under the above optimal conditions, the detection of H_2O_2 was carried out using this GQDs-based label-free colorimetric system. As shown in Figure 36A, with the increase of the concentrations of H_2O_2 , the absorbance increased in a concentration-dependent manner. This assay provided rapid detection (2

min) of H_2O_2 with the linear range from 0.1 mM to 10 mM (Figure 36B). The limit of detection was 20 μM according to the calibration curve at a signal-to-background ratio of 3. Thus, our studies suggest that the GQDs may have potential for applications in the biosensing field.

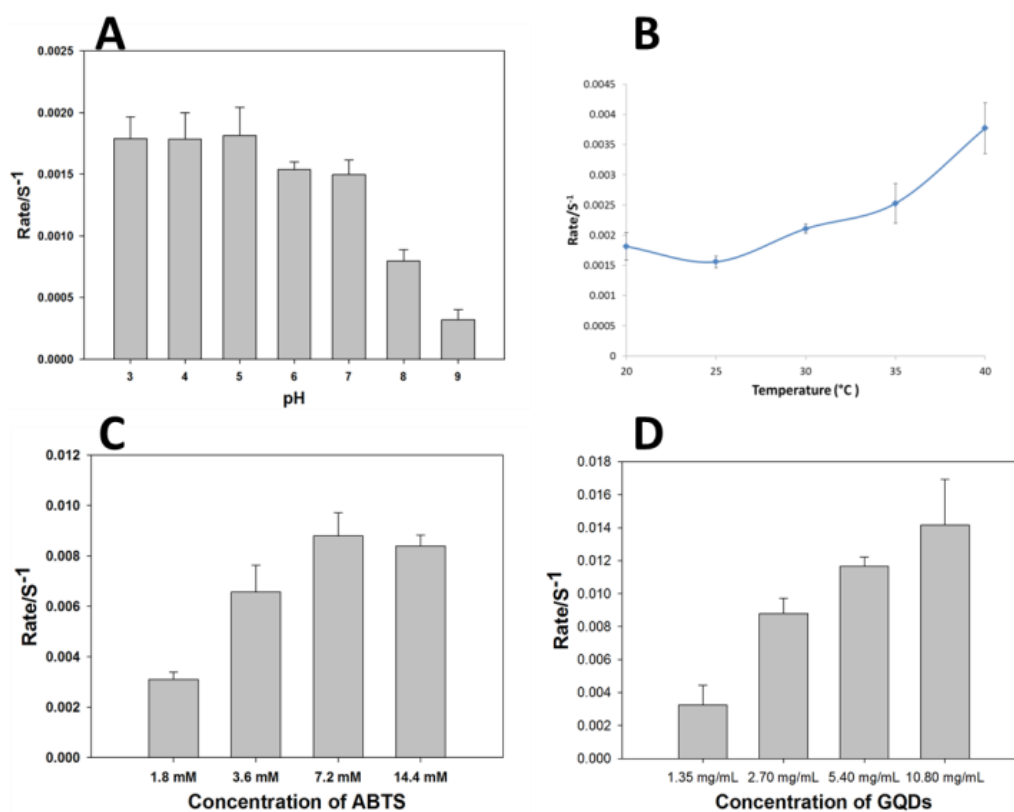


Figure 35. Optimization of the reaction conditions for the detection of H_2O_2 . (A) pH; (B) temperature; (C) concentration of ABTS; (D) concentration of GQDs.

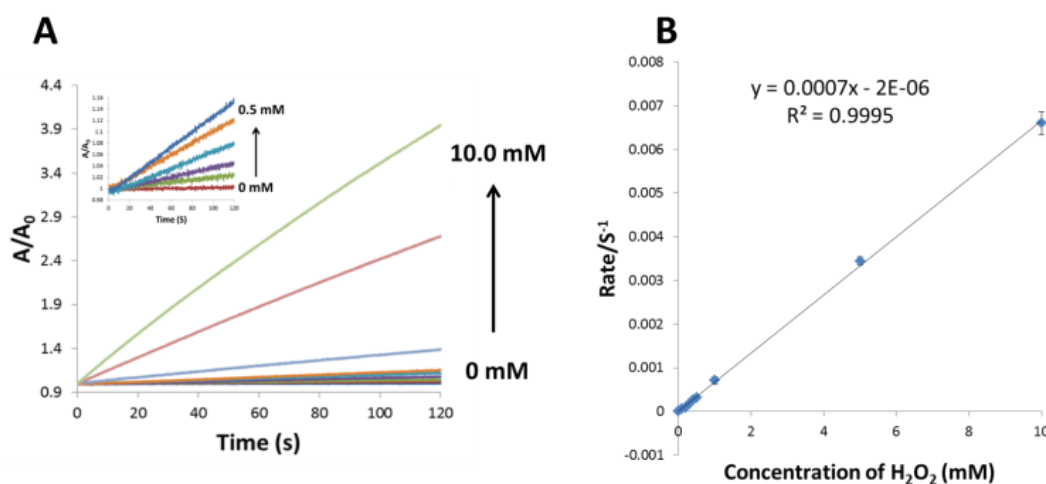


Figure 36. (A) The relationship of the absorption with the concentrations of H_2O_2 (from the bottom to the top: 0, 0.1, 0.2, 0.3, 0.4, 0.5, 1.0, 5.0 and 10.0 mM); (B) The calibration curve of the label-free colorimetric method for the detection of H_2O_2 .

4. Conclusions

In conclusion, GQDs with excellent fluorescence properties and peroxidase-like activity were developed using a direct and simple pyrolysis of an amino acid, L-glutamic acid. The GQDs not only showed a stable, strong excitation-dependent photoluminescence with high quantum yield (54.5 %) in the blue to red range but also provided an excitation-dependent NIR fluorescence emission around 815 nm. Even though the mechanism of this NIR fluorescence emission was not well understood, the application potential of the NIR fluorescence was significant. By using a strong visible irradiation, the GQDs showed the potential to be used for *in vitro* and *in vivo* fluorescence imaging. Furthermore, the GQDs possessed a peroxidase-like activity which could catalyze the reduction of H_2O_2 in the presence of the ABTS substrate. Using the labelling-free colorimetric method, the GQDs may have broad applications in detecting H_2O_2 , an important reactive oxygen species in biomedical context.

CHAPTER V

ONE-POT SYNTHESIS OF REDUCED GRAPHENE OXIDE/METAL (OXIDE) NANOCOMPOSITES AND ITS APPLICATION FOR ELECTROCHEMICAL ANALYSIS

1. Introduction

Graphene, a two-dimensional carbon nanomaterial containing a monolayer of sp^2 hybridized carbon atoms, has attracted increasing attention due to its useful electronic, thermal, and optical properties.¹²⁵⁻¹³¹ Graphene is usually synthesized by the modified Hummer's method, which forms graphene oxide (GO) from graphite with ultrasonication, afterwards oxygen-containing groups on the GO are treated to form reduced graphene oxide (RGO). The electrical and thermal conductivity of RGO exceeds those of GO even though they are still lower than pristine graphene.¹³²⁻¹³⁴ However, the residual oxygen-containing groups in RGO (carboxyl, epoxy, carbonyl, and hydroxyl) provide active sites for further chemical modification and decoration with other nanomaterials, thereby allowing electronic and optoelectronic properties to be tailored.^{135, 136} When modified with inorganic nanomaterials (*e.g.*, Au, Cu, Ag, TiO₂, Fe₃O₄, QDs, SiO₂, and *etc.*), graphene has found numerous applications in fields such as solar energy storage,¹³⁷ Li-ion battery fabrication,¹³⁸⁻¹⁴⁰ biosensors,¹⁴¹⁻¹⁴⁴ and drug delivery.¹⁴⁵⁻¹⁴⁸ For instance, Xu *et al.* adsorbed metal nanoparticles (Au, Pt and

Pd nanoparticles) on the surface of GO followed by reduction of GO to RGO using ethylene glycol.¹⁴⁹ The resulting graphene-Pt composites showed promise in direct methanol fuel cells. Lightcap *et al.* anchored semiconductor and metal nanoparticles on RGO at separate sites.¹⁵⁰ With UV irradiation, the photogenerated electrons from TiO₂ were captured and transferred through RGO to reduce silver ions to silver nanoparticles apart from TiO₂. This electron storage and shuttling ability of RGO demonstrated its potential use as a catalytic nanocomposite.

In general, there are two different pathways to fabricate graphene-inorganic nanocomposites including *ex situ* hybridization and *in situ* decoration.¹³¹ In the process of *ex situ* hybridization, the inorganic nanoparticles are synthesized separately from graphene using traditional methods. Afterwards, the well-defined inorganic nanoparticles are adsorbed onto the surface of RGO through either covalent or non-covalent binding. This method ensures better shape and size control of the inorganic nanoparticles. Meanwhile, surface modification of inorganic nanoparticles can be easily conducted prior to their hybridization with RGO. However, all the inorganic nanoparticles should be prepared in advance for *ex situ* hybridization, which complicates the preparation process. Also, loading efficiency of the inorganic nanoparticles on RGO is usually lower than *in situ* methods. Accordingly, *in situ* methods for the fabrication of RGO-inorganic nanocomposites have received increasing attention.¹⁵¹⁻¹⁵³

Several inorganic nanoparticles, especially metallic nanoparticles have been decorated on the surface of GO or RGO using *in situ* methods.¹⁵⁴⁻¹⁵⁶ Usually, the metal

precursors are added directly to the graphene materials for a one-pot synthetic method that dramatically simplifies the synthetic process. The oxygen-containing groups in GO and RGO provide nucleation sites for crystallization of the metal nanoparticles.^{135, 136} Meanwhile, with the introduction of reducing agents, the metal precursors and GO could be simultaneously reduced in solution.¹⁵⁷ However, two main limitations of these *in situ* methods are (i) the unstable dispersion of RGO in aqueous solutions due to the removal of oxygen-containing groups and (ii) the use of toxic reducing agents (e.g., hydrazine and sodium borohydride). To improve stability of the RGO-inorganic nanocomposites, surfactants and polymers can be adsorbed to the surface of RGO prior to the reducing process.¹⁵⁸⁻¹⁶⁰ To avoid toxic reducing agents, biocompatible reagents, such as ascorbic acid,¹⁵⁷ glucose,¹⁶¹ sodium citrate¹⁶² and ethylene glycol,¹⁶³ can be used to reduce GO and metal precursors. However, in most of these methods, an extra stabilizer is usually needed to disperse the resulting RGO-inorganic nanocomposites in solution. Therefore, a general simple *in situ* method to decorate RGO with inorganic nanocomposites is needed.

The present work demonstrates a generalized, environmental-friendly *in situ* method for fabrication of RGO-metal (oxide) nanocomposite materials. The environmentally benign reagent, glucose, was found synthetic to be an especially effective reductant and solution stabilizer in the one-pot process. Moreover, the process was found to be adaptable for synthesizing a variety of RGO/metal (oxide) nanocomposites, including RGO/Au, RGO/Cu₂O and RGO/Ag. Extensive characterizations were used to confirm the composition and morphology of the

designed nanocomposites. Furthermore, the electrocatalytic activity of the RGO/Au nanocomposite was demonstrated with the simultaneous analysis of L-ascorbic acid (L-AA), dopamine (DA) and uric acid (UA) under physiological solution conditions. This result illustrated the potential of the developed nanocomposites for other biomolecule detection schemes.

2. Experimental Section

2.1. Materials.

Graphene oxide was purchased from Cheap Tubes Inc., VT. Glucose ($\geq 99.5\%$, GC grade), L-ascorbic acid (L-AA, $\geq 99.0\%$, crystalline), dopamine hydrochloride (DA), uric acid (UA, $\geq 99\%$, crystalline), chloroauric acid tetrahydrate ($+ 99.9\%$), copper(II) chloride dehydrate (ACS reagent, $\geq 99.0\%$), silver nitrate (ACS reagent, $\geq 99.0\%$) and ammonium hydroxide (ACS reagent, 28.0 %) were purchased from Sigma Aldrich Inc. Phosphate buffered saline tablets and fetal bovine serum were purchased from Fisher Scientific. Deionized (DI) water (Millipore Milli-Q grade) with resistivity of $18.2 \text{ M}\Omega\cdot\text{cm}$ was used in all experiments.

2.2. Preparation of RGO/Metal (Oxide) nanocomposites.

The RGO/metal (oxide) nanocomposites were prepared using a one-pot reaction. In brief, 160.0 mg glucose was added to a stirred homogeneous GO solution (100.0 mL, 5.0 mg) and stirred for 30 min. An 80 μL aliquot of NH_4OH (28.0 %) was added quickly to the solution and the flask was heated to boiling for 20 min. During this time, the color of the solution changed from brown-yellow to dark black, indicating the formation of RGO from GO. Afterwards, 1.0 mL of the metal precursor solution

(1.0 % H₂AuCl₄, 1.0 % CuCl₂ or 0.5 % AgNO₃) was added drop wise and the mixture was boiled for 15 min. Finally, the cooled dispersed solution was centrifuged to separate the unattached metal nanoparticles that remained suspended in the supernatant during the centrifugation. The RGO/metal nanocomposite precipitate was redispersed into 20.0 mL Milli-Q water with sonication for further usage.

2.3. Characterization.

The scanning transmission electron microscopy (STEM) and scanning electron microscopy (SEM) images of RGO/metal (oxide) nanocomposites were obtained with a Hitachi SU8010 field emission scanning electron microscope. Elemental analysis for different RGO/metal nanocomposites was performed by an energy-dispersive X-ray spectroscope (EDS) (Oxford, X-Max) installed in the Hitachi SU8010 SEM. X-ray diffraction (XRD) profiles were obtained with a Bruker AXS D8 advanced powder X-ray diffraction system using Cu K α radiation. Raman spectra were obtained with an Aramis labRAM Raman spectrometer (Horiba JobinYvon) using a helium-neon laser at 542 nm. Fourier transform infrared (FTIR) spectra were obtained with a FT-IR spectrometer (Spectrum 400, PekinElmer) and UV-vis absorption spectra were recorded with a Shimadzu UV-250 spectrometer.

2.4. Electrochemical Measurement.

All cyclic voltammetry (CV) and differential pulse voltammetry (DPV) were performed with an Autolab PGSTAT302 potentiostat using a standard three-electrode cell. The cell was configured in all experiments with a Ag/AgCl (saturated KCl) reference electrode, a platinum wire counter electrode, and a modified glassy carbon

electrode (GCE, 5 mm diameter, BASi). Prior to the medication, the GCE was cleaned by polishing with an aqueous suspension of 0.05 μm alumina powders (Buehler), rinsing with DI water under sonication and then electrochemical cycling in 1.0 M H_2SO_4 from - 0.4 V to 1.5 V until a stable CV was obtained. After rinsing and drying the cleaned electrode, a 20 μL aliquot of GO, RGO or RGO/Au nanocomposites was drop-cast onto the GCE surface and dried in a 60 $^\circ\text{C}$ oven for 30 min.

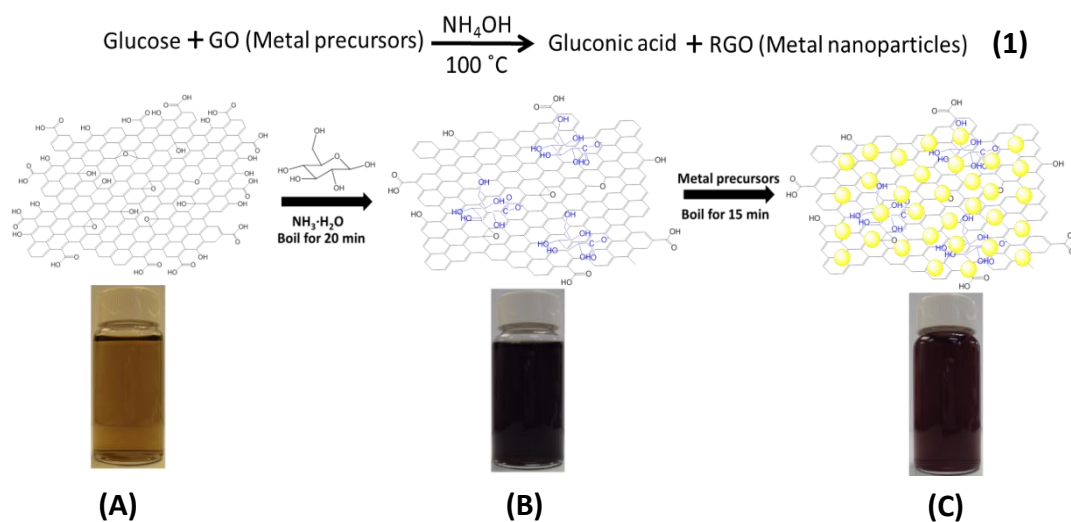
CV and DPV measurements of L-AA, DA and UA were performed at room temperature with a 0.01 M pH 7.0 PBS buffer and usually containing 10-times diluted serum to model physiological conditions. The DPV analysis was conducted with L-AA, DA and UA stock solutions spiked into the PBS buffer with diluted serum.

3. Results and Discussion

3.1. Design and Synthesis of the RGO/Metal (Oxide) Nanocomposites.

The designed one-pot synthetic process for RGO/metal (oxide) nanocomposite was shown in scheme 3. This method has three main features. First, the reductant used in the synthetic process is environmental friendly, by being natural and non-toxic. Secondly, the reductant plays multiple roles in the synthetic process as a reductant for both GO and metal precursors and as a stabilizer for protection of the product from aggregation. Thirdly, this synthetic method is general enough to produce different types of RGO/metal (oxide) nanocomposites. The rationale of selection of glucose as the reductant is based on its natural and nontoxic properties as well as its abundance and relatively gentle activity. Other natural substances, such as sucrose, fructose and L-ascorbic acid, have also been used for the reduction process.^{161, 164} However, glucose

has already been proven to be useful for the reduction of GO.¹⁶¹ After reducing GO, glucose is oxidized to gluconic acid that has also been used as a stabilizer to remain RGO stable in aqueous solution.¹⁶¹ Meanwhile, glucose has been used for the synthesis of gold and silver nanoparticles.¹⁶⁵ Inspired by these works, we developed the one-pot approach was developed for the synthesis of RGO/metal (oxide) nanocomposites using glucose as the multi-functional reducing agent and stabilizer precursor as shown in scheme 3.



Scheme 3. Illustration of the synthetic process of RGO/metal (oxide) nanocomposites using glucose as the reducing agent. (A) GO was stirred with glucose without heating; (B) GO was reduced to form RGO by glucose with boiling for 20 min; (C) RGO/Au nanocomposite was formed through the injection of HAuCl_4 in (B) for boiling another 15 min.

In Scheme 3, the oxygen-containing groups on GO, such as carboxyl and hydroxyl groups, were removed under thermal treatment with an excess of glucose as the reducing agent. The color of the solution changed from brown-yellow (Scheme 3A) to dark black (Scheme 3B) indicated the formation of the RGO from GO. In literatures, RGO was reduced by other methods, including thermal treatment and chemical reduction, which suffered from unstable suspension because most of the oxygen-

containing groups were removed from GO and electrostatic repulsion between the RGO sheets decreased significantly. In contrast, RGO reduced by glucose was more stable in water suspension due to the protection of gluconic acid on the surface of RGO.¹⁶¹ Moreover, the gluconic acid and residual oxygen groups on RGOs provided reactive sites for absorption and nucleation of different metal ions onto the surface of RGO, followed by reduction of metal ions to form the nanoparticles on these sites (Scheme 3C). The color of the solution changed with the addition of metal precursors, indicating the formation of different metal (oxide) nanoparticles on the surface of RGOs. The resulted RGO/metal (oxide) nanocomposites required several centrifugation/washing cycles with DI water to ensure separation of dispersed metal nanoparticles from the nanoparticle-decorated RGOs.

3.2. Characterization of Designed Nanocomposites.

Nanocomposites were characterized with a number of methods including imaging, elemental analysis, and spectroscopies.

3.2.1. Morphology and elemental analysis of the developed nanocomposites.

Successful decoration of different metal (oxide) nanoparticles onto RGOs was demonstrated by STEM images (Figure 37, images of 1 series) and SEM images (Figure 37, images of 2 series). First, before the reaction, the pure GO was imaged (A₁ and A₂). The both STEM and SEM images clearly showed GO sheet structures. After the reaction with glucose, little difference can be observed (B₁ and B₂) compared to A₁ and A₂, although spectroscopy results described in the next section confirmed the distinct oxidation state of RGO. When an addition of different metal precursors were added to

the RGO, the images clearly showed metal or metal oxide nanoparticles formed on the RGO surface (Figure 37 C-E). Specifically, an addition of HAuCl_4 yielded 45.3 ± 0.8 nm gold nanoparticles which fully coated RGO (Figure 37 C₁ and C₂). The energy dispersive X-ray (EDS) analysis of this sample in Figure 37C indicated that the nanoparticles were Au (Figure 38A). To test the universal potential of this phenomenon to other metal elements, an Ag precursor (AgNO_3) was added to the RGO solution. As expected, the RGO surface was successfully decorated with Ag nanoparticles (Figure 37 D₁ and D₂), and the EDS spectra indicated the presence of element of Ag (Figure 38B). In addition to the formation of pure metal nanoparticles, some metal oxide nanoparticles could be produced on the RGO surface. We treated RGO solution with a copper precursor (CuCl_2). The nanoparticles were also produced (Figure 37 E₁ and E₂). However, the elemental analysis (Figure 38 C) of the nanoparticles was significantly distinct from Au and Ag. In Figure 38C, the atomic ratio of oxygen to carbon was 2.33:1 in RGO/ Cu_2O nanocomposite, which was higher than the other two metals (2.11:1 and 2.05:1 for RGO/Au and RGO/Ag, respectively), indicating the possible formation of copper (I) oxide nanoparticles instead of copper nanoparticles.

SEM images showed that metal and metal oxide nanoparticles on each side of RGO could be easily distinguished based on their different contrast. Wrinkles of the RGO could be recognized especially from the area with nanoparticles. It seems that the nanoparticles were trapped within the RGO sheet. Average diameters of these nanoparticles were statistically calculated from the measurements of multiple

nanoparticles ($N > 50$). The results were 45.3 ± 0.8 nm (Au), 53.4 ± 0.9 nm (Ag) and 675.1 ± 9.2 nm (Cu_2O). Overall, the above results demonstrated that different metal (oxide) nanoparticles could be decorated on the surface of RGO during the *in situ* reduction process using glucose as a reductant.

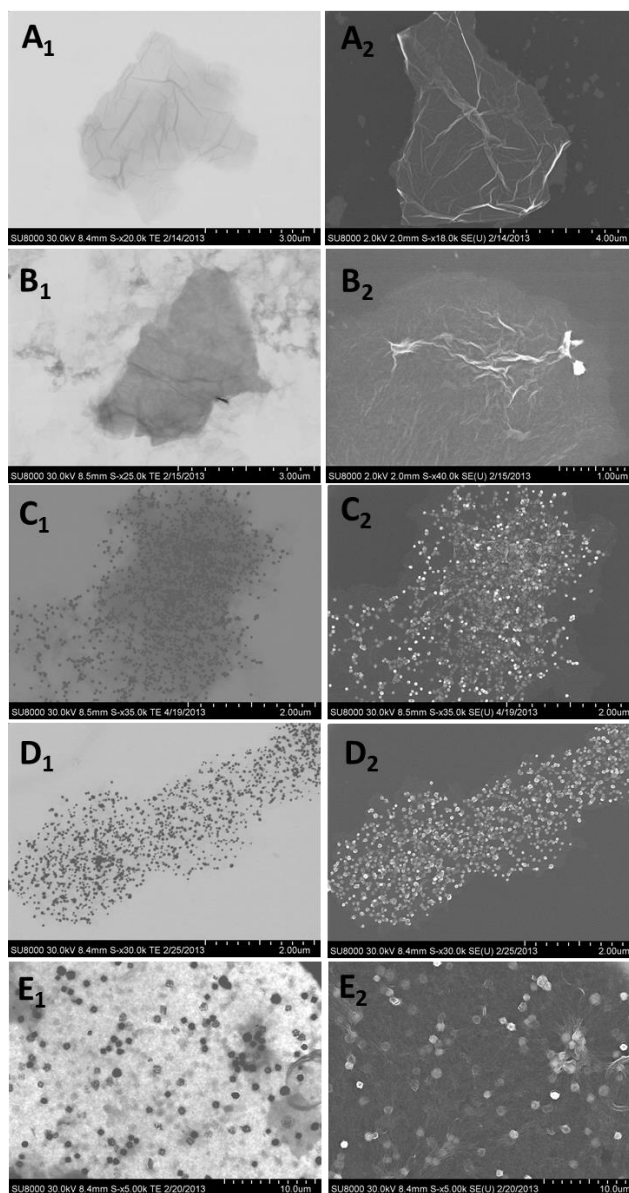


Figure 37. The STEM (A₁, B₁, C₁, D₁ and E₁) and FE-SEM (A₂, B₂, C₂, C₂, D₂ and E₂) images of GO (A₁ and A₂), RGO (B₁ and B₂), RGO/Au (C₁ and C₂), RGO/Ag (D₁ and D₂) and RGO/ Cu_2O (E₁ and E₂) nanocomposites. Reaction conditions: 100.0 mL GO solution (0.1 mg/mL), 160.0 mg of glucose, and 80 μL NH_4OH were mixed to form a homogenous solution. The solution was boiled for 20 min followed by the addition of 1.0 mL metal precursors for another 15 min of boiling.

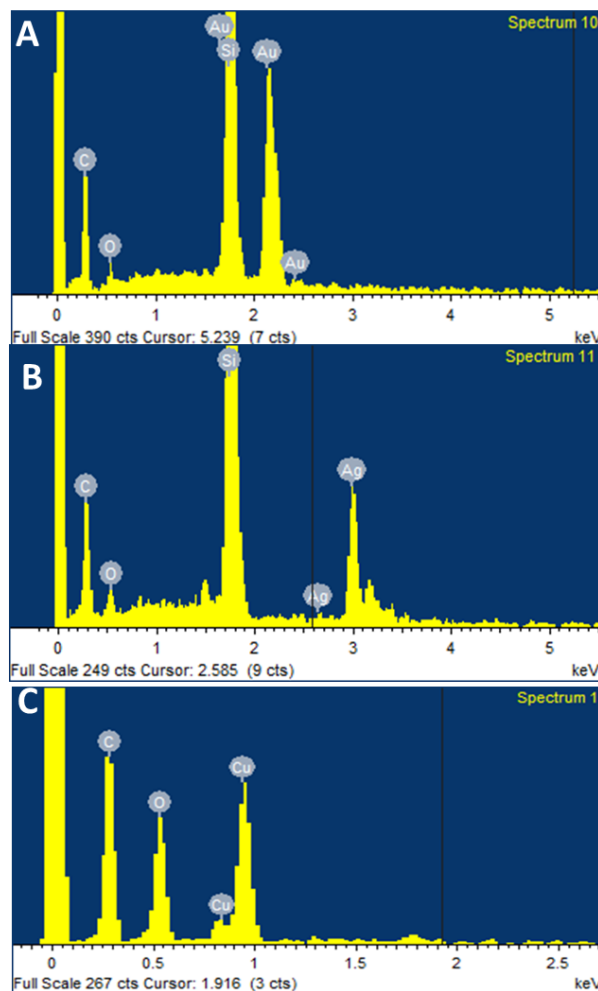


Figure 38. EDS of RGO/Au (A), RGO/Ag (B) and RGO/ Cu₂O (C) nanocomposites. Reaction conditions: 100.0 mL GO solution (0.1 mg/mL), 160.0 mg of glucose, and 80 μ L NH₄OH were mixed to form a homogenous solution. The solution was boiled for 20 min followed by the addition of 1.0 mL metal precursors for another 15 min of boiling.

3.2.2. Spectroscopic characterizations.

We further confirmed the developed nanocomposites using UV-vis spectra, FTIR, Raman spectra and XRD. First, we investigated their UV-vis spectra (Figure 39A). UV-vis absorption spectrometry is a powerful tool to distinguish the GO from RGO since they were hard to be differentiated from the previous microscopic images. It should show a red shift on the absorption peak if GO becomes RGO according to the

literature.¹⁵⁷ In our result, the pure GO showed a typical absorption peak at 230 nm (Figure 39A curve a). After 20 min of reaction with glucose, the 230 nm absorption peak was shifted to 260 nm (Figure 39A curve b). This peak shift was an indication of the change from GO to RGO. The formation of metal (oxide) nanoparticles on the RGO can also be confirmed from their UV-vis absorption spectra. After the reaction with the metal precursors, RGO remained its original absorption peak at 260 nm. Meanwhile, a second absorption peak appeared at 560 nm for Au (Figure 39A curve c), which corresponded to the red color of the RGO/Au nanocomposite. Similar to the RGO/Au nanocomposite, an absorption peak at 425 nm was formed for Ag (Figure 39A curve e), which was assigned to the color of yellow. However, the copper-based nanocomposite showed no second absorption peak (Figure 39A curve d), although the resulted RGO/Cu₂O nanocomposite appeared a light blue color in solution. which was probably due to the overlap of RGO absorption. The reduction of GO to RGO was further confirmed by other three spectroscopic methods below.

We then performed FTIR spectrometry to further confirm the reduction of GO to RGO (Figure 39B). As a control, first, the pure glucose's the FT-IR spectrum of glucose (Figure 39B curve a). Compared to the pure glucose, GO showed a strong infrared absorption band at 1725 cm⁻¹ due to C=O stretching (Figure 39B curve b). When the GO was reduced by glucose, this peak decreased significantly while the C=C stretching peak at 1620 cm⁻¹ appeared (Figure 39B curve c). The peak shift from C=O to C=C indicated the reduction of GO to RGO. Furthermore, we tested Au, Ag and Cu₂O decorated RGO. As shown in Figure 39B curves d, e, and f, their FT-IR spectra

clearly showed C=C peak around 1620 cm^{-1} but the C=O peak at 1725 cm^{-1} were not visible. The FT-IR spectrometry results supported the reduction of GO to RGO by glucose.

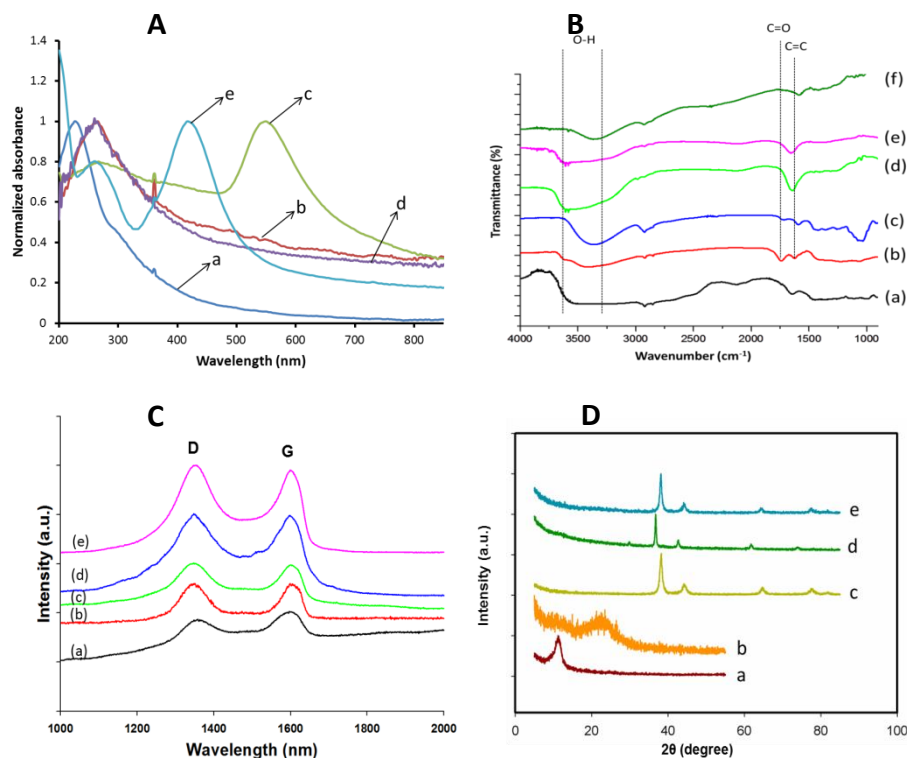


Figure 39. (A) Absorption spectra, of GO (a), RGO (b), RGO/Au (c), RGO/Cu₂O (d) and RGO/Ag (e) nanocomposites. (B) FT-IR spectra of glucose (a), GO (b), RGO (c), RGO/ Cu₂O (d), RGO/Au (e) and RGO/Ag (f) nanocomposites. (C) Raman spectra of GO (a), RGO (b), RGO/Au (c), RGO/ Cu₂O (d) and RGO/Ag (e) nanocomposites. (D) XRD patterns of GO (a), RGO (b), RGO/Au (c), RGO/ Cu₂O (d) and RGO/Ag (e) nanocomposites. Reaction conditions: 100.0 mL GO solution (0.1 mg/mL), 160.0 mg of glucose, and 80 μL NH₄OH were mixed to form a homogenous solution. The solution was boiled for 20 min followed by the addition of 1.0 mL metal precursors for another 15 min of boiling.

Raman spectra further demonstrated different structural signatures between GO and its reduced products by glucose (Figure 39C). In general when GO is reduced to RGO, one of the typical structure changes is to form sp^2 domain structure. The change could be evidenced by the increased intensity ratio of the D band at 1350 cm^{-1}

to the G band at 1595 cm^{-1} (I_D/I_G). As shown in Figure 39C, the ratio of I_D to I_G was 0.92 for the pure GO (Figure 39C curve a); however, the ratio was increased to 1.04 after the glucose was used to reduce the GO (Figure 39C curve b). The 13% increase in the ratio of I_D to I_G indicated the formation of RGO. We then tested the Au, Cu_2O and Ag nanoparticles decorated RGO (Figure 39C curve c, d and e). All these samples showed apparent D and G bands for which the ratios of I_D to I_G were 1.03, 1.08 and 1.03, respectively. These results demonstrated that GO had been reduced by glucose and formed a more sp^2 -like ordered structure.

Structures of GO, RGO, RGO/Au, RGO/ Cu_2O and RGO/Ag nanocomposites were further characterized using powder XRD (Figure 39D). GO showed a graphitic diffraction peak at 11.5° (curve a), corresponding to an interlayer d-spacing of 0.73 nm. Compared to 0.34 nm of d-spacing of pristine graphite (0.34 nm)¹⁶¹, the larger d-spacing distance indicated that the oxygenated functional groups were introduced into the carbon sheet. The the peak at 11.5° disappeared and a bump around 20° formed for the newly formed RGO (Figure 39D curve b), which demonstrated the removal of the oxygen-containing groups from GO and exfoliation of the layered RGO. Once metal (oxide) nanoparticles were introduced on the surface of the RGO, their corresponding peaks were evident. For example, RGO/Au (Figure 39D curve c) showed the peaks at 38.4° , 44.2° , and 64.7° which can be assigned to (111), (200) and (220) faces of the Au nanoparticles. RGO/ Cu_2O and RGO/Ag also showed characteristic peaks at 29.5° , 36.3° and 38.1° , 42.2° , 64.5° and 77.5° , respectively, (Figure 39D curve d and e), which were coincided to their XRD patterns in the literatures.¹⁶⁶⁻¹⁶⁸

The above characterization results have confirmed our design that the GO has been reduced to RGO and then different types of metal (oxide) nanoparticles decorated on the surface of the produced RGO. Afterwards, we optimized the synthetic conditions for making RGO/metal (oxide) nanocomposites. RGO/Au nanocomposite was chosen as an example for this optimization.

3.3. Optimization of Nanocomposite Synthesis.

Various experimental conditions would affect the formation of RGO/Au nanocomposites. Here, we investigated a few important conditions that may play crucial roles for the formation of the designed nanocomposites.

3.3.1 Effect of glucose.

As the solo reductant and stabilizer, glucose played an important role in the synthesis. Therefore, we investigate the effect of glucose on the formation of nanocomposite. First, glucose acted as a reductant for the generation of both gold nanoparticles and RGO. Thereafter, glucose served as a stabilizer for RGO and RGO/Au nanocomposite. We repeated the synthetic process without addition of any glucose to observe the resulted product. It was found that the absorption peak of GO at 230 nm still existed in either solution before (Figure 40A, curve a) and after (Figure 40A, curve b) the addition of HAuCl_4 . However, there was no peak appeared at 260 nm which attributed to RGO. This implied that GO was not reduced without the addition of glucose. Interestingly, after the addition of HAuCl_4 , red colored gold nanoparticles was still formed, with the absorption peak at 538 nm (Figure 40A, curve b). SEM image showed that all the gold nanoparticles were anchored to the surface of GO (Figure 40B).

However, compared with Figure 37C₁ and C₂, less gold nanoparticles were coated on to the surface of GO, which might be due to the loss of glucose on GO.

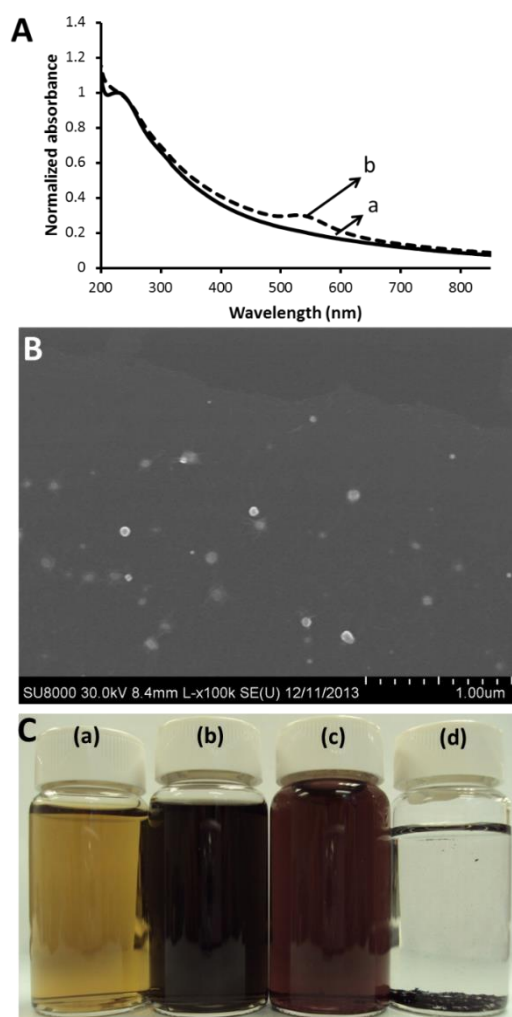


Figure 40. (A) Absorption spectra of GO (curve a) and GO/Au nanocomposite (curve b) without glucose addition. (B) SEM images of the GO/Au nanocomposites without addition of glucose. (C) Photographs of aqueous dispersions of 0.05 mg/mL GO (a), RGO reduced by glucose (b), RGO/Au nanocomposites (c) and RGO reduced by the hydrazine hydrate (d). Solution (a), (b) and (c) were stored for about 3 months. Solution (d) was stored for 1 day.

We then studied the function of glucose as a stabilizer to protect RGO from aggregation. As shown in Figure 40C, GO, RGO and RGO/Au nanocomposite reduced by glucose were stable in aqueous solution for more than 3 months (Figure 40C, a, b

and c). Usually, GO was reduced by the strong reductant, such as hydrazine hydrate. However, the instability of RGO reduced by hydrazine hydrate limited their applications in analysis. Therefore, we synthesized RGO using hydrazine hydrate as a control. The result showed that the RGO reduced by hydrazine hydrate was not stable. It started aggregation quickly. As shown in Figure 40C (d), the RGO totally precipitated in one day. This is significantly different than that three month-stable RGO obtained using glucose as a stabilizer.

3.3.2. Effect of glucose-to-HAuCl₄ ratio.

The amount of glucose and precursor added into the reaction will certainly affect the resulting product. To better investigate their effect, we choose to study the effect of glucose-to-HAuCl₄ ratio instead of their absolute amount. With a fixed concentration of GO at 0.2 mg/mL, we adjusted the glucose-to-HAuCl₄ mass/volume ratio from 1.60/1 g/mL, 0.32/1 g/mL, 0.16/1 g/mL, to 0.10/1 g/mL during the synthesis process. The concentration of the added HAuCl₄ was 1.0%. After collecting the resulting products through centrifugation, each product was characterized with SEM. As shown in Figure 41, the size of gold nanoparticles on RGO was similar for each sample, which is around 45.3 ± 0.8 nm. However, the coverage on RGO surface increased with more HAuCl₄ addition, which was illustrated by the increased numbers of bright spots on RGO in the SEM images from Figure 41A to C. The difference between Figure 41C and D was insignificant. Both images showed high coverage with almost every corner of RGO covered, indicating the saturation of the gold

nanoparticles. In the following experiments, the 0.16/1 (g/mL) ratio of glucose-to-HAuCl₄ composition (Figure 41C) was chosen as the optimum condition.

3.3.3. Effect of glucose-to-GO ratio.

The effect of amount of glucose should also be considered from its relative amount to GO. With a fixed ratio of glucose-to-HAuCl₄ as 0.16/1 (g/mL), the effect of glucose-to-GO ratio on the final RGO/Au nanocomposite was investigated (Figure 42). We changed the glucose-to-GO mass ratio from 32/1, 16/1, to 8/1. It was found on the SEM images that the diameter of the gold nanoparticles on RGO decreased from 45.3 ± 0.8 nm to 29.5 ± 4.7 nm and 25.5 ± 0.6 nm as the glucose-to-GO ratio was decreased from 32/1 to 16/1 mg and 8/1, respectively. By fixing the concentration of HAuCl₄, increased amount of GO would provide more binding sites for gold ions to anchor. Therefore, this might decrease the diameter of single gold nanoparticles on RGO.

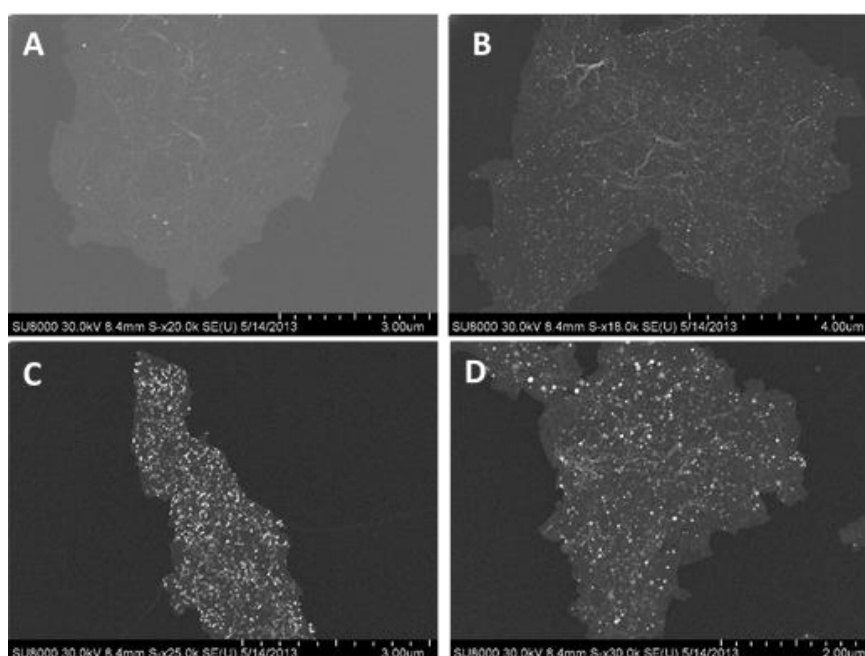


Figure 41. SEM images of the RGO/Au nanocomposites with different glucose-to-HAuCl₄ ratios. (A) 1.60/1, g/mL; (B) 0.32/1, g/mL; (C) 0.16/1, g/mL; and (D) 0.10/1, g/mL. The concentration of HAuCl₄ was 1.0%. The amount of GO was fixed at 20.0 mg.

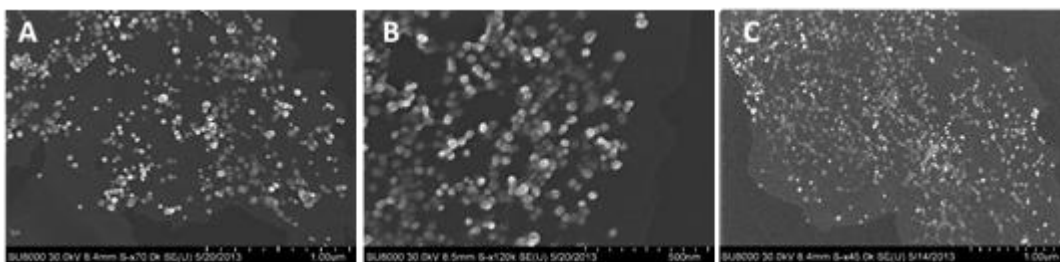


Figure 42. SEM images of the RGO/Au nanocomposites with different glucose-to-GO ratios. (A) 32/1; (B) 16/1; (C) 8/1. The amount of 1.0 % HAuCl₄ was fixed at 1.0 mL.

3.4. Electrochemical Detection of L-AA, DA and UA using a RGO/Au-Modified GCE as a Catalyst.

L-AA, DA and UA play important roles in physiological processes of the human metabolism.^{169, 170} Several disease states and disorders can be monitored by measuring the levels of these biomolecules under physiological conditions.¹⁷¹⁻¹⁷³ However, electrochemical detection through direct oxidation of these biomolecules is difficult with conventional carbon electrodes because of the sluggish and irreversible nature of these couples. Moreover, oxidation peaks of these three biomolecules occur at similar potentials, often resulting in an undistinguishable overlap when they are detected simultaneously. Modification of carbon electrodes with nitrogen-doped graphene, chitosan, carbon nanotube and gold nanoparticles improves the electrochemical oxidation of these three biomolecules and has provided a reliable means for their simultaneous detection.¹⁷⁴⁻¹⁷⁸ This improved performance has been especially true for a variety of recently developed gold nanomaterials. However, by coupling RGO with gold nanoparticles, the electrochemical analytical performance might be improved because of the large surface area and high conductivity of RGO. Meanwhile, RGO could provide a platform for gold nanoparticles to anchor on the

surface of electrode without other assistant molecules, like chitosan. Accordingly, we have investigated the electrocatalytic activity of our RGO/Au nanocomposite toward oxidation of L-AA, DA and UA, followed by the simultaneous detection of these biomolecules under physiological conditions.

3.4.1. Electrochemical activity of RGO/Au nanocomposites.

RGO has been widely used for electrochemical sensing due to its improved conductivity after reduction. Meanwhile, metal (oxide) nanoparticles have shown some electrocatalytic activity for the detection of biomolecules. Therefore, we evaluated the application of RGO/Au nanocomposites for the electrochemical detection of biomolecules.

3.4.2. L-AA detection.

The electrochemical behavior of L-AA in 0.01 M PBS (pH 7.0) at a bare GCE, GO-GCE, RGO-GCE and RGO/Au-GCE was investigated using CV and DPV. As shown in Figure 43A, the L-AA oxidation was chemically irreversible with an anodic peak that changed significantly in shape and potential with different electrode modifiers. Bare GCE and GO-modified GCE yielded broad peaks at rather positive potentials ($> +0.3$ V) consistent with sluggish electron transfer. By comparison, the oxidation peaks with RGO- and RGO/Au-modified GCE were shifted to a much lower potential (ca. 0 V). The RGO/Au-modified GCE (Figure 43A, curve d) yielded a particularly narrow peak ($E_p - E_{p/2}$ ca. 70 mV) and enhanced peak current. These characteristics are consistent with electrocatalysis of the L-AA oxidation noted for other types of gold-modified electrodes.¹⁷⁹ They also provide an enhanced signal for L-AA

detection. To evaluate the sensitivity of the RGO/Au-modifier for detection of L-AA, DPV was used for concentrations of L-AA ranging from 0.1 to 2.2 mM in 0.01 M PBS. As shown in Figure 37C, background-subtracted peak oxidation current (I'_{pa}) was centered near 0 V and increased linearly below 1 mM with a sensitivity of 4.234 $\mu\text{A}/\text{mM}$ ($R^2 = 0.9973$) L-AA (Figure 43D).

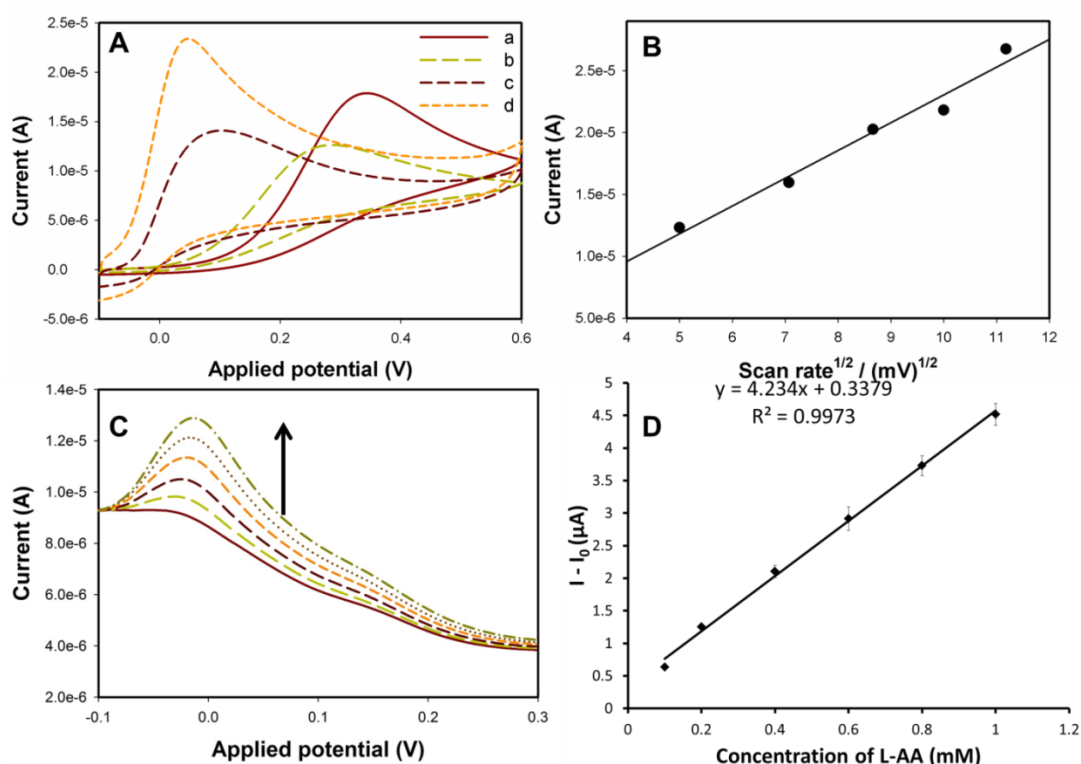


Figure 43. (A) CVs of the bare-GCE (a), GO-GCE (b), RGO-GCE (c) and RGO/Au-GCE (d) in 0.01 M PBS (pH 7.0) containing 1 mM L-AA. Scan rate: 50 mV/s; (B) Plot of oxidation peak of RGO/Au-GCE versus square root of the scan rate in 0.01 M PBS (pH 7.0) containing 1 mM L-AA; (C) DPV curves of RGO/Au-GCE in 0.01 M PBS (pH 7.0) containing different concentrations of L-AA (0.1, 0.2, 0.4, 0.6, 0.8 and 1.0 mM); (D) Plot of oxidation currents versus different concentration of L-AA at -0.014 V. I : oxidation peak current in the presence of L-AA; I_0 : oxidation peak current in the absence of L-AA. Inset shows: the calibration curve of oxidation peak current response versus concentration of L-AA in the linear range of 0.1 - 1.0 mM.

3.4.3. DA detection.

The CV and DPV behaviors of the RGO/Au-GCE for the DA detection were also investigated. As shown in Figure 44A, RGO/Au-GCE showed the highest peak currents compared to bare GCE, GO-GCE, and RGO-GCE, which indicated that the RGO/Au-GCE had the better catalytic activity and higher surface area (Figure 44A, d). Different from the CV behavior of L-AA (Figure 43A) and UA (Figure 45A), the DA showed a more chemically reversible process on the surface of

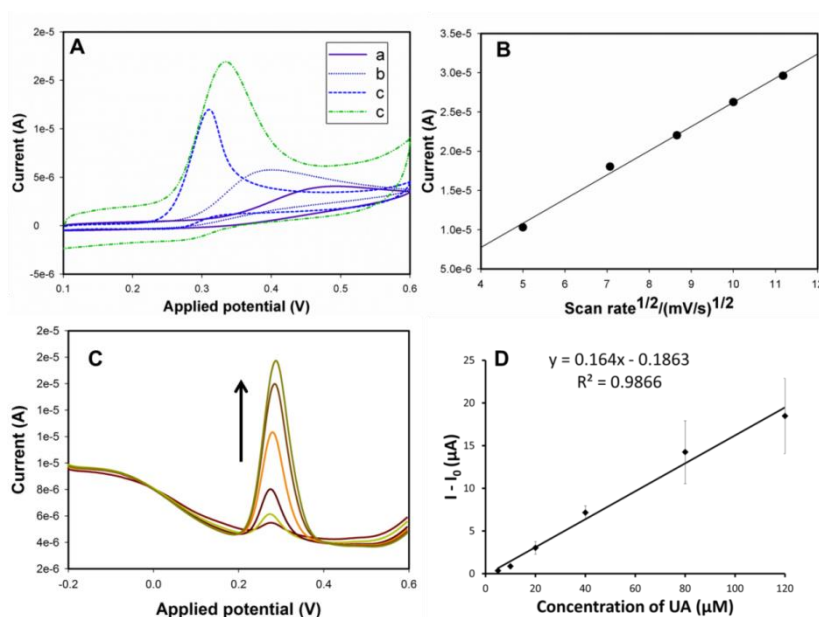


Figure 44. (A) CVs of the bare-GCE (a), GO-GCE (b), RGO-GCE (c) and RGO/Au-GCE (d) in 0.01 M PBS (pH 7.0) containing 160 μM DA. Scan rate: 50 mV/s; (B) Plot of oxidation peak of RGO/Au-GCE versus square root of the scan rate in 0.01 M PBS (pH 7.0) containing 80 μM DA; (C) DPV curves of RGO/Au-GCE in 0.01 M PBS (pH 7.0) containing different concentrations of L-AA (1.0, 2.5, 5.0, 10.0 and 20.0 μM); (D) Plot of oxidation currents versus different concentration of DA at 0.160 V. I: oxidation peak current in the presence of DA; I_0 : oxidation peak current in the absence of DA. Inset shows: the calibration curve of oxidation peak current response versus concentration of DA in the linear range of 1.0-20.0 μM .

RGO/Au-GCE. The anodic and cathodic peak currents were related to the square root of scan rate (Figure 44B), which showed that the electrochemical reaction of DA on the RGO/Au-GCE was a diffusion-controlled process. The sensitivity for DA detection was

investigated with RGO/Au-GCE using DPV. As shown in Figure 44C and D, the current at *ca.* 0.16 V increased with the addition of DA in 0.01 M PBS. The oxidation peak current of DA was linear to the DA concentration at RGO/Au-GCE with a linear function $(I-I_0) = 0.6277 C_{DA} + 0.1272$ ($R^2 = 0.9897$) in the range of 1.0 to 20 μM .

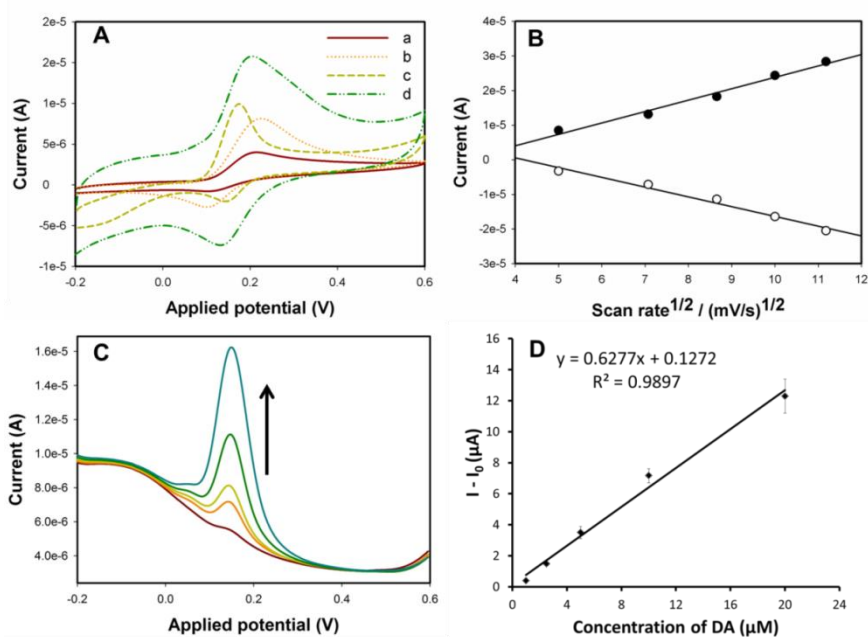


Figure 45. (A) CVs of the bare-GCE (a), GO-GCE (b), RGO-GCE (c) and RGO/Au-GCE (d) in 0.01 M PBS (pH 7.0) containing 200 μM UA. Scan rate: 50 mV/s; (B) Plot of oxidation peak of RGO/Au-GCE versus square root of the scan rate in 0.01 M PBS (pH 7.0) containing 200 μM UA; (C) DPV curves of RGO/Au-GCE in 0.01 M PBS (pH 7.0) containing different concentrations of L-AA (5, 10, 20, 40, 80 and 120 μM); (D) Plot of oxidation currents versus different concentration of UA at 0.290 V. I : oxidation peak current in the presence of UA; I_0 : oxidation peak current in the absence of UA. Inset shows: the calibration curve of oxidation peak current response versus concentration of UA in the linear range of 5-120 μM .

3.4.4. UA detection.

The same process was carried out for the detection of UA using RGO/Au-GCE in 0.01 M PBS. As shown in Figure 45, UA showed an oxidation peak potential at *ca.* 0.32 V, which is a more negative potential than that for bare GCE and GO-GCE, and with the highest peak current. Similar to the electrochemical behavior of L-AA and DA,

UA showed a linear relationship between the oxidation peak current and the square root of scan rate (Figure 45B). The DPV peak current of UA was linear to the UA concentration at RGO/Au-GCE with a linear function $(I-I_0) = 0.164 C_{UA} + 0.1863$ ($R^2=0.9866$) in the range of 5-80 μM (Figure 45C and D).

3.4.5. Simultaneous determination of L-AA, DA and UA.

Based on the above results for the detection of L-AA, DA and UA, the RGO/Au-GCE showed great potential for the simultaneous detection of these three biomolecules. The oxidation peak potential differences for L-AA/DA, DA/UA, and L-AA/UA were 200 mV, 150 mV, and 350 mV, respectively. Peak separations of their magnitude are generally sufficient for simultaneous analysis. Therefore, we investigated the simultaneous oxidation of the L-AA (2.2 mM), DA (160 μM) and UA (200 μM) using DPV with different electrodes. As shown in Figure 46A, bare GCE showed only one peak that was the overlap of DA and UA. GO-GCE showed two peaks for DA and UA, which are more positive than that from RGO-GCE and RGO/Au-GCE, but still no peak for L-AA was observed. RGO-GCE and RGO/Au-GCE were able to discriminate these three analytes. However, the peak currents for RGO/Au-GCE were higher than that of RGO-GCE, and the peak potential difference between DA and UA for RGO-GCE was smaller than that of RGO/Au-GCE. This result indicated that the Au nanoparticles and RGO all played important roles on the electrochemical catalytic activity for the simultaneous detection of L-AA, DA and UA. Two combinations of different concentrations of L-AA, DA and UA were also investigated with RGO/Au-GCE using DPV. As shown in Figure 46B, the peak currents for each molecule

increased when the concentrations of these three analytes increased. Therefore, RGO/Au-GCE showed a great potential for the simultaneous detection of L-AA, DA and UA.

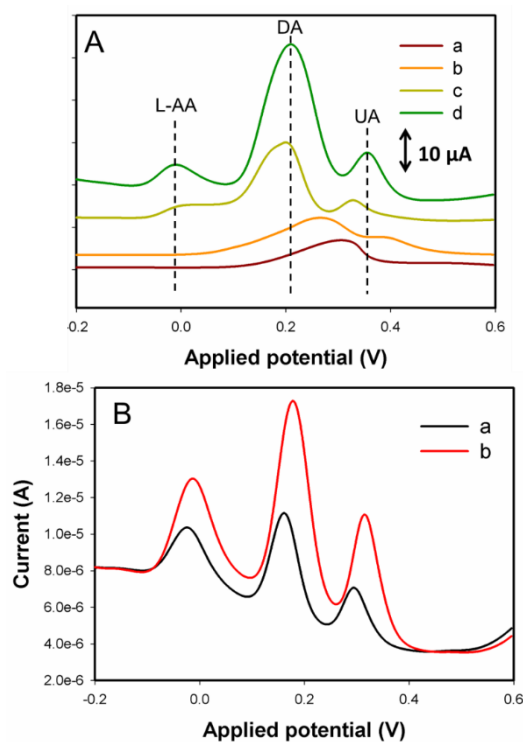


Figure 46. (A) DPV curves at bare-GCE (a), GO-GCE (b), RGO-GCE (c) and RGO/Au-GCE (d) in 0.01 M PBS (pH 7.0) containing 2.2 mM L-AA, 160 μ M DA, and 200 μ M UA; (B)DPVs curves at RGO/Au-GCE in 0.01 M PBS (pH 7.0) containing different concentrations of L-AA, DA and UA. (a) 0.6 mM L-AA, 10 μ M DA, 20 μ M UA; (b) 1.2 mM L-AA, 20 μ M DA, 40 μ M UA.

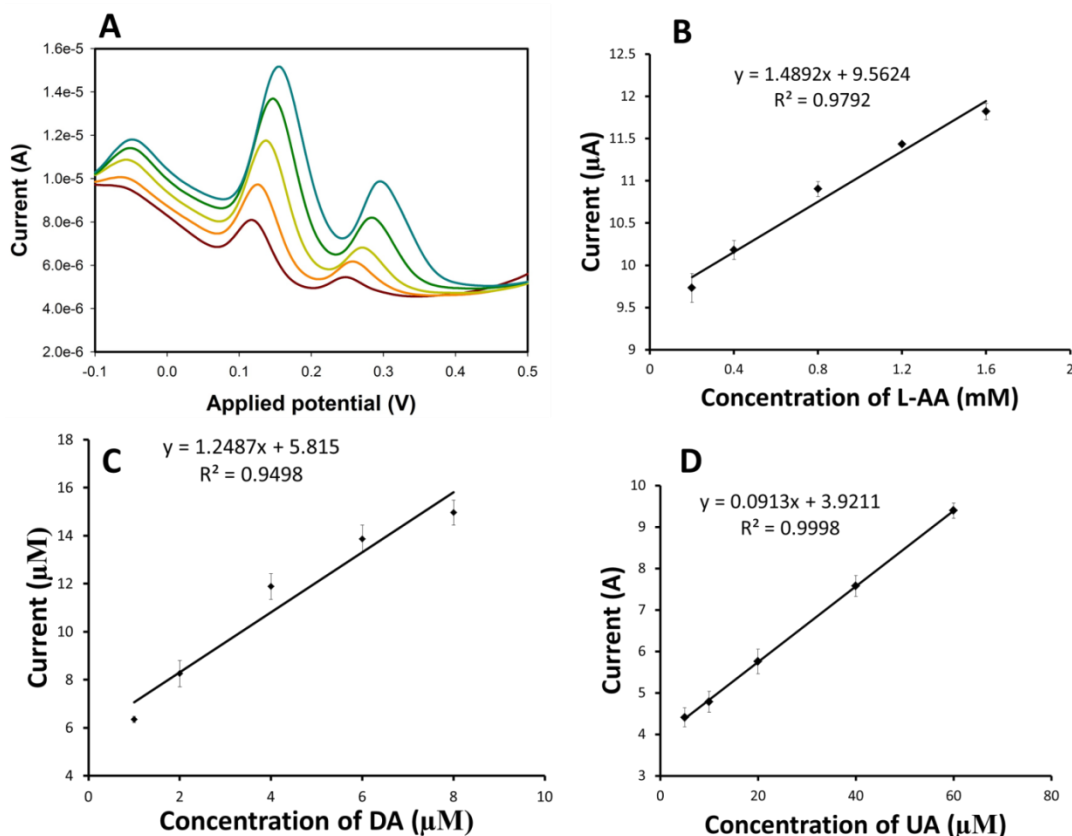


Figure 47. (A) DPV curves of the RGO/Au modified GCE in 10-times diluted serum containing individual concentration of AA, DA and UA mixture. [L-AA]: 0.2, 0.4, 0.8, 1.2, and 1.6 mM. [DA]: 1.0, 2.0, 4.0, 6.0 and 8.0 μ M. [UA]: 5.0, 10.0, 20.0, 40.0 and 60.0 μ M. The calibration curves for L-AA (B), DA (C) and UA (D) in the 10-times diluted serum.

3.4.6. Reproducibility.

Using L-AA as a model, a series of repetitive measurements were carried out in 1.0 mM L-AA solution to demonstrate the reproducibility of the RGO/Au-GCE. The results of nine measurements showed a relative standard deviation (RSD) of 3.41%, indicating excellent reproducibility for the RGO/Au-GCE.

3.4.7. Complex sample analysis.

To explore the use of a RGO/Au-GCE for practical application, the electrode was used to detect the three species in fetal bovine serum samples. The fetal bovine serum was diluted 10 times with 0.01 M PBS (pH 7.0) and then spiked with certain

amounts of L-AA, DA and UA. As shown in Figure 47A, the peak currents for each analyte increased with the increased concentrations. Compared to the plot for buffer alone, the peak potential for each analyte was shifted to more negative values, which might be due to the complex matrix of the serum samples. However, for all the analytes, the RGO/Au-GCE showed a response range and high performance linear range (Figure 47B, C and D). The results indicated that the RGO/Au-GCE can be used for the sensitive simultaneous determinations of L-AA, DA and UA in the real samples.

4. Conclusion

A one-pot synthetic method was developed for the fabrication of RGO/metal (oxide) nanocomposites using glucose as a reducing agent for both GO and metal (oxide) nanoparticles. With this simple method, RGO/Au, RGO/Cu₂O, and RGO/Ag nanocomposites were easily produced. Different characterization methods successfully demonstrated the formation of RGO/metal (oxide) nanocomposite. Using RGO/Au as a model, we found that the coverage and size of gold nanoparticles on RGO were affected by the glucose-to-HAuCl₄ ratio and glucose-to-GO ratio, respectively. Furthermore, with the high electrochemical catalytic activity of RGO/Au nanocomposites, the electrochemical behaviors of L-AA, DA and UA were investigated using CV and DPV. Compared to the bare GCE, GO-GCE, and RGO-GCE, RGO/Au-GCE showed higher peak currents and larger peak potential differences for the detection of L-AA, DA and UA. Finally, the simultaneous detection of these three different analytes with high sensitivity was achieved.

CHAPTER VI

ENHANCED SYNERGETIC ANTIBACTERIAL PROPERTIES OF REDUCE GRAPHENE OXIDE/AG NANOCOMPOSITE

1. Introduction.

Since the emergence of drug-resistant bacterial strains, it is important to develop new antibacterial agents that show better treatment efficacy in clinic.^{180, 181} Therefore, nanomaterials that possess excellent antibacterial activities provide a promising direction for combating bacterial infections.¹⁸²⁻¹⁸⁴ Several nanomaterials have been reported as antibacterial agents, such as silver nanoparticles (AgNPs),¹⁸⁵⁻¹⁸⁷ carbon nanotubes,¹⁸⁸ graphene and graphene-based nanomaterials.¹⁸⁹⁻¹⁹⁵ Among these antibacterial nanomaterials, the use of AgNPs has been deeply investigated and they are undergoing the process for clinic application.^{196, 197}

Graphene, the novel two-dimensional carbon nanomaterial discovered in 2004, has attracted tremendous attention from both chemists and biologist for its excellent mechanical, optical, thermal and electronic properties.^{125-127, 146, 198, 199} Meanwhile, the great biocompatibility of the carbon nanomaterials makes graphene and graphene-based nanomaterials excellent candidates for biomedical applications.²⁰⁰⁻²⁰² Therefore, graphene-based nanomaterials have been used for the biosensing,^{203, 204} bioimaging,^{134, 205, 206} drug delivery^{145, 207-209} and construction of theranostic agents for different diseases.²¹⁰⁻²¹² Especially, the photothermal property of

graphene can be used for targeting therapy with controlled laser irradiation.²¹³ Because of their large surface area and absorbing ability, graphene-based nanomaterials have been widely used for cancer chemotherapy and photothermal therapy.^{207, 209, 214, 215} Recently, graphene-based materials have been used as efficient potential antibacterial agents.^{190, 191} For example, Liu *et al.* investigated the antibacterial activity of four different types of graphene-based materials and found that graphene oxide (GO) showed the highest antibacterial activity, followed by reduced graphene oxide (RGO), graphite and graphite oxide.¹⁹¹ By using the photothermal effect of RGO under near-infrared (NIR) irradiation, Wu *et al.* developed magnetic nanoparticles modified RGO composite to capture and kill bacteria through photothermal effect.¹⁸⁹

To increase the antibacterial property, the AgNPs and graphene-based nanomaterials were coupled together to form graphene/silver nanocomposite using several different methods.^{192, 216-219} The resultant products showed enhanced antibacterial activity due to their combination. Although these works showed strong antibacterial ability of graphene/silver nanocomposites, to the best of our knowledge, there has no been investigation of the synergetic effect of AgNPs and photothermal effect of graphene on bacteria. By coupling these two antibacterial pathways, the graphene/silver nanocomposite might be more efficient under NIR irradiation. Therefore, in this work, we developed a facile, environmental friendly method to fabricate RGO/Ag nanocomposite using glucose as a reducing agent. Using *Escherichia coli* (*E. coli*) and *Klebsiella pneumoniae* (*Kp*) as the bacterial models, the antibacterial efficiency of RGO/Ag nanocomposite was investigated under NIR

irradiation. Furthermore, bacterial cell integrity and generation of ROS species with the treatment of RGO/Ag nanocomposite and NIR irradiation were demonstrated to uncover a possible mechanism of antibacterial activity of the RGO/Ag nanocomposite besides photothermal effect.

2. Materials and Methods.

2.1. Materials and Instruments.

Graphene oxide was purchased from Cheap Tubes Inc., VT, which was synthesized according to Hummer's method from graphite flakes. Glucose ($\geq 99.5\%$, GC grade), silver nitrate (ACS reagent, $\geq 99.0\%$) and ammonium hydroxide (ACS reagent, 28.0 %) were purchased from Sigma Aldrich Inc. Phosphate buffered saline tablets and fetal bovine serum were purchased from Fisher Scientific. Deionized (DI) water (Millipore Milli-Q grade) with resistivity of 18.2 M Ω •cm was used in all experiments. *E. coli* HB101 strain was obtained from American Tissue Culture Collection (ATCC). *Kp* Xen-39 (ATCC 93A 5370), a bioluminescent pathogenic bacterium strain expressing LUC bioluminescence was purchased from Caliper (Santa Clara, CA).

A Hitachi SU8010 field emission scanning electron microscope was used to take the SEM and STEM images of the RGO/Ag nanocomposite. Elemental analysis for different RGO/metal nanocomposites was performed by an energy-dispersive X-ray spectroscope (EDS) (Oxford, X-Max) installed in the Hitachi SU8010 SEM. X-ray diffraction (XRD) profiles were obtained with a Bruker AXS D8 advanced powder X-ray diffraction system using Cu K α radiation. Fourier transform infrared (FTIR) spectra

were obtained with a FT-IR spectrometer (Spectrum 400, PekinElmer) and UV-vis absorption spectra were recorded with a Lambda 1050 UV/VIS/NIR spectrometer. The photothermal effect study was performed by a BWF1 series fiber-coupled diode laser system (750 mW at 808 nm) (B&W TEK Inc). Luminescence imaging was taken by Caliper's Xenogen IVIS optical imaging system (Caliper, PerkinElmer, Santa Clara, CA).

2.2. Preparation of RGO/Ag Nanocomposite.

The RGO/Ag nanocomposites were prepared using a one-pot reaction. In brief, 5 mg homogeneous GO solution was mixed with 160.0 mg glucose for 30 min. An 80 μL aliquot of NH_4OH (28.0 %) was added quickly to the solution and refluxed for 20 min. During this time, the color of the solution changed from brown-yellow to dark black, indicating the formation of RGO from GO. Afterwards, 1.0 mL of 0.5 % AgNO_3 solution was added drop wise and the mixture was refluxed for 15 min. Finally, the cooled dispersed solution was filtered with 0.1 μm pore size membrane to separate the unattached silver nanoparticles from RGO/Ag nanocomposite. Finally, the RGO/Ag nanocomposite was redispersed into Milli-Q water with sonication for further use.

2.3. Antibacterial Activity Tests.

Bacteria were cultured in Lysogeny broth (LB) medium and shaken at 37 °C overnight before use. The next day, the bacterial cells were harvested by centrifuge and dispersed in PBS with an optical density at 600 nm (OD_{600}) of 1.0. Then, the bacteria were diluted to 10^8 CFU mL^{-1} with sterile PBS. The samples of GO, RGO, AgNPs, and RGO/Ag nanocomposites in PBS were incubated with bacteria suspension,

respectively. The samples were incubated at 37 °C for 2 hours followed by the irradiation of 808 nm laser for another 10 min. Finally, 100 µL of the bacteria suspension was added into 900 µL LB medium for the growth in a shaking incubator at 37 °C overnight. The concentration of bacteria was finally determined by measuring OD₆₀₀. Meanwhile, the plate count method was used to compare the killing effect of RGO/Ag nanocomposite. Briefly, the bacteria suspension in LB medium treated with RGO/Ag nanocomposites was plated on LB-agar plates, and incubated at 37 °C overnight. The photographs were taken by commercial camera and the bioluminescence images were taken by IVIS optical imaging system.

2.4. Cell Wall/Membrane Integrity Investigation.

Log phase *E. coli* (10^8 CFU mL⁻¹) cells were dispersed in 200 µL PBS with or without 15 µg/mL RGO/Ag nanocomposites. After growth for 2 h at 37 °C in the incubator, the 808 nm laser irradiation was followed for another 10 min to carry out the photothermal therapy. Then, the bacteria were stained with propidium iodide (PI, 1.25 µg/mL) and 4',6-diamidino-2-phenylindole (DAPI, 12.5 µg/mL) for 15 min in the dark, and then the cells were collected by centrifugation. The cells were then imaged using a Nikon Eclipse 80i (upright) fluorescent microscope.

2.5. Cytotoxicity of RGO/Ag Nanocomposite to Mammalian Cells.

SW620 cells and MH-S cells were cultured in 1640 medium supplemented with 10 % fetal bovine serum (FBS) at 37 °C overnight. Both cells were treated with various concentrations of RGO/Ag nanocomposites at 37 °C for 24 h. Then, each well was added 10.00 µL, 5 mg/mL MTT reagent. The cells were further incubated at 37 °C

for 4 h until the purple color developed. 100.00 μL DMSO solution was added into each well to stop reaction and dissolve the precipitant thoroughly. The absorbance of each well was recorded at 570 nm to determine the cell proliferation rate.

2.6. Detection of Reactive Oxygen Species (ROS).

The possibility of ROS production was evaluated by the 2',7'-dichlorodihydrofluorescein diacetate (H_2DCFDA) assay. Briefly, a 50 μL aliquot of bacteria ($10^8/\text{mL}$) was added with 100 μL , 0.04 mM H_2DCFDA PBS solution and incubated for 0.5 h. Then, 27 μL PBS or 0.1 mg/mL RGO/Ag nanocomposite (15 $\mu\text{g}/\text{mL}$ final) were added and incubated for 1 h. Then, the irradiation ($0.30 \text{ W}/\text{cm}^2$) was used to induce the photothermal treatment of *E. coli* for 10 min. After another 1 h incubation at 37°C , the fluorescence intensity (Ex: 485 -495 nm; Em: 515 – 525 nm) was measured using microplate reader.

3. Results and Discussion.

3.1. Synthesis and Characterization of RGO/Ag Nanocomposite.

Our goal was to develop a synergetic nanocomposite as an efficient antibacterial agent. Based on the antibacterial properties of silver nanoparticles and the photothermal effect of RGO, our hypothesis was that the combination of RGO and silver nanoparticles would generate the highly efficient antibacterial agent. As reported in our previous work, an environmentally friendly and facile method was used to prepare the RGO/Ag nanocomposite using glucose as the reducing agent and the resulted gluconic acid as the stabilizer. The silver nanoparticles were anchored on the

defects of the GO sheets. At the same time, the GO was reduced to form RGO with glucose.

We characterized the formation of the RGO/Ag nanocomposite using several methods. As shown in Figure 48 A and B, The STEM and SEM images showed that silver nanoparticles were deposited on the surface of RGO sheet. From measuring more than fifty silver nanoparticles, the average diameter of silver nanoparticles on RGO sheet was determined to be 53.4 ± 0.9 nm. Then, the energy dispersive X-ray spectroscopy (EDS) was used to analyze the content of the nanocomposites. As shown in Figure 48C, the nanocomposite contained elements of carbon and oxygen, which indicated the presence of RGO, and silver for silver nanoparticles. The copper peak was associated with the TEM sample grid.

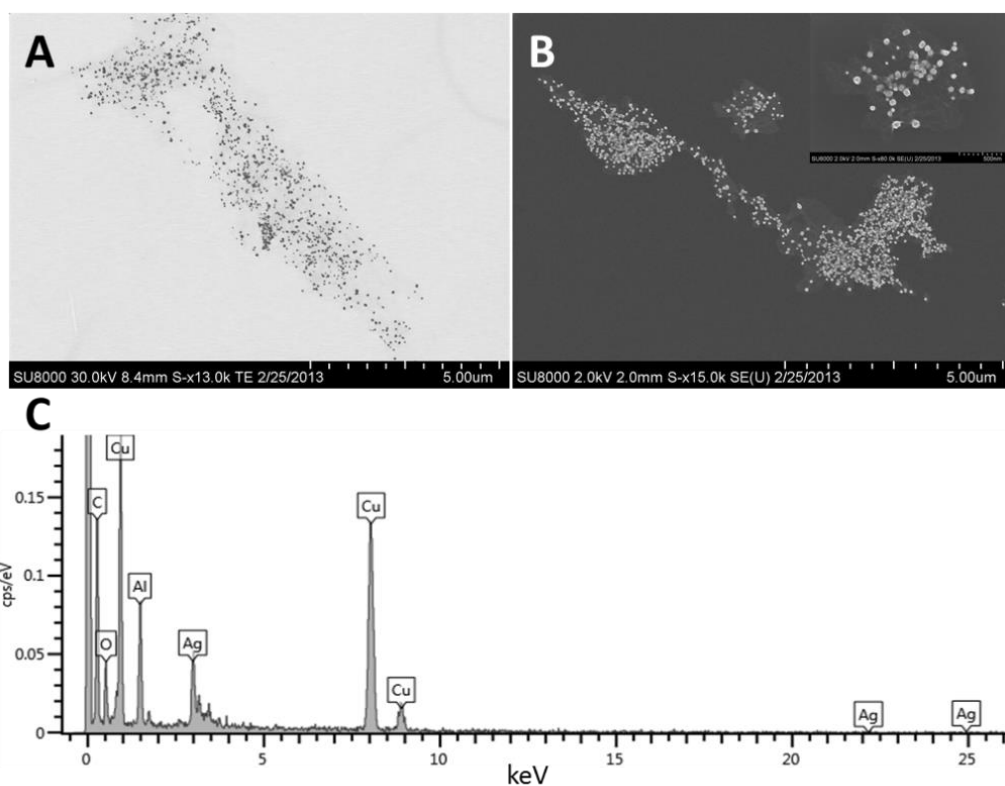


Figure 48. STEM (A) and SEM (B), and EDS (C) of RGO/Ag nanocomposite.

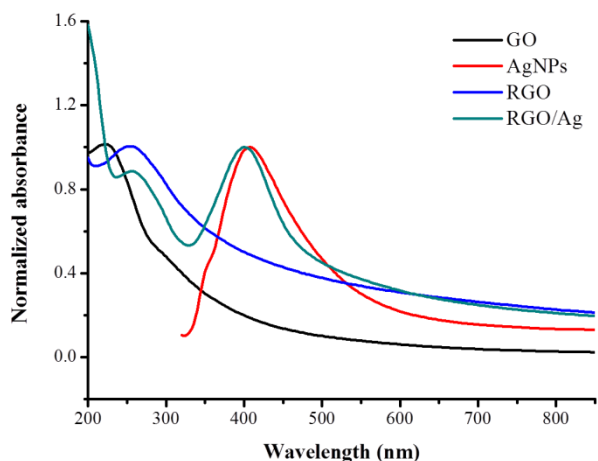


Figure 49. Absorption spectra of GO, AgNPs, RGO, RGO/Ag nanocomposite.

We further confirmed the formation of RGO/Ag nanocomposites using spectroscopic strategies. As shown in Figure 49, compared with the characteristic absorption peak of GO at 230 nm and pure silver nanoparticles at 400 nm, the RGO displayed a peak red shift to 260 nm. For RGO/Ag nanocomposites, the 260 nm absorption peak indicated the successful reduction of GO to RGO, and the 400 nm peak suggested that the silver nanoparticles were successfully deposited on the RGO sheets. During the reduction process, glucose was oxidized to gluconic acid, which may act as a stabilizer on the surface of RGO to keep the nanocomposites from aggregating. As shown in the inset of Figure 49, even one year after the synthesis, the RGO/Ag nanocomposites exhibited excellent water-dispersibility.

FTIR and XRD were used to further characterize the RGO/Ag nanocomposites. As shown in Figure 50A, compared with the curve of GO, the C=O stretching absorption band at 1725 cm^{-1} was dramatically decreased in RGO and RGO/Ag nanocomposites. Meanwhile, the C=C stretching peak at 1620 cm^{-1} increased. These changes indicated that the GO was successfully reduced during the synthesis

process. As shown in Figure 50B, the XRD pattern of RGO/Ag showed the peaks at 38.1° , 42.2° , 64.5° and 77.5° , which were the characteristic peaks of silver pattern.

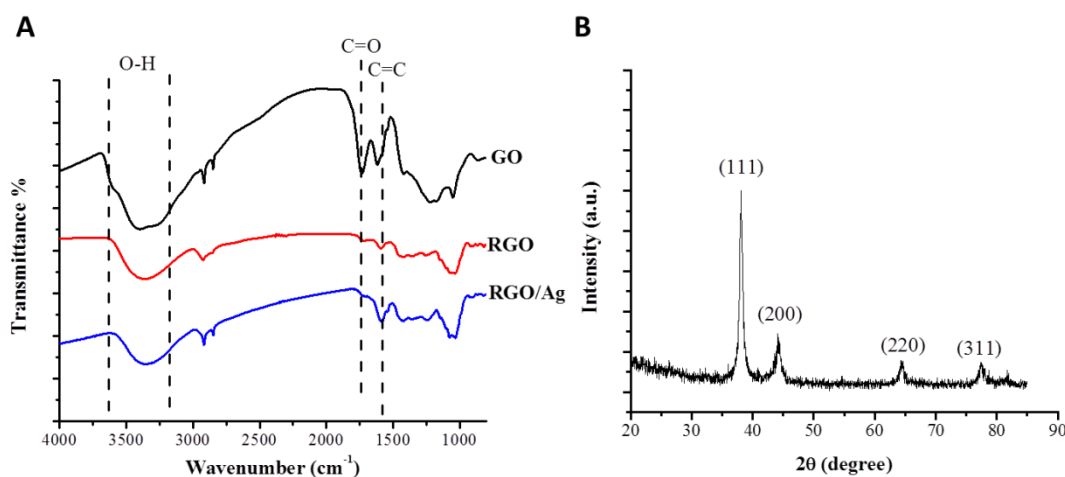


Figure 50. (A) FTIR of GO, RGO and RGO/Ag nanocomposite; (B) XRD pattern of RGO/Ag nanocomposite.

3.2. Photothermal Effect of RGO/Ag Nanocomposite.

Due to the increased absorption in the NIR region of RGO/Ag nanocomposite, the laser irradiation at 808 nm at a power density of 0.30 W/cm^2 was used to study the photothermal effect of RGO/Ag nanocomposite in solution. Four controls were used including water, GO solution, AgNPs solution and RGO solution. As shown in Figure 51, water, GO and AgNPs had virtually no change in temperature, whereas the RGO and RGO/Ag solution showed a rapid increase in temperature upon exposure to the laser in 10 min, and reached a plateau after 20 min of irradiation. With the same concentration of RGO (0.02 mg/mL), RGO/Ag nanocomposite showed a slightly higher temperature change than that of RGO solution. In addition, a larger temperature increase could be obtained by increasing the concentration of RGO/Ag nanocomposite.

These results demonstrated that the RGO/Ag nanocomposite can act as an efficient photothermal agent.

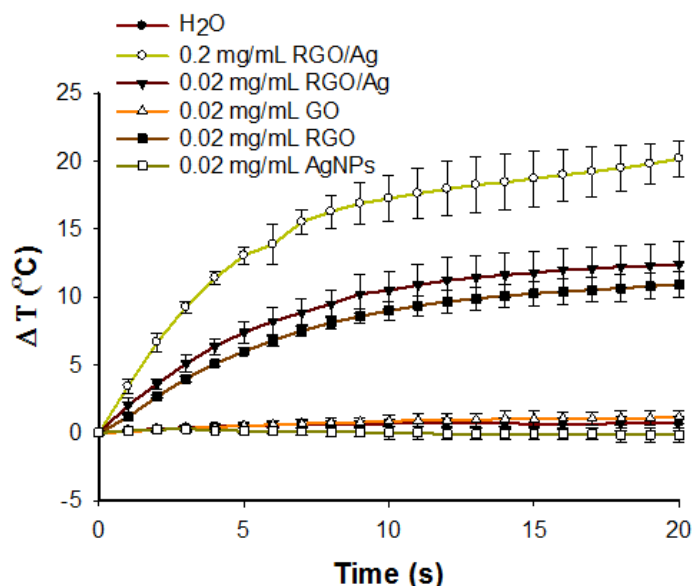


Figure 51. Temperature evolution profile of H₂O, AgNPs, GO, RGO and RGO/Ag nanocomposite upon NIR (808 nm, 0.3 W/cm²) irradiation.

3.3. Synergistically Enhanced Antibacterial Activity of RGO/Ag Nanocomposite.

In the above results, the RGO/Ag nanocomposite had efficient photothermal effect with the irradiation of 808 nm laser. Combined with the efficient antibacterial activity of silver nanoparticles, the RGO/Ag nanocomposite was expected to possess to an efficient antibacterial effect. Therefore, the synergistic antibacterial activity of RGO/Ag nanocomposite was investigated using *E. coli* and *Kp*. As shown in Figure 52A, 15 μg/mL AgNPs decreased the viabilities of *E. coli* cells to about 85 %, which indicated the intrinsic antibacterial activity of AgNPs. In the other two control groups, including GO and RGO treatment, the *E. coli* cell viabilities did not dramatically decrease without irradiation, which illustrated that the GO and RGO did not have significant impact on bacteria without the irradiation. However, when the samples were

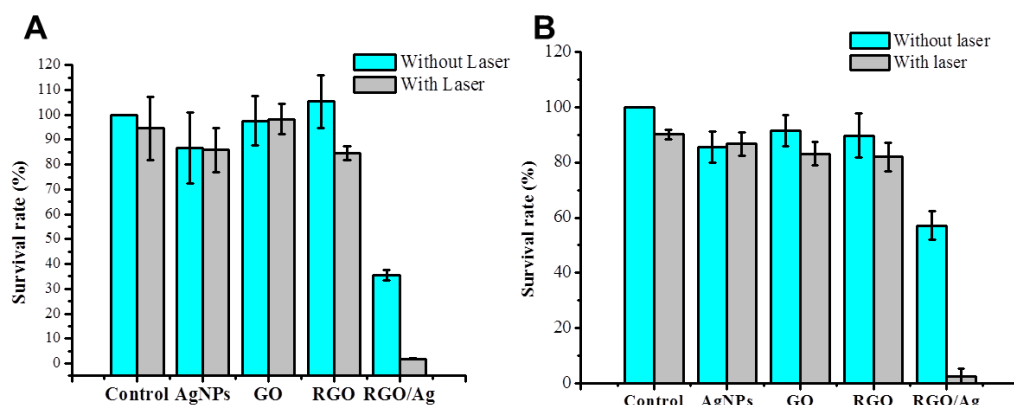


Figure 52. (A) Bacterial cell viability of *E. coli* after treatments with 15 µg/mL AgNPs, 15 µg/mL pure GO, 15 µg/mL pure RGO and 15 µg/mL RGO/Ag nanocomposite with and without NIR irradiation (808 nm, 0.3 W/cm²). (B) Bacterial cell viability of *Kp* after treatments with 30µg/mL AgNPs, 30 µg/mL pure GO, 30 µg/mL pure RGO and 30 µg/mL RGO/Ag nanocomposite with and without NIR irradiation (808 nm, 0.3 W/cm²).

treated the NIR irradiation, the photothermal effect of RGO decreased the cell viability of *E. coli* to about 84 %. In contrast, the groups treated with AgNPs and GO did not cause cell viability decrease with the NIR irradiation due to their low photothermal effect (Figure 51). However, in the group treated with RGO/Ag, the cell viability of *E. coli* decreased to about 35 % without irradiation, and the cell viability of *E. coli* was 1.8 % after 10 min irradiation. The extremely low cell viability of *E. coli* treated RGO/Ag was carried out by the combination of the intrinsic antibacterial activity of AgNPs and photothermal effect of RGO at low concentration. For the treatment of another bacterial, *Kp*, it was showed the similar results with that of *E. coli*. As shown in Figure 52B, with the same concentration at 30 µg/mL, only RGO/Ag nanocomposite killed the *Kp* cell to about 2.4 % after the irradiation. The synergistically enhanced antibacterial activity of RGO/Ag nanocomposite with NIR irradiation was clearly demonstrated.

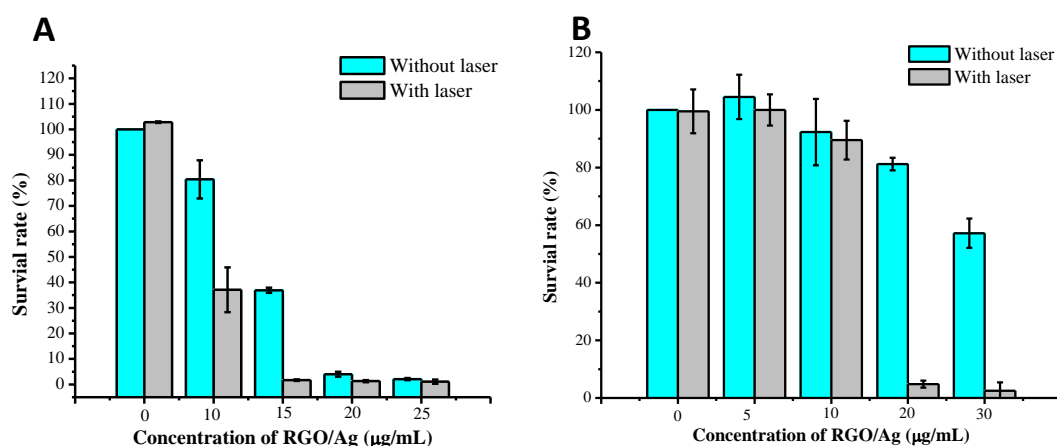


Figure 53. (A) Bacterial cell viability of *E. coli* after treatments with different concentrations of RGO/Ag nanocomposite with and without NIR irradiation (808 nm, 0.3 W/cm²). (B) Bacterial cell viability of *Kp* after treatments with different concentrations of RGO/Ag nanocomposite with and without NIR irradiation (808 nm, 0.3 W/cm²).

Then, we investigated the effect of the concentration of RGO/Ag nanocomposite on the antibacterial activity. As shown in Figure 53, with the increase of the concentration of RGO/Ag nanocomposite, the cell viability of *E. coli* and *Kp* both decreased no matter the irradiation was conducted. However, with the treatment of irradiation, the cell viability decreased faster. The IC₅₀ was estimated at about 12 and 5 μg/mL for *E. coli* without and with irradiation, respectively. Similarly, the IC₅₀ for the treatment of *Kp* was estimated at about 35 and 15 μg/mL without and with irradiation, respectively. Apparently, RGO/Ag nanocomposite exhibited a higher antibacterial activity against *E. coli* than *Kp*, indicating that the *Kp* is a hard bacterial to be removed from the infection. Furthermore, CFU counting method was used to investigate the number of viable bacterial cells after the treatment of RGO/Ag nanocomposite and irradiation. As shown in Figure 54, for both *E. coli* and *Kp* cells, nearly no bacterial colony on the LB-agar plate was formed when RGO/Ag nanocomposite and irradiation

were both treated. The groups treated with RGO/Ag nanocomposite only also decreased the colony counts, but not as low as that with irradiation at the same time. In contrast, the irradiation only has nearly no impact on the colony number.

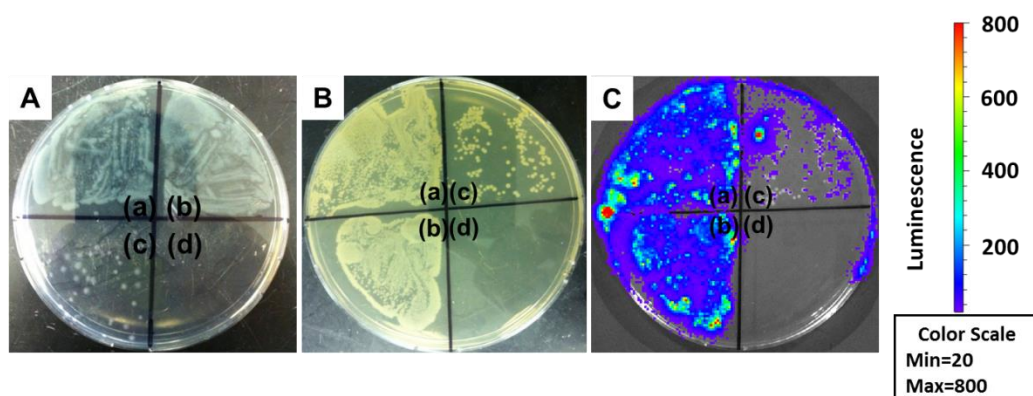


Figure 54. (A) Representing photographs of *E. coli* colonies treated with RGO/Ag nanocomposite formed on LB-agar plates. (a) control; (b) control with laser irradiation; (c) 15 $\mu\text{g/mL}$ RGO/Ag nanocomposite; (d) 15 $\mu\text{g/mL}$ RGO/Ag nanocomposite with laser irradiation. The laser irradiation was conducted under 808 nm with 0.3 W/cm^2 . Representing photographs (B) and luminescence images (C) of *Kp* colonies treated with RGO/Ag nanocomposite formed on LB-agar plates. (a) control; (b) control with laser irradiation; (c) 30 $\mu\text{g/mL}$ RGO/Ag nanocomposite; (d) 30 $\mu\text{g/mL}$ RGO/Ag nanocomposite with laser irradiation. The laser irradiation was conducted under 808 nm with 0.3 W/cm^2 .

3.4. RGO/Ag Nanocomposite Caused Cell Integrity Disruption and ROS Generation with the Irradiation.

To further explore the antibacterial mechanism of RGO/Ag with irradiation, two aspects, including cell integrity and ROS generation, were investigated using *E. coli* as a model. Two fluorescent nucleic acid dyes, DAPI and PI, were used to stain

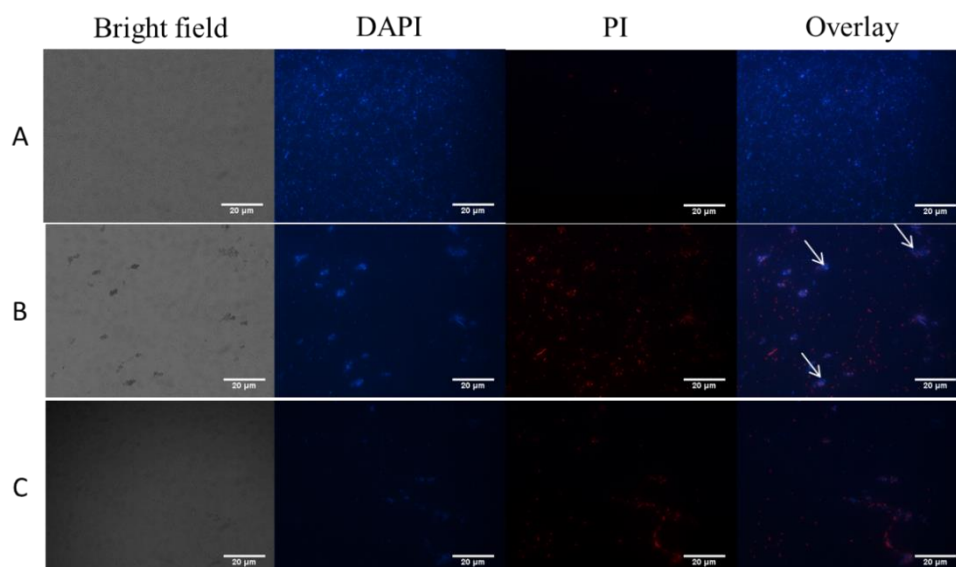


Figure 55. Fluorescence images of live and dead *E. coli* cells after incubation with 15 $\mu\text{g}/\text{mL}$ of RGO/Ag nanocomposites for 2h: (A) *E. coli* with laser treatment; (B) *E. coli* with RGO/Ag nanocomposites; (C) *E. coli* treated with RGO/Ag nanocomposite and laser irradiation. Blue fluorescence shows bacterial quasi nuclear stained with DAPI, while red fluorescence shows dead bacteria stained with PI. The scale bar is 20 μm .

the *E. coli* cells. DAPI labels all the cells, and PI can only stain the cells whose cell membranes are damaged and lost the integrity. As shown in Figure 55A, the *E. coli* cells with only irradiation treatment had few dead cells. In the group treated with RGO/Ag nanocomposite only, a large number of cells were stained by PI, but a part of accumulated cells were still stained by DAPI only (white arrow in Figure 55B). However, in the group that was treated with RGO/Ag nanocomposite and irradiation, most of the *E. coli* cells were stained by both DAPI and PI, indicating disruption of cell walls and cell membranes. Therefore, the exposure to RGO/Ag nanocomposite with/without irradiation leads to the disruption of cell integrity. The damaged

membranes were more significant when the photothermal effect of RGO/Ag nanocomposite was introduced.

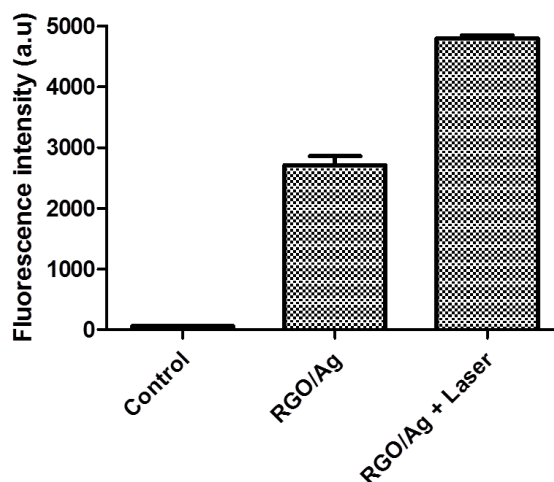


Figure 56. ROS generation of *E. coli* by the treatment of RGO/Ag nanocomposite (15 $\mu\text{g/mL}$) and 10 NIR irradiation.

Furthermore, by using H₂-DCF assay, we investigated the generation of ROS species when the RGO/Ag nanocomposite was used to treat *E. coli* with irradiation. As shown in Figure 56, compared with the control group, which the *E. coli* cells were treated with irradiation only, the fluorescent intensity significantly increased when the RGO/Ag nanocomposite was used to treat the bacteria. Moreover, when the irradiation was introduced with RGO/Ag nanocomposite, the fluorescent intensity of H₂-DCF was enhanced than that without irradiation. These results indicated that the treatment of RGO/Ag nanocomposite without/with irradiation both generated ROS species in the cells. Even though it was unclear that the generation of ROS species is direct or indirect production, the ROS species should be responsible for the antibacterial activity of RGO/Ag nanocomposite. If the ROS species was generated directly from the RGO/Ag

nanocomposite with the irradiation, the RGO/Ag nanocomposite would be potential photodynamic therapeutic agent both bacterial infection and other diseases like cancer.

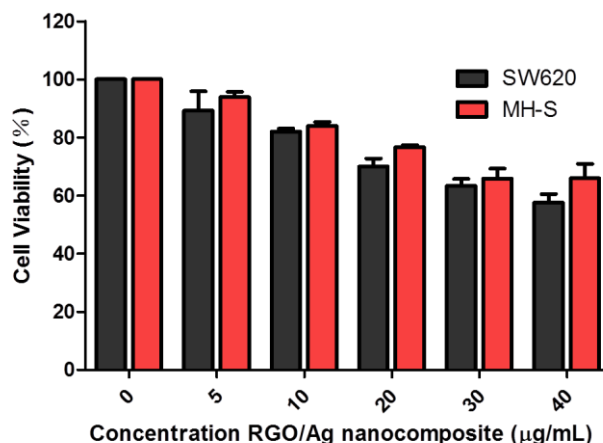


Figure 57. Relative cell viability of SW620 and MH-S after culturing with different concentrations of RGO/Ag nanocomposite varying from 0, 5, 10, 20, 30 to 40 µg/mL for 24 h at 37 °C. After the addition of MTT reagent and 4 h incubation at 37 °C, stop solution was added and followed by overnight incubation. The absorbance of each sample was recorded at 570 nm to determine the cell proliferation rate.

3.5. Cytotoxicity Investigation.

To investigate the cytotoxicity of RGO/Ag nanocomposite toward mammalian cells, two cell lines, including a macrophage cell line (MH-S) and a colon cancer cell line (SW620), were used. The cell viabilities of these cell lines treated with different concentrations of RGO/Ag nanocomposite for 24 h were investigated using MTT assay. As shown in Figure 57, after treatment of RGO/Ag nanocomposite for 24 h at 20 µg/mL, both MH-S cells and SW620 cells still have more than 75 % live cells. However, more than 98 % of *E. coli* and *Kp* were killed within 2 h followed by 10 min irradiation at the same concentration of 20 µg/mL. The viabilities of both cells retained above 60 % at higher concentrations, indicating that RGO/Ag nanocomposite may be a low cytotoxic, efficient antibacterial agent with irradiation.

4. Conclusions.

In conclusion, a facile and environmentally friendly method was introduced to prepare RGO/Ag nanocomposite using glucose as a reducing agent. With intrinsic antibacterial activity of AgNPs and photothermal effect of RGO, the RGO/Ag nanocomposite was used to kill bacterial with high efficiency. The MIC of RGO/Ag nanocomposite coupled with irradiation against *E. coli* and *Kp* were 5 $\mu\text{g/mL}$ and 10 $\mu\text{g/mL}$, respectively. The results demonstrated the the RGO/Ag nanocomposite showed better performance of bactericidal effect against *E. coli* than that toward *Kp*. Besides the photothermal effect of RGO/Ag nanocomposite, cell disruption and generation of ROS species might be other reasons for the high efficient antibacterial activity. Moreover, the RGO/Ag nanocomposite showed low cytotoxicity at the low concentrations which are sufficient for killing bacteria. Overall, the results in this work combined the intrinsic antibacterial activity of AgNPs and photothermal effect of RGO to construct an enhanced synergetic antibacterial agent that has potential to be used in industry and clinic.

CHAPTER VII

LONG RANGE FLUORESCENCE QUENCHING OF GRAPHENE OXIDE WITH RIGID SILICA SHELL AS TUNABLE SPACER

1. Introduction.

Graphene, the novel two-dimensional carbon nanomaterial, has attracted tremendous research interest due to its excellent optical, electrical, thermal, and large surface properties.^{126, 202, 220} Using the modified Hummer's method, graphene oxide (GO) can be easily produced and scaled up.²²¹ GO possesses unique optical properties compared to the pristine graphene, due to the destruction of the sp^2 carbon structure. The band-zero graphene generates adjustable band-gaps in GO, making them suitable for fluorescence imaging and construction of optical devices.²²²⁻²²⁴ In addition, oxygen-containing groups, such as carboxyl and hydroxyl groups provide the high aqueous solubility and active sites for further modification.¹⁹⁹ Furthermore, it has been reported that GO is also excellent quencher for fluorophores and quantum dots.^{100, 225-229} It has been widely used for the fabrication of fluorescent biosensors based on their quenching ability.^{127, 230, 231} Through π - π stacking, single-stranded DNA (ssDNA) modified with fluorophore can be absorbed onto the surface of GO, leading to the fluorescence quenching. When the ssDNA forms double-stranded DNA (dsDNA) or well-folded structures, the distance between the fluorophore and GO surface will be

increased to restore fluorescence emission.^{203, 232} This strategy has been used for sensitive detection of nucleic acids, proteins, small molecules and metal ions.^{204, 233-237} Therefore, sophisticated design of biosensors and bioimaging agents using GO would be dramatically improved by the fundamental investigation of the quenching ability of GO to fluorophores. However, the quenching mechanism of GO has been rarely reported.

Theoretically, the energy transfer rate from fluorophore to GO was dependent on the distance between the donor and acceptor followed a d^{-4} dependency.²³⁸ In contrast to the traditional FRET process with d^{-6} dependency,²³⁹ the quenching ability of GO should be better than traditional quencher. Recently, Huang *et al.*²⁴⁰ and Piao *et al.*²⁴¹ investigated the quenching ability of GO to fluorophores of FAM and Cy3.5, respectively. DNA strands were used to separate the fluorophores and GO in these two works with variations in the length of DNA strands and the formation of dsDNA strands. The Förster distance (d_0), which was defined as the distance for 50 % quenching, was found as 7.5 ± 0.6 nm in Huang's work.²⁴⁰ However, in these two works, DNA strands were chosen for the distance spacer, which led to a serious limitation. Due to the flexibility of DNA strands, even in the dsDNA format, they may have leaned at an angle to the surface of GO. The distance calculation through counting bases in DNA might cause the miscalculation because of the assumption that these DNA strands were perpendicular to the surface of GO. For instance, Piao *et al.* reported the quenching efficiency of GO increased after 13 bases, which implied the bended

structure of dsDNA. Therefore, a better model is necessary for more precious investigation of the quenching ability of GO to fluorophores.

Herein, we demonstrated that a rigid spacer can be used to better understand the quenching ability of GO. As we reported before, silica is an inert rigid structure that can be used to separate the fluorophores and gold nanoparticles in the investigation of the metal-enhanced fluorescence.^{242, 243} Therefore, by coating different thicknesses of silica spacers on the fluorophores, the quenching ability of GO to fluorophores can be delicately measured in this model.

2. Methods and Materials.

2.1. Materials and Instruments.

Single Layer Graphene oxide (GO) was purchased from Cheap Tubes Inc., VT. Tris(bipyridine)ruthenium(II) chloride (Rubpy), 1-Hexanol (99+ %), Tetraethylorthosilicate (TEOS, 98%), 3-ami-nopropyltriethoxysilane (APTES, 95%) were purchased from Sigma-Aldrich. Ammonium hydroxide (28.0% – 30.0%), cyclohexane (HPLC grade), and ethanol were obtained from Fisher Scientific Co. Carboxytetramethylrhodamine-succinimidyl ester (TAMRA-SE) was purchased from Molecular Probes. Deionized (DI) water (Millipore Milli-Q grade) with resistivity of 18.2 M Ω •cm was used in all experiments.

A Hitachi SU8010 field emission scanning electron microscope was used to take the SEM images of the composite of silica nanoparticles and graphene oxide. A Hitachi 7500 transmission electron microscope (TEM) was used to take the images and measure the diameters of silica nanoparticles. UV-vis absorption spectra were recorded

with a Lambda 1050 UV/VIS/NIR spectrometer. A Jobin Yvon Horiba Fluorolog spectrofluorometer was employed for fluorescence intensity measurements. Zeta potential was detected using a Zetasizer (Malvern, model of Nano-ZS). An Eppendorf 5810 R centrifuge was used to wash silica nanoparticles.

2.2. Synthesis of SiNPs@TAMRA.

First, the SiNPs cores were synthesized using the reverse microemulsion method. Briefly, 7.5 mL cyclohexane, 1.6 mL 1-hexanol, 1.8 mL Triton X-100, and 0.48 mL H₂O were mixed with vigorous stirring. After stirring for 15 min, 100 μ L NH₄OH was added followed by the addition of 400 μ L TEOS to initiate the formation of silica nanoparticles. After 30 min, 80 μ L APTES was injected to co-polymerize with the TEOS to provide amino groups on the surface of SiNPs. The reaction was allowed to proceed overnight and was followed up with ethanol and water washes. Finally, the formed SiNPs with amino groups were dispersed in 20 mL water with concentration of 4 mg/mL. For conjugating TAMRA onto the surface of SiNPs, 20 mL of 4 mg/mL SiNPs was mixed with 0.5 mL TAMRA-SE and allowed to conjugate overnight. The SiNPs@TAMRA was then washed with water three times to obtain 4 mg/mL SiNPs@TAMRA dispersed in water.

2.3. Formation of SiNPs@TAMRA@Si-NH₂.

To coat a layer of silica on the surface of SiNPs@TAMRA with different thicknesses, the modified Stöber method was used. Briefly, 10 mL EtOH, 0.2 mL of 4 mg/mL SiNPs@TAMRA prepared in the previous step, 0.18 mL water, 0.5 mL NH₄OH, and different amounts of TEOS, ranging from 0.3, 0.6, 1.0, 2.0, 3.0, 4.0, 5.0,

7.5, and 10.0 μL , were stirred together for 2 hours. Then 0.15, 0.30, 0.50, 1.00, 1.50, 2.00, 2.50, 3.25, and 7.5 μL APTES was added into the mixture to modify amino groups on the surface of silica shell. After 0.5 hour, EtOH and water were used to wash the SiNPs@TAMRA@Si-NH₂ via centrifuge.

2.4. Formation of SiNPs@Rubpy@Si-NH₂.

First, the SiNPs cores were synthesized using the reverse microemulsion method as previously mentioned. Then, a silica coating process coupled with Rubpy doping was carried out by the modified Stöber method. Briefly, 10 mL EtOH, 2 mL of 4 mg/mL SiNPs prepared in the previous step, 0.5 mL NH₄OH, 1 mL 0.1 M Rubpy solution and 20 μL TEOS were mixed to start the doping of Rubpy into the silica shell. Furthermore, to adjust the distance between the Rubpy and GO, different thicknesses of silica shell were generated by a similar process to section 2.3 of altering the amount of the TEOS and APTES during the coating process.

2.5. Fluorescence Quenching Investigation.

The experiment was carried out on a Jobin Yvon Horiba Fluorolog spectrofluorometer. Briefly, 100 μL , SiNPs@TAMRA@Si-NH₂ (*equi* 0.1 nM TAMRA) solution was placed in a quartz cuvette for the fluorescence measurement. The excitation wavelength was set at 540 nm. The fluorescence spectrum was recorded from 560 nm to 650 nm. The slits for excitation and emission were set at 5 nm. After the recording of the origin fluorescence spectrum of SiNPs@TAMRA@Si-NH₂, 1 μL of 5 mg/mL GO was added into the solution and mixed using pipette. The fluorescence spectrum was measured 2 min later to investigate the quenching ability.

2.6. Fluorescence Lifetime Measurement.

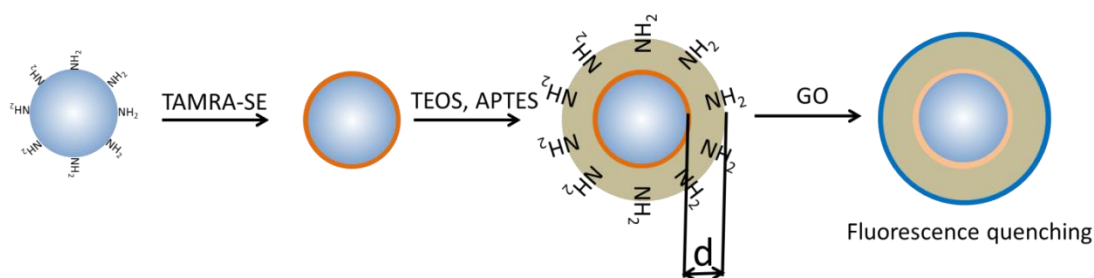
100 μ L of SiNPs@TAMRA@Si-NH₂ (*equi* 0.1 nM TAMRA) solution was loaded into a quartz cuvette for lifetime measurement. The fluorescence lifetime was collected using a Jobin Yvon Horiba Fluorolog spectrofluorometer equipped with LED laser. The LED laser light source at 494 nm was used for the excitation. The emission data was collected at 575 nm with an 8 nm slit.

3. Results and Discussion.

3.1. Design of SiNPs@TAMRA@Si-NH₂ Wrapped with GO.

The fluorescence quenching ability of GO has been widely used for the fabrication of sensitive biosensors and bioimaging agents. However, the fundamental investigation of GO quenching ability was poorly elucidated by two recently works which used flexible DNA strands as the spacer. Herein, we designed a rigid spacer between GO and fluorophores, which would diminish the effect of inaccurate distance calculation with the DNA strands spacer. In our previous study, rigid silica shell was used to investigate the fluorescence enhancement effect of gold nanoparticles by adjusting the distance between gold nanoparticles and fluorophores. Therefore, we used the silica shell as a spacer between fluorophores and GO in this work to investigate the quenching ability of GO. Silica shell is used because of its inert nature, which does not change the interaction between the fluorophores and the investigated nanomaterials. As shown in Scheme 4, amino group modified silica nanoparticles (SiNPs) was synthesized firstly using the reverse micro-emulsion method. Then, a fluorophore, named TAMRA-SE was conjugated to the SiNPs through the interaction of amino

groups and succinimidyl ester group. Therefore, SiNPs@TAMRA was therefore formed without any silica shell coating. In order to adjust the distance between TAMRA and GO in the following steps, a silica shell was coated using the Stöber method. In this coating process, APTES was added to co-polymerization with TEOS to form amino groups on the surface of final nanoparticles (SiNPs@TAMRA@Si-NH₂). The thickness (d) of the silica shell was controlled by the amount of TEOS and APTES. With addition of GO to the solution of SiNPs@TAMRA@Si-NH₂, GO would wrap the positively charged SiNPs@TAMRA@Si-NH₂ through electrostatic interaction and thereby to quench the fluorescence of TAMRA with distance dependence.



Scheme 4. Schematic of synthesis of SiNPs@TAMRA@Si-NH₂ nanocomposite and investigation of fluorescence quenching ability of GO to TAMRA with distance (d) dependent.

3.2. Characterization of GO.

GO was purchased from the commercial company and dispersed into water through 2 hours ultrasonic treatment to obtain the stable solution (5 mg/mL). The SEM and STEM in Figure 58A and 58B show that the GO sheet size is in the micrometers range. As shown in Figure 58A, the wrinkles of GO were clearly observed from the SEM image. The large size and flexibility of GO sheet ensured the ability of the GO to wrap the silica nanoparticles through electrostatic binding force. Figure 58C

demonstrated the UV-vis absorption spectrum of GO solution. The strong peak at *ca.* 230 nm was due to the π -plasmon of the sp^2 carbon structure and the shoulder around 300 nm was ascribed to the n to π^* transitions.

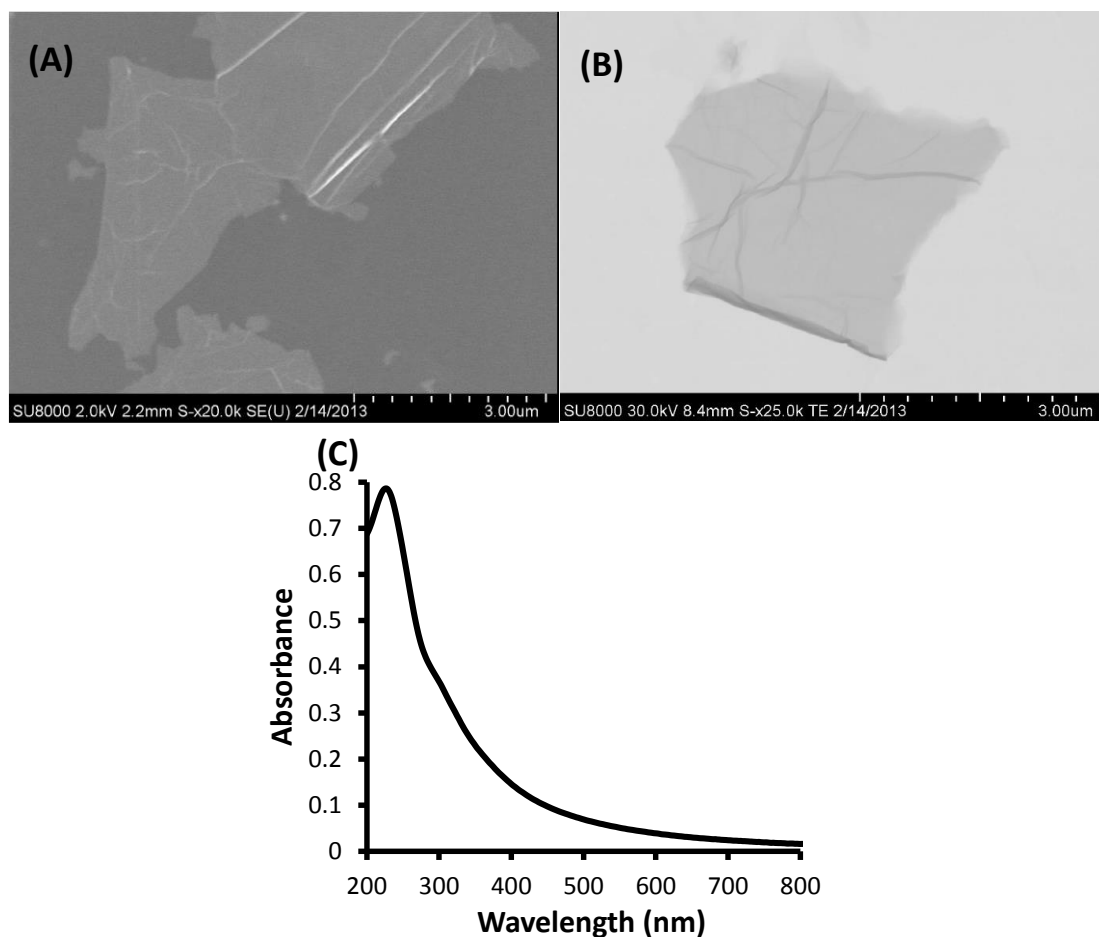


Figure 58. SEM (A), STEM (B) images and absorption spectrum (C) of GO.

3.3. Fluorescence Quenching of GO to SiNPs@TAMRA@Si-NH₂.

Graphene oxide was reported to quench several fluorescent dyes, from visible to near-infrared region. Therefore, it is useful for the fabrication of fluorescent biosensors. We initially investigated the quenching ability of GO to the TAMRA conjugated on the surface of amino groups modified silica nanoparticles (SiNPs@TAMRA). As shown in Figure 59A, the shape of absorption spectra of

SiNPs@TAMRA before (curve a) and after (curve b) incubation with GO are similar to each other. The only difference was the intensity of the two curves, which resulted from the addition of GO. However, after the addition of GO to SiNPs@TAMRA, the fluorescence intensity of TAMRA was almost quenched ($\sim 93.4\%$) (Figure 59B). To investigate the mechanism of the fluorescence quenching property of GO, the lifetimes of SiNPs@TAMRA before and after addition of GO were measured. As shown in Figure 59C, the lifetime of SiNPs@TAMRA decreased from 2.12 ± 0.02 ns to 0.20 ± 0.02 ns. The quenching efficiency was found to be 90.6% calculated from the lifetime change using $Q = 1 - \tau/\tau_0$, where τ_0 and τ are the lifetimes of SiNPs@TAMRA without and with addition of GO, respectively. The close value of quenching efficiencies calculated from the total fluorescence intensity and lifetimes indicated that the main quenching mechanism of GO to TAMRA was dynamic quenching. Meanwhile, the similar absorption spectra pattern also supported this point. Due to the electrostatic interaction between the positive charged SiNPs@TAMRA and negative charged GO, GO should have adsorbed onto the surface of SiNPs@TAMRA once they were mixed together. Therefore, TEM and SEM images were used to demonstrate the interaction between GO and SiNPs@TAMRA. As shown in Figure 59D, the wrinkles on the edges of SiNPs@TAMRA (white arrow) clearly indicated the totally coverage of the GO on the SiNPs@TAMRA. The distance between TAMRA and GO was estimated as 0 nm because the TAMRA was covalently conjugated onto the surface SiNPs and the GO was compactly wrapped on the surface of SiNPs through amino groups.

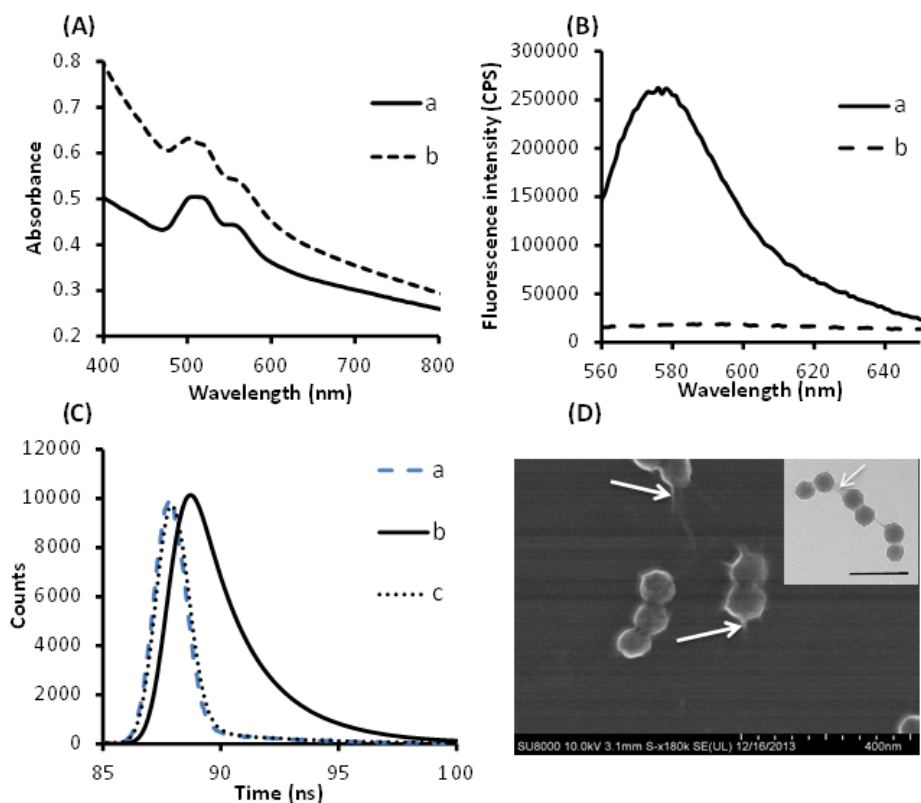


Figure 59. Absorption (A) fluorescence (B) spectra of SiNPs@TAMRA without (a) and with (b) GO. $\lambda_{\text{ex}} = 540 \text{ nm}$. (C) Lifetime measurements of SiNPs@TAMRA without (b) and with (c) GO. Curve a is the reference. 492 nm LED laser was used in the lifetime measurement. (D) SEM image of SiNPs@TAMRA with GO. Inset is TEM image of SiNPs@TAMRA with GO, bar is 200 nm. The white arrows indicate the wrinkle of GO wrapped on the surface of nanoparticles.

To find the maximum quenching efficiency of GO with SiNPs@TAMRA, we measured the fluorescence of SiNPs@TAMRA with different concentrations of GO. As shown in Figure 60, the fluorescence intensity of SiNPs@TAMRA decreased with the increase of the concentration of GO. The quenching efficiency reached a plateau after 10 $\mu\text{g/mL}$. Therefore, we chose 50 $\mu\text{g/mL}$ GO for the following experiment to ensure that the quenching efficiency was only related to the distance between TAMRA and GO but not to the concentration of GO.

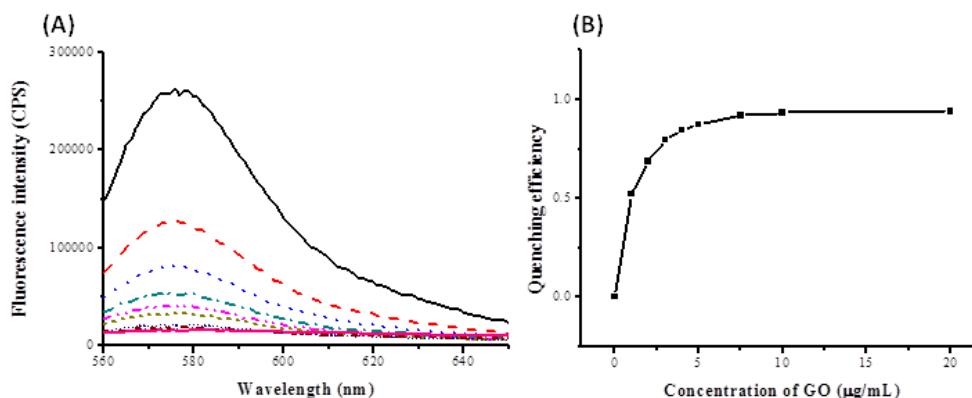


Figure 60. Fluorescence quenching of SiNPs@TAMRA with different concentration of GO. (A) Fluorescence spectra of SiNPs@TAMRA with different concentrations of GO. From top to bottom: 0, 1.0, 2.0, 3.0, 4.0, 5.0, 7.5, 10.0 and 20.0 $\mu\text{g/mL}$. (B) Quenching efficiency GO to SiNPs@TAMRA with different concentrations. $\lambda_{\text{ex}} = 540 \text{ nm}$; $\lambda_{\text{em}} = 575 \text{ nm}$.

Afterward, the distance between TAMRA and GO was adjusted by the silica shell thickness. As shown in Figure 61, the different thicknesses of silica shell were coated on the surface of SiNPs@TAMRA using the Stöber method through changing the amount of TESO and APTES. The sizes of the resulting nanoparticles were measured by TEM. The distance between TAMRA and GO was calculated by subtracting the radius of the SiNPs@TAMRA from SiNPs@TAMRA@Si-NH₂. With the increase in the amount of TEOS, the distances were calculated as 0.3, 1.2, 6.5, 14.7, and 34.5 nm. Meanwhile, the amino group modified on the outside surface of the silica nanoparticles ensured the positive charge that can be adsorbed with GO. After introduction of 50 $\mu\text{g/mL}$ GO, the fluorescence intensity of TAMRA in silica nanoparticles was quenched. With the increase of the thickness of the silica shell, the quenching efficiency decreased. As shown in Figure 62, the distance between TAMRA and GO was larger than 30 nm and the quenching efficiency of GO was still around 30 %, which indicated the long-distance quenching ability of GO.

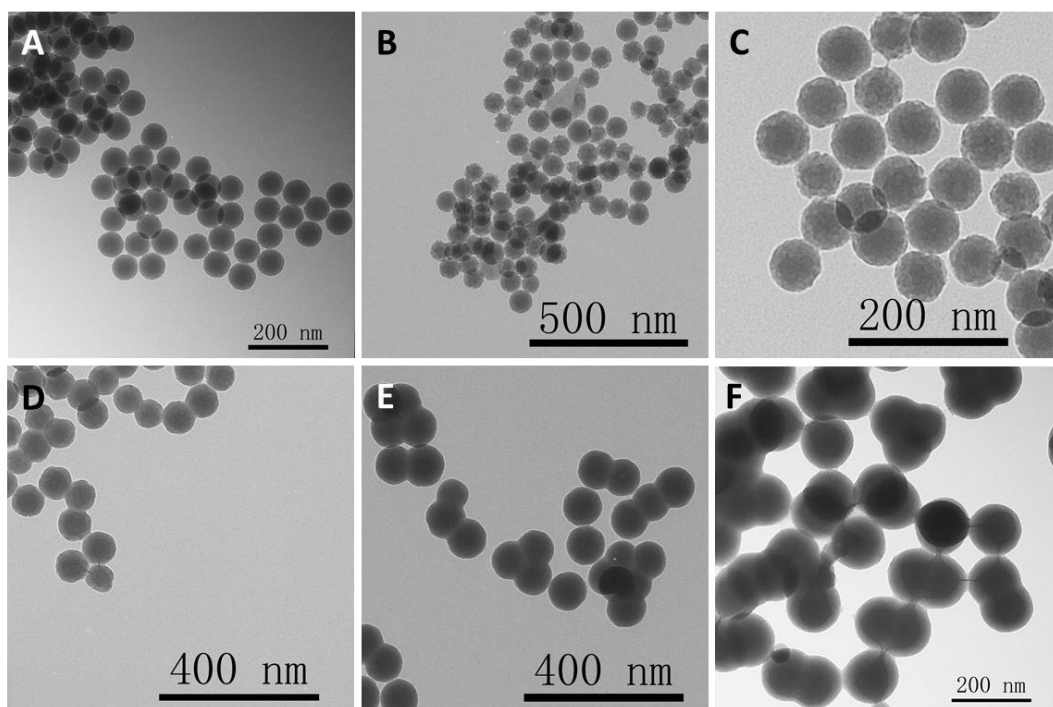


Figure 61. TEM images of SiNPs@TAMRA@Si-NH₂ with different thickness of 0, 0.3, 1.2, 6.5, 14.7, and 34.5 nm (A to F).

According to the theoretical calculations of the quenching effect of graphene, it showed a relationship of $Q = 1/[1 + (\frac{d}{d_0})^4]$, where d is the distance between graphene fluorophore and d_0 was the characteristic distance. The d_0 is reported different from each other regarding the various systems, ranging from ~ 5 to 8 nm.^{240, 244} By measuring the quenching efficiency of our TAMRA-GO system, the GO quenched the $\sim 50\%$ of TAMRA fluorescence when the silica thickness was ~ 6.54 nm (Figure 62). This concluded that the d_0 for TAMRA-GO system was about 6.54 nm.

The quenching efficiency calculated from the steady-state fluorescence reflected the total quenching, including static and dynamic components. We then measured the lifetime of TAMRA when GO was presented to quench the fluorescence. The quenching efficiency was calculated by $Q = 1 - \tau/\tau_0$, where τ_0 is the lifetime of TAMRA in the absence of GO, and τ is the lifetime of TAMRA in the presence of GO.

As shown in Figure 62B, the quenching efficiency calculated from lifetime was also plotted with the thickness of silica shell. As expected, it decreased with the increase of the thickness of silica shell. The quenching efficiencies obtained from these two methods were similar with each other, indicating that the main quenching mechanism was dynamic quenching.

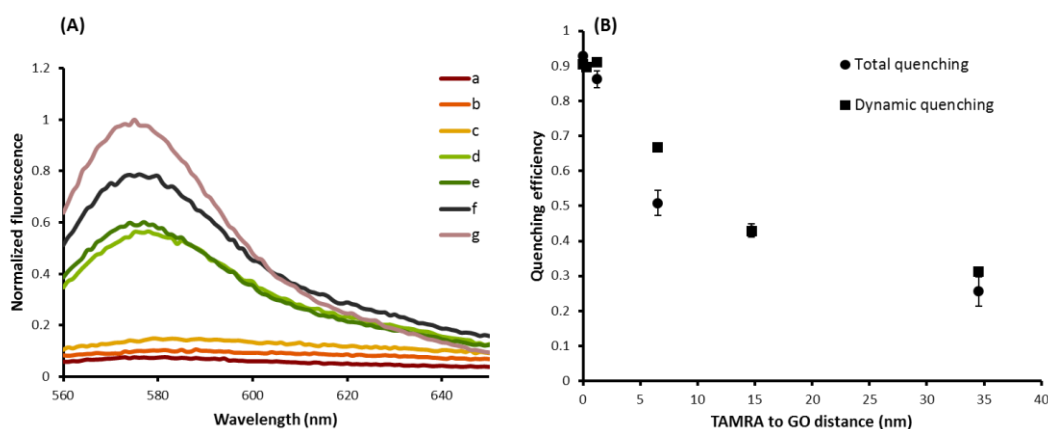


Figure 62. (A) Fluorescence spectra of SiNPs@TAMRA@Si-NH₂ with GO. The distances between TAMRA and GO were 0, 0.3, 1.2, 6.5, 14.7, 34.5 nm (curve a to f). Curve g was SiNPs@TAMRA without addition of GO. (B) Quenching efficiency of the doped TAMRA as a function of the distance. The quenching efficiency was calculated based on average fluorescence lifetime (squares) and from steady-state fluorescence intensity (circles). The concentrations of nanoparticles were equi *ca* 0.1 nM of TAMRA. $\lambda_{\text{ex}} = 540 \text{ nm}$; $\lambda_{\text{em}} = 575 \text{ nm}$.

3.4. Fluorescence Quenching of GO to SiNPs@Rubpy@Si-NH₂.

To investigate the universal quenching ability of GO, we changed the fluorophore from TAMRA to Rubpy, which is another useful dye with the emission of 600 nm. Instead of the covalent conjugation between amino groups on silica nanoparticles and TAMRA, the Rubpy was doped into a thin layer of

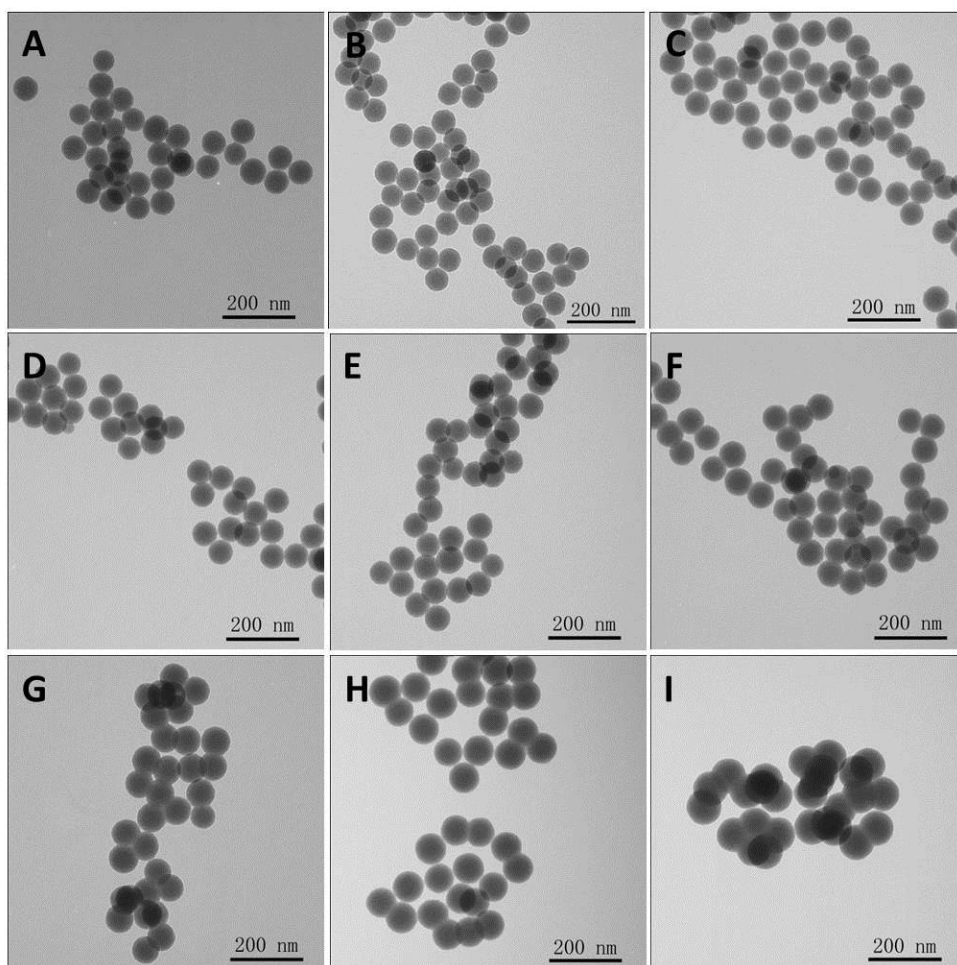


Figure 63. TEM images of SiNPs (A), SiNPs@Rubpy (B), and SiNPs@Rubpy@Si-NH₂ with different thicknesses of 2.4, 3.0, 3.7, 4.8, 7.8, 10.1, and 15.6 nm (C to I).

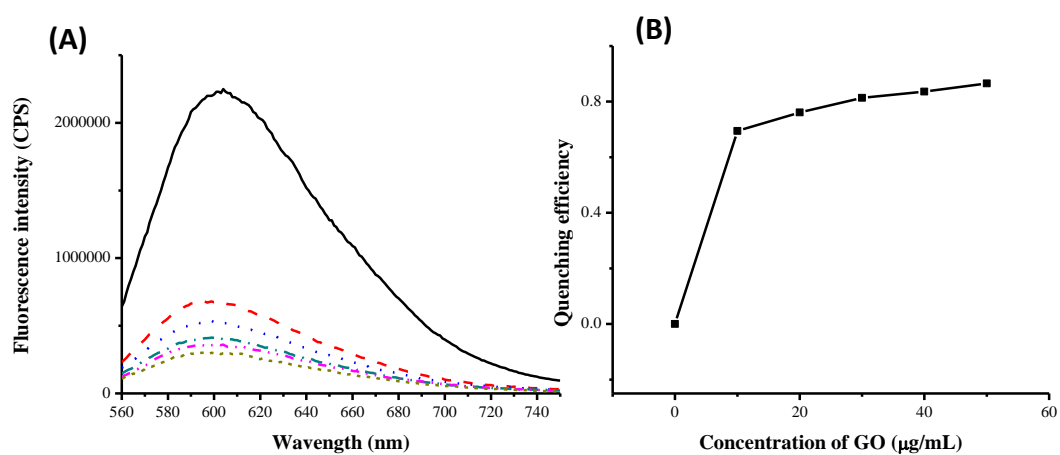


Figure 64. Fluorescence quenching of SiNPs@Rubpy with different concentrations of GO. (A) Fluorescence spectra of SiNPs@ RuBpy with different concentrations of GO. From top to bottom: 0, 10, 20, 30, 40 and 50 µg/mL. (B) Quenching efficiency GO to SiNPs@ RuBpy@Si-NH₂ with different concentrations. $\lambda_{\text{ex}} = 460 \text{ nm}$; $\lambda_{\text{em}} = 600 \text{ nm}$.

silica shell (SiNPs@Rubpy). Then, another layer of pure silica shell was coated on the surface of Rubpy-doped silica nanoparticles and followed with the modification of amino groups (SiNPs@Rubpy@Si-NH₂). The distance between Rubpy and GO was calculated by subtracting the radius of SiNPs@Rubpy@Si-NH₂ by the radius of SiNPs@Rubpy. The distances were obtained from 2.4, 3.0, 3.7, 4.8, 7.8, 10.1, to 15.6 nm (Figure 63). We first investigated the quenching efficiency of GO to SiNPs@Rubpy with different concentrations (Figure 64). As the concentration of GO increased, the fluorescence intensity of Rubpy at 600 nm decreased and reached a plateau when the concentration of GO was 50 μg/mL. Therefore, we chose 50 μg/mL of GO for the following quenching efficiency investigation. As shown in Figure 65A, by increasing the distance between Rubpy and GO, the fluorescence intensity of Rubpy recovered from the quenching state. The quenching efficiency calculated from the steady-state fluorescence intensity was plot with the distance (Figure 65B). It followed the similar trends as that of the TAMRA nanoparticles. The characteristic distance was evaluated around 5.0 nm smaller than that of the TAMRA, when the quenching efficiency was 50%. The lifetime of Rubpy was dramatically decreased when it was doped into the thin layer of silica shell, which was out of our detection limit of the instrument. Therefore, the dynamic quenching mode was not investigated. Overall, the GO can quench the fluorescence of Rubpy with a distance-dependent manner.

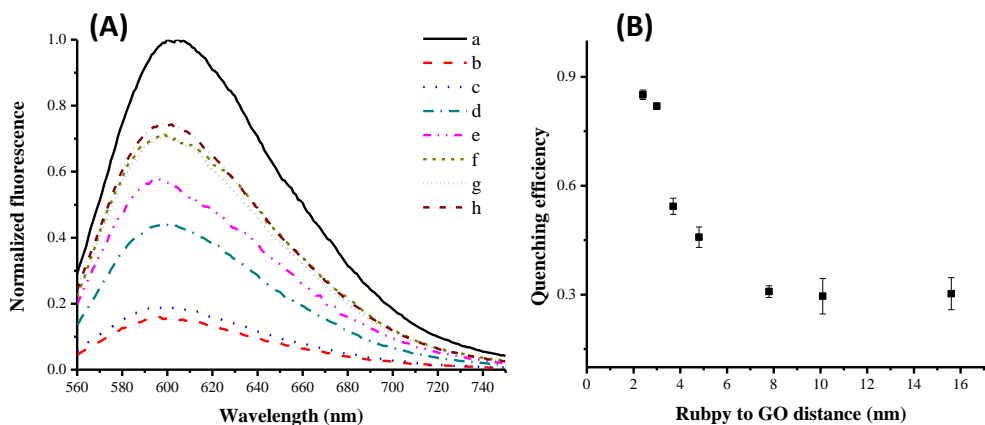


Figure 65. (A) Fluorescence spectra of SiNPs@Rubpy (a) and SiNPs@Rubpy@Si-NH₂ with 50 µg/mL GO. The distances between Rubpy and GO were separated by 2.4, 3.0, 3.7, 4.8, 7.8, 10.1, and 15.6 nm silica space (curve b to h). (B) Quenching efficiency of the doped Rubpy as a function of the distance. The concentrations of nanoparticles were equi *ca* 0.1 nM of Rubpy. $\lambda_{\text{ex}} = 460$ nm; $\lambda_{\text{em}} = 600$ nm.

4. Conclusions.

In conclusion, we have demonstrated the quenching ability of GO with two different fluorophores, TAMRA and Rubpy. The distance between the fluorophore and GO was adjusted by a rigid silica layer, which is more accurate than soft DNA strands. The quenching efficiency of GO to these two fluorophores followed a distance-dependence with characteristic distance of 6.54 and 5.0 nm, respectively. By comparing the steady-state total quenching efficiency and dynamic quenching efficiency of GO to TAMRA, we found that the main quenching mechanism was dynamic quenching. Moreover, the quenching range of GO with these fluorophores was much greater than the traditional FRET distance (10 nm). By exposing the long-range quenching properties of GO to fluorophores, we further promoted applications of GO in analytical and biomedical probes design as a carrier and fluorescence quencher.

CHAPTER VIII

GRAPHENE OXIDE KILLS KLEBSIELLA PNEUMONIA BACTERIUM IN MACROPHAGES AND IN MICE

1. Introduction

Due to the excessive use of antibiotics in the last century, super bacteria which are resistant to those antibiotics can cause serious problems in the hospital.²⁴⁵ For instance, *Klebsiella pneumoniae* (*Kp*), which is a clinical pneumococcus, continuously acquires carbapenem-resistant properties due to the wide usage of carbon penicillin antibiotics in hospitals.^{246, 247} Further, *Kp* can easily infect patients who have pre-conditions, including cystic fibrosis, asthma and emphysema.²⁴⁷ Therefore, it is urgent to develop effective new antibiotics and/or therapeutic agents to fight against the multiple-drug-resistant (MDR) bacteria.²⁴⁸ Recently, a variety of antibacterial nanomaterials have attracted attention.²⁴⁹⁻²⁵¹ The antibacterial mechanisms of nanomaterials may be different from those of conventional antibiotics and can be used as auxiliary or alternative strategy to facilitate therapy of MDR bacterial infection.^{252, 253} For example, silver nanoparticles have been reported to efficiently kill bacteria and have already entered the market.²⁵³⁻²⁵⁵ More recently, graphene, a 2-dimensional carbon nanomaterial, has shown great potential as an antibacterial agent.²⁵⁶⁻²⁵⁸

Graphene has been tested for several fields owing to its large surface area as well as excellent mechanical, electronic, and optical properties.^{199, 220} In biomedical fields, graphene-derivatives, including graphene oxide (GO), reduced graphene oxide (rGO), graphene quantum dots (GQDs) and graphene-based nanocomposites, have been widely examined for applicability in biosensors,^{233, 259} bioimaging,^{145, 205, 260} drug delivery,^{209, 215} and photothermal therapy.^{146, 201, 261} Meanwhile, graphene-derivatives can be used for killing bacteria. For example, graphene oxide and reduced graphene oxide showed toxicity to both Gram-positive and Gram-negative bacteria.^{256, 257} The contact of graphene derivatives with cell membrane caused direct damage to bacteria because of their extremely sharp edges. Liu *et al.* compared the antibacterial properties of four different carbon materials, including graphite, graphite oxide, GO and rGO.¹⁹¹ They found that GO possessed the highest antibacterial activity while graphite oxide exhibited the lowest antibacterial activity. Meanwhile, a three-step antimicrobial mechanism was proposed for graphene-based materials, which are also applicable for carbon nanotubes. Moreover, the lateral size of GO affected the antibacterial activity.²⁶² The larger GO sheets resulted in stronger antibacterial activity than that of the smaller one, as the larger GO sheets could effectively isolate bacterial from environment by wrapping the whole bacterium. Recently, the photothermal and photodynamic effects of graphene-based nanomaterials were also used to kill bacteria through different pathways.^{193, 263} However, all these studies just conducted the antibacterial activity investigation at the bacterial level, which is based on the common bacteria such as *Escherichia coli* and *Staphylococcus aureus* by evaluating their

viability. The impact on infection ability of the bacteria treated by GO was not tested. Meanwhile, the clinical MDR bacteria were seldom used for evaluating the antibacterial activity of these nanomaterials.

In this work, we used the MDR bacterium, *Kp*, as a model to investigate the antibacterial activity of GO. The invasive potency of *Kp* after treatment with GO was investigated in both cell culture and animal models. The results indicated that the *Kp* treated with GO was effectively killed and the infection ability was dramatically inhibited in cell culture and animals. To our knowledge, this is the first report studying the antibacterial property of GO *in vivo* with a MDR bacterium.

2. Methods and Materials.

2.1 Materials and Instruments.

GO was purchased from Cheap Tubes Inc. (Grafton, VT). Phosphate buffered saline tablets and fetal bovine serum were purchased from Fisher Scientific (Waltham, MA). Deionized (DI) water (Millipore Milli-Q grade) with resistivity of 18.2 M Ω •cm was used in all experiments. C57BL/6J mice were purchased from Charles River (San Diego, CA). *Kp* Xen-39 (ATCC 93A 5370), a bioluminescent pathogenic bacterium strain expressing LUC bioluminescence was purchased from Caliper (Santa Clara, CA). *Kp* (ATCC 43816 serotype II) was obtained from Dr. Virginia Miller (University of North Carolina). *Kp* Xen-39 (ATCC 93A 5370) was used in the bioluminescence imaging experiment and *Kp* (ATCC 43816 serotype II) was used for other infection of mice. *Pseudomonas aeruginosa* (Pa) WT PAO1 was a gift from S. Lory (Harvard

Medical School, Boston, MA). *E. coli* HB101 strain was obtained from American Tissue Culture Collection (ATCC). All of the animal experiments were approved by Institutional Animal Care and Use Committee (IACUC) at the University of North Dakota.

A Hitachi SU8010 field emission scanning electron microscope was used to capture SEM and STEM images of GO. A Zetasizer (Malvern, model of Nano-ZS, Westborough, MA) was used to measure the Zeta potential of GO. UV-vis absorption spectra were recorded with a Lambda 1050 UV/VIS/NIR spectrometer (PerkinElmer, Santa Clara, CA). Luminescence imaging was taken by Caliper's Xenogen IVIS optical imaging system (Caliper, PerkinElmer, Santa Clara, CA). The OD value at 560 nm for 3-(4,5-dimethyl-2-thiazolyl)-2,5-diphenyltetrazolium bromide (MTT) and nitroblue tetrazolium (NBT) assays was measured by a Multiskan spectrum spectrophotometer (Thermo Scientific, Waltham, MA).

2.2. Antibacterial Activity Tests.

Kp Xen-39 was cultured in Lysogeny broth (LB) medium with shaking at 37 °C overnight before use.²⁶⁴ The next day, the bacterial cells were harvested by centrifugation and dispersed in PBS with an optical density at 600 nm (OD₆₀₀) of 0.1 for a concentration of 10⁸ CFU mL⁻¹.²⁶⁵ The samples of GO in PBS were incubated with bacteria suspension for 2 h at 37 °C. Finally, 100 µL of the bacteria suspension was added into 900 µL LB medium for the growth in a shaking incubator at 37 °C overnight. The concentration of bacteria was finally determined by measuring OD₆₀₀ and the bioluminescence image was taken by IVIS optical imaging system. Meanwhile,

the plate count method was used to demonstrate the killing effect of GO. Briefly, the bacteria suspension in LB medium treated with GO was plated on LB-agar plates, and incubated at 37 °C overnight. The antibacterial activity of GO to *E. coli* and Pa was investigated similarly with *Kp* by changing the bacteria.

2.3. Cell Infection.

The log-phase *Kp* bacteria ($OD_{600} = 1.0$) was incubated with different concentrations of GO (*Kp*-GO) for 2 h in PBS at 37 °C. The same *Kp* bacteria without treatment of GO were used as a control. 0.1 mL *Kp*-GO and control *Kp* bacteria were both diluted with 0.9 mL LB medium for the incubation at 37 °C for overnight. Then, murine alveolar macrophage (MH-S) cells were infected with control *Kp* and *Kp*-GO for 8 h. MH-S cells were infected by *Kp* at MOI 10:1 bacteria-cell ratio and then washed three times with PBS to remove the floating bacteria. Bacteria on the surface of the cells were killed by adding 100 µL polymyxin B and left in incubation for another 1 h. The viability of MH-S cells after infection was determined by MTT assay.²⁶⁶ Briefly, 1 µg/ml MTT was added into each well incubated with the infected cells and incubated at 37 °C until color change.²⁶⁷ MTT was reduced to form a purple formazan product inside living cells. Afterward, stop solution was added to dissolve the formazan product, and the absorbance was quantified by measuring wavelength of 560 nm using a spectrometer plate reader.²⁶⁸

2.4. Mouse Infection.

First, the *Kp* bacteria ($OD_{600} = 0.1$) were treated with 0.25 mg/mL GO for 2 h in PBS at 37 °C. The *Kp* bacteria without treatment of GO were used as a control. For

in vivo imaging of the bioluminescent *Kp* Xen-39 in mice, 50 μ L GO treated and untreated *Kp* Xen-39 were intraperitoneally injected into two groups of mice after anesthesia with 40 mg/kg ketamine. The bioluminescence images were taken under IVIS optical imaging system at different time points from 0 to 24 h. The infection level was semiquantitatively evaluated by the bioluminescence intensity determined by the ROI calculation using the IVIS software.²⁶⁴

For further analysis of the antibacterial efficiency of GO *in vivo*, the mice anesthetized with 40 mg/kg ketamine were instilled with GO treated and untreated *Kp* by intranasal instillation, and sacrificed when they were moribund. Survival was determined using Kaplan–Meier curves. After bronchoalveolar lavage (BAL), the lung was excised for homogenization and fixed in 10% formalin for histological analysis. The formalin-fixed lung tissue was used for H&E staining to examine tissue damage post infection.

The viability of alveolar macrophages (AM) was evaluated by MTT assay. Briefly, the AM cells were obtained from mice infected with GO treated and untreated *Kp*. The AM cells in each well were mixed with 1 μ g/ml MTT and incubated at 37 $^{\circ}$ C until color change as above.²⁶⁹ The superoxide anion in AM cell after infection of *Kp* was measured by NBT assay. AM cells were grown in serum-containing medium at 37 $^{\circ}$ C for 4 h and then mixed with 1 μ g/ml NBT dye for another 1 h. 100 μ l of stop solution (10% DMSO; 10% SDS in 50 mM HEPES buffer) was added into each well to terminate the reaction. The absorbance at 560 nm was measured using the plate reader after overnight incubation at 37 $^{\circ}$ C.⁸⁸

To evaluate the infection severity of GO-treated *Kp* in mice, live *Kp* amounts in several organs, including the lung, liver, kidneys and spleen were analyzed. The organs were obtained from the different groups of mice at different time points. Then, the organs were grounded to determine the amount of intracellular bacteria through CFU. Briefly, the tissues were homogenized with PBS and spread on LB plates to enumerate level of bacteria. The plates were cultured in a 37 °C incubator overnight, and colonies were counted. Meanwhile, the amounts of myeloperoxidase (MPO) released from the four different organs were analyzed by MPO assay. Briefly, the 100 mg/ml tissue samples were homogenized in 50 mM hexadecyltrimethylammonium bromide, 50 mM KH₂PO₄, pH 6.0, 0.5 mM EDTA and centrifuged for 15 min at 12,000 rpm at 4 °C. Supernatants were decanted, and 100 µL of reaction buffer (0.167 mg/ml O-dianisidine, 50 mM KH₂PO₄, pH 6.0, 0.0005% mM H₂O₂) were added to 100 µL of sample. After 2 min, the absorbance was read at 460 nm using a spectrometer plate reader.

2.5. Statistical Analysis.

All experiments were performed in triplicate. Data were showed as mean ±SE (standard error) from the three independent experiments. All error bars stand for SE. Group means were compared using Student's t-test or one-way ANOVA, using Graphpad Prism 5 software (La Jolla, CA).

3. Results and Discussion.

3.1. Characterization of GO.

GO was purchased from the commercial company (Cheap Tubes Inc.) and dispersed into water through ultrasonication to obtain a stable solution. Briefly, 100 mL, 50 $\mu\text{g}/\text{mL}$ GO was added with 40 mg NaOH under ultrasonic bath for 3 h to form stable GO. The resultant GO was purified with 0.1 μm filter. The STEM in Figure 66A shows that the GO sheet has the size of micrometers. Wrinkles and folds were clearly observed from the image. Then, the composite of GO was investigated by EDS (Figure 66B), and the presence of carbon and oxygen was identified. The zeta potential of GO was -45 mV, indicating the presence of the oxygen-containing groups on the surface of GO (Figure 66C). The large negative charge of GO ensured the stability of GO solution. Then, UV-vis absorption spectrum was measured to characterize the GO solution. As shown in Figure 66D, the strong peak at *ca.* 230 nm was due to the π -plasmon of sp^2 carbon structure and the shoulder around 300 nm was ascribed to the n to π^* transitions.

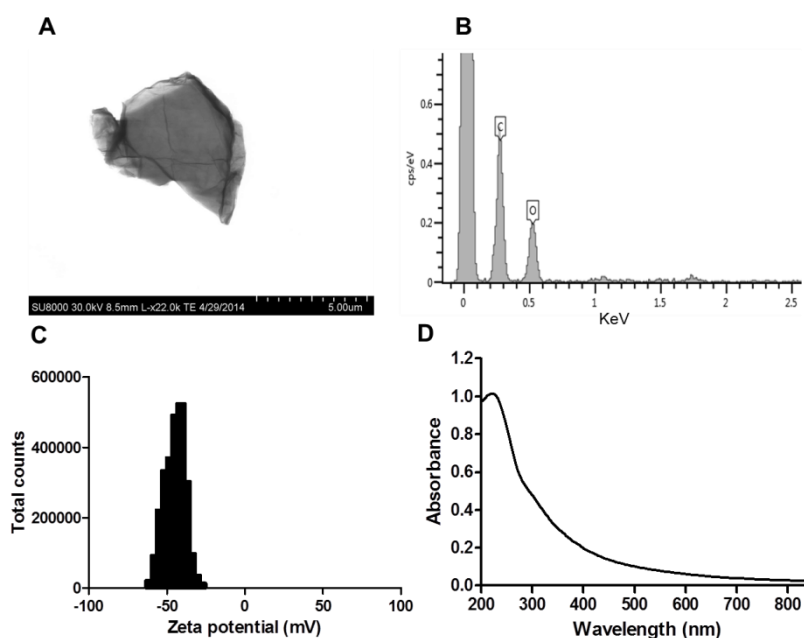


Figure 66. Characterization of GO. (A) STEM image of GO. (B) EDS pattern of GO. (C) The zeta potential of GO. (D) The UV-vis spectrum of GO.

3.2. Antibacterial Property of GO at the Level of Bacteria.

The antibacterial activity of GO was firstly investigated at the bacterial level with GO concentrations from 0 to 500.0 $\mu\text{g/mL}$. The OD_{600} value and bioluminescence intensity were measured to determine the concentration of bacteria finally to evaluate the killing efficiency of GO. As shown in the inset of Figure 67A, the bioluminescence intensity of *Kp* (a *Kp* strain emitting bioluminescence from Caliper) in LB medium decreased with the increase of GO concentrations. *Kp* survival rates followed the same trend as those of the bioluminescence intensity. The survival rates decreased from 100% to 28.8%, 15.2%, 2.8% and 3.2% when the concentrations of GO increased from 0 to 62.5, 125.0, 250.0 and 500.0 $\mu\text{g/mL}$, respectively. These results indicated that the antibacterial activity of GO is concentration-dependent. To further validate the results from the bioluminescence imaging and detection of OD_{600} , we treated *Kp* bacteria with and without GO and determined bacterial colonies using LB-agar dishes. As shown in Figure 67B, the photographs (a and b) and bioluminescent images (c and d) both showed that the amounts of colonies drastically decreased treated with 250.0 $\mu\text{g/mL}$ GO overnight. Collectively, GO exhibited excellent antibacterial activity to MDR *Kp* at the bacterial level. To evaluate whether antibacterial activity of GO is ubiquitous, we also investigated the bactericidal activity in another two bacteria *E.coli* and *P. aeruginosa* (Pa). As shown in Figure 67C and D, GO has the similar antibacterial activity to *E. coli* and Pa to *Kp*. With the increase of the concentration of GO, the survival rate of *E. coli* and Pa decreased. However, the survival rate of *E. coli* and Pa were 11.8 % and 11.9 % when treated with 250 $\mu\text{g/mL}$ GO (Figure 67C and D), which

were higher than that to *Kp* (2.8 %). In order to minimize the effect of high concentration GO on the animals, *Kp* was chosen as our model bacterial to investigate the antibacterial activity of GO *in vivo*.

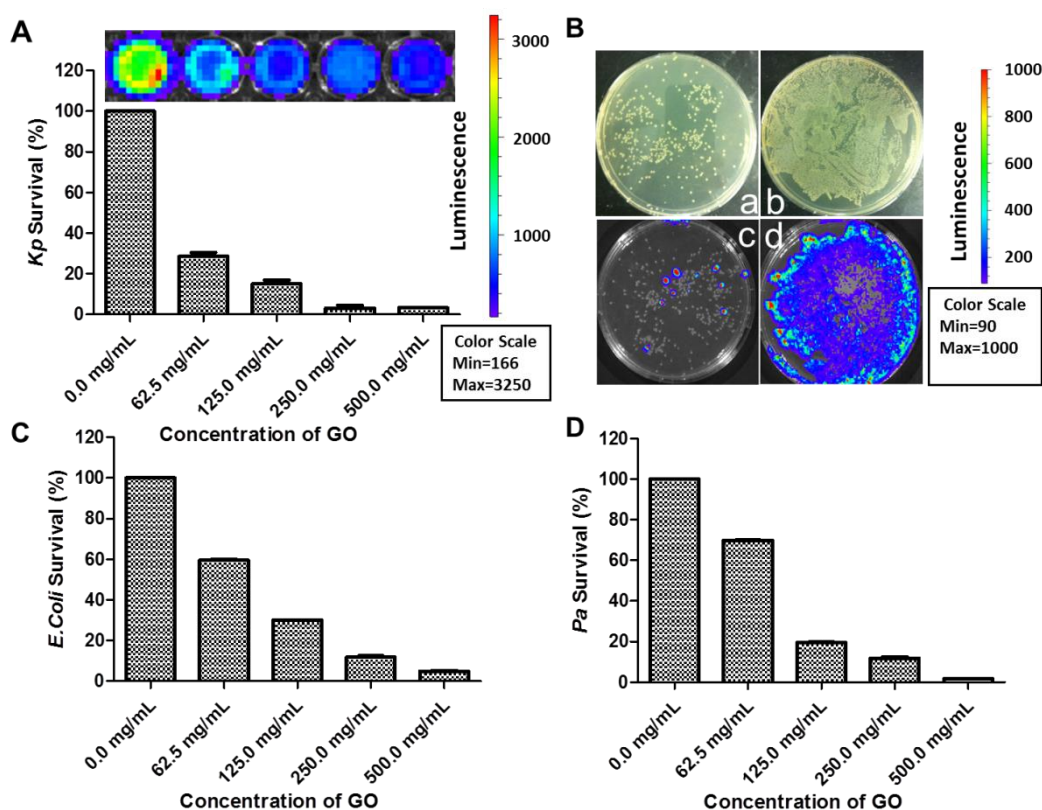


Figure 67. Antibacterial property of GO with different concentration. (A) The *Kp* survival rate after treatment of different concentrations of GO. Inset: Bioluminescence images of *Kp* bacteria after incubation with different concentrations of GO. From left to right: 0, 62.5, 125.0, 250.0, and 500.0 $\mu\text{g/mL}$. (B) Representing photographs (a and b) and bioluminescence images (c and d) of *Kp* bacterial colonies treated with (a and c) and without (b and d) GO formed on LB-agar plates. (C) The *E.coli* survival rate after treatment of different concentration of GO. (D) The *Pa* survival rate after treatment of different concentration of GO.

3.3. GO Increases Host Cells Resistance to *Kp*.

After the treatment with GO, the infection ability of *Kp* was investigated in macrophage cells. MH-S cells were infected by *Kp* (8 h), which was treated with different concentrations GO from 0 to 500.0 $\mu\text{g/mL}$. As shown in Figure 68, using the

cell without any bacterial infection as the negative control, the cell viability increased when the concentration of GO increased and reached a plateau around 65 % when the concentration of GO was 250.0 $\mu\text{g}/\text{mL}$. These results indicated that GO can kill the bacteria to some extent and inhibit the infection potency of *Kp*. However, the cell viability has not recovered to the normal level compared to the cells without treatment. This might be due to two main reasons. First, GO might have not killed all the *Kp* bacteria that would still cause cell death after the infection. Second, GO might have cytotoxicity that would affect the cell viability at high concentrations. Before GO can be used in clinics as an antibacterial agent, the biocompatibility should be fully investigated.

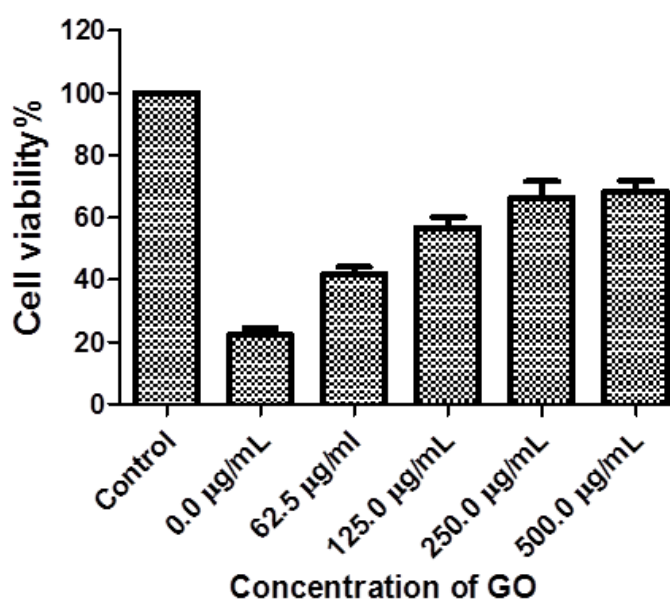


Figure 68. Relative viability of MH-S cells infected by *Kp* after treatment with different concentrations of GO (0.0, 62.5, 125.0, 250.0 and 500.0 $\mu\text{g}/\text{mL}$) at 37 $^{\circ}\text{C}$ through MTT assay.

3.4. GO Increases Resistance to *Kp* in Mice.

We found that GO was able to kill *Kp* and inhibit its infection potency in cells. However, the antibacterial activity of GO in the animal level is unexplored. Using a mouse model, we investigated whether GO treatment can reduce the infection potency in *Kp*. To this end, we intraperitoneally injected mice with GO-treated *Kp* at 1×10^5 CFU (in 50 μ L PBS) per mouse. Then, the bioluminescence imaging was carried out using IVIS Lumina XR system to monitor the invasion and dissemination of *Kp* in mice. As shown in Figure 69A, the mouse injected with the *Kp* without GO treatment showed diffusing and intense bioluminescence. While bioluminescence stayed in the enterocoelia cavity in the early time, it extended to the thoracic cavity after 8 h post injection. However, the dissemination areas and intensity of bioluminescence in mice infected by GO-treated *Kp* were more constrained (GO at 250.0 μ g/mL). Even after 24 h post injection, the translocation of *Kp* to thoracic cavity was limited when GO was used to treat *Kp*. Then, we semiquantitatively measured the bioluminescence intensity in these two groups (Figure 69B). The bioluminescence intensity of control *Kp*-infected mice was almost twice higher (1.6 - 2.0) than that of the mice infected by GO-treated *Kp*. This proved that GO was able to kill *Kp* and inhibit its infection potency *in vivo*.

Since *Kp* is a common cause of respiratory infection, we intranasally instilled *Kp* in to mouse lungs to investigate whether GO impacts the infection potency. As shown in Figure 70A, 50% mice died within 48 h with sham- treated *Kp*, and all the mice had died at 72 h. In contrast, 80% the mice infected by GO-treated *Kp* remained alive during the whole period. The results demonstrated that GO could greatly inhibit the infection potency of *Kp*, decreasing the mortality and prolonging the survival of

infected-mice. After infection *via* intranasal instillation, the damage of the lung tissue was also investigated using H&E staining. As shown in Figure 70B, the morphology was altered, including signs of inflammatory response, tissue damage, and severe pneumonia in the mice treated *Kp* without GO incubation. However, GO-treated *Kp* caused subdued inflammatory features, reduced polymorphonuclear neutrophil (PMN) penetration and decreased tissue damage. Therefore, GO can significantly alleviate the damage of lung tissue by reducing *Kp* infection ability.

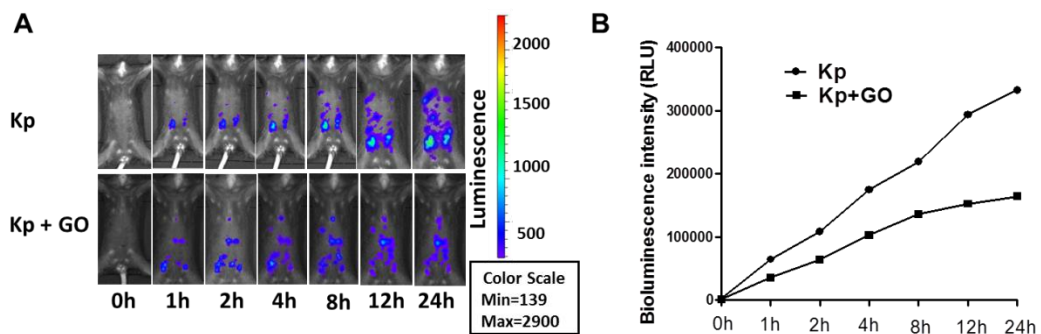


Figure 69. GO decreased infection severity in mice. (A) Bioluminescent images were obtained using IVIS Lumina XR system at different time points and the mice intraperitoneally injected with GO-treated *Kp* and untreated *Kp*. (B) Semiquantitatively bioluminescence intensity of the two groups in (A).

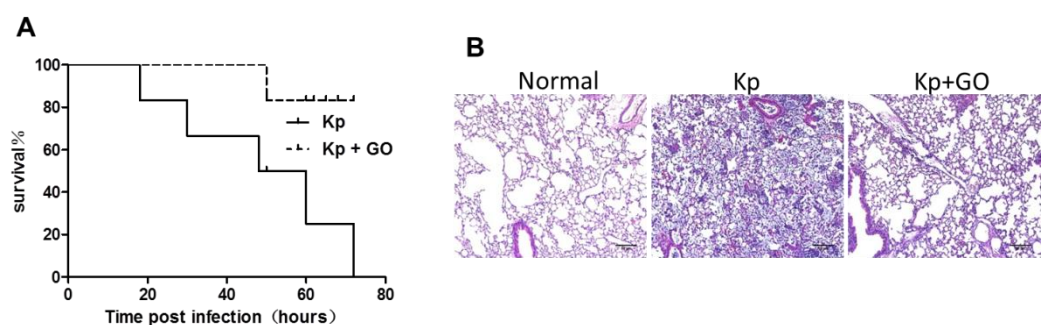


Figure 70. GO decreased mortality rates and tissue damage. (A) Kaplan-Meier survival curves were obtained by infecting mice with GO-treated and untreated *Kp*, respectively (n=5 mice per group). (B) Morphological evidence of lung injury and inflammatory responses as assessed by H & E staining histological analysis (20 \times , scale bar = 50 μ m).

To further delve into the antibacterial mechanism of GO *in vivo*, the viability of alveolar macrophages (AM) isolated from the infected mice was evaluated because AM are a key immune cell in fighting against Gram-negative bacterial infection. The viability of AM reflects the health state of the bacterial infection. As shown in Figure 71A, the survival of AM in GO-treated *Kp* infected mice increased by approximately 1.4- and 3.1-fold compared to that of the sham-*Kp* group at 24 h and 48 h post infection, respectively. Meanwhile, the phagocyte-derived reactive oxygen species (ROS) is considered another factor reflecting the extent of bacterial infection. Severe infection will lead to excessive generation of ROS species (Figure 71B). At 8 h and 24 h post injection, GO-treatment significantly decreased the generation of ROS in AM, indicating reduced infection extent. Furthermore, the quantity of PMN in BAL and blood of the infected mice were also measured to gauge inflammatory response. As shown in Figure 71C and D, PMN penetration in both BAL fluid and blood of GO treated-*Kp* group was lower than that of sham-*Kp* group at 8 h and 24 h post infection. Collectively, these data of AM cell viability, ROS species, and PMN penetration indicated that the infection potency of *Kp* after GO treatment was greatly dampened *in vivo* against the controls.

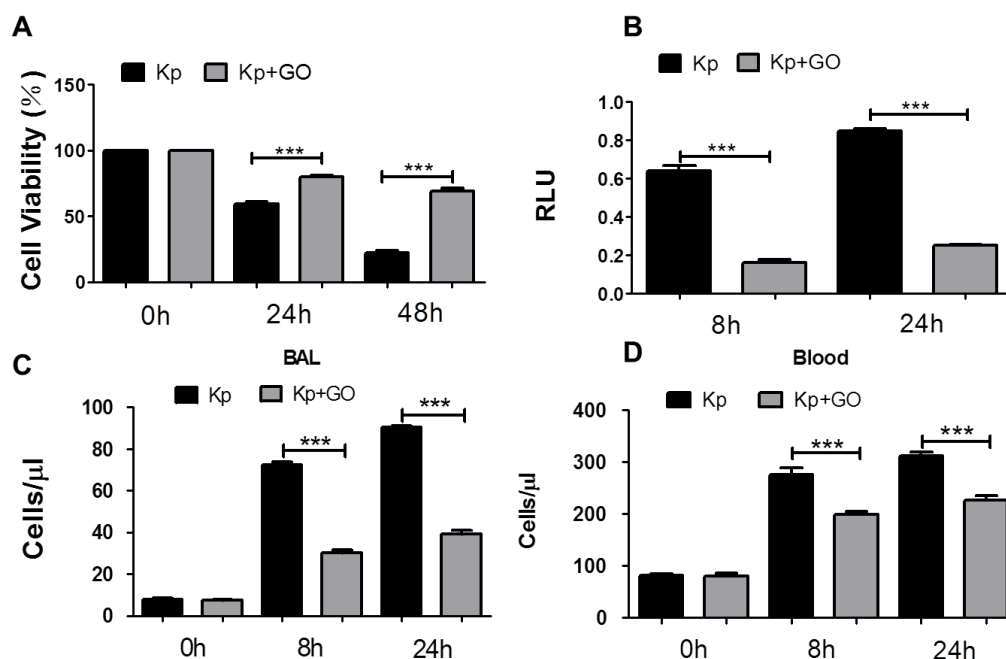


Figure 71. (A) Cell viability of AM after bacterial infection by MTT assay. (B) ROS production in AM cells detected using an NBT assay. (C and D) PMN infiltration in the BAL and blood was counted by HEMA staining (Thermofisher). *** $p < 0.001$; RLU: relative LUC units.

Bacterial spread to various organs is another mortiferous factor during sepsis. Septicemia and ultimately sepsis might be caused by bacterial dissemination during the diseases progression. Therefore, we investigated *Kp* dissemination after intranasal instillation by determining bacterial burdens in the lung, liver, spleen, and kidneys. As shown in Figure 72, the lung (A) had the highest bacterial loads, followed by the spleen (C), kidney (D) and liver (B). However, in all the organs, bacterial CFUs from the mice infected with GO-treated *Kp* were significantly lower than those from sham-treated group at 8 h and 24 h post infection. To validate this observation, we detected the activity of tissue injury, MPO, in all of the organs as MPO is released from PMN in response to various pulmonary infections. As shown in Figure 73, in all the four organs, the activity of MPO followed the same trends as that of the bacterial CFUs in Figure

72. At 8 h and 24 h post infection, the MPO activity of GO-treated *Kp* group was significantly lower than that from sham-treated *Kp* group, indicating lessened infection.

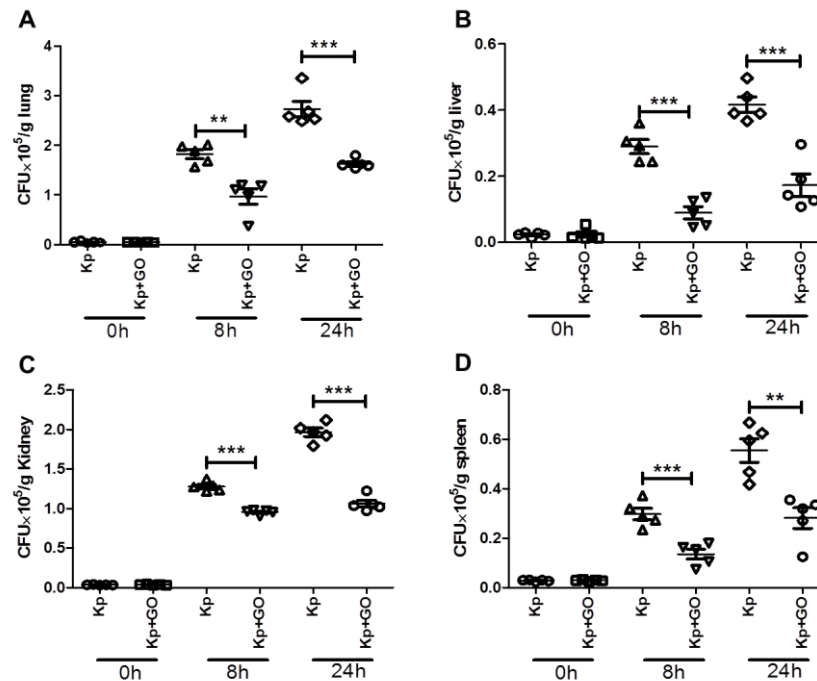


Figure 72. The lung (A), liver (B), spleen (C), and kidneys (D) showed significantly decreased bacterial burdens in GO-*Kp* infected mice (Mann Whitney U test). **p < 0.01; ***p < 0.001.

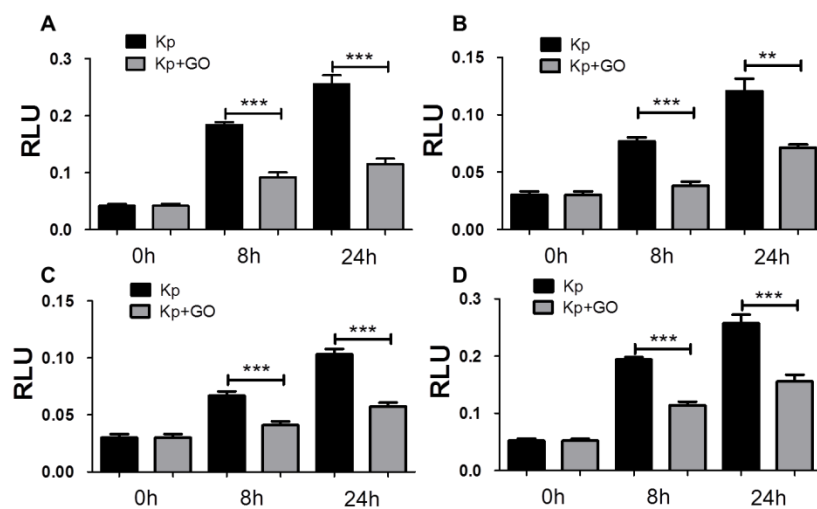


Figure 73. Decreased MPO activity in the lung (A), liver (B), spleen (C), and kidney (D) of GO-*Kp* treated mice at 8 h and 24 h. Data are shown as mean + SEM of n = 3 mice per group and are representative of three independent experiments. **p < 0.01; ***p < 0.001; one-way ANOVA (Tukey's post hoc). RLU: relative LUC units.

4. Conclusions.

In conclusion, the antibacterial activity of GO to *Kp* was investigated at the bacterial, mammalian cell and animal levels in this work. At the bacterial level, GO can kill *Kp* in a concentration-dependent manner. More than 95% *Kp* was killed when the concentration of GO was at 250.0 µg/mL. After treatment with GO, *Kp* also showed reduced infectivity to macrophage MH-S cells, thus increased cell viability. More importantly, antibacterial activity of GO was investigated in animal models. Similarly, GO can significantly inhibit the infection potency of *Kp* after peritoneal injection and intranasal instillation, respectively. The mortality of mice with *Kp* infection was decreased when GO was used. Meanwhile, the inflammatory responses in the lung, liver, spleen and kidney were also decreased after infected with GO-treated *Kp*. Taken together, these findings indicate that GO might be a potential therapeutic agent for *Kp*, which may also be used to control other MDR bacteria that cause severe disease in clinics.

REFERENCES

1. Magri, D. C.; Brown, G. J.; McClean, G. D.; de Silva, A. P. Communicating Chemical Congregation: A Molecular and Logic Gate with Three Chemical Inputs as a “Lab-on-a-Molecule” Prototype. *J. Am. Chem. Soc.* **2006**, *128*, 4950-4951.
2. Prokup, A.; Hemphill, J.; Deiters, A. DNA Computation: A Photochemically Controlled and Gate. *J. Am. Chem. Soc.* **2012**, *134*, 3810-3815.
3. Elbaz, J.; Lioubashevski, O.; Wang, F.; Remacle, F.; Levine, R. D.; Willner, I. DNA Computing Circuits Using Libraries of Dnazyme Subunits. *Nat. Nanotechnol.* **2010**, *5*, 417-422.
4. Li, T.; Wang, E.; Dong, S. Potassium-Lead-Switched G-Quadruplexes: A New Class of DNA Logic Gates. *J. Am. Chem. Soc.* **2009**, *131*, 15082-15083.
5. Szacilowski, K. Digital Information Processing in Molecular Systems. *Chem. Rev.* **2008**, *108*, 3481-3548.
6. Sakamoto, K.; Gouzu, H.; Komiya, K.; Kiga, D.; Yokoyama, S.; Yokomori, T.; Hagiya, M. Molecular Computation by DNA Hairpin Formation. *Science* **2000**, *288*, 1223-1226.
7. Huang, W. T.; Shi, Y.; Xie, W. Y.; Luo, H. Q.; Li, N. B. A Reversible Fluorescence Nanoswitch Based on Bifunctional Reduced Graphene Oxide: Use for Detection of Hg²⁺ and Molecular Logic Gate Operation. *Chem. Commun.* **2011**, *47*, 7800-7802.
8. Xie, W. Y.; Huang, W. T.; Li, N. B.; Luo, H. Q. Design of a Dual-Output Fluorescent DNA Logic Gate and Detection of Silver Ions and Cysteine Based on Graphene Oxide. *Chem. Commun.* **2012**, *48*, 82-84.
9. Shlyahovsky, B.; Li, Y.; Lioubashevski, O.; Elbaz, J.; Willner, I. Logic Gates and Antisense DNA Devices Operating on a Translator Nucleic Acid Scaffold. *ACS Nano* **2009**, *3*, 1831-1843.
10. Zhu, J.; Li, T.; Zhang, L.; Dong, S.; Wang, E. G-Quadruplex Dnazyme Based Molecular Catalytic Beacon for Label-Free Colorimetric Logic Gates. *Biomaterials* **2011**, *32*, 7318-7324.
11. Yoshida, W.; Yokobayashi, Y. Photonic Boolean Logic Gates Based on DNA Aptamers. *Chem. Commun.* **2007**, 195-197.
12. Strack, G.; Ornatska, M.; Pita, M.; Katz, E. Biocomputing Security System: Concatenated Enzyme-Based Logic Gates Operating as a Biomolecular Keypad Lock. *J. Am. Chem. Soc.* **2008**, *130*, 4234-4235.
13. Hod, O.; Baer, R.; Rabani, E. A Parallel Electromagnetic Molecular Logic Gate. *J. Am. Chem. Soc.* **2005**, *127*, 1648-1649.
14. Shen, J.; Zhu, Y.; Yang, X.; Li, C. Graphene Quantum Dots: Emergent Nanolights for Bioimaging, Sensors, Catalysis and Photovoltaic Devices. *Chem. Commun.*

- 2012**, 48, 3686-3699.
15. Ma, D. L.; He, H. Z.; Ma, V. P.; Chan, D. S.; Leung, K. H.; Zhong, H. J.; Lu, L.; Mergny, J. L.; Leung, C. H. Label-Free Sensing of Ph and Silver Nanoparticles Using an "or" Logic Gate. *Anal. Chim. Acta.* **2012**, 733, 78-83.
 16. Zhang, M.; Ye, B. C. A Reversible Fluorescent DNA Logic Gate Based on Graphene Oxide and Its Application for Iodide Sensing. *Chem. Commun.* **2012**, 48, 3647-3649.
 17. Freeman, R.; Finder, T.; Willner, I. Multiplexed Analysis of Hg²⁺ and Ag⁺ Ions by Nucleic Acid Functionalized Cdse/Zns Quantum Dots and Their Use for Logic Gate Operations. *Angew. Chem. Int. Ed.* **2009**, 48, 7818-7821.
 18. Bi, S.; Yan, Y.; Hao, S.; Zhang, S. Colorimetric Logic Gates Based on Supramolecular Dnazyme Structures. *Angew. Chem. Int. Ed.* **2010**, 49, 4438-4442.
 19. Park, K. S.; Seo, M. W.; Jung, C.; Lee, J. Y.; Park, H. G. Simple and Universal Platform for Logic Gate Operations Based on Molecular Beacon Probes. *Small* **2012**, 8, 2203-2212.
 20. Liu, X.; Aizen, R.; Freeman, R.; Yehezkeli, O.; Willner, I. Multiplexed Aptasensors and Amplified DNA Sensors Using Functionalized Graphene Oxide: Application for Logic Gate Operations. *ACS Nano* **2012**, 6, 3553-3563.
 21. Xiang, Y.; Qian, X.; Chen, Y.; Zhang, Y.; Chai, Y.; Yuan, R. A Reagentless and Disposable Electronic Genosensor: From Multiplexed Analysis to Molecular Logic Gates. *Chem. Commun.* **2011**, 47, 2080-2082.
 22. Wang, L.; Zhu, J.; Han, L.; Jin, L.; Zhu, C.; Wang, E.; Dong, S. Graphene-Based Aptamer Logic Gates and Their Application to Multiplex Detection. *ACS Nano* **2012**, 6, 6659-6666.
 23. Guo, J. H.; Kong, D. M.; Shen, H. X. Design of a Fluorescent DNA Implication Logic Gate and Detection of Ag⁺ and Cysteine with Triphenylmethane Dye/G-Quadruplex Complexes. *Biosens. Bioelectron.* **2010**, 26, 327-332.
 24. Xia, F.; Zuo, X.; Yang, R.; White, R. J.; Xiao, Y.; Kang, D.; Gong, X.; Lubin, A. A.; Vallee-Belisle, A.; Yuen, J. D.; Hsu, B. Y.; Plaxco, K. W. Label-Free, Dual-Analyte Electrochemical Biosensors: A New Class of Molecular-Electronic Logic Gates. *J. Am. Chem. Soc.* **2010**, 132, 8557-8559.
 25. He, X.; Qing, Z.; Wang, K.; Zou, Z.; Shi, H.; Huang, J. Engineering a Unimolecular Multifunctional DNA Probe for Analysis of Hg²⁺ and Ag⁺. *Anal. Method.* **2012**, 4, 345-347.
 26. Qing, Z.; He, X.; Wang, K.; Zou, Z.; Yang, X.; Huang, J.; Yan, G. Colorimetric Multiplexed Analysis of Mercury and Silver Ions by Using a Unimolecular DNA Probe and Unmodified Gold Nanoparticles. *Anal. Method.* **2012**, 4, 3320-3325.
 27. Wang, K.; Tang, Z.; Yang, C. J.; Kim, Y.; Fang, X.; Li, W.; Wu, Y.; Medley, C. D.; Cao, Z.; Li, J.; Colon, P.; Lin, H.; Tan, W. Molecular Engineering of DNA: Molecular Beacons. *Angew. Chem. Int. Ed.* **2009**, 48, 856-870.
 28. Guo, J.; Yang, R. An or Logic Gate Based on Two Molecular Beacons. *Mol. Biosyst.* **2012**, 8, 927-930.
 29. Yang, C. N.; Hsu, C. Y.; Chuang, Y. C. Molecular Beacon-Based Half-Adder and Half-Subtractor. *Chem. Commun.* **2012**, 48, 112-114.

30. Sekowski, J. W.; Malkas, L. H.; Wei, Y.; Hickey, R. J. Mercuric Ion Inhibits the Activity and Fidelity of the Human Cell DNA Synthesome. *Toxicol. Appl. Pharmacol.* **1997**, *145*, 268-276.
31. Hoyle, I.; Handy, R. D. Dose-Dependent Inorganic Mercury Absorption by Isolated Perfused Intestine of Rainbow Trout, *Oncorhynchus Mykiss*, Involves Both Amiloride-Sensitive and Energy-Dependent Pathways. *Aquat. Toxicol.* **2005**, *72*, 147-159.
32. Manz, F.; Bohmer, T.; Gartner, R.; Grossklaus, R.; Klett, M.; Schneider, R. Quantification of Iodine Supply: Representative Data on Intake and Urinary Excretion of Iodine from the German Population in 1996. *Ann. Nutr. Metab.* **2002**, *46*, 128-138.
33. Lightowler, H. J.; Davies, G. J. Assessment of Iodine Intake in Vegans: Weighed Dietary Record Vs Duplicate Portion Technique. *Eur. J. Clin. Nutr.* **2002**, *56*, 765-770.
34. Liu, C.-W.; Huang, C.-C.; Chang, H.-T. Highly Selective DNA-Based Sensor for Lead(II) and Mercury(II) Ions. *Anal. Chem.* **2009**, *81*, 2383-2387.
35. Huang, C.-C.; Chang, H.-T. Selective Gold-Nanoparticle-Based "Turn-on" Fluorescent Sensors for Detection of Mercury(II) in Aqueous Solution. *Anal. Chem.* **2006**, *78*, 8332-8338.
36. Zhang, L.; Li, T.; Li, B.; Li, J.; Wang, E. Carbon Nanotube-DNA Hybrid Fluorescent Sensor for Sensitive and Selective Detection of Mercury(II) Ion. *Chem. Commun.* **2010**, *46*, 1476-1478.
37. Zhang, J.; Xu, X.; Yang, C.; Yang, F.; Yang, X. Colorimetric Iodide Recognition and Sensing by Citrate-Stabilized Core/Shell Cu@Au Nanoparticles. *Anal. Chem.* **2011**, *83*, 3911-3917.
38. Gammon, D. B.; Evans, D. H. The 3'-to-5' Exonuclease Activity of Vaccinia Virus DNA Polymerase Is Essential and Plays a Role in Promoting Virus Genetic Recombination. *J. Virol.* **2009**, *83*, 4236-4250.
39. Song, L.; Chaudhuri, M.; Knopf, C. W.; Parris, D. S. Contribution of the 3'- to 5'- Exonuclease Activity of Herpes Simplex Virus Type 1 DNA Polymerase to the Fidelity of DNA Synthesis. *J. Biol. Chem.* **2004**, *279*, 18535-18543.
40. Paull, T. T.; Gellert, M. The 3' to 5' Exonuclease Activity of Mre11 Facilitates Repair of DNA Double-Strand Breaks. *Mol. Cell.* **1998**, *1*, 969-979.
41. Kavanagh, D.; Spitzer, D.; Kothari, P.; Shaikh, A.; Liszewski, M. K.; Richards, A.; Atkinson, J. P. New Roles for the Major Human 3'-5' Exonuclease Trex1 in Human Disease. *Cell Cycle* **2008**, *7*, 1718-1725.
42. Shevelev, I. V.; Hubscher, U. The 3[Prime]-5[Prime] Exonucleases. *Nat. Rev. Mol. Cell. Biol.* **2002**, *3*, 364-376.
43. Yan, N.; Regalado-Magdos, A. D.; Stiggelbout, B.; Lee-Kirsch, M. A.; Lieberman, J. The Cytosolic Exonuclease Trex1 Inhibits the Innate Immune Response to Human Immunodeficiency Virus Type 1. *Nat. Immunol.* **2010**, *11*, 1005-1013.
44. Yang, Y.-G.; Lindahl, T.; Barnes, D. E. Trex1 Exonuclease Degrades Ssdna to Prevent Chronic Checkpoint Activation and Autoimmune Disease. *Cell* **2007**,

- 131, 873-886.
45. Brucet, M.; Querol-Aud í J.; Bertlik, K.; Lloberas, J.; Fita, I.; Celada, A. Structural and Biochemical Studies of Trex1 Inhibition by Metals. Identification of a New Active Histidine Conserved in Deddh Exonucleases. *Protein. Sci.* **2008**, *17*, 2059-2069.
 46. Hoheisel, J. D. On the Activities of Escherichia Coli Exonuclease III. *Anal. Biochem.* **1993**, *209*, 238-246.
 47. Chen, Y.; Yang, C. J.; Wu, Y.; Conlon, P.; Kim, Y.; Lin, H.; Tan, W. Light-Switching Excimer Beacon Assays for Ribonuclease H Kinetic Study. *ChemBioChem* **2008**, *9*, 355-359.
 48. Tan, W.; Wang, K.; Drake, T. J. Molecular Beacons. *Curr. Opin. Chem. Biol.* **2004**, *8*, 547-553.
 49. Tang, Z.; Liu, P.; Ma, C.; Yang, X.; Wang, K.; Tan, W.; Lv, X. Molecular Beacon Based Bioassay for Highly Sensitive and Selective Detection of Nicotinamide Adenine Dinucleotide and the Activity of Alanine Aminotransferase. *Anal. Chem.* **2011**, *83*, 2505-2510.
 50. Dai, N.; Kool, E. T. Fluorescent DNA-Based Enzyme Sensors. *Chem. Soc. Rev.* **2011**, *40*, 5756-5770.
 51. Gührs, K.-H.; Groth, M.; Grosse, F. A Label-Free Assay of Exonuclease Activity Using a Pyrosequencing Technique. *Anal. Biochem.* **2010**, *405*, 11-18.
 52. Seidel, C. A. M.; Schulz, A.; Sauer, M. H. M. Nucleobase-Specific Quenching of Fluorescent Dyes. 1. Nucleobase One-Electron Redox Potentials and Their Correlation with Static and Dynamic Quenching Efficiencies. *J. Phys. Chem.* **1996**, *100*, 5541-5553.
 53. Leung, C.-H.; Chan, D. S.-H.; Man, B. Y.-W.; Wang, C.-J.; Lam, W.; Cheng, Y.-C.; Fong, W.-F.; Hsiao, W.-L. W.; Ma, D.-L. Simple and Convenient G-Quadruplex-Based Turn-on Fluorescence Assay for 3'-5' Exonuclease Activity. *Anal. Chem.* **2011**, *83*, 463-466.
 54. Su, X.; Zhu, X.; Zhang, C.; Xiao, X.; Zhao, M. In Situ, Real-Time Monitoring of the 3' to 5' Exonucleases Secreted by Living Cells. *Anal. Chem.* **2012**, *84*, 5059-5065.
 55. Grimes, J.; Gerasimova, Y. V.; Kolpashchikov, D. M. Real-Time SNP Analysis in Secondary-Structure-Folded Nucleic Acids. *Angew. Chem. Int. Ed.* **2010**, *49*, 8950-8953.
 56. Tyagi, S.; Kramer, F. R. Molecular Beacons: Probes that Fluoresce upon Hybridization. *Nat. Biotechnol.* **1996**, *14*, 303-308.
 57. Kang, W. J.; Cho, Y. L.; Chae, J. R.; Lee, J. D.; Choi, K.-J.; Kim, S. Molecular Beacon-Based Bioimaging of Multiple Micrnas During Myogenesis. *Biomaterials* **2011**, *32*, 1915-1922.
 58. Xie, H. P.; Meng, X. X.; Su, H.; Cai, Q. Y.; Tan, Y. J.; Huang, X. Q. Ligase-Based Ultrasensitive Detection of Dnazyme Cleavage Product Using Molecular Beacon. *Chin. Chem. Lett.* **2012**, *23*, 1177-1180.
 59. Guetschow, E.; Black, W.; Walsh, C.; Furchak, J. W. Detection of Prolactin Inducible Protein Mrna, a Biomarker for Breast Cancer Metastasis, Using a

- Molecular Beacon-Based Assay. *Anal. BioAnal. Chem.* **2012**, *404*, 399-406.
60. Kim, B.; Jung, I. H.; Kang, M.; Shim, H.-K.; Woo, H. Y. Cationic Conjugated Polyelectrolytes-Triggered Conformational Change of Molecular Beacon Aptamer for Highly Sensitive and Selective Potassium Ion Detection. *J. Am. Chem. Soc.* **2012**, *134*, 3133-3138.
 61. Chinnappan, R.; Dubé, A.; Lemay, J.-F.; Lafontaine, D. A. Fluorescence Monitoring of Riboswitch Transcription Regulation Using a Dual Molecular Beacon Assay. *Nucleic. Acids. Res.* **2013**, *41*, e106.
 62. Hamaguchi, N.; Ellington, A.; Stanton, M. Aptamer Beacons for the Direct Detection of Proteins. *Anal. Biochem.* **2001**, *294*, 126-131.
 63. Beese, L. S.; Steitz, T. A. Structural Basis for the 3'-5' Exonuclease Activity of Escherichia Coli DNA Polymerase I: A Two Metal Ion Mechanism. *EMBO J* **1991**, *10*, 25-33.
 64. Rasouli-Nia, A.; Karimi-Busheri, F.; Weinfeld, M. Stable Down-Regulation of Human Polynucleotide Kinase Enhances Spontaneous Mutation Frequency and Sensitizes Cells to Genotoxic Agents. *Proc. Natl. Acad. Sci. U. S. A.* **2004**, *101*, 6905-6910.
 65. Karimi-Busheri, F.; Rasouli-Nia, A.; Allalunis-Turner, J.; Weinfeld, M. Human Polynucleotide Kinase Participates in Repair of DNA Double-Strand Breaks by Nonhomologous End Joining but Not Homologous Recombination. *Cancer Res.* **2007**, *67*, 6619-6625.
 66. Henner, W. D.; Rodriguez, L. O.; Hecht, S. M.; Haseltine, W. A. Gamma Ray Induced Deoxyribonucleic Acid Strand Breaks. 3' Glycolate Termini. *J. Biol. Chem.* **1983**, *258*, 711-713.
 67. Torriglia, A.; Perani, P.; Brossas, J. Y.; Chaudun, E.; Treton, J.; Courtois, Y.; Counis, M. F. L-Dnase Ii, a Molecule That Links Proteases and Endonucleases in Apoptosis, Derives from the Ubiquitous Serpin Leukocyte Elastase Inhibitor. *Mol. Cell Biol.* **1998**, *18*, 3612-3619.
 68. Wang, L. K.; Lima, C. D.; Shuman, S. Structure and Mechanism of T4 Polynucleotide Kinase: An Rna Repair Enzyme. *EMBO J* **2002**, *21*, 3873-3880.
 69. Whitehouse, C. J.; Taylor, R. M.; Thistlethwaite, A.; Zhang, H.; Karimi-Busheri, F.; Lasko, D. D.; Weinfeld, M.; Caldecott, K. W. Xrcc1 Stimulates Human Polynucleotide Kinase Activity at Damaged DNA Termini and Accelerates DNA Single-Strand Break Repair. *Cell* **2001**, *104*, 107-117.
 70. Wang, L. K.; Shuman, S. Domain Structure and Mutational Analysis of T4 Polynucleotide Kinase. *J. Biol. Chem.* **2001**, *276*, 26868-26874.
 71. Karimi-Busheri, F.; Daly, G.; Robins, P.; Canas, B.; Pappin, D. J.; Sgouros, J.; Miller, G. G.; Fakhrai, H.; Davis, E. M.; Le Beau, M. M.; Weinfeld, M. Molecular Characterization of a Human DNA Kinase. *J. Biol. Chem.* **1999**, *274*, 24187-24194.
 72. Wu, T.; Liu, S.; Li, H.; Wang, L.; Sun, X. Production of Reduced Graphene Oxide by Uv Irradiation. *J. Nanosci. Nanotechnol.* **2011**, *11*, 10078-10081.
 73. Ma, C.; Yeung, E. S. Highly Sensitive Detection of DNA Phosphorylation by Counting Single Nanoparticles. *Anal. Bioanal. Chem.* **2010**, *397*, 2279-2284.

74. Wang, Y.; He, X.; Wang, K.; Ni, X.; Su, J.; Chen, Z. Ferrocene-Functionalized Swcnt for Electrochemical Detection of T4 Polynucleotide Kinase Activity. *Biosens. Bioelectron.* **2012**, *32*, 213-218.
75. Song, C.; Zhao, M. Real-Time Monitoring of the Activity and Kinetics of T4 Polynucleotide Kinase by a Singly Labeled DNA-Hairpin Smart Probe Coupled with Lambda Exonuclease Cleavage. *Anal. Chem.* **2009**, *81*, 1383-1388.
76. Lin, L.; Liu, Y.; Zhao, X.; Li, J. Sensitive and Rapid Screening of T4 Polynucleotide Kinase Activity and Inhibition Based on Coupled Exonuclease Reaction and Graphene Oxide Platform. *Anal. Chem.* **2011**, *83*, 8396-8402.
77. Tang, Z.; Wang, K.; Tan, W.; Ma, C.; Li, J.; Liu, L.; Guo, Q.; Meng, X. Real-Time Investigation of Nucleic Acids Phosphorylation Process Using Molecular Beacons. *Nucleic. Acids. Res.* **2005**, *33*, e97.
78. Webster, J. R.; Burns, M. A.; Burke, D. T.; Mastrangelo, C. H. Monolithic Capillary Electrophoresis Device with Integrated Fluorescence Detector. *Anal. Chem.* **2001**, *73*, 1622-1626.
79. Diggle, C. P.; Bentley, J.; Kiltie, A. E. Development of a Rapid, Small-Scale DNA Repair Assay for Use on Clinical Samples. *Nucleic. Acids. Res.* **2003**, *31*, e83.
80. Zipper, H.; Brunner, H.; Bernhagen, J.; Vitzthum, F. Investigations on DNA Intercalation and Surface Binding by Sybr Green I, Its Structure Determination and Methodological Implications. *Nucleic. Acids. Res.* **2004**, *32*, e103.
81. Xu, H.; Gao, S.; Liu, Q.; Pan, D.; Wang, L.; Ren, S.; Ding, M.; Chen, J.; Liu, G. A Highly Sensitive and Selective Competition Assay for the Detection of Cysteine Using Mercury-Specific DNA, Hg and Sybr Green I. *Sensors* **2011**, *11*, 10187-10196.
82. Zhu, X.; Zhou, X.; Xing, D. Ultrasensitive and Selective Detection of Mercury(II) in Aqueous Solution by Polymerase Assisted Fluorescence Amplification. *Biosens. Bioelectron.* **2011**, *26*, 2666-2669.
83. Dave, N.; Chan, M. Y.; Huang, P. J.; Smith, B. D.; Liu, J. Regenerable DNA-Functionalized Hydrogels for Ultrasensitive, Instrument-Free Mercury(II) Detection and Removal in Water. *J. Am. Chem. Soc.* **2010**, *132*, 12668-12673.
84. Pu, W.; Zhao, H.; Huang, C.; Wu, L.; Xua, D. Fluorescent Detection of Silver(I) and Cysteine Using Sybr Green I and a Silver(I)-Specific Oligonucleotide. *Microchimica. Acta.* **2012**, *177*, 137-144.
85. Little, J. W. An Exonuclease Induced by Bacteriophage Lambda. Ii. Nature of the Enzymatic Reaction. *J. Biol. Chem.* **1967**, *242*, 679-686.
86. Mei, Q.; Zhang, K.; Guan, G.; Liu, B.; Wang, S.; Zhang, Z. Highly Efficient Photoluminescent Graphene Oxide with Tunable Surface Properties. *Chem. Commun.* **2010**, *46*, 7319-7321.
87. Liu, Z.; Robinson, J. T.; Tabakman, S. M.; Yang, K.; Dai, H. Carbon Materials for Drug Delivery & Cancer Therapy. *Mater. Today.* **2011**, *14*, 316-323.
88. Lightcap, I. V.; Kamat, P. V. Fortification of Cdse Quantum Dots with Graphene Oxide. Excited State Interactions and Light Energy Conversion. *J. Am. Chem. Soc.* **2012**, *134*, 7109-7116.
89. Yang, X.; Niu, G.; Cao, X.; Wen, Y.; Xiang, R.; Duan, H.; Chen, Y. The

- Preparation of Functionalized Graphene Oxide for Targeted Intracellular Delivery of Sirna. *J. Mater. Chem.* **2012**, *22*, 6649-6654.
90. Loh, K. P.; Bao, Q.; Eda, G.; Chhowalla, M. Graphene Oxide as a Chemically Tunable Platform for Optical Applications. *Nat. Chem.* **2010**, *2*, 1015-1024.
 91. Kim, S.; Hwang, S. W.; Kim, M. K.; Shin, D. Y.; Shin, D. H.; Kim, C. O.; Yang, S. B.; Park, J. H.; Hwang, E.; Choi, S. H.; Ko, G.; Sim, S.; Sone, C.; Choi, H. J.; Bae, S.; Hong, B. H. Anomalous Behaviors of Visible Luminescence from Graphene Quantum Dots: Interplay between Size and Shape. *ACS Nano* **2012**, *6*, 8203-8208.
 92. Dong, Y.; Shao, J.; Chen, C.; Li, H.; Wang, R.; Chi, Y.; Lin, X.; Chen, G. Blue Luminescent Graphene Quantum Dots and Graphene Oxide Prepared by Tuning the Carbonization Degree of Citric Acid. *Carbon* **2012**, *50*, 4738-4743.
 93. Peng, J.; Gao, W.; Gupta, B. K.; Liu, Z.; Romero-Aburto, R.; Ge, L.; Song, L.; Alemany, L. B.; Zhan, X.; Gao, G.; Vithayathil, S. A.; Kaiparettu, B. A.; Marti, A. A.; Hayashi, T.; Zhu, J. J.; Ajayan, P. M. Graphene Quantum Dots Derived from Carbon Fibers. *Nano Lett.* **2012**, *12*, 844-849.
 94. Shen, J.; Zhu, Y.; Yang, X.; Zong, J.; Zhang, J.; Li, C. One-Pot Hydrothermal Synthesis of Graphene Quantum Dots Surface-Passivated by Polyethylene Glycol and Their Photoelectric Conversion under near-Infrared Light. *New. J. Chem.* **2012**, *36*, 97-101.
 95. Li, M.; Wu, W.; Ren, W.; Cheng, H.-M.; Tang, N.; Zhong, W.; Du, Y. Synthesis and Upconversion Luminescence of N-Doped Graphene Quantum Dots. *Appl. Phys. Lett.* **2012**, *101*, 103107-103103.
 96. Ritter, K. A.; Lyding, J. W. The Influence of Edge Structure on the Electronic Properties of Graphene Quantum Dots and Nanoribbons. *Nat. Mater.* **2009**, *8*, 235-242.
 97. Zhu, S.; Zhang, J.; Qiao, C.; Tang, S.; Li, Y.; Yuan, W.; Li, B.; Tian, L.; Liu, F.; Hu, R.; Gao, H.; Wei, H.; Zhang, H.; Sun, H.; Yang, B. Strongly Green-Photoluminescent Graphene Quantum Dots for Bioimaging Applications. *Chem. Commun.* **2011**, *47*, 6858-6860.
 98. Zhu, S.; Zhang, J.; Tang, S.; Qiao, C.; Wang, L.; Wang, H.; Liu, X.; Li, B.; Li, Y.; Yu, W.; Wang, X.; Sun, H.; Yang, B. Surface Chemistry Routes to Modulate the Photoluminescence of Graphene Quantum Dots: From Fluorescence Mechanism to up-Conversion Bioimaging Applications. *Adv. Funct. Mater.* **2012**, *22*, 4732-4740.
 99. Tang, L.; Ji, R.; Cao, X.; Lin, J.; Jiang, H.; Li, X.; Teng, K. S.; Luk, C. M.; Zeng, S.; Hao, J.; Lau, S. P. Deep Ultraviolet Photoluminescence of Water-Soluble Self-Passivated Graphene Quantum Dots. *ACS Nano* **2012**, *6*, 5102-5110.
 100. Dong, H.; Gao, W.; Yan, F.; Ji, H.; Ju, H. Fluorescence Resonance Energy Transfer between Quantum Dots and Graphene Oxide for Sensing Biomolecules. *Anal. Chem.* **2010**, *82*, 5511-5517.
 101. Di Corato, R.; Bigall, N. C.; Ragusa, A.; Dorfs, D.; Genovese, A.; Marotta, R.; Manna, L.; Pellegrino, T. Multifunctional Nanobeads Based on Quantum Dots and Magnetic Nanoparticles: Synthesis and Cancer Cell Targeting and Sorting.

- ACS Nano* **2011**, *5*, 1109-1121.
102. Gao, X.; Cui, Y.; Levenson, R. M.; Chung, L. W. K.; Nie, S. In Vivo Cancer Targeting and Imaging with Semiconductor Quantum Dots. *Nat. Biotech.* **2004**, *22*, 969-976.
 103. Ye, L.; Yong, K.-T.; Liu, L.; Roy, I.; Hu, R.; Zhu, J.; Cai, H.; Law, W.-C.; Liu, J.; Wang, K.; Liu, J.; Liu, Y.; Hu, Y.; Zhang, X.; Swihart, M. T.; Prasad, P. N. A Pilot Study in Non-Human Primates Shows No Adverse Response to Intravenous Injection of Quantum Dots. *Nat. Nano.* **2012**, *7*, 453-458.
 104. Dubertret, B.; Skourides, P.; Norris, D. J.; Noireaux, V.; Brivanlou, A. H.; Libchaber, A. In Vivo Imaging of Quantum Dots Encapsulated in Phospholipid Micelles. *Science* **2002**, *298*, 1759-1762.
 105. Gupta, V.; Chaudhary, N.; Srivastava, R.; Sharma, G. D.; Bhardwaj, R.; Chand, S. Luminescent Graphene Quantum Dots for Organic Photovoltaic Devices. *J. Am. Chem. Soc.* **2011**, *133*, 9960-9963.
 106. Ran, X.; Sun, H.; Pu, F.; Ren, J.; Qu, X. Ag Nanoparticle-Decorated Graphene Quantum Dots for Label-Free, Rapid and Sensitive Detection of Ag⁺ and Biothiols. *Chem. Commun.* **2013**, *49*, 1079-1081.
 107. Sun, X.; Liu, Z.; Welsher, K.; Robinson, J. T.; Goodwin, A.; Zaric, S.; Dai, H. Nano-Graphene Oxide for Cellular Imaging and Drug Delivery. *Nano Res.* **2008**, *1*, 203-212.
 108. Zhou, X.; Zhang, Y.; Wang, C.; Wu, X.; Yang, Y.; Zheng, B.; Wu, H.; Guo, S.; Zhang, J. Photo-Fenton Reaction of Graphene Oxide: A New Strategy to Prepare Graphene Quantum Dots for DNA Cleavage. *ACS Nano* **2012**, *6*, 6592-6599.
 109. Li, L.-L.; Ji, J.; Fei, R.; Wang, C.-Z.; Lu, Q.; Zhang, J.-R.; Jiang, L.-P.; Zhu, J.-J. A Facile Microwave Avenue to Electrochemiluminescent Two-Color Graphene Quantum Dots. *Adv. Funct. Mater.* **2012**, *22*, 2971-2979.
 110. Robinson, J. T.; Tabakman, S. M.; Liang, Y.; Wang, H.; Casalongue, H. S.; Vinh, D.; Dai, H. Ultrasmall Reduced Graphene Oxide with High near-Infrared Absorbance for Photothermal Therapy. *J. Am. Chem. Soc.* **2011**, *133*, 6825-6831.
 111. Zhuo, S.; Shao, M.; Lee, S. T. Upconversion and Downconversion Fluorescent Graphene Quantum Dots: Ultrasonic Preparation and Photocatalysis. *ACS Nano* **2012**, *6*, 1059-1064.
 112. Liu, R.; Wu, D.; Feng, X.; Mullen, K. Bottom-up Fabrication of Photoluminescent Graphene Quantum Dots with Uniform Morphology. *J. Am. Chem. Soc.* **2011**, *133*, 15221-15223.
 113. Yan, X.; Cui, X.; Li, L. S. Synthesis of Large, Stable Colloidal Graphene Quantum Dots with Tunable Size. *J. Am. Chem. Soc.* **2010**, *132*, 5944-5945.
 114. Magde, D.; Wong, R.; Seybold, P. G. Fluorescence Quantum Yields and Their Relation to Lifetimes of Rhodamine 6G and Fluorescein in Nine Solvents: Improved Absolute Standards for Quantum Yields. *Photochem. Photobiol.* **2002**, *75*, 327-334.
 115. Shen, J.; Snook, R. D. Thermal Lens Measurement of Absolute Quantum Yields Using Quenched Fluorescent Samples as References. *Chem. Phys. Lett.* **1989**, *155*, 583-586.

116. Zhai, X.; Zhang, P.; Liu, C.; Bai, T.; Li, W.; Dai, L.; Liu, W. Highly Luminescent Carbon Nanodots by Microwave-Assisted Pyrolysis. *Chem. Commun.* **2012**, *48*, 7955-7957.
117. Jiang, J.; He, Y.; Li, S.; Cui, H. Amino Acids as the Source for Producing Carbon Nanodots: Microwave Assisted One-Step Synthesis, Intrinsic Photoluminescence Property and Intense Chemiluminescence Enhancement. *Chem. Commun.* **2012**, *48*, 9634-9636.
118. Zhu, H.; Wang, X.; Li, Y.; Wang, Z.; Yang, F.; Yang, X. Microwave Synthesis of Fluorescent Carbon Nanoparticles with Electrochemiluminescence Properties. *Chem. Commun.* **2009**, 5118-5120.
119. Baskin, Y.; Meyer, L. Lattice Constants of Graphite at Low Temperatures. *Phys.Rev.* **1955**, *100*, 544-544.
120. Kwon, W.; Rhee, S. W. Facile Synthesis of Graphitic Carbon Quantum Dots with Size Tunability and Uniformity Using Reverse Micelles. *Chem. Commun.* **2012**, *48*, 5256-5258.
121. Jin, Y.; Kannan, S.; Wu, M.; Zhao, J. X. Toxicity of Luminescent Silica Nanoparticles to Living Cells. *Chem. Res. Toxicol.* **2007**, *20*, 1126-1133.
122. Guo, Y.; Deng, L.; Li, J.; Guo, S.; Wang, E.; Dong, S. Hemin-Graphene Hybrid Nanosheets with Intrinsic Peroxidase-Like Activity for Label-Free Colorimetric Detection of Single-Nucleotide Polymorphism. *ACS Nano* **2011**, *5*, 1282-1290.
123. Song, Y.; Wang, X.; Zhao, C.; Qu, K.; Ren, J.; Qu, X. Label-Free Colorimetric Detection of Single Nucleotide Polymorphism by Using Single-Walled Carbon Nanotube Intrinsic Peroxidase-Like Activity. *Chemistry* **2010**, *16*, 3617-3621.
124. Wang, X.; Qu, K.; Xu, B.; Ren, J.; Qu, X. Multicolor Luminescent Carbon Nanoparticles: Synthesis, Supramolecular Assembly with Porphyrin, Intrinsic Peroxidase-Like Catalytic Activity and Applications. *Nano Res.* **2011**, *4*, 908-920.
125. Kim, J.; Cote, L. J.; Huang, J. Two Dimensional Soft Material: New Faces of Graphene Oxide. *Acc. Chem. Res.* **2012**, *45*, 1356-1364.
126. Lightcap, I. V.; Kamat, P. V. Graphitic Design: Prospects of Graphene-Based Nanocomposites for Solar Energy Conversion, Storage, and Sensing. *Acc. Chem. Res.* **2013**, *46*, 2235-2243.
127. Chung, C.; Kim, Y.-K.; Shin, D.; Ryoo, S.-R.; Hong, B. H.; Min, D.-H. Biomedical Applications of Graphene and Graphene Oxide. *Accounts. Chem. Res.* **2013**, *46*, 2211-2224.
128. Artiles, M. S.; Rout, C. S.; Fisher, T. S. Graphene-Based Hybrid Materials and Devices for Biosensing. *Adv. Drug. Deliv. Rev.* **2011**, *63*, 1352-1360.
129. Bianco, A. Graphene: Safe or Toxic? The Two Faces of the Medal. *Angew. Chem. Int. Ed.* **2013**, *52*, 4986-4997.
130. Georgakilas, V.; Otyepka, M.; Bourlinos, A. B.; Chandra, V.; Kim, N.; Kemp, K. C.; Hobza, P.; Zboril, R.; Kim, K. S. Functionalization of Graphene: Covalent and Non-Covalent Approaches, Derivatives and Applications. *Chem. Rev.* **2012**, *112*, 6156-6214.
131. Huang, X.; Qi, X.; Boey, F.; Zhang, H. Graphene-Based Composites. *Chem. Soc. Rev.* **2012**, *41*, 666-686.

132. Wu, D.; Zhang, F.; Liang, H.; Feng, X. Nanocomposites and Macroscopic Materials: Assembly of Chemically Modified Graphene Sheets. *Chem. Soc. Rev.* **2012**, *41*, 6160-6177.
133. Yoo, H.; Kim, Y.; Lee, J.; Lee, H.; Yoon, Y.; Kim, G. N-Type Reduced Graphene Oxide Field-Effect Transistors (Fets) from Photoactive Metal Oxides. *Chemistry* **2012**, *18*, 4923-4929.
134. Robinson, J. T.; Tabakman, S. M.; Liang, Y.; Wang, H.; Sanchez Casalongue, H.; Vinh, D.; Dai, H. Ultrasmall Reduced Graphene Oxide with High near-Infrared Absorbance for Photothermal Therapy. *J. Am. Chem. Soc.* **2011**, *133*, 6825-6831.
135. Jasuja, K.; Berry, V. Implantation and Growth of Dendritic Gold Nanostructures on Graphene Derivatives: Electrical Property Tailoring and Raman Enhancement. *ACS Nano* **2009**, *3*, 2358-2366.
136. Goncalves, G.; Marques, P. A. A. P.; Granadeiro, C. M.; Nogueira, H. I. S.; Singh, M. K.; Grácio, J. Surface Modification of Graphene Nanosheets with Gold Nanoparticles: The Role of Oxygen Moieties at Graphene Surface on Gold Nucleation and Growth. *Chem. Mater.* **2009**, *21*, 4796-4802.
137. Lightcap, I. V.; Kamat, P. V. Fortification of Cdse Quantum Dots with Graphene Oxide. Excited State Interactions and Light Energy Conversion. *J. Am. Chem. Soc.* **2012**, *134*, 7109-7116.
138. Yang, S.; Feng, X.; Ivanovici, S.; Müllen, K. Fabrication of Graphene-Encapsulated Oxide Nanoparticles: Towards High-Performance Anode Materials for Lithium Storage. *Angew. Chem. Int. Ed.* **2010**, *49*, 8408-8411.
139. Yang, S.; Sun, Y.; Chen, L.; Hernandez, Y.; Feng, X.; Mullen, K. Porous Iron Oxide Ribbons Grown on Graphene for High-Performance Lithium Storage. *Sci. Rep.* **2012**, *2*, 427.
140. Lee, Y. R.; Kim, I. Y.; Kim, T. W.; Lee, J. M.; Hwang, S. J. Mixed Colloidal Suspensions of Reduced Graphene Oxide and Layered Metal Oxide Nanosheets: Useful Precursors for the Porous Nanocomposites and Hybrid Films of Graphene/Metal Oxide. *Chemistry* **2012**, *18*, 2263-2271.
141. Xiao, F.; Song, J.; Gao, H.; Zan, X.; Xu, R.; Duan, H. Coating Graphene Paper with 2d-Assembly of Electrocatalytic Nanoparticles: A Modular Approach toward High-Performance Flexible Electrodes. *ACS Nano* **2011**, *6*, 100-110.
142. Xue, Y.; Zhao, H.; Wu, Z.; Li, X.; He, Y.; Yuan, Z. The Comparison of Different Gold Nanoparticles/Graphene Nanosheets Hybrid Nanocomposites in Electrochemical Performance and the Construction of a Sensitive Uric Acid Electrochemical Sensor with Novel Hybrid Nanocomposites. *Biosens. Bioelectron.* **2011**, *29*, 102-108.
143. Hu, Y.; Wang, K.; Zhang, Q.; Li, F.; Wu, T.; Niu, L. Decorated Graphene Sheets for Label-Free DNA Impedance Biosensing. *Biomaterials* **2012**, *33*, 1097-1106.
144. Wang, Y.; Li, Z.; Hu, D.; Lin, C. T.; Li, J.; Lin, Y. Aptamer/Graphene Oxide Nanocomplex for in Situ Molecular Probing in Living Cells. *J. Am. Chem. Soc.* **2010**, *132*, 9274-9276.
145. Wang, C.; Li, J.; Amatore, C.; Chen, Y.; Jiang, H.; Wang, X.-M. Gold Nanoclusters and Graphene Nanocomposites for Drug Delivery and Imaging of

- Cancer Cells. *Angew. Chem. Int. Ed.* **2011**, *50*, 11644-11648.
146. Yang, K.; Feng, L.; Shi, X.; Liu, Z. Nano-Graphene in Biomedicine: Theranostic Applications. *Chem. Soc. Rev.* **2013**, *42*, 530-547.
 147. Sun, X.; Liu, Z.; Welsher, K.; Robinson, J.; Goodwin, A.; Zaric, S.; Dai, H. Nano-Graphene Oxide for Cellular Imaging and Drug Delivery. *Nano Res.* **2008**, *1*, 203-212.
 148. Liu, Z.; Robinson, J. T.; Sun, X.; Dai, H. Pegylated Nanographene Oxide for Delivery of Water-Insoluble Cancer Drugs. *J. Am. Chem. Soc.* **2008**, *130*, 10876-10877.
 149. Xu, C.; Wang, X.; Zhu, J. Graphene–Metal Particle Nanocomposites. *J. Phys. Chem. C* **2008**, *112*, 19841-19845.
 150. Lightcap, I. V.; Kosel, T. H.; Kamat, P. V. Anchoring Semiconductor and Metal Nanoparticles on a Two-Dimensional Catalyst Mat. Storing and Shuttling Electrons with Reduced Graphene Oxide. *Nano Lett.* **2010**, *10*, 577-583.
 151. Chen, Q.; Zhang, L.; Chen, G. Facile Preparation of Graphene-Copper Nanoparticle Composite by in Situ Chemical Reduction for Electrochemical Sensing of Carbohydrates. *Anal. Chem.* **2011**, *84*, 171-178.
 152. Song, C.; Wu, D.; Zhang, F.; Liu, P.; Lu, Q.; Feng, X. Gemini Surfactant Assisted Synthesis of Two-Dimensional Metal Nanoparticles/Graphene Composites. *Chem. Commun.* **2012**, *48*, 2119-2121.
 153. Jen Cho, S.; Suri, A.; Mei, X.; Ouyang, J. In Situ Deposition of Gold Nanostructures with Well-Defined Shapes on Unfunctionalized Reduced Graphene Oxide through Chemical Reduction of a Dry Gold Precursor with Ethylene Glycol Vapor. *RSC Adv.* **2013**, *3*, 1201-1209.
 154. Wang, Y.; Yuan, R.; Chai, Y.; Yuan, Y.; Bai, L. In Situ Enzymatic Silver Enhancement Based on Functionalized Graphene Oxide and Layer-by-Layer Assembled Gold Nanoparticles for Ultrasensitive Detection of Thrombin. *Biosens. Bioelectron.* **2012**, *38*, 50-54.
 155. Bai, S.; Shen, X.; Zhu, G.; Li, M.; Xi, H.; Chen, K. In Situ Growth of Ni(X)Co(100-X) Nanoparticles on Reduced Graphene Oxide Nanosheets and Their Magnetic and Catalytic Properties. *ACS Appl. Mater. Interfaces.* **2012**, *4*, 2378-2386.
 156. Zhou, X.; Huang, X.; Qi, X.; Wu, S.; Xue, C.; Boey, F. Y. C.; Yan, Q.; Chen, P.; Zhang, H. In Situ Synthesis of Metal Nanoparticles on Single-Layer Graphene Oxide and Reduced Graphene Oxide Surfaces. *J. Phys. Chem. C* **2009**, *113*, 10842-10846.
 157. Iliut, M.; Leordean, C.; Canpean, V.; Teodorescu, C. M.; Astilean, S. A New Green, Ascorbic Acid-Assisted Method for Versatile Synthesis of Au-Graphene Hybrids as Efficient Surface-Enhanced Raman Scattering Platforms. *J. Mater. Chem. C* **2013**, *1*, 4094-4104.
 158. Kim, Y. K.; Han, S. W.; Min, D. H. Graphene Oxide Sheath on Ag Nanoparticle/Graphene Hybrid Films as an Antioxidative Coating and Enhancer of Surface-Enhanced Raman Scattering. *ACS Appl. Mater. Interfaces.* **2012**, *4*, 6545-6551.

159. Ren, W.; Fang, Y.; Wang, E. A Binary Functional Substrate for Enrichment and Ultrasensitive Sers Spectroscopic Detection of Folic Acid Using Graphene Oxide/Ag Nanoparticle Hybrids. *ACS Nano* **2011**, *5*, 6425-6433.
160. Xu, S.; Yong, L.; Wu, P. One-Pot, Green, Rapid Synthesis of Flowerlike Gold Nanoparticles/Reduced Graphene Oxide Composite with Regenerated Silk Fibroin as Efficient Oxygen Reduction Electrocatalysts. *ACS Appl. Mater. Interfaces*. **2013**, *5*, 654-662.
161. Zhu, C.; Guo, S.; Fang, Y.; Dong, S. Reducing Sugar: New Functional Molecules for the Green Synthesis of Graphene Nanosheets. *ACS Nano* **2010**, *4*, 2429-2437.
162. Zhang, Z.; Chen, H.; Xing, C.; Guo, M.; Xu, F.; Wang, X.; Gruber, H.; Zhang, B.; Tang, J. Sodium Citrate: A Universal Reducing Agent for Reduction / Decoration of Graphene Oxide with Au Nanoparticles. *Nano Res.* **2011**, *4*, 599-611.
163. Li, Y.; Gao, W.; Ci, L.; Wang, C.; Ajayan, P. M. Catalytic Performance of Pt Nanoparticles on Reduced Graphene Oxide for Methanol Electro-Oxidation. *Carbon* **2010**, *48*, 1124-1130.
164. Zhang, J.; Yang, H.; Shen, G.; Cheng, P.; Zhang, J.; Guo, S. Reduction of Graphene Oxide Via L-Ascorbic Acid. *Chem. Commun.* **2010**, *46*, 1112-1114.
165. Raveendran, P.; Fu, J.; Wallen, S. L. A Simple and "Green" Method for the Synthesis of Au, Ag, and Au-Ag Alloy Nanoparticles. *Green Chem.* **2006**, *8*, 34-38.
166. Guan, L.; Pang, H.; Wang, J.; Lu, Q.; Yin, J.; Gao, F. Fabrication of Novel Comb-Like Cu₂O Nanorod-Based Structures through an Interface Etching Method and Their Application as Ethanol Sensors. *Chem. Commun.* **2010**, *46*, 7022-7024.
167. Dai, K.; Shi, L.; Fang, J.; Zhang, Y. Synthesis of Silver Nanoparticles on Functional Multi-Walled Carbon Nanotubes. *Mater. Sci. Eng. A* **2007**, *465*, 283-286.
168. Xu, C.; Wang, X. Fabrication of Flexible Metal-Nanoparticle Films Using Graphene Oxide Sheets as Substrates. *Small* **2009**, *5*, 2212-2217.
169. Kalimuthu, P.; John, S. A. Electropolymerized Film of Functionalized Thiadiazole on Glassy Carbon Electrode for the Simultaneous Determination of Ascorbic Acid, Dopamine and Uric Acid. *Bioelectrochemistry* **2009**, *77*, 13-18.
170. Zen, J.-M.; Chen, P.-J. A Selective Voltammetric Method for Uric Acid and Dopamine Detection Using Clay-Modified Electrodes. *Anal. Chem.* **1997**, *69*, 5087-5093.
171. Randrup, A. Role of Brain Dopamine in the Antipsychotic Effect of Neuroleptics. Evidence from Studies of Amphetamine-Neuroleptic Interaction. *Mod. Probl. Pharmacopsychiatry.* **1970**, *5*, 60-65.
172. Fraga, C. G.; Motchnik, P. A.; Shigenaga, M. K.; Helbock, H. J.; Jacob, R. A.; Ames, B. N. Ascorbic Acid Protects against Endogenous Oxidative DNA Damage in Human Sperm. *Proc. Natl. Acad. Sci. U. S. A.* **1991**, *88*, 11003-11006.
173. Hare, J. M.; Johnson, R. J. Uric Acid Predicts Clinical Outcomes in Heart Failure: Insights Regarding the Role of Xanthine Oxidase and Uric Acid in Disease Pathophysiology. *Circulation* **2003**, *107*, 1951-1953.
174. Li, S.-M.; Yang, S.-Y.; Wang, Y.-S.; Lien, C.-H.; Tien, H.-W.; Hsiao, S.-T.; Liao,

- W.-H.; Tsai, H.-P.; Chang, C.-L.; Ma, C.-C. M.; Hu, C.-C. Controllable Synthesis of Nitrogen-Doped Graphene and Its Effect on the Simultaneous Electrochemical Determination of Ascorbic Acid, Dopamine, and Uric Acid. *Carbon*. **2013**, *59*, 418-429.
175. Han, D.; Han, T.; Shan, C.; Ivaska, A.; Niu, L. Simultaneous Determination of Ascorbic Acid, Dopamine and Uric Acid with Chitosan-Graphene Modified Electrode. *Electroanalysis* **2010**, *22*, 2001-2008.
176. Sun, C.-L.; Chang, C.-T.; Lee, H.-H.; Zhou, J.; Wang, J.; Sham, T.-K.; Pong, W.-F. Microwave-Assisted Synthesis of a Core-Shell Mwcnt/Gonr Heterostructure for the Electrochemical Detection of Ascorbic Acid, Dopamine, and Uric Acid. *ACS Nano* **2011**, *5*, 7788-7795.
177. Zhang, L.; Jiang, X. Attachment of Gold Nanoparticles to Glassy Carbon Electrode and Its Application for the Voltammetric Resolution of Ascorbic Acid and Dopamine. *J. ElectroAnal. Chem.* **2005**, *583*, 292-299.
178. Hu, G.; Ma, Y.; Guo, Y.; Shao, S. Electrocatalytic Oxidation and Simultaneous Determination of Uric Acid and Ascorbic Acid on the Gold Nanoparticles-Modified Glassy Carbon Electrode. *Electrochimica. Acta.* **2008**, *53*, 6610-6615.
179. Sun, C.-L.; Lee, H.-H.; Yang, J.-M.; Wu, C.-C. The Simultaneous Electrochemical Detection of Ascorbic Acid, Dopamine, and Uric Acid Using Graphene/Size-Selected Pt Nanocomposites. *Biosens. Bioelectron.* **2011**, *26*, 3450-3455.
180. Payne, D. J.; Gwynn, M. N.; Holmes, D. J.; Pompliano, D. L. Drugs for Bad Bugs: Confronting the Challenges of Antibacterial Discovery. *Nat. Rev. Drug. Discov.* **2007**, *6*, 29-40.
181. Kumarasamy, K. K.; Toleman, M. A.; Walsh, T. R.; Bagaria, J.; Butt, F.; Balakrishnan, R.; Chaudhary, U.; Doumith, M.; Giske, C. G.; Irfan, S.; Krishnan, P.; Kumar, A. V.; Maharjan, S.; Mushtaq, S.; Noorie, T.; Paterson, D. L.; Pearson, A.; Perry, C.; Pike, R.; Rao, B.; Ray, U.; Sarma, J. B.; Sharma, M.; Sheridan, E.; Thirunarayan, M. A.; Turton, J.; Upadhyay, S.; Warner, M.; Welfare, W.; Livermore, D. M.; Woodford, N. Emergence of a New Antibiotic Resistance Mechanism in India, Pakistan, and the Uk: A Molecular, Biological, and Epidemiological Study. *Lancet. Infect. Dis.* **2010**, *10*, 597-602.
182. Mallick, S.; Sharma, S.; Banerjee, M.; Ghosh, S. S.; Chattopadhyay, A.; Paul, A. Iodine-Stabilized Cu Nanoparticle Chitosan Composite for Antibacterial Applications. *ACS Appl. Mater. Interfaces.* **2012**, *4*, 1313-1323.
183. Dastjerdi, R.; Montazer, M. A Review on the Application of Inorganic Nano-Structured Materials in the Modification of Textiles: Focus on Anti-Microbial Properties. *Colloids. Surf B: Biointerfaces.* **2010**, *79*, 5-18.
184. Seil, J. T.; Webster, T. J. Antimicrobial Applications of Nanotechnology: Methods and Literature. *Int. J. Nanomedicine.* **2012**, *7*, 2767-2781.
185. Kim, K. J.; Sung, W. S.; Suh, B. K.; Moon, S. K.; Choi, J. S.; Kim, J. G.; Lee, D. G. Antifungal Activity and Mode of Action of Silver Nano-Particles on *Candida Albicans*. *Biometals* **2009**, *22*, 235-242.
186. Martínez-Castañón, G. A.; Niño-Martínez, N.; Martínez-Gutiérrez, F.; Martínez-

- Mendoza, J. R.; Ruiz, F. Synthesis and Antibacterial Activity of Silver Nanoparticles with Different Sizes. *J. Nanoparticle. Res.* **2008**, *10*, 1343-1348.
187. Marambio-Jones, C.; Hoek, E. V. A Review of the Antibacterial Effects of Silver Nanomaterials and Potential Implications for Human Health and the Environment. *J. Nanoparticle. Res.* **2010**, *12*, 1531-1551.
188. Kang, S.; Pinault, M.; Pfefferle, L. D.; Elimelech, M. Single-Walled Carbon Nanotubes Exhibit Strong Antimicrobial Activity. *Langmuir* **2007**, *23*, 8670-8673.
189. Wu, M.-C.; Deokar, A. R.; Liao, J.-H.; Shih, P.-Y.; Ling, Y.-C. Graphene-Based Photothermal Agent for Rapid and Effective Killing of Bacteria. *ACS Nano* **2013**, *7*, 1281-1290.
190. Kholmanov, I. N.; Stoller, M. D.; Edgeworth, J.; Lee, W. H.; Li, H.; Lee, J.; Barnhart, C.; Potts, J. R.; Piner, R.; Akinwande, D.; Barrick, J. E.; Ruoff, R. S. Nanostructured Hybrid Transparent Conductive Films with Antibacterial Properties. *ACS Nano* **2012**, *6*, 5157-5163.
191. Liu, S.; Zeng, T. H.; Hofmann, M.; Burcombe, E.; Wei, J.; Jiang, R.; Kong, J.; Chen, Y. Antibacterial Activity of Graphite, Graphite Oxide, Graphene Oxide, and Reduced Graphene Oxide: Membrane and Oxidative Stress. *ACS Nano* **2011**, *5*, 6971-6980.
192. Ocsoy, I.; Paret, M. L.; Ocsoy, M. A.; Kunwar, S.; Chen, T.; You, M.; Tan, W. Nanotechnology in Plant Disease Management: DNA-Directed Silver Nanoparticles on Graphene Oxide as an Antibacterial against *Xanthomonas Perforans*. *ACS Nano* **2013**, *7*, 8972-8980.
193. Ristic, B. Z.; Milenkovic, M. M.; Dakic, I. R.; Todorovic-Markovic, B. M.; Milosavljevic, M. S.; Budimir, M. D.; Paunovic, V. G.; Dramicanin, M. D.; Markovic, Z. M.; Trajkovic, V. S. Photodynamic Antibacterial Effect of Graphene Quantum Dots. *Biomaterials* **2014**, *35*, 4428-4435.
194. Tu, Y.; Lv, M.; Xiu, P.; Huynh, T.; Zhang, M.; Castelli, M.; Liu, Z.; Huang, Q.; Fan, C.; Fang, H.; Zhou, R. Destructive Extraction of Phospholipids from *Escherichia Coli* Membranes by Graphene Nanosheets. *Nat. Nanotechnol.* **2013**, *8*, 594-601.
195. Kellici, S.; Acord, J.; Ball, J.; Reehal, H. S.; Morgan, D.; Saha, B. A Single Rapid Route for the Synthesis of Reduced Graphene Oxide with Antibacterial Activities. *RSC Adv.* **2014**, *4*, 14858-14861.
196. Siddhartha, S.; Tanmay, B.; Arnab, R.; Gajendra, S.; Ramachandrarao, P.; Debabrata, D. Characterization of Enhanced Antibacterial Effects of Novel Silver Nanoparticles. *Nanotechnology* **2007**, *18*, 225103.
197. Kim, J. S.; Kuk, E.; Yu, K. N.; Kim, J.-H.; Park, S. J.; Lee, H. J.; Kim, S. H.; Park, Y. K.; Park, Y. H.; Hwang, C.-Y.; Kim, Y.-K.; Lee, Y.-S.; Jeong, D. H.; Cho, M.-H. Antimicrobial Effects of Silver Nanoparticles. *Nanomedicine: NBM.* **2007**, *3*, 95-101.
198. Feng, L.; Wu, L.; Qu, X. New Horizons for Diagnostics and Therapeutic Applications of Graphene and Graphene Oxide. *Adv. Mater.* **2013**, *25*, 168-186.
199. Dreyer, D. R.; Park, S.; Bielawski, C. W.; Ruoff, R. S. The Chemistry of Graphene Oxide. *Chem. Soc. Rev.* **2010**, *39*, 228-240.

200. Jastrzębska, A.; Kurtycz, P.; Olszyna, A. Recent Advances in Graphene Family Materials Toxicity Investigations. *J. Nanoparticle. Res.* **2012**, *14*, 1-21.
201. Feng, L.; Liu, Z. Graphene in Biomedicine: Opportunities and Challenges. *Nanomedicine* **2011**, *6*, 317-324.
202. Yang, K.; Li, Y.; Tan, X.; Peng, R.; Liu, Z. Behavior and Toxicity of Graphene and Its Functionalized Derivatives in Biological Systems. *Small* **2013**, *9*, 1492-1503.
203. Li, F.; Pei, H.; Wang, L.; Lu, J.; Gao, J.; Jiang, B.; Zhao, X.; Fan, C. Nanomaterial-Based Fluorescent DNA Analysis: A Comparative Study of the Quenching Effects of Graphene Oxide, Carbon Nanotubes, and Gold Nanoparticles. *Adv. Funct. Mater.* **2013**, *23*, 4140-4148.
204. Jang, H.; Ryoo, S.-R.; Kim, Y.-K.; Yoon, S.; Kim, H.; Han, S. W.; Choi, B.-S.; Kim, D.-E.; Min, D.-H. Discovery of Hepatitis C Virus Ns3 Helicase Inhibitors by a Multiplexed, High-Throughput Helicase Activity Assay Based on Graphene Oxide. *Angew. Chem. Int. Ed.* **2013**, *52*, 2340-2344.
205. Shi, S.; Yang, K.; Hong, H.; Valdovinos, H. F.; Nayak, T. R.; Zhang, Y.; Theuer, C. P.; Barnhart, T. E.; Liu, Z.; Cai, W. Tumor Vasculature Targeting and Imaging in Living Mice with Reduced Graphene Oxide. *Biomaterials* **2013**, *34*, 3002-3009.
206. Liu, Q.; Guo, B.; Rao, Z.; Zhang, B.; Gong, J. R. Strong Two-Photon-Induced Fluorescence from Photostable, Biocompatible Nitrogen-Doped Graphene Quantum Dots for Cellular and Deep-Tissue Imaging. *Nano Lett.* **2013**, *13*, 2436-2441.
207. Kim, H.; Lee, D.; Kim, J.; Kim, T.-i.; Kim, W. J. Photothermally Triggered Cytosolic Drug Delivery Via Endosome Disruption Using a Functionalized Reduced Graphene Oxide. *ACS Nano* **2013**, *7*, 6735-6746.
208. Chen, Y.; Xu, P.; Shu, Z.; Wu, M.; Wang, L.; Zhang, S.; Zheng, Y.; Chen, H.; Wang, J.; Li, Y.; Shi, J. Multifunctional Graphene Oxide-Based Triple Stimuli-Responsive Nanotheranostics. *Adv. Funct. Mater.* **2014**, *24*, 4386-4396.
209. Wang, Y.; Wang, K.; Zhao, J.; Liu, X.; Bu, J.; Yan, X.; Huang, R. Multifunctional Mesoporous Silica-Coated Graphene Nanosheet Used for Chemo-Photothermal Synergistic Targeted Therapy of Glioma. *J. Am. Chem. Soc.* **2013**, *135*, 4799-4804.
210. Hu, S. H.; Chen, Y. W.; Hung, W. T.; Chen, I. W.; Chen, S. Y. Quantum-Dot-Tagged Reduced Graphene Oxide Nanocomposites for Bright Fluorescence Bioimaging and Photothermal Therapy Monitored in Situ. *Adv. Mater.* **2012**, *24*, 1748-1754.
211. Chen, Y.-W.; Chen, P.-J.; Hu, S.-H.; Chen, I. W.; Chen, S.-Y. Nir-Triggered Synergic Photo-Chemothermal Therapy Delivered by Reduced Graphene Oxide/Carbon/Mesoporous Silica Nanocookies. *Adv. Funct. Mater.* **2014**, *24*, 451-459.
212. Li, M.; Yang, X.; Ren, J.; Qu, K.; Qu, X. Using Graphene Oxide High near-Infrared Absorbance for Photothermal Treatment of Alzheimer's Disease. *Adv. Mater.* **2012**, *24*, 1722-1728.
213. Lim, D.-K.; Barhoumi, A.; Wylie, R. G.; Reznor, G.; Langer, R. S.; Kohane, D.

- S. Enhanced Photothermal Effect of Plasmonic Nanoparticles Coated with Reduced Graphene Oxide. *Nano Lett.* **2013**, *13*, 4075-4079.
214. Tian, B.; Wang, C.; Zhang, S.; Feng, L.; Liu, Z. Photothermally Enhanced Photodynamic Therapy Delivered by Nano-Graphene Oxide. *ACS Nano* **2011**, *5*, 7000-7009.
215. Zhang, W.; Guo, Z.; Huang, D.; Liu, Z.; Guo, X.; Zhong, H. Synergistic Effect of Chemo-Photothermal Therapy Using Pegylated Graphene Oxide. *Biomaterials* **2011**, *32*, 8555-8561.
216. Tang, J.; Chen, Q.; Xu, L.; Zhang, S.; Feng, L.; Cheng, L.; Xu, H.; Liu, Z.; Peng, R. Graphene Oxide–Silver Nanocomposite as a Highly Effective Antibacterial Agent with Species-Specific Mechanisms. *ACS Appl. Mater. Interfaces.* **2013**, *5*, 3867-3874.
217. Fan, Z.; Liu, B.; Wang, J.; Zhang, S.; Lin, Q.; Gong, P.; Ma, L.; Yang, S. A Novel Wound Dressing Based on Ag/Graphene Polymer Hydrogel: Effectively Kill Bacteria and Accelerate Wound Healing. *Adv. Funct. Mater.* **2014**, *24*, 3933-3943.
218. Cai, X.; Lin, M.; Tan, S.; Mai, W.; Zhang, Y.; Liang, Z.; Lin, Z.; Zhang, X. The Use of Polyethyleneimine-Modified Reduced Graphene Oxide as a Substrate for Silver Nanoparticles to Produce a Material with Lower Cytotoxicity and Long-Term Antibacterial Activity. *Carbon* **2012**, *50*, 3407-3415.
219. Joshi, M. K.; Pant, H. R.; Kim, H. J.; Kim, J. H.; Kim, C. S. One-Pot Synthesis of Ag-Iron Oxide/Reduced Graphene Oxide Nanocomposite Via Hydrothermal Treatment. *Colloids. Surfaces. A* **2014**, *446*, 102-108.
220. Novoselov, K. S.; Falko, V. I.; Colombo, L.; Gellert, P. R.; Schwab, M. G.; Kim, K. A Roadmap for Graphene. *Nature* **2012**, *490*, 192-200.
221. Chen, D.; Feng, H.; Li, J. Graphene Oxide: Preparation, Functionalization, and Electrochemical Applications. *Chem. Rev.* **2012**, *112*, 6027-6053.
222. Eda, G.; Lin, Y.-Y.; Mattevi, C.; Yamaguchi, H.; Chen, H.-A.; Chen, I. S.; Chen, C.-W.; Chhowalla, M. Blue Photoluminescence from Chemically Derived Graphene Oxide. *Adv. Mater.* **2010**, *22*, 505-509.
223. Chien, C. T.; Li, S. S.; Lai, W. J.; Yeh, Y. C.; Chen, H. A.; Chen, I. S.; Chen, L. C.; Chen, K. H.; Nemoto, T.; Isoda, S.; Chen, M.; Fujita, T.; Eda, G.; Yamaguchi, H.; Chhowalla, M.; Chen, C. W. Tunable Photoluminescence from Graphene Oxide. *Angew. Chem. Int. Ed.* **2012**, *51*, 6662-6666.
224. Luo, Z.; Vora, P. M.; Mele, E. J.; Johnson, A. T. C.; Kikkawa, J. M. Photoluminescence and Band Gap Modulation in Graphene Oxide. *Appl. Phys. Lett.* **2009**, *94*, 111909-111903.
225. Ramakrishna Matte, H. S. S.; Subrahmanyam, K. S.; Venkata Rao, K.; George, S. J.; Rao, C. N. R. Quenching of Fluorescence of Aromatic Molecules by Graphene Due to Electron Transfer. *Chem. Phys. Lett.* **2011**, *506*, 260-264.
226. Liu, Y.; Liu, C.-y.; Liu, Y. Investigation on Fluorescence Quenching of Dyes by Graphite Oxide and Graphene. *Appl. Surface. Sci.* **2011**, *257*, 5513-5518.
227. Dong, H.; Zhang, J.; Ju, H.; Lu, H.; Wang, S.; Jin, S.; Hao, K.; Du, H.; Zhang, X. Highly Sensitive Multiple Microrna Detection Based on Fluorescence Quenching of Graphene Oxide and Isothermal Strand-Displacement Polymerase Reaction.

- Anal. Chem.* **2012**, *84*, 4587-4593.
228. Huang, P. J.; Liu, J. Molecular Beacon Lighting up on Graphene Oxide. *Anal. Chem.* **2012**, *84*, 4192-4198.
229. Wu, S.; Duan, N.; Ma, X.; Xia, Y.; Wang, H.; Wang, Z.; Zhang, Q. Multiplexed Fluorescence Resonance Energy Transfer Aptasensor between Upconversion Nanoparticles and Graphene Oxide for the Simultaneous Determination of Mycotoxins. *Anal. Chem.* **2012**, *84*, 6263-6270.
230. Liu, Y.; Dong, X.; Chen, P. Biological and Chemical Sensors Based on Graphene Materials. *Chem. Soc. Rev.* **2012**, *41*, 2283-2307.
231. Sreejith, S.; Ma, X.; Zhao, Y. Graphene Oxide Wrapping on Squaraine-Loaded Mesoporous Silica Nanoparticles for Bioimaging. *J. Am. Chem. Soc.* **2012**, *134*, 17346-17349.
232. He, S.; Song, B.; Li, D.; Zhu, C.; Qi, W.; Wen, Y.; Wang, L.; Song, S.; Fang, H.; Fan, C. A Graphene Nanoprobe for Rapid, Sensitive, and Multicolor Fluorescent DNA Analysis. *Adv. Funct. Mater.* **2010**, *20*, 453-459.
233. Tu, Y.; Li, W.; Wu, P.; Zhang, H.; Cai, C. Fluorescence Quenching of Graphene Oxide Integrating with the Site-Specific Cleavage of the Endonuclease for Sensitive and Selective MicroRNA Detection. *Anal. Chem.* **2013**, *85*, 2536-2542.
234. Jang, H.; Kim, Y. K.; Kwon, H. M.; Yeo, W. S.; Kim, D. E.; Min, D. H. A Graphene-Based Platform for the Assay of Duplex-DNA Unwinding by Helicase. *Angew. Chem. Int. Ed.* **2010**, *49*, 5703-5707.
235. Lu, C. H.; Yang, H. H.; Zhu, C. L.; Chen, X.; Chen, G. N. A Graphene Platform for Sensing Biomolecules. *Angew. Chem. Int. Ed.* **2009**, *48*, 4785-4787.
236. Zhang, C.; Yuan, Y.; Zhang, S.; Wang, Y.; Liu, Z. Biosensing Platform Based on Fluorescence Resonance Energy Transfer from Upconverting Nanocrystals to Graphene Oxide. *Angew. Chem. Int. Ed.* **2011**, *50*, 6851-6854.
237. Zhang, M.; Yin, B. C.; Tan, W.; Ye, B. C. A Versatile Graphene-Based Fluorescence "on/off" Switch for Multiplex Detection of Various Targets. *Biosens. Bioelectron.* **2011**, *26*, 3260-3265.
238. Swathi, R. S.; Sebastian, K. L. Long Range Resonance Energy Transfer from a Dye Molecule to Graphene Has (Distance)⁻⁴ Dependence. *J. Chem. Phys.* **2009**, *130*, 086101.
239. Schaufele, F.; Demarco, I.; Day, R. N. 4 - FRET Imaging in the Wide-Field Microscope. In *Molecular Imaging*, Periasamy, A.; Day, R. N., Eds. American Physiological Society: San Diego, 2005; pp 72-94.
240. Huang, P.-J. J.; Liu, J. DNA-Length-Dependent Fluorescence Signaling on Graphene Oxide Surface. *Small* **2012**, *8*, 977-983.
241. Piao, Y.; Liu, F.; Seo, T. S. The Photoluminescent Graphene Oxide Serves as an Acceptor Rather Than a Donor in the Fluorescence Resonance Energy Transfer Pair of Cy3.5-Graphene Oxide. *Chem. Commun.* **2011**, *47*, 12149-12151.
242. Xu, S.; Hartvickson, S.; Zhao, J. X. Engineering of SiO₂-Au-SiO₂ Sandwich Nanoaggregates Using a Building Block: Single, Double, and Triple Cores for Enhancement of near Infrared Fluorescence. *Langmuir* **2008**, *24*, 7492-7499.
243. Chen, J.; Jin, Y.; Fahrudin, N.; Zhao, J. X. Development of Gold Nanoparticle-

- Enhanced Fluorescent Nanocomposites. *Langmuir* **2013**, *29*, 1584-1591.
244. Wang, Y.; Kurunthu, D.; Scott, G. W.; Bardeen, C. J. Fluorescence Quenching in Conjugated Polymers Blended with Reduced Graphitic Oxide. *J. Phys. Chem. C* **2010**, *114*, 4153-4159.
 245. Peters, B. M.; Shirtliff, M. E.; Jabra-Rizk, M. A. Antimicrobial Peptides: Primeval Molecules or Future Drugs? *PLoS Pathog* **2010**, *6*, e1001067.
 246. Pompilio, A.; Crocetta, V.; Scocchi, M.; Pomponio, S.; Di Vincenzo, V.; Mardirossian, M.; Gherardi, G.; Fiscarelli, E.; Dicuonzo, G.; Gennaro, R.; Di Bonaventura, G. Potential Novel Therapeutic Strategies in Cystic Fibrosis: Antimicrobial and Anti-Biofilm Activity of Natural and Designed Alpha-Helical Peptides against *Staphylococcus Aureus*, *Pseudomonas Aeruginosa*, and *Stenotrophomonas Maltophilia*. *BMC. Microbiol.* **2012**, *12*, 145.
 247. Lopes, S. P.; Ceri, H.; Azevedo, N. F.; Pereira, M. O. Antibiotic Resistance of Mixed Biofilms in Cystic Fibrosis: Impact of Emerging Microorganisms on Treatment of Infection. *Int. J. Antimicrob. Agents.* **2012**, *40*, 260-263.
 248. Lee, J.-K.; Park, S.-C.; Hahm, K.-S.; Park, Y. A Helix-Pxxp-Helix Peptide with Antibacterial Activity without Cytotoxicity against Mdrpa-Infected Mice. *Biomaterials* **2014**, *35*, 1025-1039.
 249. Beyth, N.; Yudovin-Farber, I.; Bahir, R.; Domb, A. J.; Weiss, E. I. Antibacterial Activity of Dental Composites Containing Quaternary Ammonium Polyethylenimine Nanoparticles against *Streptococcus Mutans*. *Biomaterials* **2006**, *27*, 3995-4002.
 250. Guzman, M.; Dille, J.; Godet, S. Synthesis and Antibacterial Activity of Silver Nanoparticles against Gram-Positive and Gram-Negative Bacteria. *Nanomedicine: NBM.* **2012**, *8*, 37-45.
 251. Wang, H.; Liu, J.; Wu, X.; Tong, Z.; Deng, Z. Tailor-Made Au@Ag Core-Shell Nanoparticle 2d Arrays on Protein-Coated Graphene Oxide with Assembly Enhanced Antibacterial Activity. *Nanotechnology* **2013**, *24*, 205102.
 252. Chen, J.; Peng, H.; Wang, X.; Shao, F.; Yuan, Z.; Han, H. Graphene Oxide Exhibits Broad-Spectrum Antimicrobial Activity against Bacterial Phytopathogens and Fungal Conidia by Intertwining and Membrane Perturbation. *Nanoscale* **2014**, *6*, 1879-1889.
 253. Chernousova, S.; Epple, M. Silver as Antibacterial Agent: Ion, Nanoparticle, and Metal. *Angew. Chem. Int. Ed.* **2013**, *52*, 1636-1653.
 254. Panáček, A.; Kvítek, L.; Pucek, R.; Kolář, M.; Večeřová, R.; Pizúrová, N.; Sharma, V. K.; Nevěčná, T. j.; Zbořil, R. Silver Colloid Nanoparticles: Synthesis, Characterization, and Their Antibacterial Activity. *J. Phys. Chem. B* **2006**, *110*, 16248-16253.
 255. Xiu, Z.-m.; Zhang, Q.-b.; Puppala, H. L.; Colvin, V. L.; Alvarez, P. J. J. Negligible Particle-Specific Antibacterial Activity of Silver Nanoparticles. *Nano Lett.* **2012**, *12*, 4271-4275.
 256. Hu, W.; Peng, C.; Luo, W.; Lv, M.; Li, X.; Li, D.; Huang, Q.; Fan, C. Graphene-Based Antibacterial Paper. *ACS Nano* **2010**, *4*, 4317-4323.
 257. Akhavan, O.; Ghaderi, E. Toxicity of Graphene and Graphene Oxide Nanowalls

- against Bacteria. *ACS Nano* **2010**, *4*, 5731-5736.
258. Tu, Y.; Lv, M.; Xiu, P.; Huynh, T.; Zhang, M.; Castelli, M.; Liu, Z.; Huang, Q.; Fan, C.; Fang, H.; Zhou, R. Destructive Extraction of Phospholipids from Escherichia Coli Membranes by Graphene Nanosheets. *Nat. Nanotechnol.* **2013**, *8*, 594-601.
 259. Kalita, M.; Balivada, S.; Swarup, V. P.; Mencio, C.; Raman, K.; Desai, U. R.; Troyer, D.; Kuberan, B. A Nanosensor for Ultrasensitive Detection of Oversulfated Chondroitin Sulfate Contaminant in Heparin. *J. Am. Chem. Soc.* **2014**, *136*, 554-557.
 260. Wu, X.; Tian, F.; Wang, W.; Chen, J.; Wu, M.; Zhao, J. X. Fabrication of Highly Fluorescent Graphene Quantum Dots Using L-Glutamic Acid for in Vitro/in Vivo Imaging and Sensing. *J. Mater. Chem. C* **2013**, *1*, 4676-4684.
 261. Pan, Y.; Sahoo, N. G.; Li, L. The Application of Graphene Oxide in Drug Delivery. *Expert. Opin. Drug. Deliv.* **2012**, *9*, 1365-1376.
 262. Liu, S.; Hu, M.; Zeng, T. H.; Wu, R.; Jiang, R.; Wei, J.; Wang, L.; Kong, J.; Chen, Y. Lateral Dimension-Dependent Antibacterial Activity of Graphene Oxide Sheets. *Langmuir* **2012**, *28*, 12364-12372.
 263. Wu, M. C.; Deokar, A. R.; Liao, J. H.; Shih, P. Y.; Ling, Y. C. Graphene-Based Photothermal Agent for Rapid and Effective Killing of Bacteria. *ACS Nano* **2013**, *7*, 1281-1290.
 264. Li, X.; Zhou, X.; Ye, Y.; Li, Y.; Li, J.; Privratsky, B.; Wu, E.; Gao, H.; Huang, C.; Wu, M. Lyn Regulates Inflammatory Responses in Klebsiella Pneumoniae Infection Via the P38/Nf-Kappab Pathway. *Eur. J. Immunol.* **2014**, *44*, 763-773.
 265. Guo, Q.; Shen, N.; Yuan, K.; Li, J.; Wu, H.; Zeng, Y.; Fox, J., 3rd; Bansal, A. K.; Singh, B. B.; Gao, H.; Wu, M. Caveolin-1 Plays a Critical Role in Host Immunity against Klebsiella Pneumoniae by Regulating Stat5 and Akt Activity. *Eur. J. Immunol.* **2012**, *42*, 1500-1511.
 266. Kannan, S.; Pang, H.; Foster, D. C.; Rao, Z.; Wu, M. Human 8-Oxoguanine DNA Glycosylase Increases Resistance to Hyperoxic Cytotoxicity in Lung Epithelial Cells and Involvement with Altered Mapk Activity. *Cell. Death. Differ.* **2006**, *13*, 311-323.
 267. He, Y. H.; Wu, M.; Kobune, M.; Xu, Y.; Kelley, M. R.; Martin, W. J., 2nd. Expression of Yeast Apurinic/Apyrimidinic Endonuclease (Apn1) Protects Lung Epithelial Cells from Bleomycin Toxicity. *Am. J. Respir. Cell. Mol. Biol.* **2001**, *25*, 692-698.
 268. Yuan, K.; Huang, C.; Fox, J.; Laternus, D.; Carlson, E.; Zhang, B.; Yin, Q.; Gao, H.; Wu, M. Autophagy Plays an Essential Role in the Clearance of Pseudomonas Aeruginosa by Alveolar Macrophages. *J. Cell. Sci.* **2012**, *125*, 507-515.
 269. He, Y. H.; Xu, Y.; Kobune, M.; Wu, M.; Kelley, M. R.; Martin, W. J., 2nd. Escherichia Coli Fpg and Human Ogg1 Reduce DNA Damage and Cytotoxicity by Bcnu in Human Lung Cells. *Am. J. Physiol. Lung. Cell. Mol. Physiol.* **2002**, *282*, L50-55.